Experimental Study of Transitional Flow Behavior in a Simulated Low Pressure Turbine

Ki Hyeon Sohn and Kenneth J. De Witt

University of Toledo

Toledo, Ohio

August 1998

Prepared for
NASA Lewis Research Center
Under Grant NCC3-288

ABSTRACT

A detailed investigation of the flow physics occurring on the suction side of a simulated Low Pressure Turbine (LPT) blade was performed. A contoured upper wall was designed to simulate the pressure distribution of an actual LPT airfoil onto a flat lower plate. The experiments were carried out for the Reynolds numbers of 35,000, 70,000, 100,000 and 250,000 with four levels of freestream turbulence ranging from 1 % to 4 %. For the three lower Reynolds numbers, the boundary layer on the flat plate was separated and formed a bubble. The size of laminar separation bubble was measured to be inversely proportional to the freestream turbulence levels and Reynolds numbers. However, no separation was observed for the Re = 250,000 case.

The transition on a separated flow was found to proceed through the formation of turbulent spots in the free shear layer as evidenced in the intermittency profiles for Re = 35,000, 70,000 and 100,000. Spectral data show no evidence of Kelvin-Helmholtz or Tollmien-Schlichting instability waves in the free shear layer over a separation bubble (bypass transition). However, the flow visualization revealed the large vortex structures just outside of the bubble and their development to turbulent flow for Re = 50,000, which is similar to that in the free shear layer (separated-flow transition). Therefore, it is fair to say that the bypass and separated-flow transition modes coexist in the transitional flows over the separation bubble for certain conditions. Transition onset and end locations and length determined from intermittency profiles decrease as Reynolds number and freestream turbulence levels increase.

ACKNOWLEDGEMENTS

This experimental study was supported by NASA Lewis Research Center under grant number NAG 3-288. The grant monitors were Mr. Fred Simon and Dr. David Ashpis. The authors appreciate their support and patience.

TABLE OF CONTENTS

	Page
ABSTRACT	i
ACKNOWLEDGEMENTS	ii
TABLE OF CONTENTS	iii
NOMENCLATURE	v
CHAPTER I INTRODUCTION	1
CHAPTER II EXPERIMENTAL FACILITY AND INSTRUMENTATION	8
Wind Tunnel	8
Test Section	9
Design of Contoured Wall	10
Instrumentation	12
CHAPTER III DATA REDUCTION	16
Velocity and Integral Data	16
Intermittency	17
Integral Length Scale	19
Power Spectra	20
CHAPTER IV RESULTS AND DISCUSSION	23
FREESTREAM CONDITIONS	24
FLOW VISUALIZATION	27

STATIC PRESSURE DISTRIBUTION 30

CHARACTERISTICS OF SEPARATION AND TRANSITION 33

Freestream Turbulence Effects on the Flow Field 33

Mean Velocity Profiles 33

Fluctuating RMS Velocity Profiles 41

Integral Quantities 47

Intermittency Profiles 50

Power Spectra 54

Reynolds Number Effects on the Separated Flow 58

Flow with Freestream Turbulence level of 1 % (Grid 0) 59

Flow with Freestream Turbulence level of 2 % (Grid 2) 63

Flow with Freestream Turbulence level of 3 % (Grid 3) 67

Transition Model of the Separated Flow 70

CHAPTER V SUMMARY AND CONCLUSIONS 75

REFERENCES 78

TABLES 81

FIGURES 97

NOMENCLATURE

C_P	Static pressure coefficient [$= (p_s - p_{s_{exit}})/\frac{1}{2}\rho U^2_{e_{exit}}$]
f	Frequency, Hz
FSTI	Freestream turbulence level [$= u'_{rms}/U_{in}$], %
H_{12}	Shape factor [$= \delta^*/\theta$]
H_{32}	Shape factor [$= \varepsilon/\theta$]
L	Integral length scale [$= PSD(0)\ U_e / 4\,u'^2_{rms}$], inch
l	Effective plate length, inch
$l1$	Streamwise distance between separation and max. bubble height, inch
p_s	Local static pressure, psi
p_t	Total pressure, psi
PSD	Normalized power spectral density [$= \varphi(\omega)\,2\pi\ u'^2_{rms}$], m^2/Hz
$\overline{P}$	Gaster's pressure parameter [$= (\theta_s{}^2/\nu)(\Delta U/\Delta x)$]
R(r)	Correlation coefficient $\left[= \overline{u_1(x)\,u_2(x+r)} \Big/ \left(\sqrt{\overline{u_1^2(x)}}\sqrt{\overline{u_2^2(x+r)}} \right)\right]$
$R(\tau)$	Autocorrelation coefficient [$= \overline{u(t)u(t+\tau)}\,/\,u'^2_{rms}$]
r	Spatial distance in correlation coefficient
Re	Test section Reynolds number [$= U_{e_{exit}} l/\nu$]
Re_{l1}	Reynolds number based on the streamwise distance between separation and max. bubble height
Re_{LT}	Reynolds number based on transition length

$Re_{X_{st}}$	Reynolds number based on the distance between separation and start of transition
$Re_{\theta s}$	Momentum thickness Reynolds number at separation [$= U_{e_s}\theta_s/\nu$]
t	Time, sec
Tu	Local freestream turbulence intensity [$=u'_{rms}/U_e$], %
U	Streamwise mean velocity, ft/sec
u	Streamwise instantaneous velocity, ft/sec
u'_{rms}	Streamwise fluctuating rms velocity, ft/sec
X, x	Streamwise distance from leading edge, inch
X_{LT}	Transition length [$= X_{te} - X_{ts}$], inch
y	Normal distance from surface, inch

Greek

$\delta_{.995}$	Boundary layer thickness at $U/U_e = 0.995$, inch
δ^*	Displacement thickness $\left[= \int_0^\infty (1 - U/U_e)dy\right]$, inch
θ	Momentum thickness $\left[= \int_0^\infty (U/U_e)(1 - U/U_e)dy\right]$, inch
ε	Energy thickness $\left[= \int_0^\infty (U/U_e)(1 - U^2/U_e^2)dy\right]$, inch
γ	Intermittency
τ	Time delay in autocorrelation function
$\varphi(\omega)$	Power spectral density $\left[= \frac{2}{\pi}\int_0^\infty R(\tau)\cos(\omega\tau)d\tau\right]$

ψ_i	Stream function $\left[= \int_0^{y_i} (U/U_{in})dy \right]$
ν	Kinematic viscosity, ft^2/sec
ω	Frequency, radians/sec

Subscripts

B	Bubble
e	Edge of boundary layer
exit	Test section exit condition
in	Inlet condition
R	Reattachment
rms	Root mean square
S, s	Separation
te	End of transition
ts	Start of transition

CHAPTER I

INTRODUCTION

Gas turbine engine designers are constantly seeking ways to improve engine efficiency. Turbine engines are usually designed for peak performance at high Reynolds number take-off conditions. Since turbine engines are operated at various flow conditions, the optimally designed engines for one condition may perform poorly under different conditions and have a substantial loss of engine efficiency. This efficiency loss can result in increased fuel consumption and operating cost. However, the engine performance in various off-design-operating conditions is difficult to access due to lack of data and understanding of the detailed flow physics. This is true especially for engine components such as the compressor and the low pressure turbine (LPT). The flows on turbine airfoils are quite complex in nature since so many factors are interacting in a non-linear fashion. Some of the primary factors are freestream turbulence, Reynolds numbers, blade loading, wake passing and interaction with boundary layers, unsteadiness, three dimensional effects, etc. It is first important to understand the individual effects these factors have on the engine performance one at a time, and through accumulation of knowledge, understanding of the real complex engine flows can be approached with confidence.

On typical low pressure turbine blades, the velocity gradient on the pressure surface is always of an accelerating nature. Transition on the pressure surface usually

begins before the maximum pressure point. The subsequent boundary layer development is quite delayed due to a strong acceleration, and relaminarization of the boundary layer frequently occurs near the trailing edge. The strong acceleration generates much lower profile losses than encountered in zero pressure gradient or flows on the suction surface, and constitutes only about 15 to 20 percent of the total profile loss. The remainder of the loss is due to the boundary layer on the suction surface.

At the high Reynolds number take-off condition, transition usually begins on the suction surface near the minimum pressure point and the boundary layer remains attached on the low pressure turbine airfoils. Since incoming freestream turbulence is highly disturbed, the initial disturbance level is large enough to be considered non-linear so that the boundary layer undergoes a bypass transition. However, at the high altitude cruising condition of low Reynolds number, the boundary layer has a tendency to remain laminar. Due to the adverse pressure gradient, this laminar flow might separate on the surface before it becomes turbulent, especially under conditions of higher incident angles for various ranges of Reynolds numbers. This separation bubble may or may not reattach depending on the conditions. The long (bursting) separation bubble at these off-design conditions can cause a drastic loss of lift and increase in drag, which results in a significant degradation of engine performance. The transition process on the separated flow is believed to be occurring along the free shear layer of the separation bubble by way of either bypass or separated flow modes, depending on the environmental factors, primarily due to Reynolds numbers (Mayle, 1991).

The accurate prediction of the separation and transition processes on LPT blades under the influence of adverse pressure gradients, altitude Reynolds numbers, and various freestream turbulence levels can lead directly to improved engine efficiency and lower specific fuel consumption. According to Hourmouziadis (1989, in Mayle, 1991), the above prediction can easily increase low pressure turbine efficiency by several percentage points. One concern is the lack of understanding of boundary layer behavior in the turbine engine environment. Thus, the low pressure turbine (LPT) boundary layer program was established to develop and evaluate technology that can increase engine efficiency through understanding and utilizing knowledge concerning separated flow transition over a bubble in advanced gas turbine engines. The detailed understanding of the flow physics of boundary layer development on turbine airfoils is one of the important aspects of turbomachinery research activities at the NASA Lewis Research Center and is of great concern to the turbine engine manufacturers. The primary objective of this experimental work is studying the flow characteristics typical of those found on the suction surface of low pressure turbine airfoils in order to improve the efficiency of current turbine engines.

Mayle (1991) studied the laminar-turbulent transition phenomena and their role in aerodynamics and heat transfer in gas turbine engines. He reviewed transition phenomena on engine throughflow components from both theoretical and experimental standpoints, and developed various correlation models on different transition modes. Mayle emphasized the importance of freestream turbulence (level and scale) and periodic unsteady wake effects on transition. As for the flow on the suction surface of a LPT

airfoil, he pointed out that the transition occurring in a separated laminar boundary layer might or might not involve instability of the Tollmien-Schlichting type. Gaster (1969) detected Tollmien-Schlichting instability waves in the 'long' bubbles since much of the flow in the bubble is laminar with low freestream turbulence levels. The existence of Tollmien-Schlichting instability is not known for the case for higher turbulence levels even though Mayle speculated it is possible.

Gadner et al. (1981) performed experimental studies on the effect of loading on LPT blades. The results showed that, when designed properly, highly loaded blades exhibit higher performance than blades designed with a lower loading profile. Thus, modern LPT blades are now designed to be more highly loaded and have a lower aspect ratio, introducing more severe adverse pressure gradients into the flow field. Thus, the flow has a tendency to separate easily from the blade surface at certain off-design conditions. More systematic and well-controlled experiments are required to help improve modeling and computational analyses of the flow behavior on a LPT blade.

Halstead et al. (1995a, 1995b, and 1995c) performed an experimental study of boundary layer development on the suction surface of airfoils in compressors and an embedded stage of a low pressure turbine (General Electric). This study revealed substantial regions of laminar and transitional flow on the suction surface. They found that unsteady, periodic boundary layers were developed on turbine airfoils along the following separate two paths that are coupled by a calmed region: a wake-induced path which generates the calmed region and a path between wakes which contains the calmed regions. The higher shear stress in the calmed region was effective in suppressing the

flow separation. They observed bypass and separated-flow transition modes on both the suction and pressure surfaces.

Halstead et al. (1995d) also did a computational study on the flows in compressors and low pressure turbines using several existing codes with various turbulent models. Conventional steady flow codes predicted the general features of the boundary layer reasonably well for compressors and turbines at high Reynolds numbers, provided transition onset was adequately specified. They also found that since no codes incorporate the calming effects, the codes prematurely predict the onset of transition between wakes at low cruise Reynolds number for turbines.

Morin and Patrick (1991) performed a detailed study of a large scale laminar separation bubble on the wedge flow over a flat plate. Their comprehensive flow visualization revealed two distinct transition processes for the separated and attached flows. The transition path in the shear layer over a separation bubble is similar to that in a laminar free shear layer, which is caused by large scale coherent eddy structures. They also found that the reattachment location of the short bubble was unsteady and intermittently separated. Since the boundary layer approached fully turbulent boundary layer form very slowly, conventional eddy-viscosity models for the turbulent boundary layer were not valid until far downstream from reattachment. The equilibrium turbulent boundary layer was not achieved even at 200 bubble heights downstream from reattachment. Even a short bubble had a critical role in defining of the initial boundary condition for the turbulent boundary layer calculation.

Malkiel and Mayle (1995) observed that laminar shear layers in separation bubbles can be characterized as a cross between attached boundary layers and free shear layers. The intermittency development in separation bubbles is modeled with the turbulent spot theory used in attached boundary layers and there is also evidence of Kelvin-Helmholtz vortex pairing in the transition region. The difference is that the turbulent spot production rate is several orders of magnitude higher than that found in attached boundary layers on a flat plate with the same order of adverse pressure gradients.

It was assumed by many earlier researchers (Gaster, 1969; Roberts, 1975, 1980; Mueller and Batill, 1980; O'Meara and Mueller, 1986) that transition over a short separation bubble happens instantaneously (point transition) at the maximum height of the bubble since the transition usually occurs in a very short distance. The transition length referred to in these earlier studies was the streamwise distance between separation and the maximum bubble height location. However, more recent studies on the separation bubble (Mayle, 1991; Malkiel and Mayle, 1995; Simon and Qiu, 1997) clearly demonstrate that transition usually occurs on the laminar portion of the separation bubble. It is clear from the measurements of intermittency that the transition proceeded over a finite streamwise distance. The transition length referred to in these more recent studies is the actual distance between transition onset and end locations.

For the present study the upper contoured wall was constructed to mimic the pressure distribution on the suction surface of a generic low pressure turbine airfoil. The experiments were conducted to investigate the effects of Reynolds number and

freestream turbulence level on the transition over the separated and attached flows. The effects of wake-induced unsteadiness were not included in the present study. The pressure, velocity, intermittency profiles and integral quantities along with spectral data were measured for various conditions. The existence of a separation bubble for certain conditions was confirmed by flow visualization. The characteristics of the separation and transition with various levels of freestream turbulence (1 % - 4 %) for four different Reynolds numbers (Re = 35,000, 70,000, 100,000 and 250,000) will be discussed in detail. The results of flow characteristics over the separation bubbles for a Reynolds number of 100,000 with grids 0, 2 and 3 are summarized and presented by Sohn, Shyne and DeWitt (1998).

CHAPTER II

EXPERIMENTAL FACILITY AND INSTRUMENTATION

Wind Tunnel

The experiments were performed in a low-speed, closed-loop wind tunnel located at the NASA Lewis Research Center. This wind tunnel was designed to generate large scale, two dimensional, incompressible boundary layers. The schematic diagram of the wind tunnel is shown in figure 1. The main air flow is generated by a Chicago Blower Corporation SISW Class III centrifugal blower with a capacity of 10,000 CFM. A fan is driven by a 3-phase, 220V, 25HP electric AC motor. The motor rpm and directions are controlled with an Eclipse Multiprocessor based digital AC control unit made by Emerson Industrial Controls. An electronic noise filter is attached to the power line to get rid of electronic noise introduced by the AC control unit. Upon exiting the blower, the air enters the flow-conditioning plenum chamber, where any flow irregularities caused by the blower are removed and the freestream turbulence levels are reduced. At the downstream end of the plenum chamber, rectangular bar type turbulence generating grids could be positioned to set the freestream turbulence levels of the test section. A two-dimensional nozzle with a 3.6:1 contraction ratio is attached to the downstream end of the flow-conditioning chamber in order to accelerate the flow into the test section. The vortices of the streamwise component are stretched to get the dominant fluctuating velocity in that direction. The test section flow exits into a diffuser where the air

velocity is reduced prior to entering the return duct. The return duct consisting of the air heater, filter and air cooler completes the wind tunnel loop. The air temperature is maintained within ± 0.5° F by using a constant stream of cooled water inside the radiator type air cooler. The coolant water temperature and volumes are monitored and adjusted to set the air temperature in the test section. A more detailed description of the tunnel components including the dimensions of grids can be obtained in Suder et al. (1988) and Sohn and Reshotko (1991).

Test Section

The test section has a rectangular cross-section that measures 27 inches wide, 12 inches long and 6 inches high. The bottom and two side walls of the test section are made with 0.5 inch thick Plexiglas. A removable upper wall is made of aluminum plate with contoured wooden blocks. A schematic of the test section along with the coordinates of the contoured upper wall is shown in figure 2. A contoured upper wall was designed to generate a pressure distribution on the bottom test surface that matches the pressure gradient generated by the suction surface of the generic LPT blade. In order to properly match the Reynolds number in a full scale LPT, a splitter plate was inserted in the middle of the test section to bifurcate the test section flow. Since operating the tunnel blower at a low flow setting is unstable, it was necessary to bifurcate the test section to achieve a low Reynolds number. The splitter plate working as a test plate has a 4:1 elliptic leading edge and a trailing deflector which forces the stagnation point to fall on the top working surface at the leading edge by generating circulation. The test

plate is 27 inches wide and 14 inches long with a 1.5 inch long 25° inclined deflector flap, as described in the schematic diagram shown in figure 3. Fourteen flush-mounted hot-films are located on the centerline and eighteen static pressure tabs are mounted at 1 inch off center on the test plate. The porous wall bleed system for suction was added to the contoured upper wall to prevent massive separation just downstream of the minimum pressure point in the adverse pressure gradient region. With this upper wall suction the separation bubble was induced on the lower test plate if a bubble existed (refer to the flow visualization photographs shown in figures 11-11a). A 5HP AC motor was used to bleed off the air and this air was returned to the main flow chamber. The suction air rate was adjusted with the sliding gate located at the back of the return duct.

The specially designed probe traversing system composed with 3 directional stepping motors and a controlling PC, which is called the PACS (Probe Actuation Control System), is used to precisely position the probe in increments as small as 0.00033 inches. Streamwise and spanwise positioning of the probe is made through the pre-cut slots along the centerline and off-center locations in the upper wall.

Design of Contoured Wall

The modern LPT blade geometry was supplied from an engine company (Pratt and Whitney PAK B blade). This geometry is representative of the blade design and loading used in modern LPT stages. The test section design was created by matching the mass flow from the generic LPT blade cascade through a flow channel with a contoured upper wall and a flat lower wall. An inviscid panel code developed by McFarland

(1982) was used to compute the blade velocity and pressure distribution. The flow field data computed by the panel code are a function of the area change throughout the channel. One and two body options were then used in the panel code to generate the upper wall shape and the continuity equation was utilized to account for the difference between the two options. The test section contour was then analyzed using the NPARC full Navier-Stokes computational code. This analysis of the test section contour was performed to validate the effect of the contoured upper wall. The NPARC analysis did reveal a separated region just downstream of the minimum pressure point on the contoured upper wall. This separation on the upper wall in the adverse pressure gradient region was conformed in the flow visualization. An upper wall bleed suction system was added to alleviate this problem and to generate the proper pressure distribution.

A comparison of the pressure distributions is presented in figure 4, for the generic LPT blade (labeled LPT), for the test section geometry (labeled Duct), and the experimental profile (labeled Exp) at design take-off condition. The pressure distributions compare favorably in the accelerating portion of the flow reflected by the closeness of the pressure gradients. The minimum pressure points differ for each curve due to a slight difference in the exit to critical velocity ratio. The difference between the experimental pressure distribution and the blade and/or test section (both calculated by the inviscid panel code) is more pronounced in the adverse pressure gradient region primarily due to viscous effects. It can be seen from this figure 4 that the representative plate length should be the same order as the actual distance along the suction surface of the generic LPT (about 6 inches) regardless of the actual plate length. The length

Reynolds number is obtained based on this "effective" test plate length and exit velocity of the test section. Detailed procedures generating the contoured upper wall were described in the paper by Shyne and DeWitt (1998).

Instrumentation

The wind tunnel is equipped with many pressure taps and thermocouples to monitor ambient conditions. Two in-situ Pitot tubes along with thermocouples located in the inlet and exit of the test section are used to monitor the incoming and outgoing flow velocities and temperature. The velocity signals from the hot-wire probe were monitored on a digital oscilloscope. Some appropriate instantaneous signals were digitally recorded for post-processing data reduction. In addition, a FFT analyzer was used to measure boundary layer and freestream spectra.

Two types of commercially available single sensor hot-wire probes, TSI model 1218-T1.5 boundary layer type and Dantec model 55M10 straight type hot-wire probe, were used to measure the streamwise component of mean and fluctuating rms velocities. Due to the upper wall suction mechanism as described in the previous section, a boundary layer type hot-wire sensor with a conventional straight probe holder cannot reach to the upstream accelerating zone. A straight type hot wire with a special 90 degree bent probe holder was used to access this limited upstream accelerating zone. The streamwise measurement locations were from x = 1 inch to 7.25 inches with the Dantec straight type hot-wire probe and from x = 4.75 inches to 9.25 inches with the TSI boundary layer type hot-wire. The mean and rms velocities measured with both probes

in the overlapping region from x = 4.75 inches to 7.25 inches show excellent agreement. Both probes were operated in the constant temperature mode. The safety legs of the boundary layer type probes were removed to allow the probe to approach as close to the wall as possible. A series of TSI model 1237 standard flush mounted hot film gauges instrumented along the centerline on the test plate was used to depict the two distinct patterns of the transition process.

The digital data acquisition system, DANTEC Streamline System, consisted of multichannel hot-wire anemometers and an A/D converter. The hot-wire anemometer was mainly controlled using accompanying PC software called Streamware. The following can all be accomplished using Streamware: 1) the settings of hot and cold resistance and operating temperature for the hot-wire probe, 2) the settings of the hot-wire anemometer signal conditioner for low-pass and high-pass filters, input offset, gain and sampling rate, 3) digitization of analog time signal and conversion to velocity signal, 4) post-processing of data and 5) storing. Once the system is properly setup, the operation is quite automatic from data collecting to processing. The calibration of the probes was performed using a DANTEC calibration module and Flow Unit. The Flow Unit contains calibrated flow nozzles, a pressure transducer and a temperature measuring sensor. This unit was connected to the Streamline system via the calibration module and to a shop air supply line. The calibration of probes was performed automatically in the pre-defined velocity range, simultaneously storing the distributions of calibrating jet temperature and pressure and generating the coefficients of a 4^{th} order polynomial relationship between velocity and voltage signals. The calibration temperature can be

later applied to the temperature correction for hot-wire signals measured in the wind tunnel.

The PC based National Instruments AT-MIO-16E-1 A/D convert board and SC-2040 simultaneous sample and hold (SSH) board were used in the hot-wire system. This is a 16-bit board with total a maximum sampling rate of 1.2 MHz. In this experiment, the low-pass filter was set to 10 KHz, which should be at most equal to the Nyquist frequency to minimize the digitization rollback error. The Nyquist frequency is usually set at half of the sampling frequency. The sampling frequency was set at 20 KHz throughout the whole data acquisition.

Spectral data were acquire using a Nicolet Scientific Corporation model 660A dual channel FFT analyzer, which features a maximum of 2048-point, 12-bit A/D conversion with a maximum sampling rate of 100 KHz. The sampling rate is 2.56 times the selected frequency. In this spectral measurement, the sampling range was set to 5 KHz, which results in the sampling rate of 12.8 KHz.

Steady-state tunnel conditions, ambient pressure and temperature and freestream velocity as well as pressure distribution on the test plate, were monitored by means of a Lab-wise multichannel data acquisition system, ESCORT D. The ESCORT D system has real time data acquisition capability and used a facility located DEC VAX computer for data processing. The pressure readings from pressure transducers were electronically scanned using a PSI ESP (Electronic Scanning Pressure) system and were updated every second. The ESP system is composed of a 32-channel module, separate transducers for each module, and is networked to the ESCORT D system. Three 15 psi modules were

used for the high Reynolds number cases. These modules were replaced with three modules capable of measuring pressures up to 1/3 inches of water for low speed measurements. Additionally, two Setra pressure transducers capable of measuring a differential pressure as low as 7.5 inches of water were used for the static and total pressures from the inlet and exit Pitot tubes.

CHAPTER III

DATA REDUCTION

Velocity and Integral Data

The instantaneous velocity signals of single hot-wire probe were digitized and stored in the computer for post-processing. Mean and rms velocity, various integral quantities and intermittency profiles were computed from the digitally stored instantaneous velocity signals for each condition. The sampling rate was set to 20 KHz. The numbers of data samples, N, are 65536 points for Re = 35,000 and 70,000 and 32768 for Re = 100,000 and 250,000. Total sampling time was 3.28 seconds for Re = 35,000 and 70,000 and 1.64 seconds for Re = 100,000 and 250,000 cases.

The statistical mean velocity, U, and fluctuating rms velocity, u'_{rms}, are calculated using the following equations:

$$U = \frac{1}{N}\sum_{i=1}^{N} u_i$$

$$u'_{rms} = \sqrt{\frac{1}{N-1}\sum_{i=1}^{N}(u_i - U)^2}$$

The uncertainty for hot-wire data was calculated based on the method of Yavuzkurt (1984). The uncertainty for mean and rms velocities turns out to be 1.45 %. The detailed procedure for determining the uncertainty of hot-wire data was described in Shyne and DeWitt (1988).

The integral quantities, displacement (δ^*), momentum (θ) and energy (ε) thickness were computed from the mean velocities using the following equations:

$$\delta^* = \int_0^{\delta} \left(1 - \frac{U}{U_e}\right) dy$$

$$\theta = \int_0^{\delta} \left(\frac{U}{U_e}\right)\left(1 - \frac{U}{U_e}\right) dy$$

$$\varepsilon = \int_0^{\delta} \left(\frac{U}{U_e}\right)\left(1 - \frac{U^2}{U_e^2}\right) dy$$

where U is the local mean velocity and U_e is the local mean velocity measured at the edge of the boundary layer.

Intermittency

In the transition of laminar to turbulent shear flow over a streamwise distance, intermittency is observed. The distinctive feature of the turbulent flow is its highly rotational nature. Thus vortical fluctuation is one very appropriate choice for discrimination between non-turbulent and turbulent flow but this technique needs simultaneous measurements of at least two components of velocity fluctuations in the streamwise and normal directions along with their variations in each direction. This requires a complex geometry of four sensor hot-wire probes. The alternative method used herein is to differentiate the velocity fluctuation (detector function) and emphasize the high frequency component for turbulent flow. Then smoothing of the detector function is applied. After a certain threshold value is determined, the signal is defined as

turbulent if the value of the smoothed detector function is greater than the threshold value; otherwise the signal is defined as non-turbulent.

As a logical choice for the detector function, squares of the first and second derivatives of the velocity fluctuation signal with time are appropriate and practical in many engineering applications.

Detector functions: $\left(\frac{\partial u}{\partial t}\right)^2$ and $\left(\frac{\partial^2 u}{\partial t^2}\right)^2$

The reasons for using these two derivatives as detector functions are explained as follows. There will be some period of time when the detector function might have some zeros within the turbulent zone since the first derivative of the fluctuation signal alternates its signs very rapidly. When the first derivative of the signal is compared to a threshold value, it is seen that the signal becomes smaller than the threshold level as it crosses zero even though it is "turbulent-like" flow. This problem is referred to as a zero crossing. Therefore, it is required to use the second derivatives of the signal to correct this problem. It is also necessary to smooth out the derivatives over a short period of time in order to eliminate excessive zeros. The smallest possible value of smoothing time depends on the sampling rate of data acquisition and the resolution of the probe used. The smoothing time is about 15 to 35 times the Kolmogorov scale. Setting the smoothing time as 4 times the sampling rate (50μs), the smoothing window size is approximately 30 times the Kolmogorov scale in this study. Picking up the threshold value turned out to be trickier than selecting the smoothing time. It is required at each measurement location to carefully compare the resulting indicator function with an actual

instantaneous signal to confirm the threshold value selected. For more details of detector and smoothing functions, refer to the paper by Hedley and Keffer (1974). If both first and second derivatives of smoothing functions were smaller than their respective threshold values, the signal was declared as non-turbulent. Otherwise, it was defined as turbulent flow. Determination of the indicator function allows calculating the intermittency. The intermittency is the fraction of time when the flow is turbulent. The more detailed description of this conditional sampling technique from the digitized instantaneous velocity signals can be found in Sohn and Reshotko (1991).

Integral Length Scales

The integral length scale of the turbulence is conceptually the scale that describes the average eddy size associated with the random motion in the turbulence. The integral length scale of fluctuating motion is determined by integrating the correlation coefficient of the fluctuating velocities over the length between two points. However, this two-point correlation requires two hot-wire probe measurements which is not feasible due to interference of each other probe. The integral length scale, L, can be written as follows:

$$L = \int_0^\infty R(r)\, dr$$

where

$$R(r) = \frac{\overline{u_1(x)\ u_2(x+r)}}{\sqrt{\overline{u_1^2(x)}}\ \sqrt{\overline{u_2^2(x+r)}}}$$

R(r) is the correlation coefficient. u_1 and u_2 are velocity fluctuations measured at

different spatial locations in the streamwise direction with a distance of r.

Taylor's hypothesis of frozen turbulence states that if the turbulent velocity fluctuation is small compared to the mean velocity, the eddies do not change appreciably in shape as they pass a given point. According to Bradshaw (1971), if Taylor's hypothesis is valid, then the autocorrelation of the fluctuating velocity will be the same as the spatial correlation with separation, $U_e\tau$ in the streamwise direction, where U_e is freestream mean velocity and τ is time delay. The integral length scale, L, can be expressed as

$$L = U_e \int_0^\infty R(\tau)\, d\tau$$

where

$$R(\tau) = \frac{\overline{u(t)\, u(t+\tau)}}{u'^2_{rms}}$$

$R(\tau)$ is the autocorrelation coefficient. u'_{rms} is the root mean square of the streamwise components of fluctuating velocity.

Power Spectra

The contribution of the u'^2 within each frequency bandwidth to the overall turbulence level squared is referred to as the power spectral density. The distribution of the power spectral density as a function of frequency is defined as the power spectrum. The power spectra were acquired using a Nicolet FFT spectrum analyzer from the signals of a single hot-wire probe. Only the streamwise component of the turbulent kinetic

energy, u'^2, was acquired in this experimental study, thereby resulting in a 1-D power spectrum. The data were obtained both at freestream and inside the boundary layer location where u'_{rms} was maximum for each condition.

It is known that the autocorrelation coefficient and the power spectral density functions are related as the Fourier transform pair as follows:

$$R(\tau) = \int_0^\infty \varphi(\omega)\cos(\omega\tau)\, d\omega$$

$$\varphi(\omega) = \frac{2}{\pi}\int_0^\infty R(\tau)\cos(\omega\tau)\, d\tau$$

where $\varphi(\omega)$ is the power spectral density as a function of frequency, ω, in radians per second.

The normalized power spectral density, PSD, is defined in the following equation as a function of frequency in Hz.

$$\text{PSD(f)} = \varphi(\omega)\, 2\pi\, u'^2_{rms}$$

The integral of the power spectral density function over all frequencies results in u'^2_{rms}. If we evaluate the value of the power spectral density function at zero frequency,

$$\varphi(0) = \frac{2}{\pi}\int_0^\infty R(\tau)\, d\tau$$

The integral length scale, L, becomes as follows:

$$L = U_e \int_0^\infty R(\tau)\, d\tau = U_e\, \varphi(0)\, \frac{\pi}{2} = \frac{U_e}{4\, u'^2_{rms}} PSD(0)$$

The integral length scale can be evaluated using either the power spectrum or the autocorrelation. In this experiment the freestream power spectra measured at x = 1 inch were used to evaluate the integral length scale of incoming turbulence.

CHAPTER IV

RESULTS AND DISCUSSION

Detailed flow field measurements have been conducted over an entire test section for both accelerating and decelerating flow regions at four different Reynolds numbers of 35,000, 70,000, 100,000 and 250,000 with various levels of freestream disturbances. These Reynolds numbers are evaluated based on the "effective" plate length (l = 6 inches) and the flow velocity measured at the exit of the test section. The mean and rms velocity profiles were measured at sixteen streamwise measurement locations ranging from x = 1.75 inches to 9.25 inches with an increment of 0.5 inches using two types of single hot-wire probes as discussed in Chapter II. The primary emphasis in this paper is placed on the flow field survey in the adverse pressure gradient region where the laminar boundary layer was separated and short bubbles formed. The freestream turbulence intensity (FSTI) in the test section was generated by means of the rectangular bar-type grids. Four different levels of freestream turbulence (1 %, 2 %, 3 % and 4 %) were used for the two lower Reynolds numbers and three levels of freestream turbulence (1 %, 2 % and 3 %) for the two higher Reynolds numbers. The nominal FSTI of 1% is measured without any grid (grid 0) and the highest FSTI for the current configuration is about 4 % generated by the coarsest grid (grid 4). Table 1 lists all the cases that have been investigated in the experiment. The experimental results of both single and X-type hot-wire data (streamwise and vertical components of mean velocity profiles, corresponding fluctuating

rms velocity profiles and spectral data as well as Reynolds shear stress profiles) for two Reynolds numbers of 100,000 and 250,000 with grids 0, 2 and 3 were discussed and presented in Shyne and DeWitt (1998).

FREESTREAM CONDITIONS

The test section was designed to simulate the flow on the suction surface of a low pressure turbine for high Reynolds number take-off conditions. The flow within the test section was characterized by freestream turbulence levels, length scales and spectra for each Reynolds number. The streamwise mean velocity, U_e, was measured at spanwise and vertical centerline in the test section to depict the flow pattern in the freestream for each condition. The typical distributions of U_e for Re = 35,000, 70,000, 100,000 and 250,000 under the flow condition generated with grid 0 are presented in figure 5. The flow accelerates up to throat and then decelerates until it levels out to the exit value. It can be noted in the figure that there is a near-constant velocity zone shortly after the maximum velocity point for the three lower Reynolds number cases. For grid 0 this constant velocity zone extends from $x \approx 4$ inches to 8 inches. There is a tendency of reducing of this zone with increasing grid number. This near-constant velocity zone will be identified as the front part of the separation bubble. Since the freestream mean velocity is directly related to the pressure in the boundary layer, the feature of near-constant velocity in the separation bubble will be discussed in detail later in the static pressure section. Note that the effective plate length is from x = 1 to 7 inches (See figure 4), where x is the distance measured from the leading edge of the test plate. Both the

contoured upper wall and the splitter test plate were extended five more inches to prevent any flow distortion at the exit. Refer to figure 2 for the coordinates of the upper contoured wall.

The freestream turbulence in the test section was generated using four types of interchangeable rectangular bar-type grids. The grid becomes coarser with higher grid number. However, the open area is almost the same for all grids, being 62 %. Grid 0 refers to no grid. The typical variation of freestream turbulence intensity, defined as FSTI = u'_{rms}/U_{in} with all four grids used for Re = 70,000 is shown in figure 6, where U_{in} is the streamwise freestream mean velocity measured at mid-channel height and a streamwise location of 1 inch downstream from the leading edge of the flat plate since the "effective" plate starts at x = 1 inch. The U_{in} is also used as the reference velocity for normalization of mean and rms velocities. The freestream turbulence level increases with increasing grid number. Also, the variation of FSTI is more pronounced and is higher as the grid becomes coarser. The nominal FSTI values referred to throughout this experiment are 1 % (grid 0), 2 % (grid 2), 3 % (grid 3) and 4 % (grid 4), respectively.

Due to the frequency content of the disturbances, it is necessary to measure spectra in order to see the distribution of disturbance spectral energy (square of velocity fluctuation) as a function of frequency bandwidth. The one-dimensional freestream power spectra were measured with the analog spectrum analyzer for the same measurement locations as for the freestream mean velocity. The distribution of freestream power spectral density (PSD) function for each grid measured at x = 1 inch is shown in figures 7-10 for Reynolds numbers of 35,000, 70,000, 100,000 and 250,000,

respectively. The same power spectral density functions multiplied by the frequency (f * PSD) are presented in figures 7a–10a for each Reynolds number. In these energy coordinates of figures 7a-10a, the area under each PSD curve in any frequency band is directly proportional to the energy in that frequency bandwidth. As shown in figure 7a, the energy is concentrated in low frequency band (less than 800 Hz) with an energy peak at 70 – 90 Hz for Re = 35.000 regardless of freestream turbulence levels. The energy level increases as FSTI increases.

The Reynolds number effects on the spectral energy can be observed when PSD plots of figures 7a-10a are compared with each other. First, it can be noted that with an increase of Reynolds number the energy level is getting broad banded. As shown in figures 8a-10a, the energy contained frequency band is expanded from 800 Hz for Re = 35,000 to 2 KHz for Re = 70,000, 3 KHz for Re = 100,000 and 6 KHz for Re = 250,000. Second, the energy peaks move to higher frequency with increasing Reynolds number, i.e., 200 Hz for Re = 70,000, 300 Hz for Re = 100,000 and 800 Hz for Re = 250,000. However, the energy peaks move slightly to the lower frequency band with higher FSTI (from grid 0 to 3), especially for the two higher Reynolds numbers of 100,00 and 250,00 (figures 9a and 10a). Third, the spectral energy levels increase quite noticeably as the Reynolds number increases for all frequency bands. For grid 0, the peak energy levels (maximum of f * PSD) are 0.001 for Re = 35,000, 0.0035 for Re = 70,000, 0.009 for Re = 100,000 and 0.065 for Re = 250,000. The trend of increasing energy peaks with increasing Reynolds number for other higher grids is the same as for grid 0 case. Like in the case of Re = 35,000, the energy level increases with FSTI for each Reynolds number

throughout the whole frequency band. A bigger effect of FSTI on spectral energy is observed at a low frequency band ($f < 500$ Hz) for each condition. Electronic noise (spikes in $f > 1{,}500$ Hz) is noticeable in grid 0 for Re = 35,000 (figure 7), even though the level is quite low (in between -10^{th} and -11^{th} power).

The integral length scale of the freestream turbulence is used to describe the average eddy size associated with the fluctuations in the turbulent flow. The integral length scale was computed from the freestream power spectrum extrapolated to zero frequency for each condition as discussed in Chapter III. Thus determined integral length scales of incoming freestream turbulence measured at x = 1 inch are listed in Table 2. The integral length scale increases with increasing freestream turbulence level and Reynolds number. The average eddy size increases substantially as the freestream turbulence level increases from 1 % (grid 0) to 3 % (grid 3) for each Reynolds number. However, for higher freestream turbulence levels of 3 % (grid 3) and 4 % (grid 4), the minimal increase of eddy size is observed.

FLOW VISUALIZATION

Smoke wire flow visualization was conducted to capture the qualitative features of the flow field. Smoke traces were generated using a thin nichrome wire connected to the power supply. The nichrome wire was located at the inlet of the test section just downstream of the flow nozzle section of the tunnel. The nichrome wire was pulled out of the tunnel and swabbed with a thin layer of oil (smoke fluid) and placed back into the tunnel, repeatedly. The nichrome wire and camera control units were synchronized with

the timing of the voltage supplied to the wire and the duration of the burn to generate the smoke. The duration of the burn time was about two seconds with 20 volts of power supplied. This flow visualization was performed with grid 0 for a Reynolds number of 50,000 (based on an exit velocity of 15 ft/s). Due to rapid dispersion of the smoke for higher Reynolds numbers and intense mixing at higher freestream turbulence levels, good quality photographs could not be obtained for the higher Reynolds numbers and FSTI conditions.

A representative photograph of the smoke trace throughout the test section is shown in figure 11. Due to the reflection of the flashlight on the bottom test plate, the plate surface looks like rough one, but it is a smooth Plexiglas plate. This photograph shows a massive separation on the contoured upper wall at the downstream end of the diverging section, which was previously predicted by the NPARC code. Thus, it is required to apply suction to prevent the separation on the upper wall and to force the probable separation bubble onto the bottom test plate.

Figure 11a shows three instantaneous photographs of smoke traces with upper wall suction turned on. These figures are a time lapse sequence of photographs that clearly show a separation bubble on the lower wall and no separation on the upper wall. No traces of smoke are apparent in the region between the separated shear layer and the test surface within the front part of the separation bubble due to infinitesimal viscous shear stress and little or no turbulent energy diffusion. This flow field is called the 'dead-air' region and looks similar in each photograph, indicating the steady laminar region of the separation bubble. However, there is a substantial difference of the flow pattern in the

region downstream of the maximum bubble height in each photograph taken at different times. This indicates that the transition and the reattachment processes on the separation bubbles are unsteady. A large eddy structure is apparent in the middle photograph downstream from the maximum bubble height in the shear layer. These eddies eventually become unstable, and through interaction with each other, finally develop into a turbulent boundary layer. The transition process is similar in behavior to a laminar free shear layer, where discrete spanwise vortices form due to the Kelvin-Helmholtz instability and eventually break down into a fully turbulent shear layer. This kind of transition mode on the separation bubble is called a separated-flow transition (Mayle, 1991). A detailed flow visualization study performed by Morin and Patrick (1991) on a diverging channel flow also revealed this large eddy formation in the shear layer.

A hint of a vortex rollup can be seen in the bottom photograph of figure 11a as the flow starts to reattach. However, no clear eddy structures due to vortex rollup and their breakdown can be seen in the top photograph. The flow pattern in the shear layer is rather similar to that of the attached boundary layer. It is unclear from the flow visualization that the separated-flow transition is the only mode on the flow over the separation bubble. The existence of the separation bubble on the lower wall is an important feature in the simulation of a generic LPT blade at off-design condition. The photographs of figure 11a help to validate that the flow in the test geometry generated by the panel code does indeed simulate the flow physics of the real blade. The one row of tuffs in the spanwise direction attached just downstream of the throat also helped to visualize the flow near the upper

wall during testing. The proper suction rates were adjusted for the tuffs to stay attached on the upper wall for all test conditions.

STATIC PRESSURE DISTRIBUTION

The pressure distributions in the flow were obtained from the pressure taps located 1 inch off center on the surface of the lower flat plate at various FSTI and Reynolds numbers. The pressure coefficient, C_p, was evaluated based on exit static and total pressures. For Re = 35,000 and 70,000, the pressure transducer was switched to one capable of measuring as low as 1/3 inches of water differential pressure. However, even this pressure transducer were not good enough to properly measure the pressure variation due to low speed for the Re = 35,000 case. The digitized voltage count from the transducer varied only from 0 to 20 (maximum pressure reading for Re = 35,000) in the maximum span of 3000 counts. The pressure readings were simply fluctuating without any trend. The pressure distribution for Re = 35,000 cannot be measured directly using pressure taps. As the flow speed increases the voltage counts from the pressure transducer increase enough to give a smooth pressure variation. Since the flow is incompressible and the total pressure is constant throughout the test section, the C_p can be computed from the freestream mean velocity profiles as follows:

$$C_p = \frac{p_s - p_{s_{exit}}}{p_t - p_{s_{exit}}} = \frac{p_s - p_{s_{exit}}}{\frac{1}{2}\rho U^2_{e_{exit}}} = 1 - \left(\frac{U_e}{U_{e_{exit}}} \right)^2$$

where p_t and p_s represent the total and local static pressures. U_e is the local freestream mean velocity and the subscript exit means the conditions at the exit of the test section.

The distribution of pressure coefficient for Re = 35,000 calculated from freestream mean velocity profiles is shown in figure 12. The variation of C_p measured directly from pressure taps are presented in figures 13-15 for Re = 70,000, 100,000 and 250,000, respectively. For the three higher Reynolds number cases, the C_p was also computed and compared with the measured values. Both measurements are in good agreement with each other. The pressure coefficient decreases to a minimum value at the throat as the flow accelerates in the converging portion of the test section and then increases to the exit level as the flow decelerates in the diverging section due to the adverse pressure gradient for each condition. If the adverse pressure gradient is sufficient, the laminar boundary layer separates from the surface. Figures 13 and 14 show that downstream of the minimum pressure point, the pressure increases steadily and then reaches a nearly constant level. This constant pressure plateau is identified as the dead-air region in the flow visualization. Downstream from the constant pressure region the pressure rises sharply over a short distance to the level that would be achieved without the separation bubble, then slowly increases to the exit pressure level. However, this constant pressure region disappears for Re = 250,000 regardless of the freestream turbulence levels, as shown in figure 15. Any noticeable C_p variation with respect to the freestream turbulence levels cannot be seen in the figure. All three plots are nearly identical to each other.

The pressure distribution plays an important role in identifying the separation bubble. The separation location can be determined by identifying the beginning of the constant pressure region as shown in figures 12-14 for Re = 35,000, 70,000 and 100,000, respectively. The location of maximum bubble thickness can be obtained from the

downstream end of the constant pressure region. At the end of the constant pressure region, the pressure increases rapidly to a point where the pressure is nearly equal to a value that would exist without the separation bubble. This location is identified as a reattachment point of the bubble. The reattachment occurs mainly because of increased turbulent diffusion due to transition in the shear layer. Gaster (1969) and other researchers measured pressure distributions for both separated and attached boundary layers and determined the bubble location and extent in this manner. Due to the limited pressure data in the short separation zone, the separation locations for all test conditions are estimated by linear interpolation of the adjacent data points and compared to the corresponding values determined from the integral quantities of mean velocity profiles (this will be explained in a later section). The separation bubble identified in the flow visualization and the pressure distribution data can be seen as a small perturbation of the inviscid flow such that a constant pressure region rises under the laminar shear layer. Since no constant pressure regions can be detected in figure 15 for Re = 250,000 with any grids, it can be said that the boundary layers do not separate at any freestream turbulence levels tested.

It is noted in the figures 12-14 that the beginning of the constant pressure region is fairly identical, indicating the freestream turbulence level has little or no effect on the separation location. However, with increasing freestream turbulence level, the extent of the constant pressure region progressively shrinks and the downstream end of the sudden pressure recovery point (reattachment location) moves upstream, indicating the bubble length has decreased. For each freestream turbulence level, the constant pressure region

also shrinks down and the reattachment location moves upstream, again with increase of the Reynolds number, which indicates that the bubble length is inversely proportional to the Reynolds number.

CHARACTERISTICS OF SEPARATION AND TRANSITION

To investigate the effects of freestream turbulence intensity and Reynolds number on the flow field on the suction side of the LPT, the experiments were carried out with a number of different grids and flow speeds for the conditions listed in Table 1 of the test matrix (14 cases). First, the general description of the entire flow filed is given for each condition. The effects of FSTI on shear layer separation and transition are investigated by comparing the flow parameters of the mean and rms velocity profiles, integral quantities, intermittency profiles and spectra for each Reynolds number. Second, the variations of the mean and fluctuating rms velocities as well as intermittency profiles with Reynolds number at each streamwise measurement location around the laminar separation bubbles are compared for each FSTI. Finally, the measured data are compared with various transition models for separated flows.

Freestream Turbulence Intensity Effects on the Flow Field

Mean Velocity Profiles

The mean flow field can be visualized with the aid of a series of plots of streamwise mean velocity profile. Figure 16 presents the variation of the mean velocity

profiles normalized with the incoming freestream velocity (U_{in}) with grid 0 at Re = 35,000 for the entire test section from x = 1.75 inches to 9.25 inches with an increment of 0.5 inches. To show the details within the boundary layer, the y-scale has been expanded by a factor of 15 – 16.5 relative to the x-scale depending on the Reynolds number. The first four upstream velocity profiles from x = 1.75 inches to 3.25 inches show typical attached laminar boundary layer profiles in the accelerating region. The profile at x = 3.75 inches starts to show a deflection near the wall. This is because the flow decelerates in the adverse pressure gradient region downstream of the throat (x = 3.3 inches). The measurement point in the normal direction is about y = 0.005 inches for each streamwise location due to the volume of hot wire. The separated zone shown as a nearly zero velocity gradient very near the wall expands as the flow goes further downstream. This zero velocity gradient portion of the profile begins to shrink down around x = 7.25 inches. The zero velocity gradient zone disappears starting at x = 8.25 inches as the flow reattaches. The velocity profile is getting fuller and becomes that of a fully turbulent boundary layer farther downstream. The actual reattachment locations for each condition will be determined from the shape factor plots, which will be discussed in a later section on Integral Quantities. It should be pointed out that the "effective" plate considered throughout this experiment is from x = 1 inch to 7 inches as discussed in Chapter II. If a separation bubble reattaches downstream of x = 7 inches on the extension of the actual test plate, it can be assumed that this separation bubble might not be closed and become a long bursting bubble on an actual suction surface of a LPT. The separation bubble for the configuration of grid 0 and Re = 35,000 case falls in this category and can be assumed as

a bursting one.

To show the details of the separated flow region, the same mean velocity profiles around the laminar separation bubble from x = 3.25 inches to 7.75 inches were plotted in figure 16a for the case of grid 0 and Re = 35,000. The stream function, ψ_I, determined by integrating the mean velocity profiles from the wall to any point y_i, up to the vicinity of the upper contoured wall, is defined as follows:

$$\psi_i = \int_0^{y_i} \frac{U}{U_{in}} dy.$$

The lines connecting the equal values of ψ_i used to define the mean flow field streamline patterns are also shown in figure 16a. The mean velocity profile at x = 3.75 inches starts to show an inflection point very near the test surface imposed by the adverse pressure gradient, which is the precursor of boundary layer separation. The separation location for this case is just downstream of x = 3.75 inches. Downstream of the separation location a series of velocity profiles show a distortion in the near-wall region. This region expands up to y = 0.05 inches at a streamwise measurement location of x = 6.75 inches and starts to shrink down farther downstream. The hump of streamlines downstream from x = 3.75 inches was detected in the figure. Due to the inability of the hot-wire to determine the flow direction, no reverse flow could be detected. Instead, nearly constant velocity profiles were measured near the test surface. The front part of the bubble (identified as a dead-air region in the flow visualization) is usually characterized by a practically constant velocity gradient. The approximate bubble height can be determined by interpolating the

extent of this constant velocity region at the transition location determined from the pressure measurement.

Figures 17, 18 and 19 present the carpet plots of the mean velocity profiles showing mean flow fields for Re = 35,000 with grids 2, 3 and 4, respectively. Corresponding expanded plots of the same mean velocity profiles around the separation bubble are shown in figures 17a, 18a and 19a along with the streamline patterns. Comparing the figures of Re = 35,000 with four different FSTI, it is noted that the mean velocity profiles start to distort just downstream of x = 3.75 inches for all four grid cases. The boundary layer separation locations are almost identical to each other. The profiles with a near-wall constant velocity region are detected up to x = 6.75 inches for grid 2 and to x = 6.25 inches for grids 3 and 4. The velocity profile just downstream of each separation bubble shows double inflection points, indicating the flows are already reattached, and finally develop to a fully attached turbulent boundary layer farther downstream.

The flow near the wall is distorted by the bubble, as shown in figures 17a, 18a and 19a. Generally, these short bubbles only alter the local flow field, not affecting the global flow pattern away from the wall. The extent of the near-wall distorted region that is related to the bubble height shrinks with FSTI. It is obvious that the bubble length and height are all inversely proportional to the freestream turbulence level. However, the separation locations are either not or very little affected by changing FSTI.

The flow field on the separation bubble is described as follows for the case of Re = 35,000 with grid 0. The boundary layer starts laminar in the accelerating flow region.

The boundary layer stays laminar for a while just downstream of throat in the adverse pressure gradient region. Farther downstream, the adverse pressure gradient imposed on the diverging section retards the near-wall fluid, and the boundary layer separates from the surface. The laminar part of the separation bubble grows subsequently in the free shear layer. The turbulent energy increase due to transition is brought down to the near-wall region by turbulent transport to overcome the adverse pressure gradient. The flow is finally reattached to the surface and the bubble is closed. Then the attached boundary layer develops to fully turbulent farther downstream. The properties of transition on the separated flow will be discussed later in conjunction with intermittency profiles.

Figures 20-23 show mean velocity profiles for Re = 70,000 with grids 0, 2, 3 and 4, respectively. The expanded velocity plots around the separation bubbles, with each corresponding streamline pattern, are shown in figures 20a-23a. The velocity profiles behave similarly to those of Re = 35,000 for each grid except for the separation location and the separation bubble length. The mean velocity profile at x = 4.25 inches starts to show an inflection point in the near-wall region for all grids and profiles at x = 4.75 inches show a near constant velocity very near the wall, indicating the flow is already separated. It is obvious that the boundary layer separation occurs between x = 4.25 inches and 4.75 inches for Re = 70,000 regardless of FSTI. The near-wall distorted region is extended to x = 6.75 inches for grid 0, x = 6.25 inches for grid 2 and to x = 5.75 inches for grids 3 and 4. As expected, the total bubble length and height decrease with increasing FSTI.

Figures 24-26 present mean velocity profiles for Re = 100,000 with grids 0, 2 and 3, respectively. To get detailed pictures of the separation bubble, the expanded velocity plots around the separation bubbles with each corresponding streamline pattern are shown in figures 24a-26a for grids 0, 2 and 3, respectively. Once again, the velocity profiles behave very similarly to those of Re = 70,000 except for delayed separation locations and a smaller separation bubble for corresponding grids. The profiles at x = 4.75 inches show a hint of separation for all grids. The separation location is just downstream of x = 4.75 inches for Re = 100,000 for all grids 0-3 tested. The separation locations were determined to be x = 4.8 inches for all three FSTI with Re = 100,000. The near-wall constant mean velocity region is extended to x = 6.75 inches for grid 0, x = 6.25 inches for grid 2 and to x = 5.75 inches for grid 3. The total bubble length and height are inversely proportional to FSTI. Comparing the streamline patterns for the three Reynolds number cases shown in figures 17a-26a, it can be noted that these separation bubbles have little effect on the global flow field. The global mean streamlines for each condition are almost identical, even though the separation bubbles are substantially different in size. This invariance of the global streamline pattern in spite of the existence of a small separation bubble was also observed by the LDV experiment by Morin and Patrick (1991).

A series of mean velocity profiles for Re = 250,000 are plotted in figures 27-29 for grids 0, 2 and 3, respectively. In these three figures any discernable near-wall distortion of the mean velocity profiles can not be observed. Due to the high flow speed, the boundary layers can overcome the adverse pressure effects and stay attached for each level of freestream turbulence throughout the measurement locations. This attached

boundary layer changes from laminar to turbulent through transition on the surface. The transition locations of this attached boundary layer for Re = 250,000 and three FSTI will be determined later from the intermittency profiles.

The contour plots of the same mean velocity distributions (U/U_{in}) of Re = 35,000 for grids 0, 2, 3 and 4 are shown in figures 30-33, respectively. These plots were generated from evenly spaced mean velocity data in the adverse pressure gradient region from x = 4.25 inches to 9.25 inches with an increment of 0.5 inches. The y-scale has been expanded by a factor of 17 relative to the x-scale to show the details in the boundary layer. The general shape of the bubble can be determined from this contour plot. Consider the contour lines with the values of U/U_{in} from 0.1 to 1.3 in the region between x = 4.25 inches and 6.75 inches for grid 0 in figure 30, which are almost parallel to each other. The velocity gradient is nearly constant in the separated laminar shear layer just outside the front part of the bubble, indicating that the flow is not expanding. The bubble has a shallow triangular dead-air region and a rather steep closing area due to high turbulent diffusion brought down to the near-wall region by turbulent transport. At the end of the dead-air region (maximum bubble height), the profiles show a sudden increase in the magnitude of velocity near the wall in the reverse flow region. Due to inability of the hot-wire to detect the direction of flow, this reverse flow could be falsely read by the hot-wire as a forward flow, which results in a higher velocity reading. This steep closing of the bubble in the reverse flow region might not be true, possibly happening at a much milder pace in the real situation than shown in this contour plot. The flow reattaches probably a little farther downstream than the location that can be obtained from this

contour plot. Comparing this contour plot with a corresponding carpet plot of mean velocity profiles with grid 0 for Re = 35,000, the profile at x = 7.75 inches as seen in figure 16 still shows a constant velocity zone near the wall and the flow reattaches in between x = 7.75 inches and 8.25 inches, while the contour plots in figure 30 show earlier reattachment around x = 7.25 inches. The contour plots in or around the reverse flow region between the maximum bubble height and the reattachment locations are misleading. The reattachment locations are determined from the shape factors rather than from these contour plots.

From this contour plot, it can be observed that the velocity gradient decreases to a minimum value around the reattachment location and continues to increase again to a turbulent value. The values of U/U_{in} change from 0.1 to 0.2 over the y distance of 0.07 inches around x = 7.25 inches, so the velocity gradient is the minimum there throughout the measurement locations. The velocity gradient at or near the reattachment location should be zero since there is no skin friction, but because of the limitations of the hot-wire, a small velocity gradient was measured.

The contour plots for grids 2, 3 and 4 (figures 31-33) exhibit the same trends as that for grid 0 except for the earlier reattachment, resulting in a smaller bubble size. The contour plots for higher FSTI (grids 3 and 4) show a more gentle closing of the separation bubble. Since the size of the separation bubble is so small (less than 1.5 inches) for these higher FSTI the corresponding reverse flow zone becomes proportionally smaller compared to the two lower FSTI cases. The falsely high declaring velocity zone is reduced substantially. The reattachment locations determined from the contour plot for

these higher FSTI cases are in fair agreement with those determined from the shape factors.

Figures 34-37 present the contour plots of mean velocity profiles for Re = 70,000 with grids 0, 2, 3 and 4, respectively. The similar contour plots of Re = 100,000 for grids 0, 2 and 3 are shown in figures 38-40, respectively. The effects of FSTI for each Reynolds number are the same as for Re = 35,000. The flow in the free shear layer around the separation bubble behaves quite similarly to those for the Re = 35,000 case. The bubble sizes shrink with increasing FSTI for each Reynolds number and the velocity gradient is at its minimum around the reattachment locations. The contour plots of mean velocity profiles for Re = 250,000 are shown in figures 41-43 for grids 0, 2 and 3, respectively. Since the flow for Re = 250,000 is attached throughout the measurement locations, no distortion of contours can be observed for any FSTI cases. The velocity profiles are simply getting fuller as the flow goes downstream.

Fluctuating RMS Velocity Profiles

The fluctuating rms velocity profiles normalized with inlet freestream mean velocity (u'_{rms}/U_{in}) for Re = 35,000 with grid 0 are shown in figure 44. The scales used in the rms velocity profiles are exactly same as the counterpart of mean velocity profiles. To get the details around the separation bubble the expanded plot of rms velocity profiles in the adverse pressure gradient region from x = 3.25 inches to 7.75 inches are shown in figure 44a using the same scales as in the expanded mean velocity plots. Also included in this figure are the same streamlines plotted in the mean velocity profiles in figure 16a. In

the laminar boundary layer for a low freestream turbulence level (grid 0), the rms velocity profile shows a nearly flat profile with small magnitudes in the region from the first streamwise measurement location of x = 1.75 inches up to x = 6.25 inches. The small peak starts to show up in the near-wall region and a broad hump appears just outside of the separated flow region at x = 6.75 inches. It will be shown later in the intermittency profiles that the flow starts to transition at this location. Those two humps grow in magnitude at x = 7.25 inches and merge together farther downstream. The fluctuating energy increases its strength as the flow goes through transition. This increased turbulent energy is transported to near the wall and then overcomes the adverse pressure gradient effect, and finally makes the flow reattach on the surface. The location of the maximum rms velocity moves toward the wall as the flow goes downstream and the rms velocity profile resembles that of a fully turbulent boundary layer.

Figures 45-47 show the distributions of rms velocity profiles throughout the entire measurement location for Re = 35,000 with grids 2, 3 and 4. The same rms velocity profiles around the separation bubble are shown in figures 45a-47a. The rms velocity profiles show a small laminar peak around y = 0.025 inches at x = 1.75 inches in the laminar boundary layer. This small near-wall peak starts to grow in magnitude and moves away from the wall up to the location of the maximum bubble height for each flow. This peak in the shear layer grows rapidly after the maximum bubble height and triggers a slowing of bubble growth due to turbulent energy dispersion. The fluctuating energy is brought down to the near-wall region by turbulent transport. Once the flow is reattached, then the turbulent rms hump broadens its size toward the wall and the rms velocity profile

evolves closer to that of a fully turbulent boundary layer. The flow behavior for these three grids is similar to each other. For higher freestream turbulence levels (grids 3 and 4), the peak is bigger than that of grid 2 at the first measurement station due to higher freestream turbulence levels.

Figures 48-51 present the fluctuating velocity profiles for Re = 70,000 with grids 0, 2, 3 and 4, respectively. The flow behavior is similar to the corresponding flow for Re = 35,000. Another slight hint of the small peak is noticed inside the bubble at x = 6.25 inches for grid 0 as the flow goes through transition. This second peak developed inside the bubble grows in magnitude at x = 6.75 inches. As the flow reattaches, the near-wall peak merges with the other peak developed in the free shear layer. In the LDV experiment on the diverging channel flow performed by Morin and Patrick (1991), they observed that the second peak developed inside the bubble substantially outgrew the first peak and they merged together farther downstream. They also found that the third peak developed around the edge of the boundary layer.

For higher freestream turbulence levels (grids 2, 3 and 4), the peak is bigger in magnitude than that for grid 0 at the first streamwise measurement station because the laminar boundary layer is buffeted by higher freestream turbulence. No second peaks are observed inside the bubble of the reverse flow region due to much smaller bubble length for higher FSTI as well as the limitation of the hot wire. Generally, the laminar peak grows in strength and moves away from the wall, having maximum strength in the shear layer around the reattachment region. The near-wall rms velocities are gaining the strength farther downstream and the rms velocity profiles are getting closer to those of the

fully turbulent attached boundary layer. However, the fluctuating velocity profiles measured even at the farthest downstream measurement station (x = 9.25 inches) still deviate from that of the equilibrium flat plate turbulent boundary layer suggested by Klebanoff (1955) for each condition. The flow behavior is similar to each other except the location and magnitude of the maximum rms peak due to earlier transition and reattachment for higher FSTI cases.

Figures 52-54 present the carpet plots of rms velocity profiles for Re = 100,000 with grids 0, 2 and 3, respectively. Corresponding expanded profiles for Re = 100,000 are shown in figures 52a-54a. Two peaks of rms velocity profiles are apparent at x = 6.25 inches for the grid 0 case. Due to smaller size of the reverse flow zone than that of Re = 70,000, the development of the near-wall peak cannot be further observed. Once again, as the flow reattaches around x = 6.75 inches, the two peaks merge and the peak strength reaches the maximum value. The rms velocity profiles develop into those of a fully turbulent boundary layer farther downstream. For higher FSTI (grids 2 and 3), no clear near-wall peak is observed. The development of the rms velocity profiles from the laminar attached boundary layer through transition in the shear layer over the separation bubble to the reattached boundary layer is similar to each other except for earlier reattachment and transition for grid 3. Comparing the rms velocity profiles for the lower Reynolds number cases, it is observed that rms double peaks with one in the free shear layer and another inside the bubble appear for the lowest FSTI (grid 0). However no clear rms peak inside the bubble is observed for grids 2-4 cases. Only one broad rms peak appears just outside the separated flow.

Figures 55-57 show the development of rms velocity profiles for Re = 250,000 with grids 0, 2 and 3, respectively. As shown in the counterpart mean velocity profiles (figures 27-29), no separation of the boundary layer is observed in the flow field with any grids. The rms near-wall peak in the laminar boundary layer at x = 1.75 inches grows in magnitude and moves slightly away from the wall as the flow moves downstream and changes to turbulent through transition for each condition. For higher FSTI, the flow becomes turbulent earlier in the boundary layer due to earlier transition. The locations of transition will be determined based on the intermittency profiles later in this chapter.

Figures 58-61 show the contour plots of the same fluctuating rms velocity distributions (u'_{rms}/U_{in}) of Re = 35,000 for grids 0, 2, 3 and 4, respectively. These plots were generated from evenly spaced fluctuating rms velocity data in the diverging section from x = 4.25 inches to 9.25 inches with an increment of 0.5 inches. The scales used in these contour plots are exactly the same as in the corresponding contour plots of the mean velocity profiles. The y-scale has been expanded 17 times compared to the x-scale to show the details in the near-wall region. For grid 0 (FSTI = 1 %) as shown in figure 58, u'_{rms}/U_{in} is less than 0.04 in the region up to x = 6.5 inches since the fluctuating energy is quite low in the laminar portion of the separation bubble all the way up to freestream. The fluctuating energy starts to gain its strength in the free shear layer around y = 0.15 inches outside the separation bubble at x = 6.75 inches. As the flow goes through transition, the fluctuating energy propagates into the surface and the flow finally reattaches. The maximum turbulent energy occurs at or just downstream of the reattachment location in the shear layer at y = 0.08 inches above the surface for grid 0

case. For grid 2, the fluctuating energy shows the highest level of $u'_{rms}/U_{in} = 0.06$ at y = 0.06 inches just outside of the separation bubble at x = 4.25 inches. This turbulent energy peak moves away from the wall to y = 0.1 inches around x = 6 inches and the maximum energy level increases to $u'_{rms}/U_{in} = 0.16$ as the flow goes through transition. This turbulent energy propagates both toward the wall and into the freestream as the flow goes downstream. The highest level of fluctuating energy ($u'_{rms}/U_{in} = 0.24$) shows at or just downstream of the reattachment location and around y = 0.1 inches in the shear layer. For higher FSTI of grids 3 and 4, the trend is similar to that of the grid 2 case. As FSTI increases, the maximum level of energy peak gets higher due to higher freestream turbulence energy (max of $u'_{rms}/U_{in} = 0.26$ for grid 3 and 0.28 for grid 4) and the maximum energy peak locates upstream due to earlier reattachment (x = 6.6 inches for grid 3 and 6.3 inches for grid 4). However, the y location of maximum turbulent energy peak is almost the same at y = 0.1 inches regardless of FSTI.

Figures 62-65 present the contour plots of the fluctuating rms velocity distributions (u'_{rms}/U_{in}) of the Re = 70,000 case for grids 0, 2, 3 and 4, respectively. The development of fluctuating velocity profiles and propagation of turbulent energy are similar to the counterparts at Re = 35,000 for each condition. Since the separation bubble is getting shallower with increasing Reynolds number, the maximum energy peak outside of the separation bubble at x = 4.25 inches for grids 2-4 is located around y = 0.03 inches closer to the wall than that for Re = 35,000. This energy peak moves away from the wall and gains strength farther downstream. Through transition the turbulent energy propagates deeper into the near-wall area than the Re = 35,000 case. The maximum

energy peak just downstream of the reattachment location occurs at around y = 0.06 inches for each condition, which is closer to the surface than that for the Re = 35,000 case. Once again as FSTI increases, the maximum level of energy peak increases (max of u'_{rms}/U_{in} = 0.24 for grid 3 and 0.26 for grid 4) and the streamwise location of the maximum energy peak moves upstream.

The contour plots of fluctuating velocity profiles for Re = 100,000 are shown in figures 66-68 for grids 0, 2 and 3, respectively. The trend of development of turbulent energy is identical to the counterparts of Re = 70,000. The deeper penetration of turbulent energy into the near-wall region than previous for the two lower Reynolds number cases is obvious for each FSTI. The maximum turbulent energy peak just downstream of the reattachment location is around y = 0.05 inches for each condition.

Integral Quantities

The variations of displacement (δ^*), momentum (θ) and energy (ε) thicknesses in the streamwise direction determined by integrating the mean velocity profiles from the surface to the edge of the boundary layer for Re = 35,000 with grids 0-4 are shown in figure 69. The energy thickness is a measure of the energy dissipation in the boundary layer due to viscous and turbulent stresses. The values of displacement thickness decrease with an increase of FSTI as the separation bubble shrinks. For each FSTI, δ^* increases rapidly to a local maximum near the maximum bubble height, decreases to a local minimum and then slightly increases to an exit value. The maximum value of displacement thickness decreases with an increase of FSTI and moves upstream

progressively. The momentum and energy thicknesses increase monotonically throughout the test section. The growth rates of δ^* is the greatest among the three integral thicknesses in the separated flow region. The growth rates of both θ and ε are similar to each other in the laminar portion of the separation bubble. Both values of θ and ε increase with an increase of FSTI (from grid 0 to 3) up to the maximum bubble height. There is, however, no clear trend farther downstream.

The characteristics of the separation bubbles are generally described by the properties at separation. At separation the displacement thickness changes rather rapidly, while the momentum thickness varies quite slowly due to negligible skin friction. Thus θ is a much more suitable choice than δ^* to describe bubble behavior (Gaster, 1969; O'Meara and Mueller, 1986).

The plots of shape factors, H_{12} (= δ^*/θ) and H_{32} (= ε/θ), for Re = 35,000 with four grids are presented in figure 70. For each condition, H_{12} monotonically increases to a local maximum around the maximum bubble height and sharply decreases to a local minimum downstream from reattachment and then levels out to the values of a turbulent boundary layer. The peak values move upstream with increasing FSTI. This trend is very similar to that observed in the δ^* variation. The opposite trends are obvious in the variation of H_{32} for each condition.

The variations of δ^*, θ and ε for Re = 70,000 with four grids are shown in figure 71. Their distributions of shape factors are shown in figure 72. For Re = 100,000 the variations of integral thicknesses and shape factors with grids 0-3 are plotted in figures 73

and 74, respectively. The trend of each 5 integral quantities for Re = 70,000 and 100,000 is the same as their counterpart for the Re = 35,000 case. For each Reynolds number, both δ^* and H_{12} are inversely proportional to FSTI and their local maxima move upstream with increasing FSTI. However, H_{32} is proportionally changing with FSTI.

The distributions of integral quantities for Re = 250,000 with grids 0, 2 and 3 are shown in figures 75 and 76. All three quantities, δ^*, θ and ε, increase monotonically as the attached boundary layers develop downstream for each FSTI. While there is no clear variation of δ^* with FSTI, the momentum and turbulent energy increase with increasing FSTI throughout the test section. The shape factors for Re = 250,000 behave as expected. The values of H_{12} and H_{32} start with those of a laminar boundary layer and change to those of a turbulent boundary layer as the flow moves downstream. The characteristics of flow parameters including freestream and boundary layer properties throughout the entire test section from x = 1.75 inches to 9.25 inches are listed in Tables 3-16 for all 14 test cases.

The most commonly used parameter for determining the separation location is the shape factor H_{12}. However, as noted in the figures 70, 72 and 74, H_{12} varies rapidly at the separation point due to the large gradient of δ^* and scatters in the upstream region up to the maximum bubble height for different levels of freestream turbulence. On the other hand, H_{32} changes quite slowly throughout the separated flow and is nearly identical up to the separation location regardless of freestream turbulence levels. H_{32} is, thus, a more logical choice for determining the separation point. The separation locations are determined in this experiment from a careful examination of the mean velocity profiles with the aid of the distribution of H_{32} (close to 1.52) for each condition.

Reattachment models based on shape factors H_{12} and H_{32} have proven to be useful in previous separation bubble calculations. Horton (1969) suggested a universal velocity profile at reattachment with values of H_{12} and H_{32} of 3.5 and 1.51, respectively. The reattachment locations in this study were determined to be where H_{32} is equal to 1.51 for each condition. The separation and reattachment locations determined from the shape factors are closely matched to those obtained from the pressure and mean velocity distribution within experimental error. The streamwise separation and reattachment locations are listed in Tables 17-19 for Re = 35,000, 70,000 and 100,000, respectively.

Intermittency Profiles

Intermittency values were computed from the digitally recorded instantaneous velocity signals. Each instantaneous velocity signal was segregated into turbulent and non-turbulent parts based on the criteria of the first and second derivatives of the signals as described in Chapter III. Intermittency, γ, is defined as the fraction of time during which the flow at a given position remains turbulent after the onset of transition. A flow is considered fully turbulent if $\gamma = 1$ and fully laminar if $\gamma = 0$. The transition start and end locations are determined based on the intermittency profiles. The start location of transition is where γ starts to deviate from zero, while the end location is where $\gamma = 0.99$.

The variations of the intermittency profiles in the normal direction, y, for Re = 35,000 with four grid configurations are shown in figures 77-80. As shown in figure 77 for grid 0, the flow is laminar up to x = 6.25 inches. Transition begins just downstream of x = 6.25 inches, but doesn't end even at the last measurement location for Re = 35,000

with grid 0 due to low speed and FSTI. A peak intermittency occurs at y = 0.025 inches for a streamwise station of x = 6.75 inches. As the flow proceeds downstream and becomes fully turbulent in the test section, the peak intermittency values move toward the wall. As shown in figures 78-80, the transition starts around x = 5.75 inches for grid 2, between x = 5.25 and 5.75 inches for grid 3 and around x = 5.25 inches for grid 4. The transition ends at x = 7.25 inches for grid 2, around 6.75 inches for grid 3 and x = 6.25 inches for grid 4. It is clear that both transition start and end points move upstream progressively with an increase of FSTI. The rates at which the transition end points move upstream is faster than that for transition start points with FSTI, so the transition length decreases with an increase of FSTI. The actual transition start and end locations will be determined based on the Narasimha's (1984) model for each condition in the last section of intermittency profiles. It is noted that the transition is initiated on the laminar portion of the separation bubble, and due to increased turbulent energy caused by transition, the separated flow reattaches as transition progresses as discussed in the section of fluctuating rms velocity profiles.

The distributions of intermittency profiles are presented in figures 81-84 for Re = 70,000 with grids 0-4 and in figures 85-87 for Re = 100,000 with grids 0-3. Higher FSTI causes earlier transition over a shorter distance for each Reynolds number so the flow becomes turbulent more quickly. As shown in figures 85-87 for Re = 100,000, the intermittency has its peak around y = 0.05 inches at x = 6.25 inches for grids 0 and at x = 5.75 inches for grid 2. The intermittency peak occurs around y = 0.025 inches for grid 3. It can be said that transition is initiated predominantly in the free shear layer just outside

of the separation bubble and propagates toward the wall as the transition is completed. The intermittency profiles also clearly indicate the existence of a finite transition length over a separated flow region even for the highest Reynolds number and FSTI. In earlier studies (Gaster, 1969; Roberts, 1975, 1980), the transition on a short separation bubble was assumed to happen instantaneously at the maximum height of the bubble. However, more recent studies on the separation bubble (Malkiel and Mayle, 1995; Simon and Qiu, 1997) clearly demonstrate the transition zone from the intermittency measurements.

The intermittency profiles for Re = 250,000 are shown in figures 88-90 for grids 0, 2 and 3, respectively. The trend of earlier transition over a shorter distance with higher FSTI is detected. Due to high speed the boundary layer is attached and relatively thin. So the transition possibly occurs in a near-wall region ($y < 0.15$ inches), producing a shallow intermittency profile for each condition.

The intermittency profiles are used to determine the transition onset and end locations. Based on the Emmons' (1951) turbulent spot theory, Narasimha (1984) suggested a model with which transition locations can be obtained systematically. The following function, $f(\gamma)$, is evaluated for the maximum intermittency value, γ, in the normal direction, y, at each streamwise measurement location, x.

$$f(\gamma) = \sqrt{-\ln(1-\gamma)}$$

Figure 91 presents the variation of $f(\gamma)$ with x for Re = 35,000. A least-square fit to those data points for each grid is extrapolated to $f(0) = 0$ and $f(0.99) = 2.146$. The streamwise locations for two extrapolated points are taken as the onset and end locations of transition.

The transition locations and length determined from f(γ) are listed in Tables 17-20 for Re = 35,000, 70,000, 100,000 and 250,000, respectively.

It is observed that the transition end location is farther downstream than the reattachment location for Re = 35,000 case regardless of FSTI. The transition process is quite delayed due to a very low speed. However, as the flow speed increases for the Re = 70,000 and 100,000 cases, the flow becomes turbulent through transition earlier and quicker than that for the Re = 35,000 case. Due to substantially increased turbulent fluctuating energy through transition over a shorter distance, the flow becomes turbulent and finally reattaches. The transition data from a cascade experiment on simulated LPT by Simon and Qiu (1997) also show the same trends. For their lowest Reynolds number of 50,000 the transition is delayed past the reattachment location regardless of FSTI. For higher Reynolds numbers of 100,000 and 300,000 the transition ends and flow becomes turbulent before the flow reattaches.

Dhawan and Narasimha (1958) proposed a model for describing the intermittency within the transition zone, which is

$$\gamma = 1 - e^{-0.412\xi^2}$$

where

$$\xi = (x - x_{ts})/(x_{te} - x_{ts})$$

Dhawan and Narasimha (1958) used x_{ts} taken at $\gamma = 0.25$ and x_{te} taken at $\gamma = 0.75$. Volino and Simon (1995) algebraically modified the original Dhawan and Narasimha model as follows to use the actual start and end locations of transition.

$$\gamma = 1 - e^{-4.6[(x-x_{ts})/(x_{te}-x_{ts})]^2}$$

where x_{ts} taken at $\gamma = 0$ and x_{te} taken at $\gamma = 0.99$.

Figure 92 shows the distribution of intermittency within the transition zone along with the curve of the modified version of the Dhawan and Narasimha model. The transition locations determined from $f(\gamma)$ as described in figure 91 for the separated flow are in good agreement with the model for each condition, even though this model is for unaccelerated flow. Note that the transition is initiated in the laminar part of the separated flow where there is no or little pressure variation as shown in C_p distributions of figures 12-14. That's probably the reason that the intermittency model for unaccelerated flow works well for the separated flow.

Power Spectra

Spectral data were taken to help understand the character and nature of the disturbances in the boundary layer and freestream regions of the flow field. Power spectral data were measured using a Dantec straight type single hot-wire probe. The sampling rate was set at 12.8 kHz and the spectra were averaged over 100 scans. The power spectral density (PSD) data were measured at the normal position where the fluctuating rms velocity was a maximum in the boundary layer for each condition from x = 1.75 inches to 9.25 inches. Figures 93-96 present the distribution of the PSD function for Re = 70,000 with grids 0, 2, 3 and 4, respectively. For clarity the PSD functions measured at streamwise locations from x = 5.25 inches to 7.25 inches are plotted in these

figures. The same power spectral density functions multiplied by the frequency (f * PSD) are presented in figures 93a-96a for grids 0, 2, 3 and 4, respectively. In these energy coordinates of figures 93a-96a, the area under each PSD curve in any frequency band is directly proportional to the energy in that frequency bandwidth. As shown in figure 93 for grid 0, the low levels of fluctuating energy are confined in the frequencies less than 300 Hz at x = 5.25 and 5.75 inches, resembling a laminar flow-field spectra. The flow field was contaminated by the main and bleed blowers' noise and their sub-harmonics. When the transition starts and is in early stage at x = 6.25 inches, the PSD in the range of frequency between 50 Hz and 900 Hz increase slightly, but the values of PSD decrease outside of this frequency range. The same PSD data in energy coordinates shown in figure 94 show no turbulent energy at any frequencies up to x = 6.25 inches. As transition progresses farther downstream, the PSD jumps substantially. About a two-order of PSD magnitude increase from x = 6.25 inches to 6.75 inches and one-order of PSD jump from x = 6.75 inches to 7.25 inches can be observed for all frequency bandwidth of 5 KHz.

For grid 2 as shown in figures 94 and 94a, the energy of the laminar flow is confined in f < 200 Hz with a peak at f = 12 Hz for the profiles at x = 5.25 inches and 5.75 inches. As transition progresses energy containing frequency is expanded to 2 KHz. The energy level in the range of f > 30 Hz increases substantially, but the low frequency energy (f < 30 Hz) decreases. The energy peak moves from an f * PSD value of 0.1 at f = 12 Hz (x = 5.75 inches) to 0.6 at f = 120 Hz (x = 7.25 inches) as the flow goes downstream. It can be noted that due to increased freestream turbulence the PSD magnitude for grid 2 is about two-orders higher than the corresponding values for grid 0

up to x = 6.25 inches and about one-order higher at x = 6.75 inches. However, when the flow becomes turbulent the increase of PSD due to increased FSTI is minimal.

The development of PSD profiles for Re = 70,000 with grids 3 and 4 can be seen in figures 95-96 and 95a-96a (energy coordinates). Due to increased FSTI, the energy levels in laminar and transitional flow substantially grow. However, no effect of FSTI on turbulent energy is observed when the flow becomes turbulent. Comparing the magnitude of energy peak (maximum f * PSD) at x = 5.25 inches, it is increased from 0.5 for grid 3 to 0.65 for grid 4. At x = 5.75 inches the peak values of f * PSD increase from 0.35 for grid 3 to 0.6 for grid 4. The low frequency energy level contained in f < 40 Hz is decreasing in magnitude as the flow develops for the grids 3 and 4 cases. This low frequency energy peak at f = 12 Hz moves to f = 120 Hz as flow goes farther downstream, similar to the case of grid 2.

Figures 97-99 show the PSD functions for Re = 100,000 with grids 0, 2 and 3, respectively. The same data plotted in energy coordinates are presented in figures 97a-99a. The general feature of PSD variation for Re = 100,000 is similar to that of Re = 70,000 for each condition except for the energy peak levels and locations due to different flow speed. The energy levels in the laminar and transitional flow for grid 0 are lower than the counterparts for higher FSTI. Due to low freestream turbulence level of 1 % for grid 0, the flow is susceptible to environment noise. As with grid 0 for Re = 70,000 (figure 93), a narrow banded PSD hump around f = 120 Hz is evident which is related to the main blower noise. As shown in figures 97a for the grid 0 case, no noticeable turbulent energy can be found at streamwise locations up to 6.25 inches. As the flow

develops through transition the high frequency energy level increases substantially at x = 6.75 inches and 7.25 inches. The maximum energy peak occurs at f = 250 Hz with grid 0.

As shown in figure 98a, the energy is contained in f < 400 Hz at x = 5.25 inches and in f < 1 KHz at x = 5.75 inches with grid 2. As transition progresses the spectral energy becomes broad banded. The high frequency energy level increases while the low frequency energy (f < 60 Hz) decreases. The maximum energy peak moves to the higher frequency from f = 12 Hz at x = 5.75 inches to f = 300 Hz at x = 6.75 inches as flow develops. For grid 3 as shown in figure 99a, the energy is contained f < 1 KHz with a peak at f = 12 Hz and x = 5.25 inches. Once again as transition progresses, high frequency energy increases but low frequency energy decreases. The maximum energy peak moves to the higher frequency from f = 12 Hz at x = 5.75 inches to f = 300 Hz at x = 6.75 inches. The energy level drops to the fully turbulent level, as the flow becomes fully turbulent farther downstream.

As for the Reynolds number effects on the spectral energy, the low frequency energy peak for the flow in the laminar or early transitional stage is observed at f = 12 Hz regardless of Reynolds numbers. As flow develops the turbulent energy is more broad-banded and the maximum energy peak moves to higher frequency for both Reynolds numbers. As the Reynolds number increases, the flow shows more high frequency content. The maximum energy peak occurs at higher frequency as the Reynolds number increases. It is f = 120 Hz for Re = 70,000 and f = 300 Hz for Re = 100,000.

It is believed that the transition process over the separation bubble for low freestream turbulence level is similar to that of the free shear layer, which is caused by a

Kelvin-Helmholtz type instability in the flow field. However, Malkiel and Mayle (1995) argued that the intermittency development in separation bubbles is modeled with the turbulent spot theory used in attached boundary layers and there is also evidence of Kelvin-Helmholtz vortex pairing in the transition region. The present PSD data over the separation bubble shows no broad band disturbance hump around f = 1500 Hz., which would be caused by a Kelvin-Helmholtz type instability wave. Since no Tollmien-Schlichting or Kelvin-Helmholtz instabilities related turbulent energy humps are detected in the present spectral data for any cases, it can be speculated that the transition process of the present experiment is related to a bypass transition.

Reynolds Number Effects on the Separated Flow

The flow separation and subsequent transition processes on a separated flow are strongly affected by freestream turbulence levels and Reynolds numbers. In the previous section, a discussion was given to clarify the effects of freestream turbulence level on the flow separation and transition for each Reynolds number. Generally the mean and fluctuating rms velocity profiles, intermittency profiles and power spectral data with different levels of freestream turbulence were compared with each other for each Reynolds number. In this section, the variations of mean velocity profiles, fluctuating rms velocity profiles and intermittency profiles with respect to Reynolds numbers at some selected streamwise measurement locations around the separation bubbles will be investigated for each FSTI. Since no laminar separation bubbles are observed for Re = 250,000 with any FSTI, the flow for this configuration will not be included in this

discussion. For grid 0 (FSTI = 1 %), the discussion will be made in the region from x = 4.25 inches to 7.75 inches and for grid 2 (FSTI = 2 %) and grid 3 (FSTI = 3 %), from x = 4.25 inches to 7.25 inches.

Flow with Freestream Turbulence level of 1 % (Grid 0)

Figure 100 presents the variation of the mean velocity (U/U_{in}) profiles with Reynolds number at x = 4.25 inches for grid 0. The corresponding fluctuating velocity or turbulent intensity (u'_{rms}/U_{in}) profiles are shown in figure 101. The separation location was determined to be at x = 3.85 inches for Re = 35,000. The mean velocity profile at x = 3.75 inches starts to show an inflection point in the profile near the wall, which is a precursor to boundary layer separation. The mean velocity profile for Re = 35,000 at x = 4.25 inches shows a very small constant velocity zone near the wall indicating the flow is already separated. The mean velocity profiles for the Re = 70,000 and 100,000 are typical attached laminar boundary layer profiles. The fluctuating velocity plots are typical laminar profiles. Intermittency values are all zeros at x = 4.25 inches for any Reynolds numbers, indicating the flows are either laminar separated flow for Re = 35,000 or laminar attached flows for Re = 70,000 and 100,000.

Mean and fluctuating rms velocity profiles at x = 4.75 inches are shown in figures 102 and 103. Intermittency values at x = 4.75 inches are all zeros, indication all laminar flows for all three Reynolds number cases. The near-wall constant velocity zone for Re = 35,000 does not grow much compared to that at x = 4.25 inches. The mean velocity profile for Re = 70,000 starts to show a deflection near the wall, while the mean velocity

profile for Re = 100,000 shows an attached laminar profile. The rms velocity profiles for all three Reynolds number cases are quite similar to those at x = 4.25 inches, showing typical laminar profiles.

Figures 104 and 105 present the mean and rms velocity profiles at x = 5.25 inches. The flows are separated for these three Reynolds numbers. The near-wall separation zone for Re = 35,000 starts to grow up to y = 0.02 inches and this zone is extended a little further for Re = 70,000 than that at x = 4.75 inches. The mean velocity profile for Re = 100,000 shows a near-wall deflection, indicating flow separation. The rms velocity profiles are similar to the two previous cases, showing no peculiar features. The intermittency values are still zero throughout the boundary layer. All flows are laminar from the dead-air zone inside the bubble to the laminar free shear layer outside of the bubble without any hint of transition.

Mean and rms velocity profiles at x = 5.75 inches for grid 0 are shown in figures 106 and 107. Corresponding intermittency profiles at x = 5.75 inches are presented in figure 108. The near-wall separation zone is extended to y = 0.03 inches for Re = 35,000 and around y = 0.025 inches for Re = 70,000 and 100,000. The fluctuating velocity profiles start to show a small hump just outside of the separation bubble for each Reynolds number. This small hump moves slightly toward the wall with an increase of Reynolds number. The intermittency values are all zeros except for a small portion of maximum γ of 2 % around y = 0.03 inches for Re = 100,000. The transition on the separated flow is about to start at x = 5.75 inches for Re = 100,000. The flows for Re = 35,000 and 70,000 are still in the laminar stage.

Figures 109-111 present the mean velocity, fluctuating velocity, and intermittency profiles at x = 6.25 inches, respectively. The near-wall separation zone is extended up to y = 0.05 inches for Re = 35,000 and to y = 0.04 inches for Re = 70,000 and 100,000. The turbulent intensity profile for Re = 35,000 shows a small hump around y = 0.15 inches. The peak values of u'_{rms}/U_{in} of 4 % for Re = 70,000 and 5 % for Re = 100,000 at x = 6.25 inches are observed in figure 110. These fluctuating velocity peaks are all located just outside of the separation bubble for all three Reynolds number cases. This fluctuating velocity peak moves toward the wall as the Reynolds number increases. The intermittency profiles shown in figure 111 provide an interesting feature, namely double peaks, one inside the separation bubble and another just outside the bubble in the shear layer. For Re = 100,000, the intermittency value of the sharp peak is 67 % just outside of the bubble and 38 % inside the bubble. The intermittency values of the sharp peaks are about 50 % for both peaks for Re = 70,000. No transition is yet evident for flow of Re = 35,000. It is noted that the intermittency is confined in a shallow region of y < 0.05 inches since transition is in its early stages even though peak values are relatively high in the shallow region for the two high Reynolds number cases.

The mean and fluctuating rms velocity profiles at x = 6.75 inches are shown in figures 112 and 113. The intermittency profiles obtained from the instantaneous velocity signals at x = 6.75 inches are presented in figure 114. From the mean velocity profiles, it is noted that the near-wall separated flow zone has increased to y = 0.07 inches for Re = 35,000. This near-wall separated region is about the same at y = 0.04 inches as in the x = 6.25 inches case for Re = 70,000, but it is reduced to y = 0.025 inches for Re = 100,000.

As shown in the fluctuating velocity profiles, the turbulent energy is increased substantially as transition proceeds into the final stage for Re = 70,000 and 100,000. The maximum intermittency values are about 95 % for Re = 70,000 and 98 % for Re = 100,000 as shown in figure 114. This increased turbulent energy in the shear layer just outside of the bubble propagates into the wall to overcome the adverse pressure gradient effect and causes the flow to reattach. The peak rms velocity locations are at about y = 0.1 inches for Re = 70,000 and y = 0.08 inches for Re = 100,000. The turbulent energy hump at y = 0.2 inches for Re = 35,000 is the indication of the start of transition, which is evidenced in the intermittency profiles.

Figures 115-117 show the mean velocity, fluctuating velocity, and intermittency profiles for grid 0 at x = 7.25 inches, respectively. The near-wall separation zone has ceased to grow for Re = 35,000 as shown in the mean velocity profiles. The near-wall double inflection points in the mean velocity profile for Re = 35,000 indicate that the flow is starting to reattach. The flow for Re = 100,000 is already reattached. For Re = 70,000 case, due to increased turbulent energy in the shear layer as shown in the fluctuating velocity profile, the turbulent energy is brought down to the near-wall zone through turbulent transport. This increased near-wall turbulent energy makes the flow reattach to the wall for Re = 70,000. The intermittency values of 98 % and 100 % for the two highest Reynolds number cases indicate that transition is almost finished and the flows become turbulent in the near-wall zone of $y < 0.07$ inches. The transition is still in its early stage for Re = 35,000 as shown in intermittency profiles (max of $\gamma = 40$ %) and in the fluctuating velocity profiles with a max value of $u'_{rms}/U_{in} = 0.07$ at y = 0.15 inches.

Figures 118-120 show the mean velocity, fluctuating velocity, and intermittency profiles for grid 0 at x = 7.75 inches, respectively. The near-wall separation zone further shrinks down as shown in the mean velocity profiles for Re = 35,000 since the flow is about to reattach. Double inflection points in the mean velocity profile are still evident. For Re = 70,000 and 100,000 the boundary layers are attached and turbulent as indicated in the intermittency values of unity near the wall (y < 0.03 inches). Also shown in the fluctuating rms velocity profiles (figure 119), the flows for these two high Reynolds numbers are still progressing to that of fully turbulent boundary layer flow. For flow of Re = 35,000, the transition is still in progress with a maximum intermittency of around 60 %. The transition proceeds at a slow pace over the separated flow region for Re = 35,000. The transition is not completed even at the last measurement location of x = 9.25 inches for Re = 35,000, as the intermittency is measured to be less than unity there.

Flow with Freestream Turbulence level of 2 % (Grid 2)

Since the separation locations for grid 2 are almost the same as the grid 0 case for each Reynolds number, as discussed in the previous section, it is speculated that the development of flow over a separation bubble with grid 2 is similar in nature to the grid 0 case for each Reynolds number. Due to increased freestream turbulence intensity, earlier transition over a shorter separation bubble and increased values of fluctuating rms velocity are expected. Figure 121 presents the variation of the mean velocity (U/U_{in}) profiles with Reynolds number at x = 4.25 inches for the grid 2 case. The corresponding fluctuating velocity profiles are shown in figure 122. The separation location for grid 2

was just downstream of x = 3.75 inches for Re = 35,000. The mean velocity profile at x = 4.25 inches for Re = 35,000 shows a deflection zone near the wall, indicating flow separation. The mean velocity profiles for the other two Reynolds numbers are typical attached laminar boundary layer profiles. The fluctuating velocity profiles also show the typical laminar profiles. The energy humps are located at y = 0.05 inches for Re = 35,000, at y = 0.03 inches for Re = 70,000 and y = 0.02 inches for Re = 100,000. This turbulent energy hump moves toward the wall with increasing Reynolds number. Intermittency values are all zeros at x = 4.25 inches for any Reynolds numbers, indicating the flows are laminar separated flow for Re = 35,000 or laminar attached flows for Re = 70,000 and 100,000 cases.

Mean velocity and fluctuating rms velocity profiles at x = 4.75 inches are shown in figures 123 and 124. Intermittency values at x = 4.75 inches are all zeros, indicating all laminar flows for all three Reynolds number cases. The near-wall constant velocity zone for Re = 35,000 does not grow much compared to that at x = 4.25 inches. The mean velocity profile for Re = 70,000 shows a slight hint of deflection near the wall, while the mean velocity profile for Re = 100,000 is still an attached laminar profile. The rms velocity profiles for all three Reynolds numbers are quite similar to those at x = 4.25 inches with a slight increase of peak values showing typical laminar profiles.

Figures 125–127 present the mean and fluctuating rms velocity and intermittency profiles at x = 5.25 inches, respectively. The flows are separated for these three Reynolds numbers. The near-wall separation zone for the two lower Reynolds numbers starts to extend a little further than that at x = 4.75 inches. The flow for Re = 100,000 starts to

show a near-wall separation. The rms velocity profiles are similar to the x = 4.75 inches case with a slight increase of peak magnitude. The intermittency values are still zero throughout the boundary layer. The separated laminar flow is evident for all three Reynolds numbers.

Mean and rms velocity profiles at x = 5.75 inches for grid 2 are shown in figures 128 and 129. Corresponding intermittency profiles at x = 5.75 inches are presented in figure 130. The near-wall separation zone is extended to y = 0.035 inches for Re = 35,000 and to around y = 0.03 inches for Re = 70,000 and 100,000. The turbulent intensity profiles show an increase of peak magnitude compared to the case at x = 5.25 inches for all three Reynolds number cases. These fluctuating velocity peaks are all located just outside of the separation bubble and they move toward the wall as the Reynolds numbers increase. The intermittency profiles show that the flows are all in the transitional stage with the higher Reynolds number cases being in further progression. The peak intermittency values are 60 % around y = 0.04 inches for Re = 100,000, 33 % around y = 0.02 inches for Re = 70,000 and only 5 % around y = 0.02 inches for Re = 35,000.

Figures 131-133 present the mean and fluctuating velocity, and intermittency profiles at x = 6.25 inches, respectively. The near-wall separation zone is extended up to y = 0.05 inches for Re = 35,000. The separation zone has ceased to expand and near-wall double inflection points are observed for Re = 70,000 and 100,000, indicating the flows are starting to reattach to the wall due to increased turbulent energy. Again, the turbulent intensity profiles show an increase of peak value compared to the case at x = 5.75 inches

for all three Reynolds numbers. These fluctuating velocity peaks are about 20 % and are located just outside of the separation bubble. Again, the peaks move toward the wall as the Reynolds numbers increase. The intermittency values of 95 % and 98 % for the two highest Reynolds number cases indicate that transition is almost finished and the flows become turbulent in the near-wall zone of $y < 0.07$ inches. The transition is in its early stage for Re = 35,000 case as shown in intermittency profiles (max of $\gamma = 43$ %).

The mean and fluctuating rms velocity profiles and corresponding intermittency profiles at x = 6.75 inches are shown in figures 134-136. The mean velocity profiles show the double inflection points near the wall for Re = 35,000. As shown in the fluctuating velocity profiles, the turbulent energy is increased substantially as transition proceeds into the final stage (peak intermittency value of 85 %) for Re = 35,000. Again, this increased turbulent energy in the shear layer just outside of the bubble propagates into the wall to overcome the adverse pressure gradient effect and causes the flow to reattach. The mean velocity profiles show that the flow for the Re = 70,000 case is almost attached and for Re = 100,000 is already attached and has developed to a turbulent profile. The fluctuating velocity profile for Re = 100,000 show that the magnitude is reduced compared to that in the x = 6.25 inches case and is approaching the shape of a fully turbulent boundary layer.

Figures 137-139 show the mean and fluctuating velocity, and intermittency profiles for grid 2 at x = 7.25 inches, respectively. The mean velocity profiles show that the flows are all attached for all three Reynolds number cases. The flow is about reattached for Re = 35,000 case, though. The flows for the two higher Reynolds numbers

are becoming mature into the fully turbulent stage. The fluctuating rms velocity profiles indicate that previous sharp rms velocity peaks have become more rounded and further reduced in magnitude, approaching fully turbulent values for the Re = 70,000 and 100,000 cases. The flows are all turbulent as indicated in the intermittency values of unity near the wall for all Reynolds numbers.

Flow with Freestream Turbulence level of 3 % (Grid 3)

Figure 140 presents the variation of the mean velocity profiles with three different Reynolds numbers at x = 4.25 inches for grid 3. The corresponding fluctuating velocity profiles are shown in figure 141. The boundary layer was separated just downstream of x = 3.75 inches for Re = 35,000 as discussed in the previous section. The mean velocity profile with grid 3 for Re = 35,000 shows a small deflection zone near the wall indicating flow separation. The mean velocity profiles for the other two Reynolds numbers are typical for attached laminar boundary layer profiles. The fluctuating velocity profiles show sharp peaks at y = 0.06 inches for Re = 35,000, at y = 0.04 inches for Re = 70,000 and at y = 0.02 inches for Re = 100,000. Due to elevated freestream turbulence intensity, the levels of rms velocity are higher than those for the two previous low FSTI cases. Again, this turbulent energy peak moves toward the wall with increasing Reynolds number. Intermittency values are all zeros at x = 4.25 inches for all three Reynolds number cases indicating the flows are laminar separated flow for Re = 35,000 or laminar attached flows for the Re = 70,000 and 100,000 cases.

Mean velocity and fluctuating rms velocity profiles at x = 4.75 inches are shown in figures 142 and 143. Intermittency values at x = 4.75 inches are all zeros, indicating laminar flows for all three Reynolds number cases. The near-wall constant velocity zone for the Re = 35,000 case does not grow much compared to that at x = 4.25 inches. The mean velocity profile for Re = 70,000 shows a slight hint of deflection near the wall, and the mean velocity profile for Re = 100,000 is still for an attached laminar profile. The rms velocity profiles for all three Reynolds number cases are similar to those at x = 4.25 inches with an increase of peak values up to 14 %.

Figures 144–146 present the mean and fluctuating rms velocity and intermittency profiles at x = 5.25 inches, respectively. The flows are separated for all three Reynolds numbers. Due to elevated FSTI, the size of the separation bubble shrinks. The near-wall separation zone for the two lower Reynolds numbers starts to extend a little further than that at x = 4.75 inches. The flow for the Re = 100,000 case starts to show near-wall separation. The rms velocity profiles are similar to the x = 4.75 inches case with a further increase of peak magnitude to 17 % - 20 %. The intermittency values for Re = 35,000 are still zero throughout the boundary layer, indicating separated laminar flow. However, the intermittency profiles show that the flow for Re = 70,000 just begins transition, while for Re = 100,000 the transition progresses to 25 % just outside of the bubble.

Mean and rms velocity profiles at x = 5.75 inches are shown in figures 147 and 148. Corresponding intermittency profiles for grid 3 are presented in figure 149. The near-wall separation zone is extended to y = 0.025 inches for Re = 35,000 and around y = 0.02 inches for Re = 70,000 and 100,000. The increment of the separation zone is

minimal due to increased FSTI. The rms velocity profiles are similar to the x = 5.25 inches case with a further increase of peak magnitude to 22 % - 24 %. The intermittency profiles show that the flows are all in the transitional stage. The transition for the Re = 35,000 case is in the early stage, while for the two higher Reynolds numbers, they are close to their final stage. The peak intermittency values are 95 % for Re = 100,000, 85 % for Re = 70,000 and 32 % for Re = 35,000.

Figures 150-152 present the mean and fluctuating velocity, and intermittency profiles at x = 6.25 inches, respectively. The mean velocity profiles show double inflection points near the wall for Re = 35,000. As shown in the fluctuating velocity profiles, the turbulent energy is increased substantially to 27 % as transition proceeds into the final stage (peak intermittency value of 80 %) for Re = 35,000. Again, this increased turbulent energy in the shear layer just outside of the bubble propagates into the wall to overcome the adverse pressure gradient effect and causes the flow to reattach. The mean velocity profiles show that the flow for the Re = 70,000 case is turbulent and just attached, and for Re = 100,000 is already attached and is developing into fully turbulent flow. The fluctuating velocity profile for Re = 100,000 shows that the peak magnitude is reduced compared to that in the x = 5.75 inches case, and is approaching fully turbulent boundary layer form.

The mean and fluctuating rms velocity profiles and corresponding intermittency profiles at x = 6.75 inches are shown in figures 153-155. The mean velocity profiles show that the flows are all attached for all three Reynolds number cases. The flow is just reattached for the Re = 35,000 case. The flows for the two higher Reynolds numbers are

getting mature into the fully turbulent stage. The fluctuating rms velocity profiles indicate that previous sharp rms velocity peaks have become more rounded and further reduced in magnitude and are approaching fully turbulent values for Re = 70,000 and 100,000. The flows are all turbulent as indicated in the intermittency values of unity near the wall for all Reynolds numbers.

Figures 156-158 show the mean velocity, fluctuating velocity, and intermittency profiles for grid 3 at x = 7.25 inches, respectively. Once again, the mean velocity profiles show that the flows are all attached for all three Reynolds number cases. The high levels of rms velocity (26 %) for Re = 35,000 indicate that this flow is still far from being fully turbulent. For Re = 70,000, the flow is becoming mature into the fully turbulent stage. The flow for Re = 100,000 is close to fully turbulent showing more rounded rms velocity peaks and reduced rms peak (13 %) approaching fully turbulent values. The flows are all turbulent as indicated in the intermittency values of unity near the wall for all Reynolds numbers.

Transition Models of the Separated Flow

Gaster (1969) proposed a two parameter bubble bursting criterion using a relationship between momentum Reynolds number at separation and pressure parameter $\overline{P} = (\theta_s^2/\upsilon)(\Delta U/\Delta x)$, based on his two sets of airfoil data and other researcher's experimental and calculated data. For the pressure parameter, ΔU is the rise in the freestream velocity that would occur over the bubble length Δx in an unseparated inviscid flow. According to Gaster's (1969) criterion, the separation bubbles can be either 'short'

or 'long' type, with the distinction between the two being their effects on the overall pressure distribution. Short bubbles have only a local displacement effect as discussed above in the distribution of the mean velocity profiles (see the streamlines in figures 17a-26a), so that the pressure distribution is close to that predicted for the flow over the surface without separation. However, long bubbles interact with the exterior flow to such an extent that the pressure distribution is different from that predicted without them. Since bubbles can be easily changed from short to long with small changes in the Reynolds number or angle of attack of an airfoil, leading to a dramatic loss in lift and possible stall, it is important to understand the process (Mayle, 1991).

After reexamining Gaster's (1969) and other researchers' low freestream turbulence data (0.2 % < FSTI < 0.5 %), Mayle (1991) developed several transition models for short and long bubbles relating Reynolds number based on the length between separation and transition start location, $Re_{x_{st}}$, to momentum thickness Reynolds numbers at separation, $Re_{\theta s}$.

$$Re_{x_{st}} = 300\, Re_{\theta s}^{0.7} \quad \text{(short bubbles)}$$

$$Re_{x_{st}} = 1000\, Re_{\theta s}^{0.7} \quad \text{(long bubbles)}$$

The Reynolds numbers, $Re_{x_{st}}$ are calculated from the data of separation and transition locations for each condition. The distributions of $Re_{x_{st}}$ along with the two Mayle transition models on the separated flows are presented in figure 159 for Re = 35,000, 70,000 and 100,000. Two dotted lines included in the figure indicate the bounding limits of the present data with coefficients of 120 and 540. The data are scattered along the

short bubble relationship. Generally speaking, as Reynolds number and FSTI increase, the data fall below the short bubble relationship. The separation location is affected by Reynolds number, but not by FSTI and neither is $Re_{\theta s}$. But the distance between separation and transition start is strongly affected by Reynolds number and FSTI. Thus, $Re_{x_{st}}$ is strongly affected by FSTI. It is speculated that the above two Mayle models cannot predict accurately the high FSTI flows. The FSTI effects should be included in the model to predict the transition on the separated flows with high FSTI such as in the real compressor or LPT.

Mayle (1991) also developed a model accounting for the actual transition length on the separation bubble,

$$Re_{LT} = 400\, Re_{\theta s}^{0.7}$$

where Re_{LT} is the Reynolds number based on the transition length. The variation of transition length Reynolds number along with Mayle's model is shown in figure 160 for Re = 35,000, 70,000 and 100,000. Two dotted bounding lines of the present data are also included in figure 160 with coefficients of 280 and 550. The data are clustered close to the line. The transition length model works fairly well. According to Mayle (1991), the transition length Reynolds number is independent of whether the bubble is short or long. The difference between long and short bubbles is not the length of transition, but the length of the unstable laminar shear layer.

Several empirical correlations have been developed accounting for the effects of freestream turbulence on the separation bubble length. Roberts (1980) related the

transition length of the separation bubble to the turbulence scale factor, which depends on the freestream turbulence levels and turbulent length scales. The turbulence scale is the quantity not easily obtained in experiments. Davis et al. (1985) modified the Roberts' correlation to replace the freestream turbulence factor with the local freestream turbulence level, Tu ($= u'_{rms}/U_e$) as follows:

$$Re_{x_{st}} = 25{,}000 \cdot \log_{10}\{\coth[17.32 \cdot Tu)]\}$$

The plots of Reynolds number based on the streamwise length between separation and transition start versus local freestream turbulent along with Roberts' modified correlation are presented in figure 161. The measured data generally follow the trend but are consistently lower than the correlation. The coefficients in the Davis et al.'s (1985) correlation are modified to generate the best fit the present data and are as shown in the figure as the dotted curve, which is

$$Re_{x_{st}} = 17{,}200 \cdot \log_{10}\{\coth[15.4 \cdot Tu)]\}$$

It is clear that the values of $Re_{x_{st}}$ decrease with increase of local freestream turbulence for each Reynolds number. Decrease of $Re_{x_{st}}$ with increase of Reynolds number for each freestream turbulence level is also observed.

It should be noted that the Reynolds numbers used in the Roberts' and its modified correlations are the transition length Reynolds number based on the streamwise length between separation and the maximum bubble height. That's because the transition over the separation bubble was believed to occur instantly at the maximum bubble height in many earlier studies as mentioned in the previous sections. To check the validity of

Roberts' correlation, the streamwise locations at the maximum bubble height are estimated from the series of mean velocity profiles for each condition. The Reynolds numbers based on the streamwise distance between separation and the maximum bubble height, Re_{l1}, are computed and plotted in figure 162 along with the same Davies et al's (1985) correlation. Since the transition starts at the streamwise location prior to the maximum bubble height and proceeds over a finite zone as already discussed in the above sections, it is expected that Re_{l1} is bigger than $Re_{x_{st}}$ for each condition. The measured Re_{l1} show good agreement with the model. It is suggested that the transition models on a separated flow should be modified to account for the distance from the real transition locations, possibly not from the location at the maximum bubble height. The real transition locations can be determined from the intermittency variations throughout the boundary layer.

CHAPTER V

SUMMARY AND CONCLUSIONS

The parametric investigation of the flow field on a simulated LPT blade was performed at four levels of freestream turbulence (FSTI = 1 %, 2 %, 3 % and 4 %) for Reynolds numbers of 35,000, 70,000, 100,000 and 250,000. Flows for the lower three Reynolds number cases are separated from the surface and generate short bubbles for all freestream turbulence levels tested. However, the flow for Re = 250,000 is attached throughout the whole test section regardless of the freestream turbulence level. The photographs of flow visualization reveal that the laminar portion of the bubble is steady, while the regions downstream from transition are unsteady. The separation locations were determined by careful examination of pressure and mean velocity profiles for each condition. The reattachment locations were estimated from the shape factor (H_{32} = 1.51) based on Horton's (1969) universal velocity profile. The separation location moves progressively downstream with increasing Reynolds numbers, but it is almost invariant with freestream turbulence intensity. However, the reattachment location shifts upstream, resulting in a smaller bubble size with increasing Reynolds number and freestream turbulence intensity.

The point transition on the separation bubble at maximum bubble height was believed in the past. However the transition from laminar to turbulent flow proceeds over a finite zone for all test cases, as Mayle (1991) has pointed out. The transition

locations are determined from the intermittency profiles. The start and end locations of transition as well as transition length are strongly affected by the Reynolds number and freestream turbulence level. Both transition start and end locations shift upstream and the transition length shrinks with increase of Reynolds number and freestream turbulence level.

The transition end location is farther downstream than the reattachment location in Re = 35,000 case for all freestream turbulence levels tested possibly due to low flow speed. However, the transition ends before the flow reattaches for higher Reynolds number cases. The increased turbulent energy due to transition causes the flow to reattach on the surface.

The transition on a separated flow was found to proceed through the formation of turbulent spots in the free shear layer as evidenced in the intermittency profiles for Re = 35,000, 70,000 and 100,000. As far as the transition modes are concerned, no hints of Kelvin-Helmholtz instability or Tollmien-Schlichting instability waves were detected in the spectral data. It is believed that the mode of transition occurring in the separated flow is bypass type. However, flow visualization revealed large vortex structures just outside of the bubble and their development to turbulent flow through interaction with each other for Re = 50,000, which is similar to the transition mode in the free shear layer (separated-flow transition). Therefore, it is fair to say that both bypass and separated-flow transition modes existed in the transitional flows over the separation bubble depending on the conditions.

Mayle's (1991) transition models predict the Reynolds number effect fairly well

for low freestream turbulent flow. They need improvement for high freestream turbulent flows. A modified Roberts' correlation suggested by Davis et al. (1985) fairly predicts the trend of the Reynolds numbers based on the length between separation and the transition onset with freestream turbulence level, but the magnitudes are consistently lower than the values obtained from the correlation. When the Reynolds numbers based on the streamwise distance between separation and the maximum bubble height were compared as used in the Roberts' correlation, the measured data show an good agreement with the correlation. Davies et al.'s (1985) transition model should be modified to account for the real transition locations to accurately predict the transition length variation with freestream turbulence intensity in the separated flow.

REFERENCES

Bradshaw, P. (1971), An Introduction to Turbulence and its Measurement, Pergamon Press, New York, NY.

Davis, R. L., Carter, J. E., and Reshotko, E. (1985), "Analysis of Transitional Separation Bubbles on Infinite Swept Wings," *AIAA-85-1685.*

Dhawan, S. and Narasimha, R. (1958), "Some Properties of Boundary Layer Flow During the Transition from Laminar to Turbulent Motion," *J. Fluid Mech.* Vol. 3, pp. 418-436.

Emmons, H. W. (1951), "The Laminar-Turbulent Transition in a Boundary Layer – Part I," *J. Aeronautical Science*, Vol. 18, pp. 490-498.

Gardner, W. B. (1981), "Energy Efficient Engine Low Pressure Turbine Boundary Layer Program Technology Report," *NASA CR-165338.*

Gaster, M. (1969), "The Structure and Behavior of Laminar Separation Bubbles," *A.R.C. R&M 3595.*

Halstead, D. E., Wisler, D. C., Okiishi, T. H., Walker, G. J., Hodson, H. P. and Shin, H-W. (1995a), "Boundary Layer Development in Axial Compressors and Turbines. Part 1 of 4: Composite Picture," *ASME paper 95-GT-461.*

Halstead, D. E., Wisler, D. C., Okiishi, T. H., Walker, G. J., Hodson, H. P. and Shin, H-W. (1995b), "Boundary Layer Development in Axial Compressors and Turbines. Part 2 of 4: Compressors," *ASME paper 95-GT-462.*

Halstead, D. E., Wisler, D. C., Okiishi, T. H., Walker, G. J., Hodson, H. P. and Shin, H-W. (1995c), "Boundary Layer Development in Axial Compressors and Turbines. Part 3 of 4: LP Turbines," *ASME paper 95-GT-463.*

Halstead, D. E., Wisler, D. C., Okiishi, T. H., Walker, G. J., Hodson, H. P. and Shin, H-W. (1995d), "Boundary Layer Development in Axial Compressors and Turbines. Part 4 of 4: Computations & Analyses," *ASME paper 95-GT-464.*

Hedley, T. B. and Keffer, J. F. (1974), "Turbulent/Non-Turbulent Decisions in an Intermittent Flow," *J. Fluid Mech.*, Vol. 64, pp. 625-644.

Horton, H. P. (1969), "A Semi-empirical Theory for the Growth and Bursting of Laminar Separation Bubbles," *A.R.C. CP-1073.*

Klebanoff, P. S. (1955), "Characteristics of Turbulence in a Boundary Layer with Zero Pressure Gradient," *NACA Rep. No. 1247.*

Malkiel, E. and Mayle, R. E. (1995), "Transition in a Separation Bubble," *ASME paper 95-GT-32.*

Mayle, R. E. (1991), "The Role of Laminar-Turbulent Transition in Gas Turbine Engines," *ASME J. of Turbomachinery*, Vol. 113, pp. 509-537.

McFarland, E. R. (1982), "Solution of Plane Cascade Flow Using Improved Surface Singularity Methods," *ASME J. of Eng. for Power*, Vol. 104, pp. 668-674.

Morin, B. L. and Patrick, W. P. (1991), "Detailed Studies of a Large-Scale Laminar Separation Bubble on a Flat Plate Volume 1 - Experimental Technique, Summarized Results, and Discussion," *UTRC Rep. R91-956786-1.*

Mueller, T. J. and Batill, S. M. (1980), "Experimental Studies of Separation on a Two-Dimensional Airfoil at Low Reynolds Numbers," *AIAA 80-1440.*

Narasimha, R. (1984), "On the Distribution of Intermittency in the Transition Region of a Boundary Layer," *J. of Aero. Sci.*, Vol. 24, pp. 711-712.

O'Meara, M. M. and Mueller, T. J. (1986), "Experimental Determination of the Laminar Separation Bubble Characteristics of an Airfoil at Low Reynolds Numbers," *AIAA-86-1065.*

Roberts, W. B. (1975), "The Effect of Reynolds Number and Laminar Separation on Axial Cascade Performance," *ASME J. of Eng. for Power*, pp. 261-274.

Roberts, W. B. (1980), "Calculation of Laminar Separation Bubbles and Their Effect on Airfoil Performance," *AIAA J.*, Vol. 18, No. 1, pp. 25-30.

Schlichting, H. (1979), Boundary Layer Theory, 7th edition, McGraw-Hill, New York, NY.

Shyne, R. J. and DeWitt, K. J. (1998), "Experimental Study of Boundary Layer Behavior in a Simulated Low Pressure Turbine," submitted for *NASA TM* (Also, Ph.D. Dissertation of R. J. Shyne, Univ. of Toledo, 1998).

Simon, T. W. and Qiu, S., (1997), "Measurements in a Transitional Boundary Layer Under Low-Pressure Turbine Airfoil Conditions," submitted for *NASA CR.*

Sohn, K. H. and Reshotko, E. (1991), "Experimental Study of Boundary Layer Transition with Elevated Freestream Turbulence on a Heated Flat Plate," *NASA CR-187068.*

Sohn, K. H., Shyne, R. J. and DeWitt, K. J. (1998), "Experimental Investigation of Boundary Layer Behavior in a Simulated Low Pressure Turbine," *ASME paper 98-GT-34* (Also *NASA TM-1998-207921*).

Suder, K. L., O'Brien, J. E., and Reshotko, E. (1988), "Experimental Study of Bypass Transition in a Boundary Layer," *NASA TM-100913.*

Volino, R. J. and Simon, T. W. (1995), "Measurements in Transitional Boundary Layers Under High Free-Stream Turbulence and Strong Acceleration Conditions," *NASA CR-198413.*

Yavuzkurt, S. (1984), "A Guide to Uncertainty Analysis of Hot-Wire Data," *ASME J. of Fluids Eng.*, Vol. 106, pp. 181-186.

Table 1. Test matrix

	Re = 35,000	Re = 70,000	Re = 100,000	Re = 250,000
Grid 0 (FSTI = 1%)	✓	✓	✓	✓
Grid 2 (FSTI = 2%)	✓	✓	✓	✓
Grid 3 (FSTI = 3%)	✓	✓	✓	✓
Grid 4 (FSTI = 4%)	✓	✓		

Table 2. The variation of integral length scale

	Re = 35,000	Re = 70,000	Re = 100,000	Re =250,000
Grid 0 (FSTI = 1%)	0.207	0.215	0.227	0.330
Grid 2 (FSTI = 2%)	0.560	0.601	0.620	0.740
Grid 3 (FSTI = 3%)	0.714	1.200	1.301	1.340
Grid 4 (FSTI = 4%)	0.765	1.232		

(Dimension: inch)

Table 3. Integral quantities and local Reynolds number variation, Re = 35,000 Grid 0

X (in)	U_e (ft/s)	δ^* (in)	θ (in)	ε (in)	H_{12}	H_{32}	Re_x	Re_θ
1.75	11.08	0.02226	0.00942	0.01519	2.363	1.613	9615	51.75
2.25	12.21	0.03086	0.01745	0.03093	1.769	1.773	13618	105.6
2.75	13.09	0.03252	0.01862	0.03302	1.747	1.774	17846	120.81
3.25	13.73	0.03894	0.02324	0.04166	1.675	1.792	22105	158.1
3.75	13.42	0.04211	0.02084	0.03618	2.020	1.736	24921	138.51
4.25	12.49	0.04869	0.01486	0.02304	3.276	1.550	26302	91.98
4.75	12.34	0.04635	0.01557	0.02396	2.977	1.539	30388	99.62
5.25	12.25	0.06824	0.01865	0.02829	3.659	1.517	33310	118.33
5.75	12.17	0.09600	0.02134	0.03221	4.498	1.509	36266	134.62
6.25	12.08	0.12999	0.02487	0.03676	5.226	1.478	39093	155.57
6.75	12.04	0.15161	0.02778	0.04057	5.457	1.460	42092	173.25
7.25	11.94	0.13745	0.03498	0.05096	3.929	1.457	44827	216.31
7.75	11.85	0.12058	0.03874	0.05806	3.112	1.499	47577	237.84
8.25	11.22	0.10800	0.04683	0.07524	2.306	1.607	47980	272.35
8.75	11.04	0.09153	0.04731	0.07851	1.935	1.660	50068	270.72
9.25	10.95	0.08334	0.04794	0.08047	1.764	1.703	52518	272.19

Table 4. Integral quantities and local Reynolds number variation, Re = 35,000 Grid 2

X (in)	U_e (ft/s)	δ^* (in)	θ (in)	ε (in)	H_{12}	H_{32}	Re_x	Re_θ
1.75	10.95	0.02265	0.00963	0.01550	2.353	1.610	9546	52.51
2.25	11.84	0.02385	0.01008	0.01629	2.367	1.617	13268	59.41
2.75	12.73	0.02551	0.01102	0.01800	2.315	1.633	17424	69.84
3.25	13.25	0.03177	0.01434	0.02410	2.215	1.680	21453	94.67
3.75	13.11	0.03424	0.01302	0.02071	2.630	1.591	24467	84.94
4.25	12.19	0.05122	0.01548	0.02391	3.309	1.545	25791	93.95
4.75	12.07	0.05426	0.01635	0.02517	3.319	1.540	29531	101.63
5.25	11.93	0.07315	0.01926	0.02945	3.797	1.529	32269	118.41
5.75	11.84	0.10055	0.02216	0.03339	4.537	1.507	35073	135.17
6.25	11.76	0.12634	0.02596	0.03833	4.866	1.476	37868	157.31
6.75	11.71	0.12307	0.03392	0.04939	3.628	1.456	40671	204.39
7.25	11.17	0.10866	0.04210	0.06467	2.581	1.536	41705	242.20
7.75	10.85	0.09271	0.04591	0.07671	1.976	1.635	43333	256.69
8.25	10.71	0.08401	0.04817	0.08159	1.744	1.694	45502	265.66
8.75	10.64	0.07721	0.04682	0.08062	1.649	1.722	47939	256.50
9.25	10.63	0.07677	0.04705	0.08172	1.632	1.737	50658	257.70

Table 5. Integral quantities and local Reynolds number variation, Re = 35,000 Grid 3

X (in)	U_e (ft/s)	δ^* (in)	θ (in)	ε (in)	H_{12}	H_{32}	Re_x	Re_θ
1.75	11.10	0.02226	0.00948	0.01528	2.347	1.611	9641	52.26
2.25	12.06	0.02499	0.01170	0.01958	2.137	1.674	13474	70.05
2.75	13.09	0.03391	0.01896	0.03359	1.789	1.772	17881	123.27
3.25	13.67	0.04032	0.02315	0.04136	1.742	1.787	22042	156.99
3.75	13.46	0.04285	0.02049	0.03542	2.091	1.729	25029	136.75
4.25	12.48	0.04753	0.01524	0.02372	3.119	1.557	26306	94.33
4.75	12.36	0.05135	0.01653	0.02562	3.107	1.550	30614	106.53
5.25	12.22	0.07129	0.01940	0.02964	3.674	1.528	33415	123.50
5.75	12.11	0.09557	0.02259	0.03400	4.230	1.505	36272	142.51
6.25	12.01	0.10898	0.02938	0.04347	3.710	1.480	39102	183.80
6.75	11.53	0.09979	0.03744	0.05732	2.666	1.531	40535	224.81
7.25	11.07	0.09042	0.04480	0.07229	2.018	1.614	41802	258.32
7.75	10.93	0.08274	0.04712	0.07895	1.756	1.675	44081	268.03
8.25	10.91	0.08082	0.04884	0.08365	1.655	1.713	46817	277.16
8.75	10.88	0.08013	0.04982	0.08633	1.608	1.733	49550	282.15
9.25	10.85	0.08247	0.05212	0.09105	1.582	1.747	52223	294.25

Table 6. Integral quantities and local Reynolds number variation, Re = 35,000 Grid 4

X (in)	U_e (ft/s)	δ^* (in)	θ (in)	ε (in)	H_{12}	H_{32}	Re_x	Re_θ
1.75	10.84	0.02218	0.00951	0.01539	2.333	1.619	9399	51.08
2.25	11.85	0.02445	0.01095	0.01815	2.233	1.658	13216	64.32
2.75	12.81	0.03055	0.01661	0.02920	1.840	1.758	17467	105.49
3.25	13.47	0.03730	0.02218	0.03976	1.682	1.793	21703	148.09
3.75	13.35	0.03834	0.01887	0.03259	2.032	1.727	24813	124.85
4.25	12.37	0.04320	0.01440	0.02254	2.999	1.565	26042	88.25
4.75	12.21	0.05183	0.01641	0.02537	3.158	1.546	30128	104.10
5.25	12.09	0.07001	0.01912	0.02900	3.661	1.517	32969	120.07
5.75	12.00	0.09431	0.02436	0.03676	3.871	1.509	35880	152.02
6.25	11.72	0.09530	0.02891	0.04343	3.296	1.502	38026	175.91
6.75	11.22	0.08604	0.03466	0.05407	2.482	1.560	39294	201.79
7.25	10.88	0.08163	0.04136	0.06778	1.973	1.639	40952	233.65
7.75	10.78	0.07238	0.04106	0.06969	1.763	1.697	43367	229.79
8.25	10.78	0.07167	0.04274	0.07369	1.677	1.724	46198	239.33
8.75	10.74	0.07193	0.04369	0.07571	1.647	1.733	48803	243.66
9.25	10.69	0.07202	0.04399	0.07666	1.637	1.743	51263	243.79

Table 7. Integral quantities and local Reynolds number variation, Re = 70,000 Grid 0

X (in)	U_e (ft/s)	δ^* (in)	θ (in)	ε (in)	H_{12}	H_{32}	Re_x	Re_θ
1.75	23.32	0.01665	0.00650	0.01037	2.562	1.595	20240	75.16
2.25	25.42	0.02200	0.01195	0.02115	1.840	1.770	28361	150.67
2.75	27.49	0.02293	0.01294	0.02309	1.772	1.784	37454	176.28
3.25	28.67	0.02770	0.01612	0.02903	1.719	1.801	46122	228.74
3.75	28.68	0.02984	0.01612	0.02864	1.851	1.777	53230	228.86
4.25	27.54	0.02683	0.00962	0.01509	2.790	1.569	57886	131.01
4.75	26.32	0.03282	0.01078	0.01671	3.045	1.550	61675	139.92
5.25	25.96	0.04856	0.01317	0.02016	3.687	1.531	67230	168.65
5.75	25.54	0.06923	0.01528	0.02295	4.531	1.502	72434	192.47
6.25	25.42	0.09859	0.01848	0.02718	5.334	1.470	78430	231.94
6.75	25.03	0.08838	0.02449	0.03538	3.609	1.445	83371	302.49
7.25	23.63	0.07142	0.03265	0.05251	2.187	1.608	84623	381.07
7.75	23.19	0.06202	0.03445	0.06039	1.656	1.719	88767	394.56
8.25	22.96	0.05501	0.03527	0.06181	1.560	1.752	93618	400.21
8.75	22.94	0.05462	0.03605	0.06384	1.515	1.771	99218	408.81
9.25	22.99	0.05332	0.03666	0.06425	1.538	1.767	105185	416.88

Table 8. Integral quantities and local Reynolds number variation, Re = 70,000 Grid 2

X (in)	U_e (ft/s)	δ^* (in)	θ (in)	ε (in)	H_{12}	H_{32}	Re_x	Re_θ
1.75	22.71	0.01619	0.00650	0.01045	2.491	1.608	19610	72.82
2.25	24.83	0.01655	0.00693	0.01130	2.387	1.630	27576	84.96
2.75	26.84	0.02200	0.01176	0.02071	1.871	1.762	36436	155.80
3.25	28.23	0.02668	0.01558	0.02801	1.713	1.799	45247	216.84
3.75	28.12	0.03107	0.01700	0.03034	1.828	1.785	52042	235.89
4.25	26.94	0.02866	0.01016	0.01600	2.820	1.575	56500	135.13
4.75	26.00	0.03576	0.01154	0.01794	3.100	1.556	61505	149.36
5.25	25.79	0.05185	0.01379	0.02112	3.759	1.531	67424	177.15
5.75	25.51	0.07735	0.01650	0.02483	4.688	1.505	73047	209.59
6.25	25.03	0.07805	0.02287	0.03361	3.413	1.470	77873	284.92
6.75	23.44	0.06580	0.03004	0.04767	2.190	1.587	78828	350.85
7.25	22.97	0.05812	0.03421	0.05812	1.699	1.699	83034	391.85
7.75	22.83	0.05660	0.03584	0.06242	1.579	1.742	88131	407.55
8.25	22.87	0.05763	0.03773	0.06654	1.528	1.764	93946	429.61
8.75	22.82	0.05689	0.03781	0.06703	1.504	1.773	99549	430.20
9.25	22.80	0.05796	0.03822	0.06765	1.517	1.770	105004	433.82

Table 9. Integral quantities and local Reynolds number variation, Re = 70,000 Grid 3

X (in)	U_e (ft/s)	δ^* (in)	θ (in)	ε (in)	H_{12}	H_{32}	Re_x	Re_θ
1.75	22.60	0.01676	0.00663	0.01064	2.530	1.605	19554	74.03
2.25	24.78	0.01724	0.00796	0.01337	2.167	1.680	27564	97.50
2.75	26.97	0.02478	0.01465	0.02644	1.692	1.805	36684	195.41
3.25	28.21	0.02781	0.01627	0.02933	1.709	1.802	45346	227.05
3.75	28.22	0.03145	0.01724	0.03073	1.825	1.783	52317	240.52
4.25	26.88	0.02904	0.01037	0.01640	2.802	1.582	56427	137.62
4.75	25.78	0.03515	0.01152	0.01793	3.051	1.556	61070	148.14
5.25	25.51	0.05293	0.01421	0.02174	3.725	1.530	66811	180.84
5.75	25.04	0.06704	0.01749	0.02616	3.832	1.496	71783	218.37
6.25	23.88	0.06344	0.02454	0.03784	2.585	1.542	74364	291.97
6.75	23.12	0.05738	0.03121	0.05199	1.839	1.666	77785	359.60
7.25	22.69	0.05391	0.03244	0.05558	1.662	1.713	81962	366.70
7.75	22.58	0.05330	0.03348	0.05822	1.592	1.739	87191	376.70
8.25	22.66	0.05566	0.03572	0.06259	1.558	1.752	93099	403.07
8.75	22.47	0.05745	0.03756	0.06615	1.529	1.761	97730	419.52
9.25	22.43	0.06014	0.03970	0.07025	1.515	1.769	103139	442.70

Table 10. Integral quantities and local Reynolds number variation, Re = 70,000 Grid 4

X (in)	U_e (ft/s)	δ^* (in)	θ (in)	ε (in)	H_{12}	H_{32}	Re_x	Re_θ
1.75	22.47	0.01652	0.00666	0.01076	2.479	1.615	19305	73.50
2.25	24.60	0.01724	0.00742	0.01222	2.324	1.648	27164	89.55
2.75	26.67	0.02432	0.01419	0.02552	1.714	1.798	35951	185.54
3.25	28.07	0.03038	0.01939	0.03551	1.567	1.831	44714	266.82
3.75	27.86	0.03106	0.01706	0.03042	1.821	1.783	51116	232.55
4.25	26.81	0.03008	0.01050	0.01674	2.866	1.594	55710	137.60
4.75	25.76	0.03698	0.01166	0.01819	3.170	1.559	60753	149.19
5.25	25.28	0.05159	0.01407	0.02154	3.665	1.530	65884	176.62
5.75	24.62	0.06346	0.01807	0.02726	3.512	1.508	70217	220.65
6.25	23.59	0.05638	0.02340	0.03671	2.409	1.569	73129	273.78
6.75	22.84	0.05162	0.02858	0.04793	1.806	1.677	76412	323.58
7.25	22.60	0.04970	0.02981	0.05112	1.667	1.715	81258	334.14
7.75	22.51	0.05033	0.03139	0.05458	1.604	1.739	86526	350.45
8.25	22.45	0.05127	0.03274	0.05735	1.566	1.752	91828	364.39
8.75	22.31	0.05251	0.03352	0.05885	1.567	1.756	96849	371.00
9.25	22.42	0.05428	0.03521	0.06197	1.541	1.760	102902	391.73

Table 11. Integral quantities and local Reynolds number variation, Re = 100,000 Grid 0

X (in)	U_e (ft/s)	δ^* (in)	θ (in)	ε (in)	H_{12}	H_{32}	Re_x	Re_θ
1.75	31.65	0.01372	0.00545	0.00876	2.515	1.607	27601	86.03
2.25	34.34	0.01404	0.00562	0.00905	2.496	1.610	38474	96.18
2.75	36.95	0.01439	0.00605	0.00991	2.378	1.637	50588	111.32
3.25	38.36	0.01917	0.00977	0.01705	1.963	1.746	62109	186.63
3.75	38.80	0.02416	0.01202	0.02106	2.010	1.751	72423	232.18
4.25	37.84	0.02371	0.00826	0.01294	2.872	1.568	80078	155.56
4.75	35.44	0.02681	0.00997	0.01556	2.691	1.562	84927	178.17
5.25	35.15	0.04441	0.01247	0.01897	3.562	1.522	93144	221.22
5.75	34.78	0.06703	0.01531	0.02279	4.377	1.488	100822	268.49
6.25	34.49	0.08432	0.01763	0.02582	4.782	1.464	108847	307.07
6.75	34.36	0.06855	0.02339	0.03483	2.931	1.489	117132	405.89
7.25	32.34	0.05353	0.03064	0.05132	1.747	1.675	118642	501.43
7.75	31.68	0.04758	0.03176	0.05545	1.498	1.746	124726	511.13
8.25	31.64	0.04756	0.03264	0.05785	1.457	1.773	132712	524.98
8.75	31.64	0.04803	0.03303	0.05886	1.454	1.782	140728	531.25
9.25	31.70	0.04921	0.03372	0.06022	1.459	1.786	149003	543.23

Table 12. Integral quantities and local Reynolds number variation, Re = 100,000 Grid 2

X (in)	U_e (ft/s)	δ^* (in)	θ (in)	ε (in)	H_{12}	H_{32}	Re_x	Re_θ
1.75	32.66	0.01368	0.00502	0.00800	2.725	1.595	28479	81.67
2.25	35.34	0.01373	0.00525	0.00846	2.614	1.612	39594	92.39
2.75	37.97	0.01619	0.00641	0.01065	2.528	1.662	51980	121.09
3.25	39.67	0.01665	0.00694	0.01161	2.398	1.672	64223	137.22
3.75	39.96	0.01919	0.00806	0.01353	2.380	1.677	74603	160.45
4.25	38.77	0.02321	0.00742	0.01169	3.130	1.576	82043	143.18
4.75	36.82	0.03180	0.01028	0.01609	3.024	1.565	88491	191.50
5.25	36.46	0.04646	0.01257	0.01914	3.696	1.522	96670	231.49
5.75	36.19	0.06653	0.01502	0.02233	4.429	1.486	105029	274.37
6.25	35.84	0.06515	0.02200	0.03289	2.961	1.495	113057	397.99
6.75	34.26	0.05013	0.02782	0.04600	1.802	1.653	116958	482.12
7.25	32.95	0.04658	0.03086	0.05329	1.509	1.727	120888	514.62
7.75	32.81	0.04594	0.03164	0.05560	1.452	1.758	128872	526.06
8.25	32.82	0.04668	0.03239	0.05742	1.441	1.773	137193	538.56
8.75	32.75	0.04806	0.03404	0.06056	1.412	1.779	145236	564.96
9.25	32.74	0.05035	0.03462	0.06161	1.454	1.779	153423	574.28

Table 13. Integral quantities and local Reynolds number variation, Re = 100,000 Grid 3

X (in)	U_e (ft/s)	δ^* (in)	θ (in)	ε (in)	H_{12}	H_{32}	Re_x	Re_θ
1.75	33.30	0.01281	0.00496	0.00799	2.580	1.610	29037	82.38
2.25	35.89	0.01277	0.00490	0.00788	2.608	1.609	40210	87.49
2.75	38.59	0.01503	0.00575	0.00944	2.615	1.643	52835	110.42
3.25	40.30	0.01993	0.00956	0.01682	2.084	1.759	65240	191.94
3.75	40.79	0.01878	0.00808	0.01368	2.325	1.693	76147	164.05
4.25	39.53	0.02018	0.00721	0.01153	2.799	1.599	83650	141.94
4.75	37.56	0.03004	0.01055	0.01658	2.847	1.572	90462	200.93
5.25	37.34	0.04871	0.01337	0.02036	3.643	1.523	99354	253.07
5.75	36.55	0.05572	0.01701	0.02567	3.275	1.509	106414	314.85
6.25	34.74	0.04821	0.02296	0.03671	2.169	1.599	109963	403.94
6.75	33.95	0.04223	0.02584	0.04421	1.634	1.711	116251	445.05
7.25	33.66	0.04181	0.02823	0.04911	1.481	1.740	124020	482.86
7.75	33.55	0.04410	0.02964	0.05220	1.488	1.761	132121	505.28
8.25	33.47	0.04576	0.03145	0.05557	1.455	1.767	140312	534.89
9.25	33.46	0.05074	0.03430	0.06098	1.479	1.778	157357	583.58

Table 14. Integral quantities and local Reynolds number variation, Re = 250,000 Grid 0

X (in)	U_e (ft/s)	δ^* (in)	θ (in)	ε (in)	H_{12}	H_{32}	Re_x	Re_θ
1.75	72.69	0.01174	0.00643	0.01128	1.827	1.756	63390	232.91
2.25	78.87	0.01030	0.00513	0.00876	2.010	1.709	88371	201.49
2.75	85.36	0.01056	0.00521	0.00897	2.027	1.722	116858	221.39
3.25	91.48	0.01119	0.00555	0.00959	2.017	1.728	148106	252.92
3.75	94.78	0.01162	0.00561	0.00964	2.071	1.719	176933	264.69
4.25	95.49	0.01178	0.00515	0.00863	2.286	1.675	202094	244.89
4.75	94.33	0.01192	0.00483	0.00791	2.470	1.639	220664	224.38
5.25	93.18	0.01406	0.00550	0.00877	2.556	1.595	240588	252.04
5.75	92.02	0.01501	0.00600	0.00954	2.501	1.588	260221	271.53
6.25	90.69	0.01788	0.00693	0.01093	2.580	1.576	279040	309.40
6.75	88.81	0.02039	0.00757	0.01184	2.693	1.563	295828	331.77
7.25	88.14	0.02309	0.00823	0.01274	2.807	1.549	315217	357.83
7.75	85.95	0.02704	0.00928	0.01432	2.915	1.543	328277	393.09
8.25	84.65	0.02771	0.01100	0.01714	2.519	1.558	344931	459.91
9.25	81.33	0.02652	0.01629	0.02849	1.628	1.749	371485	654.22

Table 15. Integral quantities and local Reynolds number variation, Re = 250,000 Grid 2

X (in)	U_e (ft/s)	δ^* (in)	θ (in)	ε (in)	H_{12}	H_{32}	Re_x	Re_θ
1.75	74.16	0.00921	0.00414	0.00677	2.223	1.635	64672	152.99
2.25	80.66	0.01022	0.00493	0.00834	2.073	1.692	90377	198.03
2.75	85.11	0.01116	0.00556	0.00959	2.009	1.727	116516	235.57
3.25	90.51	0.01126	0.00529	0.00905	2.110	1.710	146535	238.51
3.75	94.75	0.01133	0.00512	0.00863	2.215	1.686	176877	241.50
4.25	95.43	0.01168	0.00509	0.00845	2.296	1.661	201967	241.89
4.75	93.62	0.01237	0.00527	0.00865	2.346	1.641	220067	244.16
5.25	92.46	0.01466	0.00583	0.00932	2.515	1.599	240298	266.85
5.75	91.20	0.01675	0.00652	0.01042	2.569	1.597	258551	293.17
6.25	89.59	0.01935	0.00747	0.01186	2.591	1.588	276256	330.18
6.75	87.90	0.02146	0.00842	0.01327	2.548	1.576	292914	.365.38
7.25	86.88	0.02525	0.01018	0.01608	2.479	1.579	311784	437.79
7.75	85.01	0.02673	0.01203	0.01922	2.222	1.597	326768	507.23
8.25	83.04	0.02530	0.01371	0.02308	1.846	1.684	338767	562.97
9.25	80.76	0.02751	0.01760	0.03100	1.563	1.761	370628	705.19

Table 16. Integral quantities and local Reynolds number variation, Re = 250,000 Grid 3

X (in)	U_e (ft/s)	δ^* (in)	θ (in)	ε (in)	H_{12}	H_{32}	Re_x	Re_θ
1.75	72.46	0.01024	0.00490	0.00826	2.087	1.683	63189	176.93
2.25	77.87	0.01048	0.00508	0.00867	2.065	1.707	87251	196.99
2.75	84.51	0.01133	0.00582	0.01012	1.948	1.740	115695	244.85
3.25	90.14	0.01238	0.00658	0.01158	1.881	1.761	145936	295.46
3.75	93.41	0.01286	0.00670	0.01177	1.919	1.756	174376	311.55
4.25	94.23	0.01303	0.00697	0.01166	2.015	1.725	199427	327.06
4.75	93.53	0.01451	0.00633	0.01034	2.293	1.635	221119	294.67
5.25	92.39	0.01681	0.00697	0.01111	2.413	1.596	241900	321.15
5.75	91.61	0.01820	0.00751	0.01207	2.422	1.607	261313	341.30
6.25	90.18	0.02044	0.00881	0.01428	2.320	1.620	280070	394.79
6.75	88.52	0.02025	0.00964	0.01585	2.101	1.645	296908	424.03
7.25	86.76	0.02305	0.01203	0.02006	1.916	1.668	312560	518.63
7.75	85.09	0.02407	0.01412	0.02435	1.705	1.724	327904	597.42
8.25	83.36	0.02439	0.01526	0.02685	1.598	1.759	342680	633.85
9.25	81.32	0.02767	0.01800	0.03196	1.537	1.775	375936	731.55

Table 17 Characteristics of separation bubbles and transition for Re = 35,000

	X_S (in)	X_R (in)	X_{ts} (in)	X_{te} (in)	X_{LT} (in)	$Re_{\theta S}$	$Re_{x_{st}}$	Re_{LT}
Grid 0	3.85	7.81	6.26	-	-	129.8	15928	-
Grid 2	3.85	7.12	5.56	7.43	1.87	86.9	11000	11965
Grid 3	3.85	6.61	5.30	6.88	1.58	127.9	9537	10392
Grid 4	3.85	6.37	5.13	6.61	1.48	117.2	8344	9583

Table 18 Characteristics of separation bubbles and transition for Re = 70,000

	X_S (in)	X_R (in)	X_{ts} (in)	X_{te} (in)	X_{LT} (in)	$Re_{\theta S}$	$Re_{x_{st}}$	Re_{LT}
Grid 0	4.55	7.03	5.79	6.93	1.14	136.7	16437	15112
Grid 2	4.55	6.48	5.48	6.40	0.92	143.0	12105	11974
Grid 3	4.55	6.08	5.21	6.05	0.84	143.2	8546	10877
Grid 4	4.55	5.80	5.05	5.76	0.71	143.3	6400	9088

Table 19 Characteristics of separation bubbles and transition for Re = 100,000

	X_S (in)	X_R (in)	X_{ts} (in)	X_{te} (in)	X_{LT} (in)	$Re_{\theta S}$	$Re_{x_{st}}$	Re_{LT}
Grid 0	4.80	6.85	5.69	6.78	1.09	186.2	16223	19869
Grid 2	4.80	6.31	5.35	6.25	0.90	207.2	10843	17743
Grid 3	4.80	5.80	5.07	5.78	0.71	210.3	5243	13539

Table 20 Characteristics of separation bubbles and transition for Re = 250,000

	X_S (in)	X_R (in)	X_{ts} (in)	X_{te} (in)	X_{LT} (in)	$Re_{\theta S}$	$Re_{x_{st}}$	Re_{LT}
Grid 0	-	-	5.55	6.60	1.05	-	-	48415
Grid 2	-	-	5.16	6.03	0.87	-	-	40059
Grid 3	-	-	5.08	5.75	0.67	-	-	31000

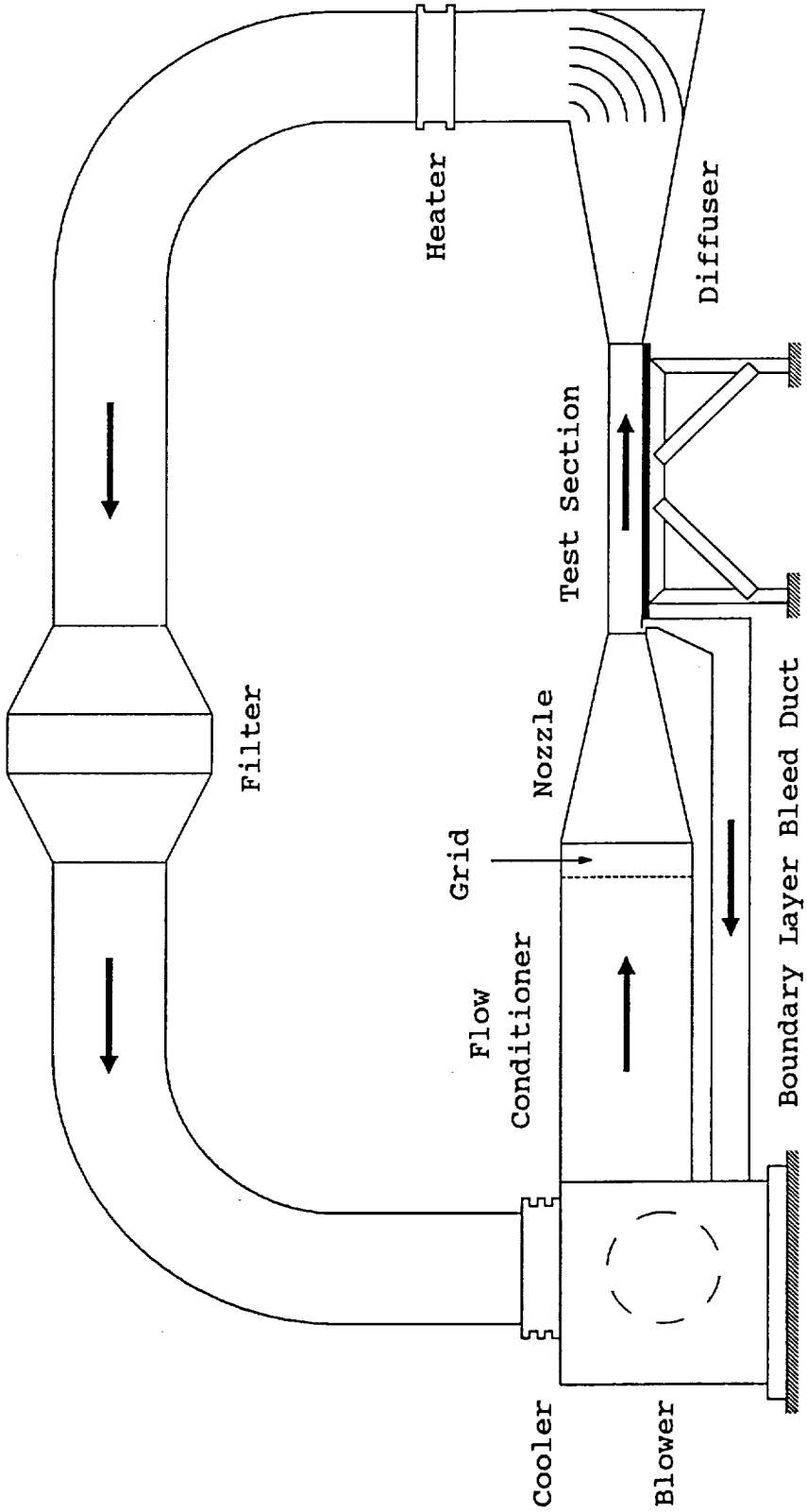

Figure 1 Schematic diagram of wind tunnel

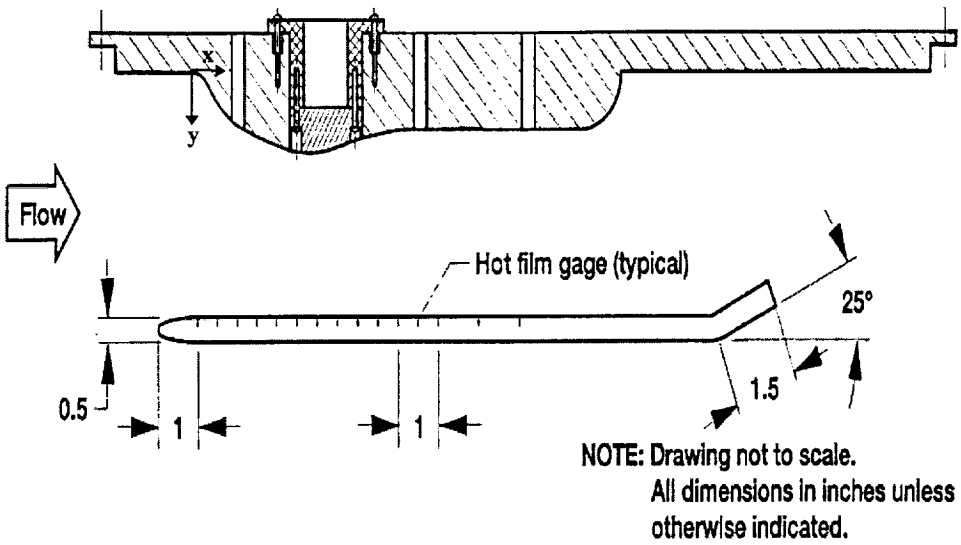

x	0.00000	0.25000	0.38007	0.41542	0.46054	0.52728	0.60429	0.68840	0.77711	0.86292	0.95349
y	0.00000	0.06667	0.14264	0.22245	0.29850	0.39879	0.49147	0.59047	0.68539	0.76987	0.84932

x	1.05089	1.15307	1.26895	1.38835	1.52370	1.66092	1.80703	1.95376	2.10131	2.24904	2.38700
y	0.92223	0.98827	1.05117	1.10709	1.16304	1.21432	1.26672	1.31734	1.36792	1.41792	1.46481

x	2.52542	2.65217	2.78008	2.90179	3.02482	3.14910	3.27399	3.40641	3.53850	3.67882	3.81840
y	1.51018	1.54955	1.58503	1.61328	1.63528	1.64905	1.65517	1.65257	1.64268	1.62593	1.60385

x	3.96434	4.10962	4.26152	4.41305	4.56412	4.71519	4.86378	5.01266	5.15955	5.30678	5.43854
y	1.57651	1.54566	1.51055	1.47370	1.43624	1.39897	1.36362	1.32954	1.29786	1.26775	1.24083

x	5.57100	5.70549	5.84060	5.99427	6.14799	6.30642	6.46490	6.62375	6.78259	6.94165	7.10066
y	1.21755	1.20138	1.19120	1.18860	1.19005	1.18992	1.18972	1.18901	1.18806	1.18711	1.18612

x	7.25979	7.41893	7.57798	7.73704	7.89596	8.05485	8.21366	8.37242	8.53102	8.68962	8.84809
y	1.18504	1.18397	1.18285	1.18178	1.18070	1.17971	1.17880	1.17797	1.17723	1.17665	1.17623

x	9.00657	9.16492	9.32323	9.48137	9.63951	9.79757	9.95559	10.11345	10.27130	10.42899	10.58668
y	1.17603	1.17594	1.17611	1.17652	1.17718	1.17814	1.17938	1.18091	1.18281	1.18521	1.18802

x	10.72472	10.86277	10.98257	11.10221	11.21172	11.32008	11.42251	11.52206	11.61734	11.70791	11.79372
y	1.19166	1.19356	1.19298	1.18719	1.17512	1.15518	1.12690	1.08968	1.04315	0.98798	0.92405

x	11.87337	11.94682	12.01295	12.07122	12.12142	12.16240	12.19499	12.22394	12.23449
y	0.85259	0.77372	0.68869	0.59858	0.50375	0.40690	0.30690	0.15537	0.00149

Figure 2 Schematic diagram of test section with the coordinates of upper wall

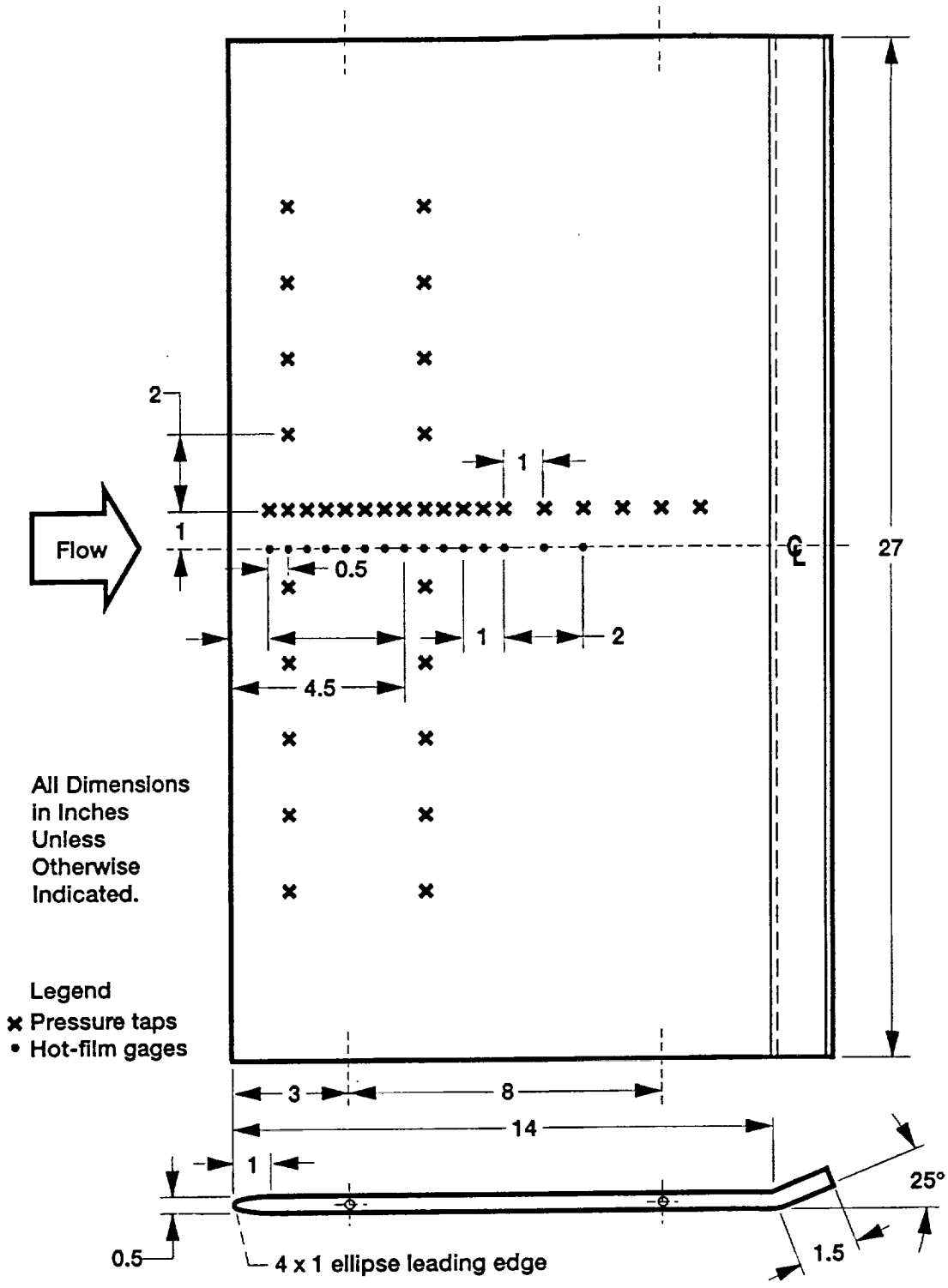

Figure 3 Schematic diagram of lower flat test plate

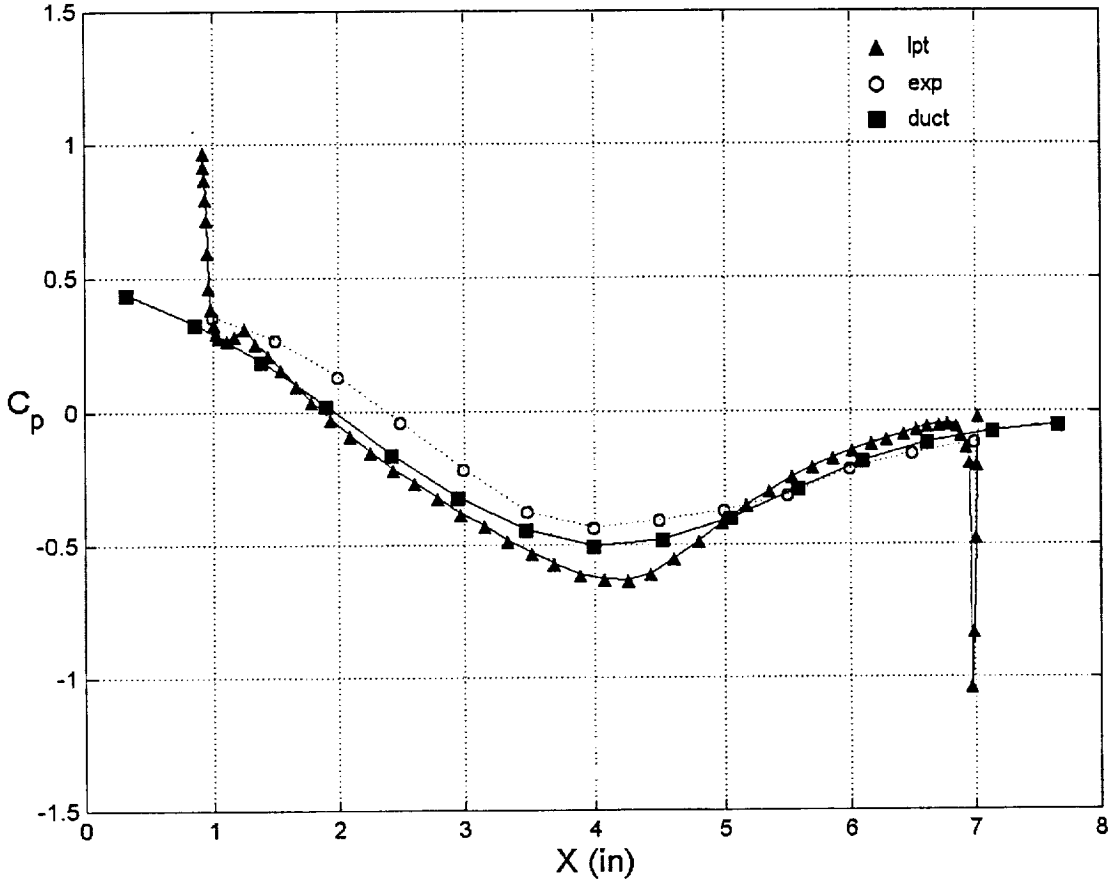

Figure 4 Pressure distribution comparison - for the generic LPT blade (LPT), Test section geometry (Duct) and Experiment profile (Exp), Re = 250,000

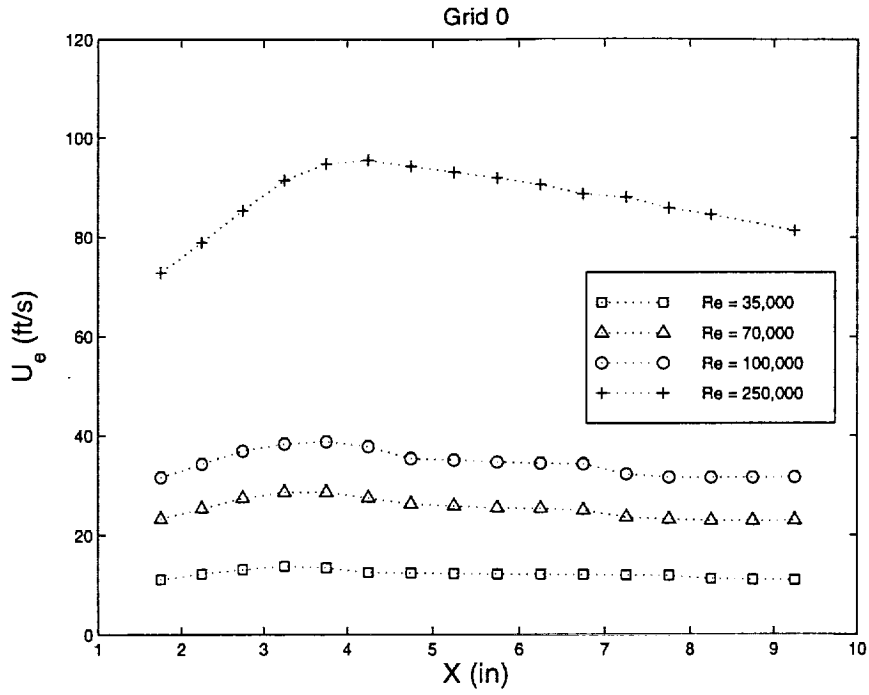

Figure 5 Freestream velocity variation in the test section with Reynolds number

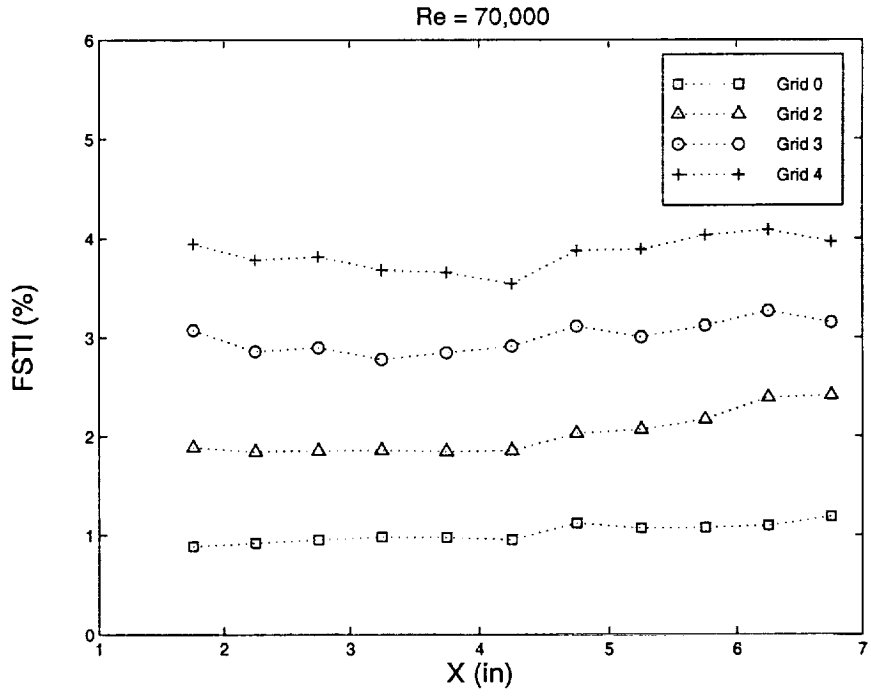

Figure 6 Inlet freestream turbulent intensity (FSTI = u'_{rms}/U_{in}) variation with grids

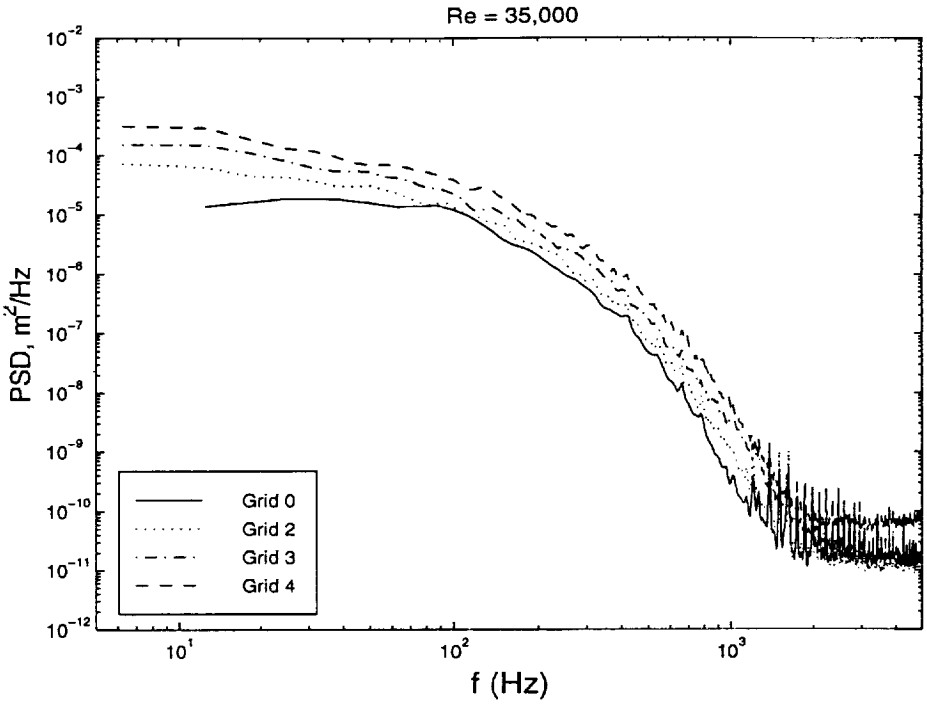

Figure 7 Freestream power spectral density plot for Re = 35,000

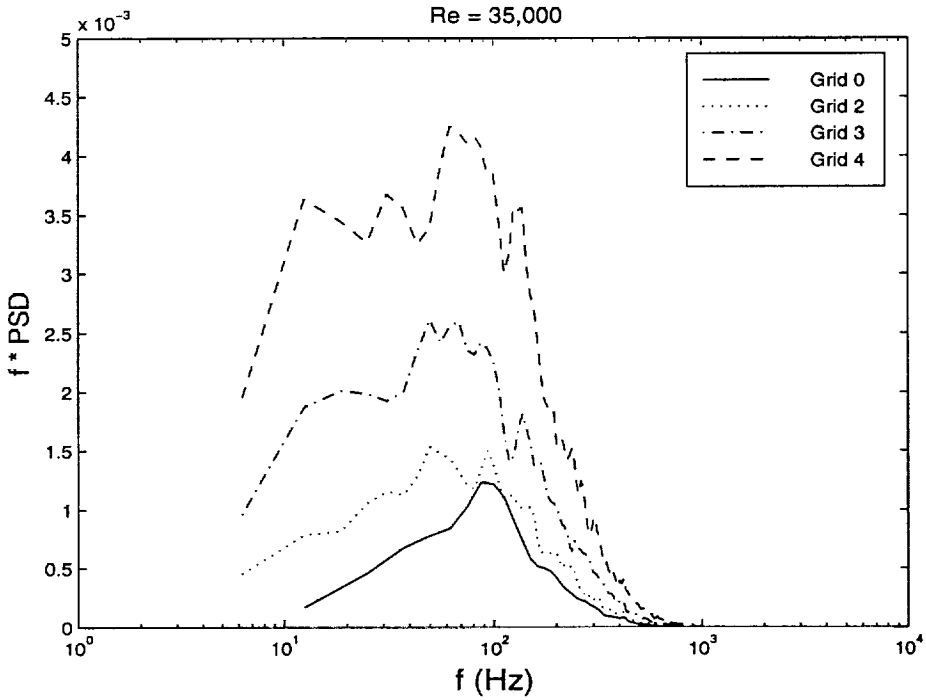

Figure 7a Freestream power spectral density plot in energy coordinates for Re = 35,000

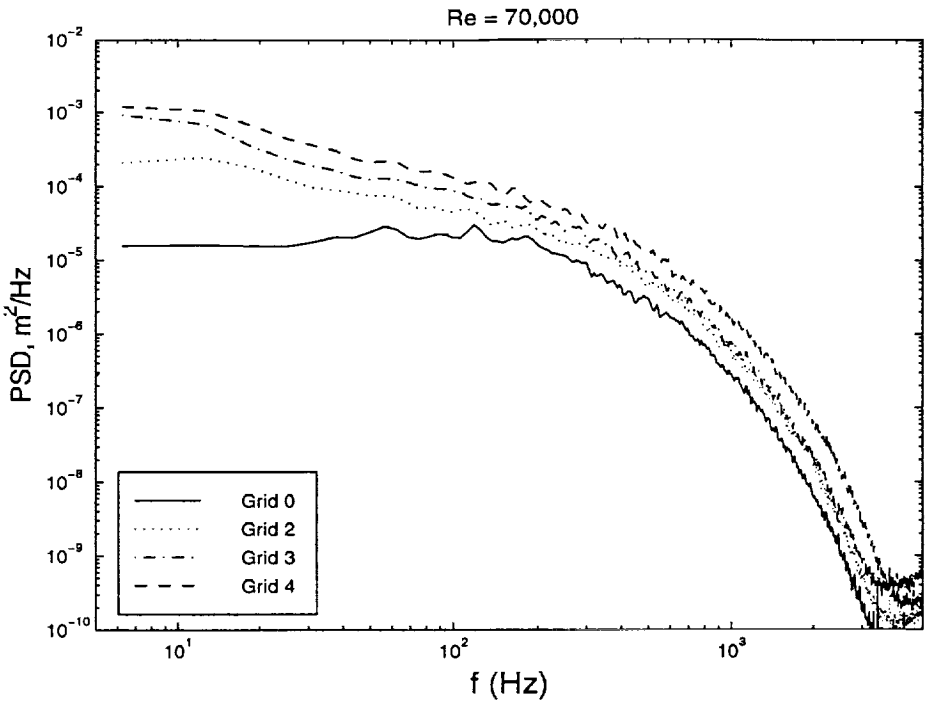

Figure 8 Freestream power spectral density plot for Re = 70,000

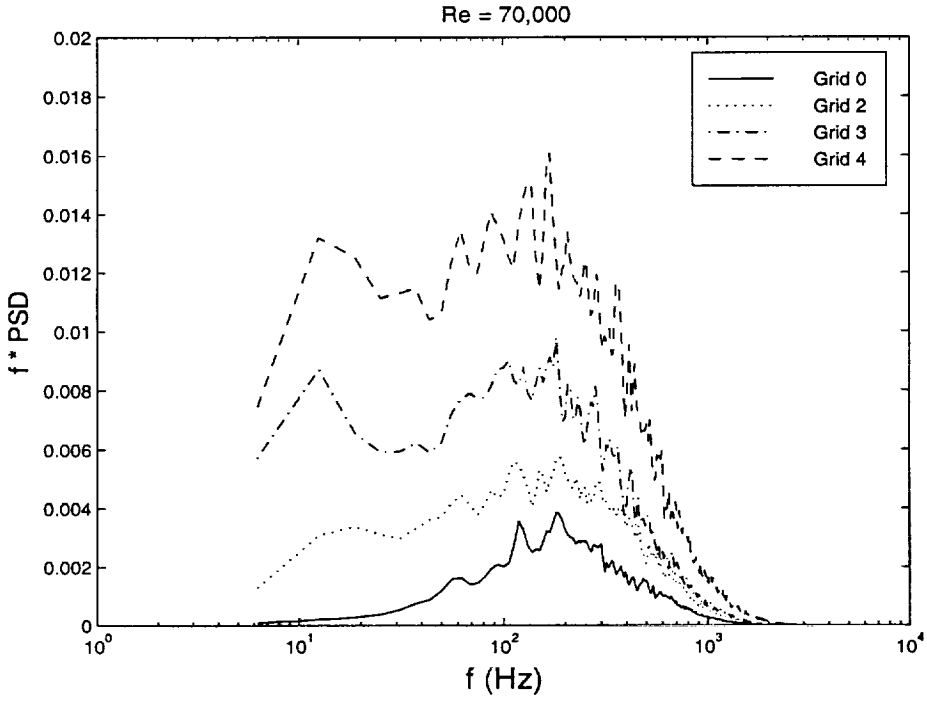

Figure 8a Freestream power spectral density plot in energy coordinates for Re = 70,000

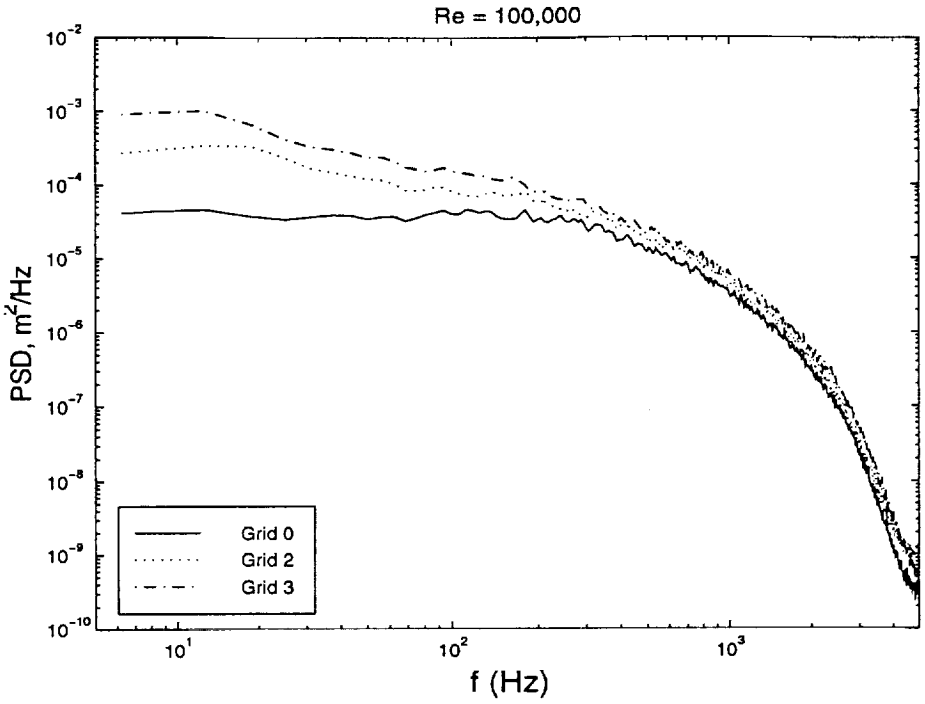

Figure 9 Freestream power spectral density plot for Re = 100,000

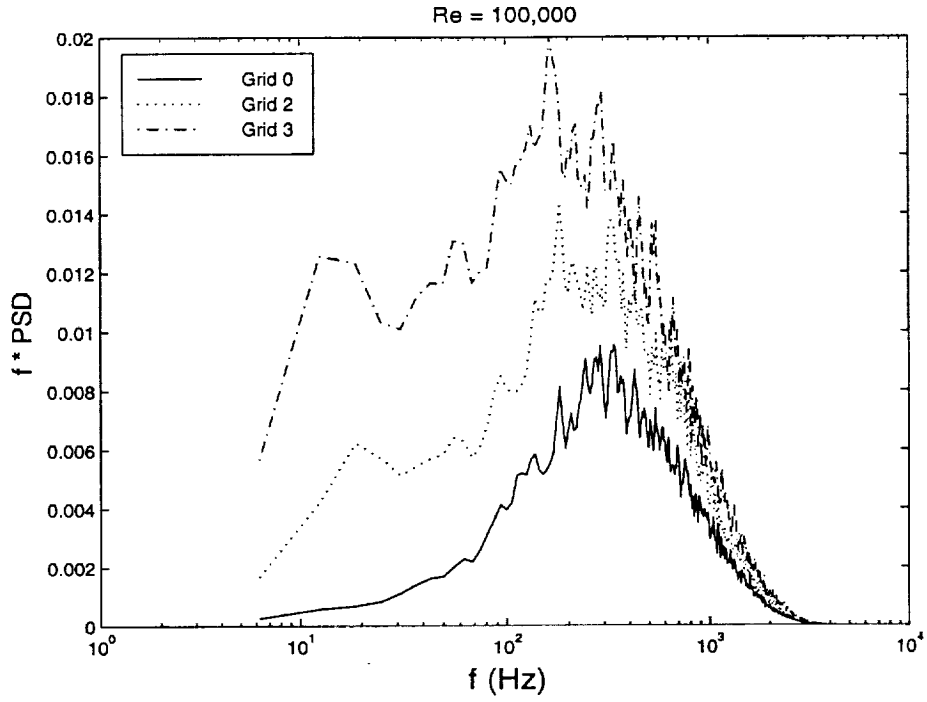

Figure 9a Freestream power spectral density plot in energy coordinates for Re = 100,000

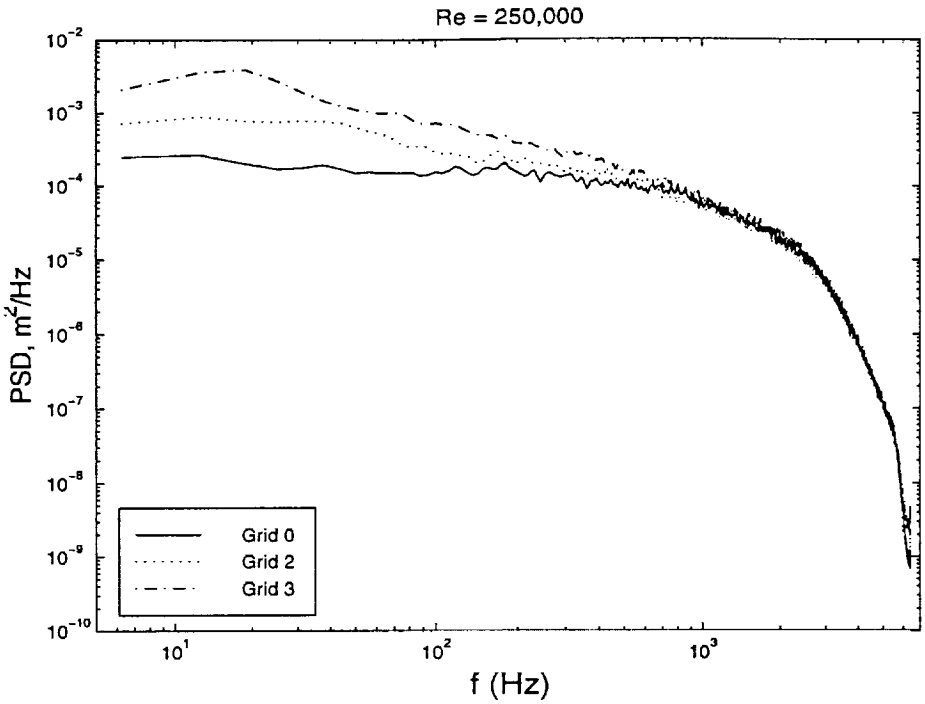

Figure 10 Freestream power spectral density plot for Re = 250,000

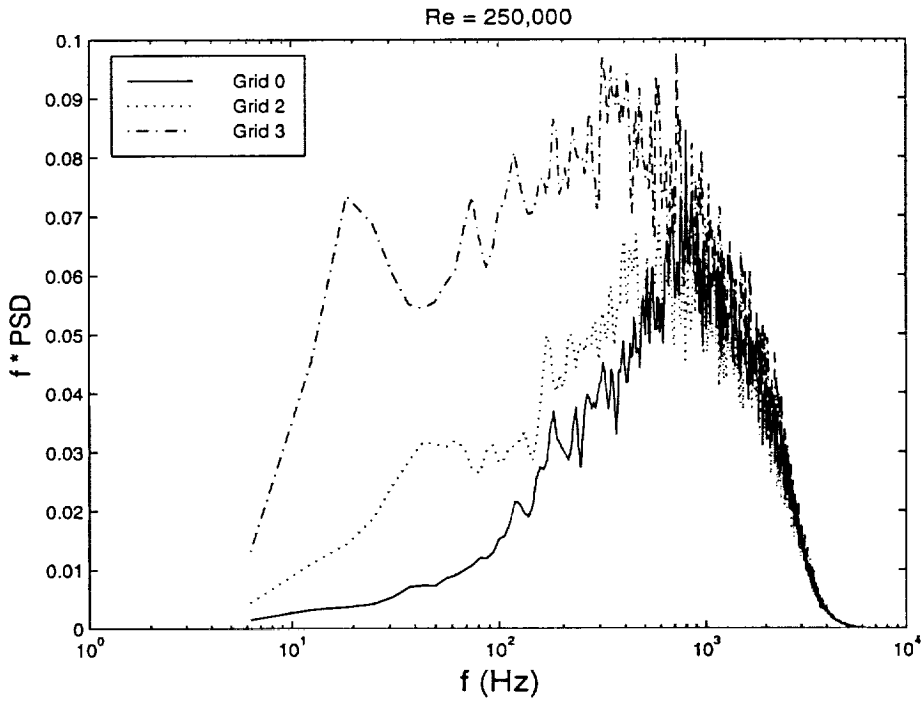

Figure 10a Freestream power spectral density plot in energy coordinates for Re= 250,000

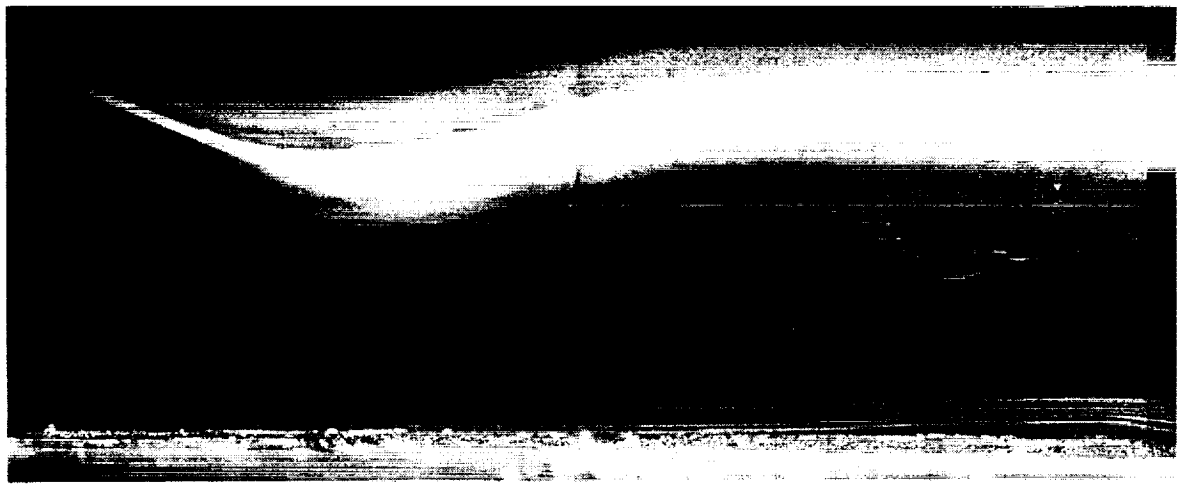

Figure 11 Smoke-wire flow visualization of separation bubble without upper wall suction, Re = 50,000, Grid 0 (flow comes from left to right)

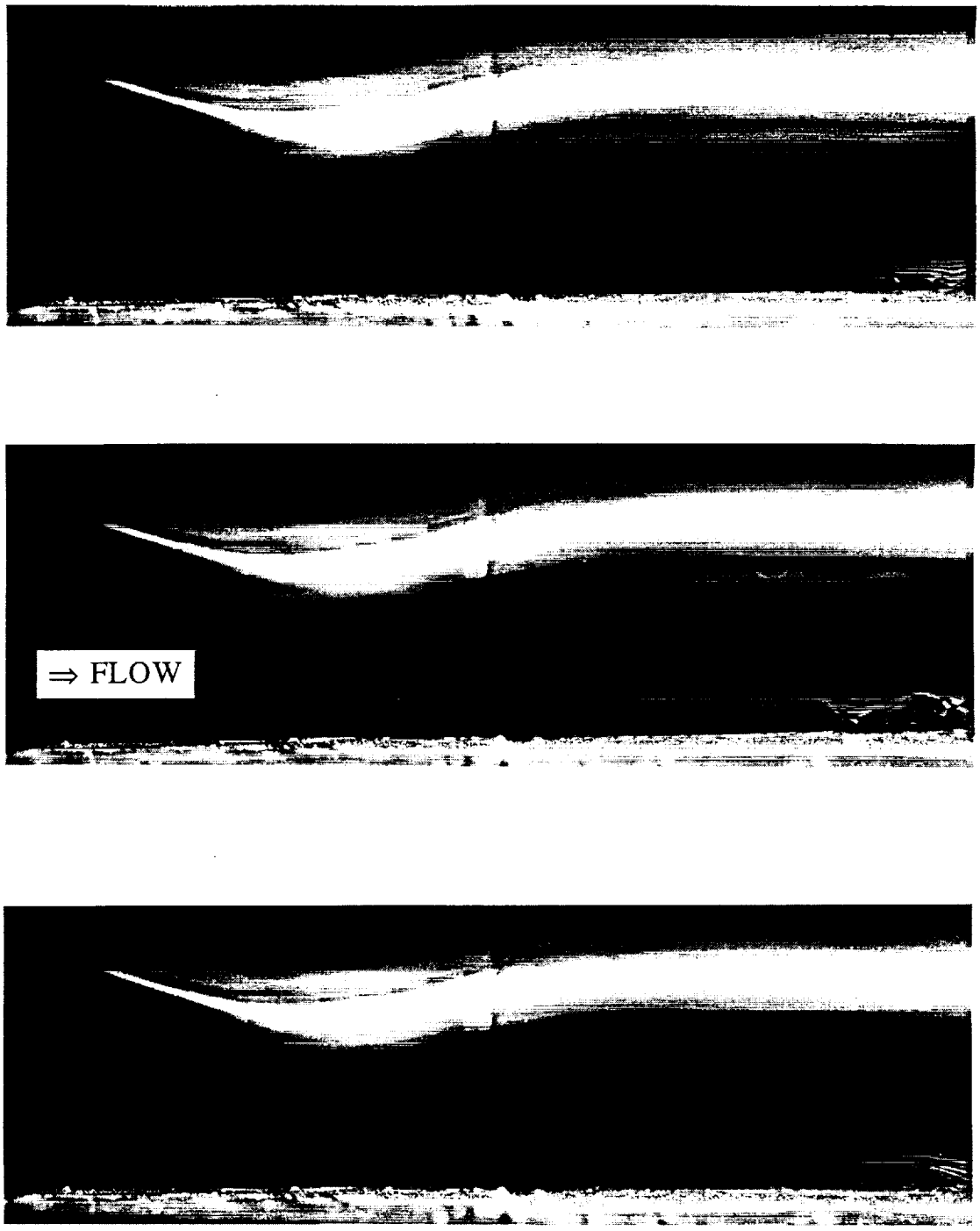

Figure 11a Smoke-wire flow visualization of separation bubble with upper wall suction, Re = 50,000, Grid 0

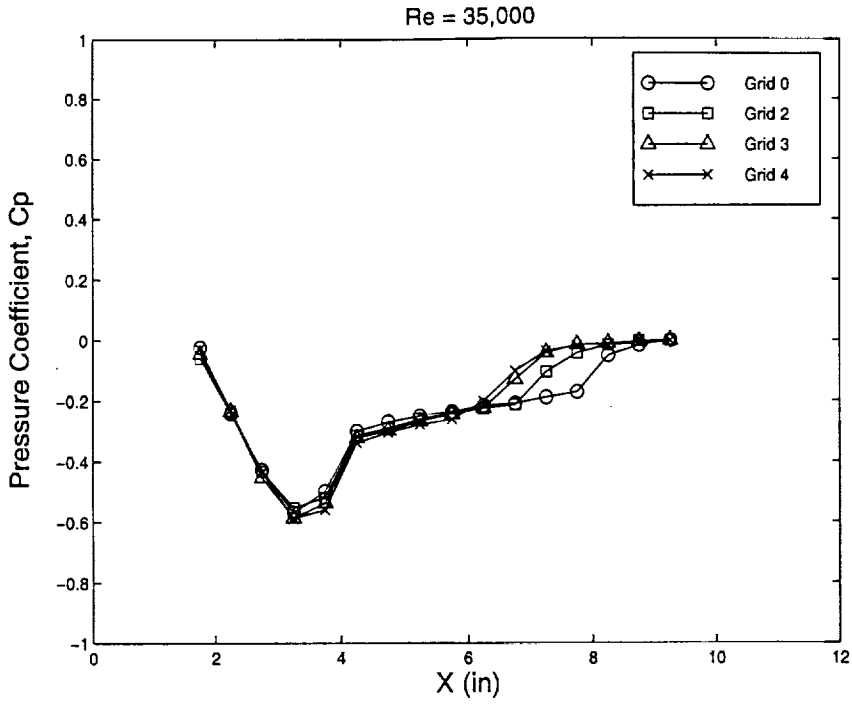

Figure 12 Static pressure distribution on a test plate, Re = 35,000

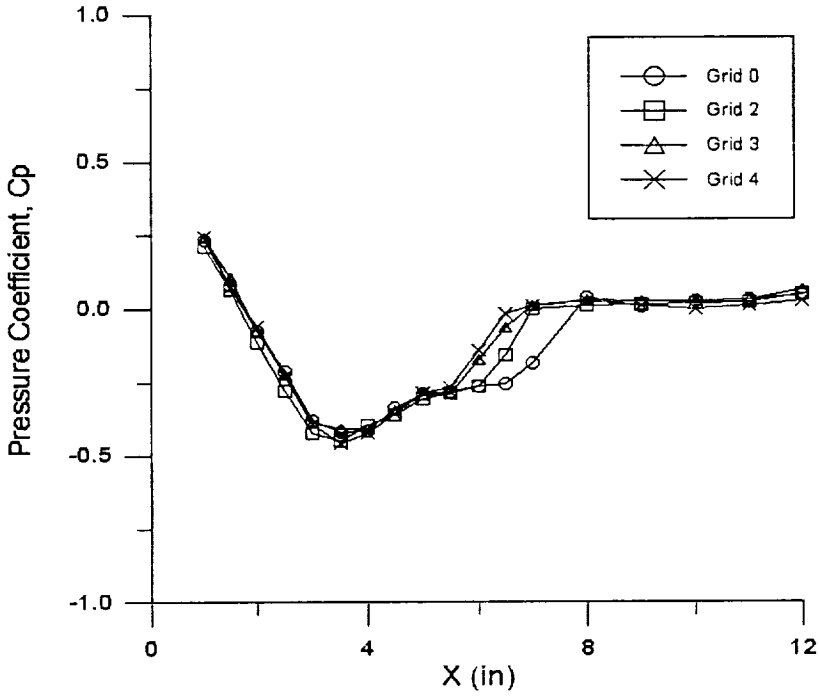

Figure 13 Static pressure distribution on a test plate, Re = 70,000

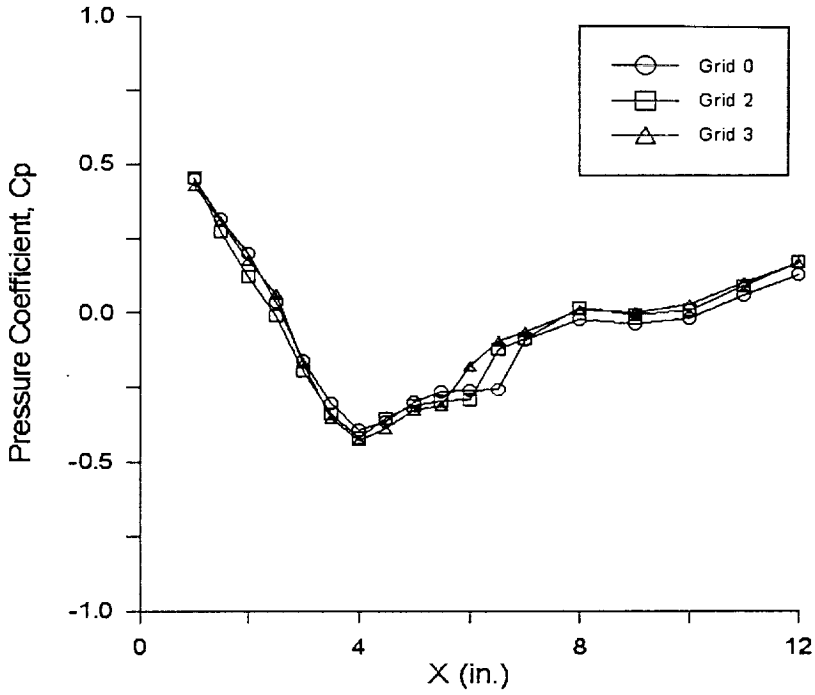

Figure 14 Static pressure distribution on a test plate, Re = 100,000

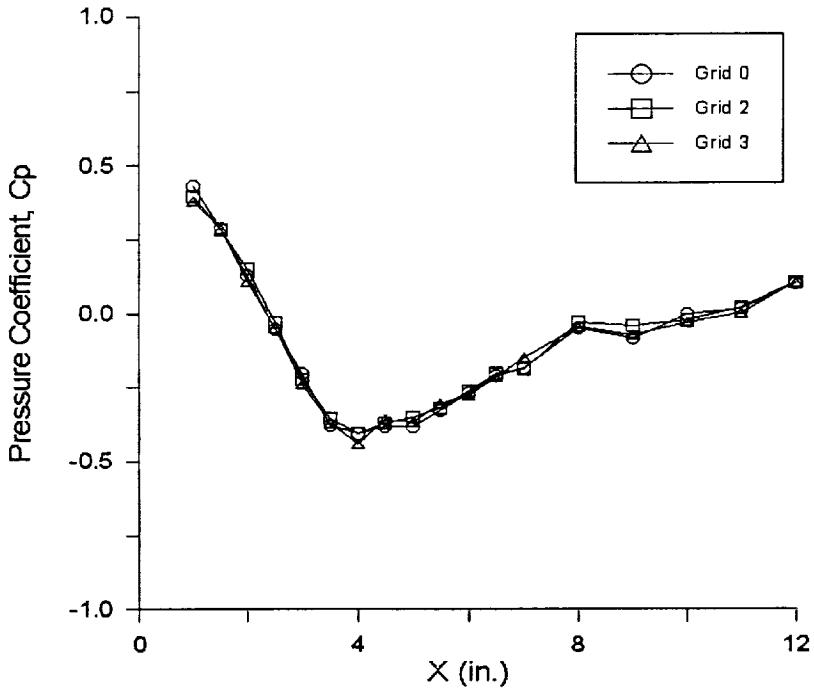

Figure 15 Static pressure distribution on a test plate, Re = 250,000

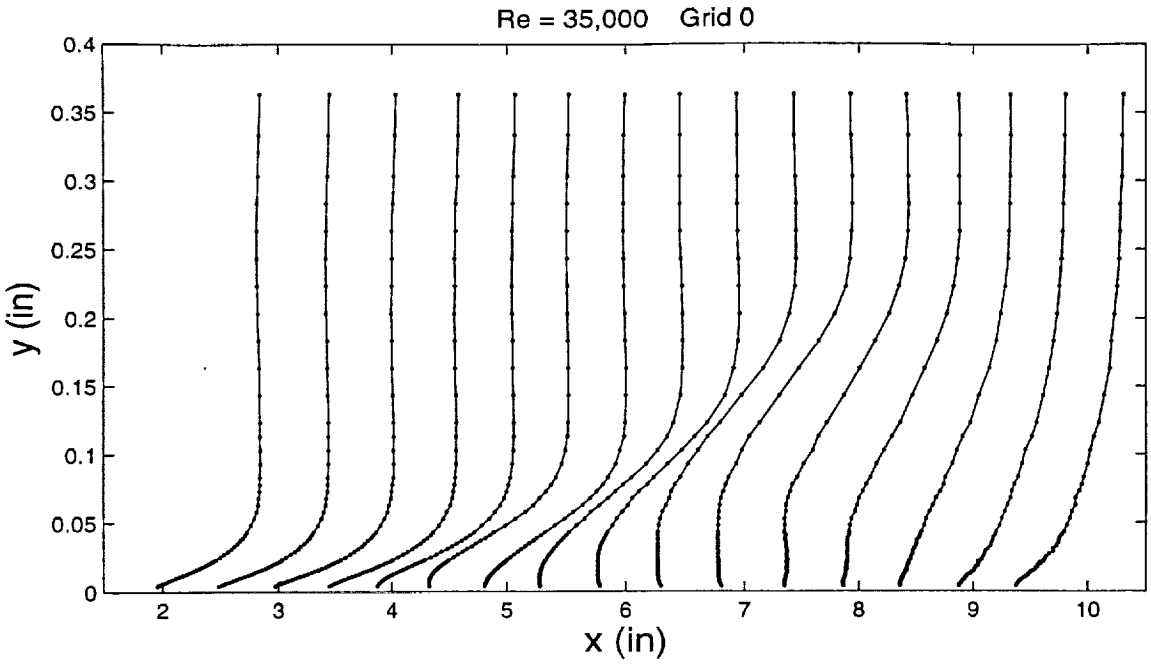

Figure 16 Distribution of U/U_{in} for Re = 35,000, Grid 0

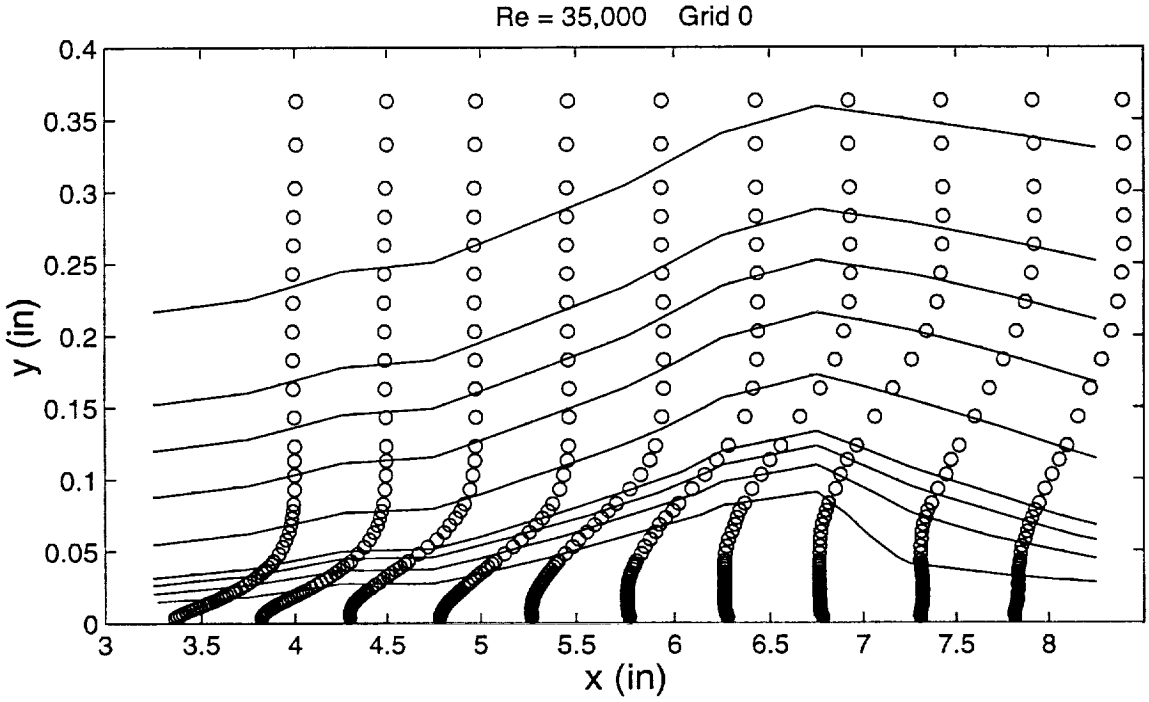

Figure 16a Distribution of U/U_{in} around separation bubble along with streamlines for Re = 35,000, Grid 0

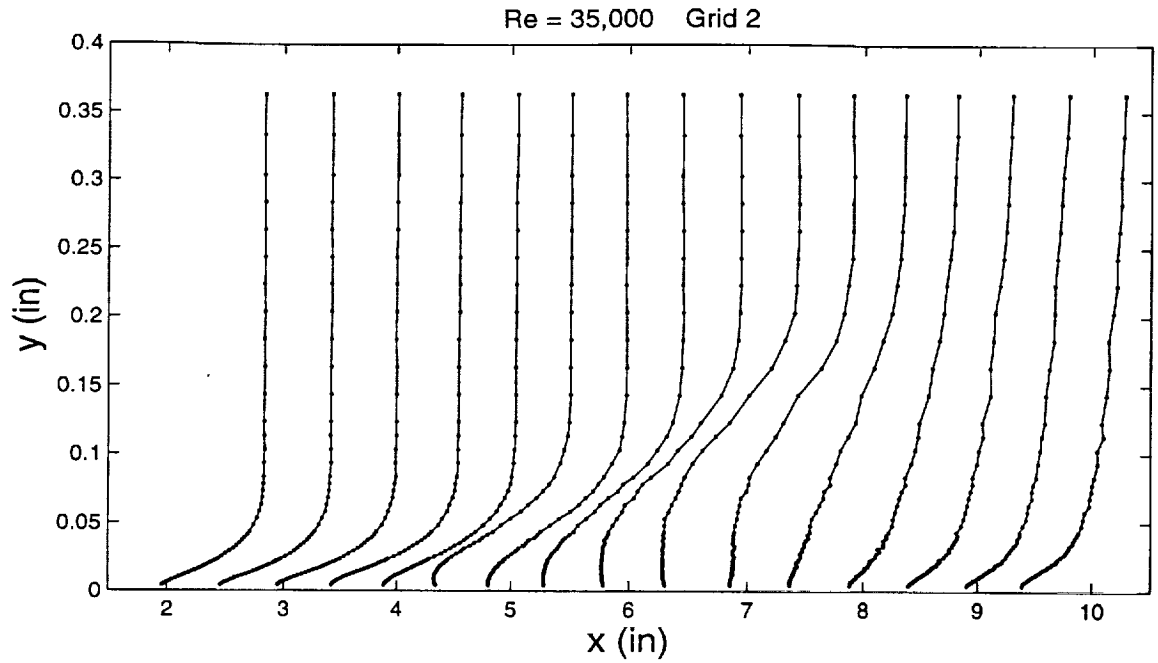

Figure 17 Distribution of U/U_{in} for Re = 35,000, Grid 2

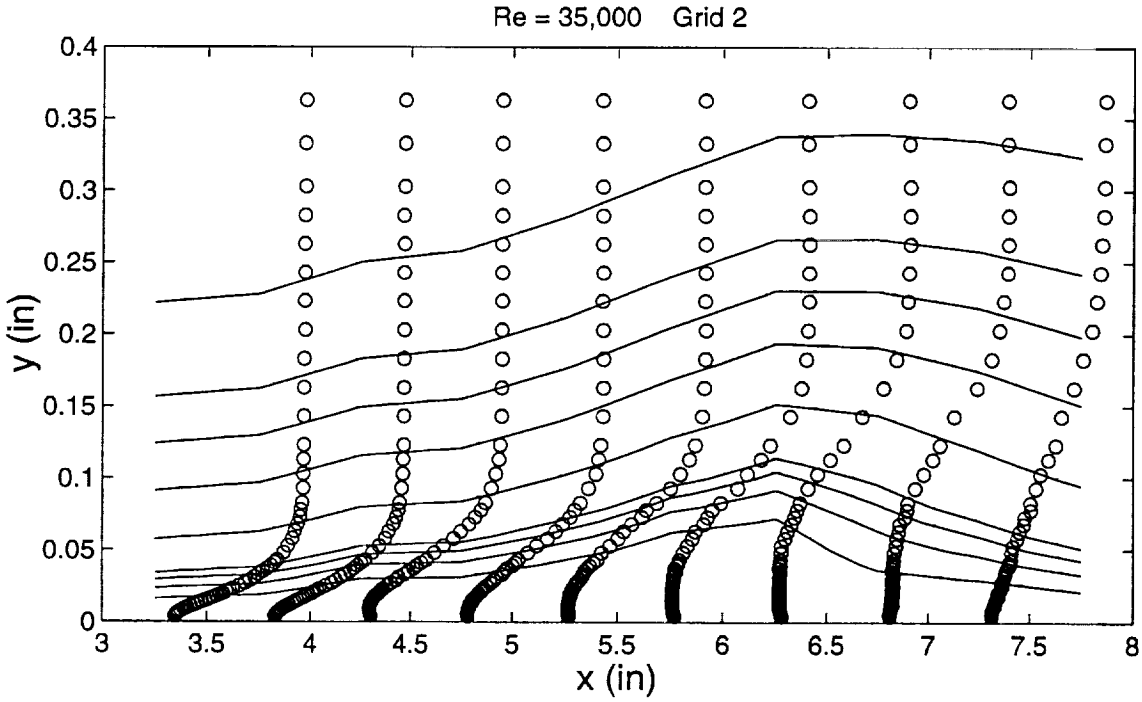

Figure 17a Distribution of U/U_{in} around separation bubble along with streamlines for Re = 35,000, Grid 2

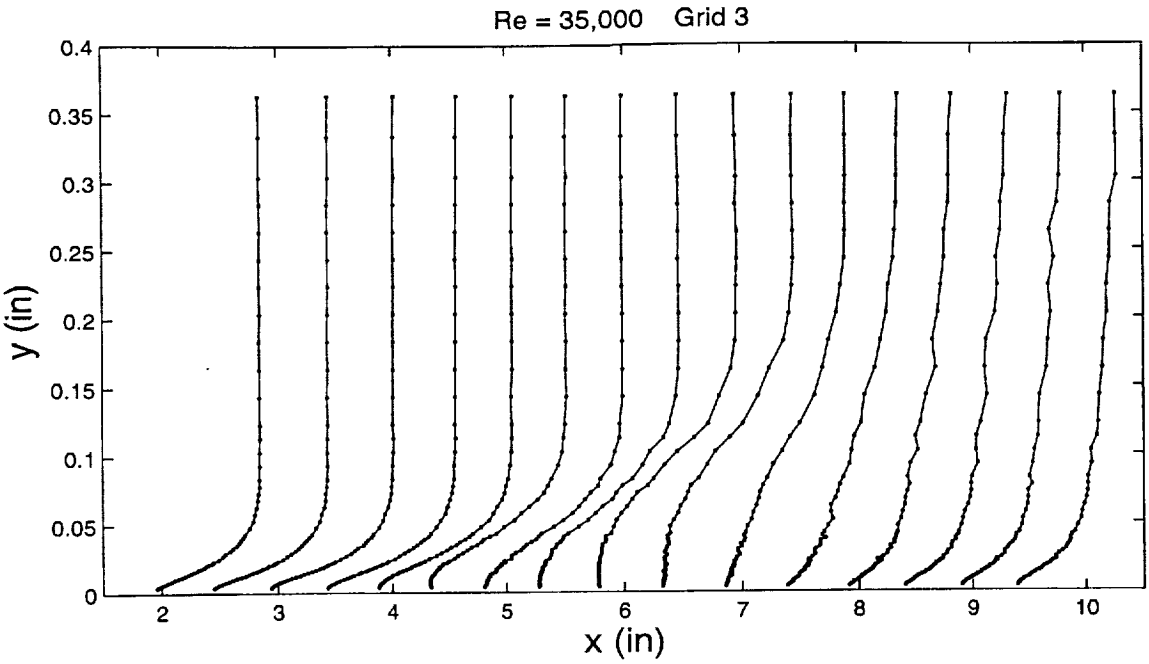

Figure 18 Distribution of U/U_{in} for Re = 35,000, Grid 3

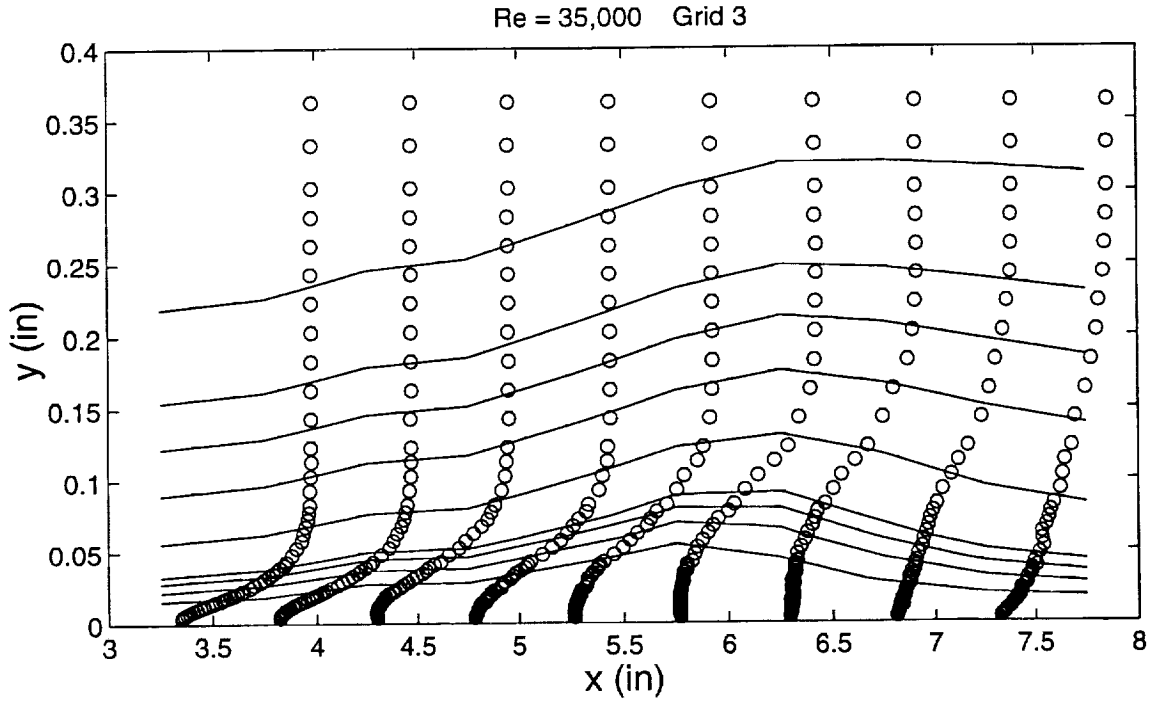

Figure 18a Distribution of U/U_{in} around separation bubble along with streamlines for Re = 35,000, Grid 3

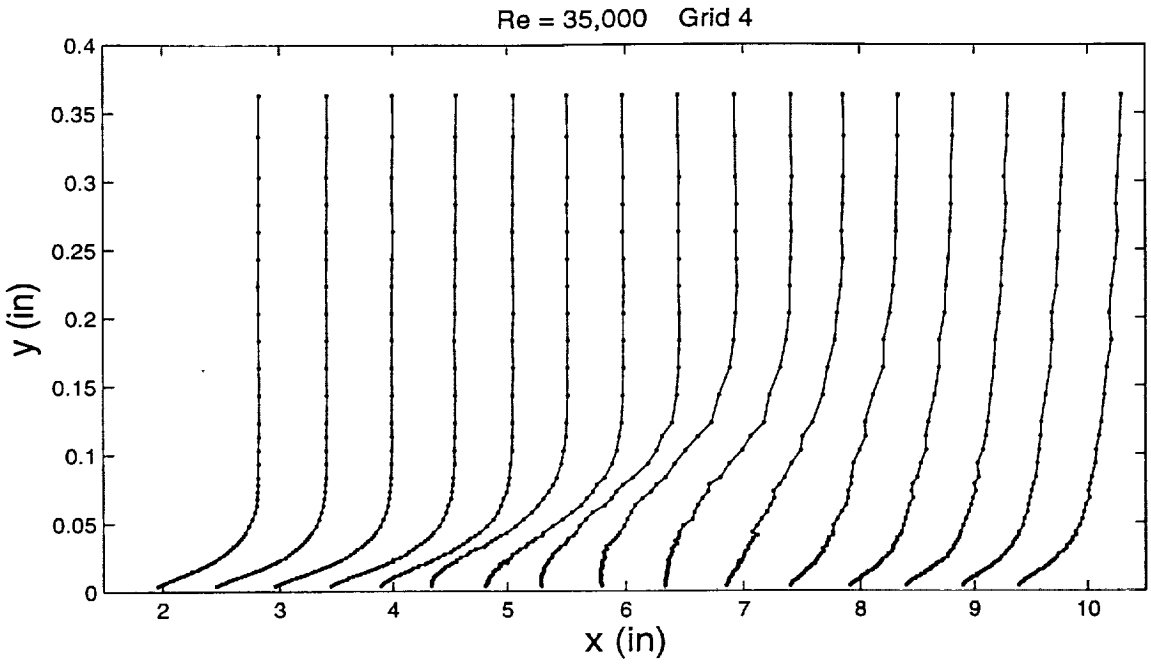

Figure 19 Distribution of U/U_{in} for Re = 35,000, Grid 4

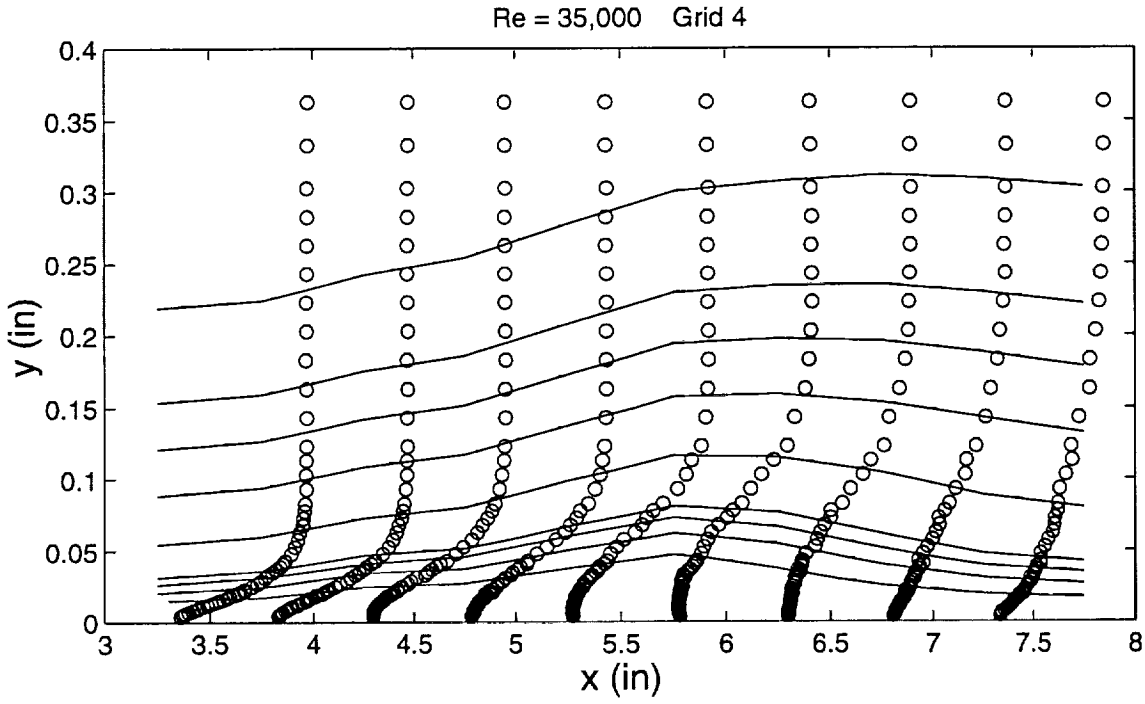

Figure 19a Distribution of U/U_{in} around separation bubble along with streamlines for Re = 35,000, Grid 4

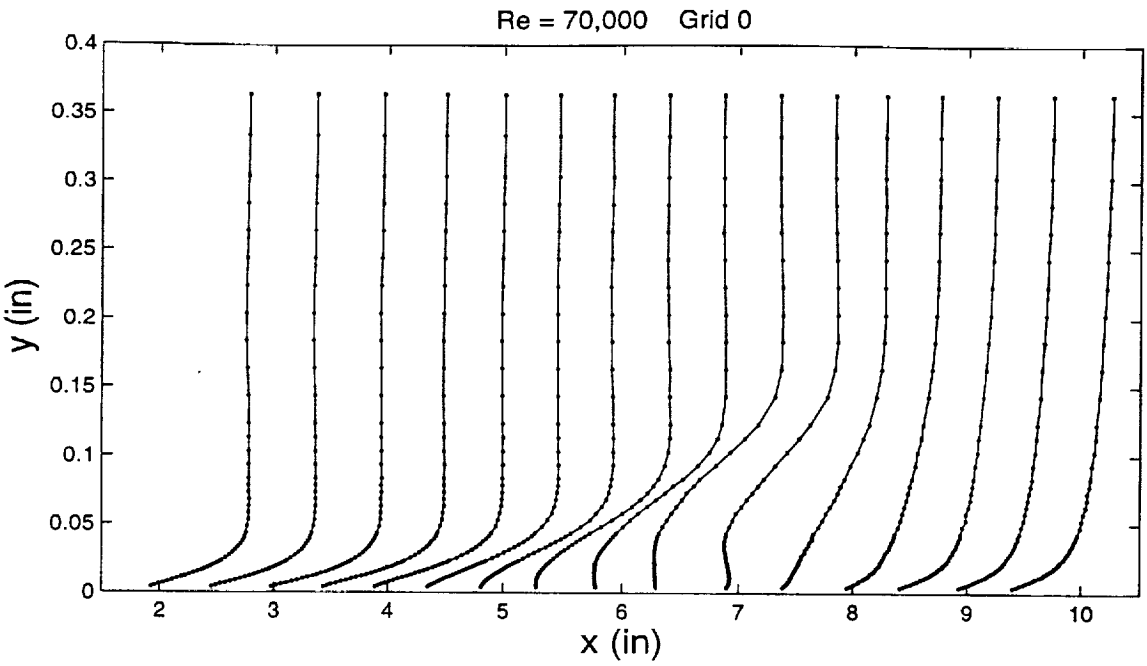

Figure 20 Distribution of U/U_{in} for Re = 70,000, Grid 0

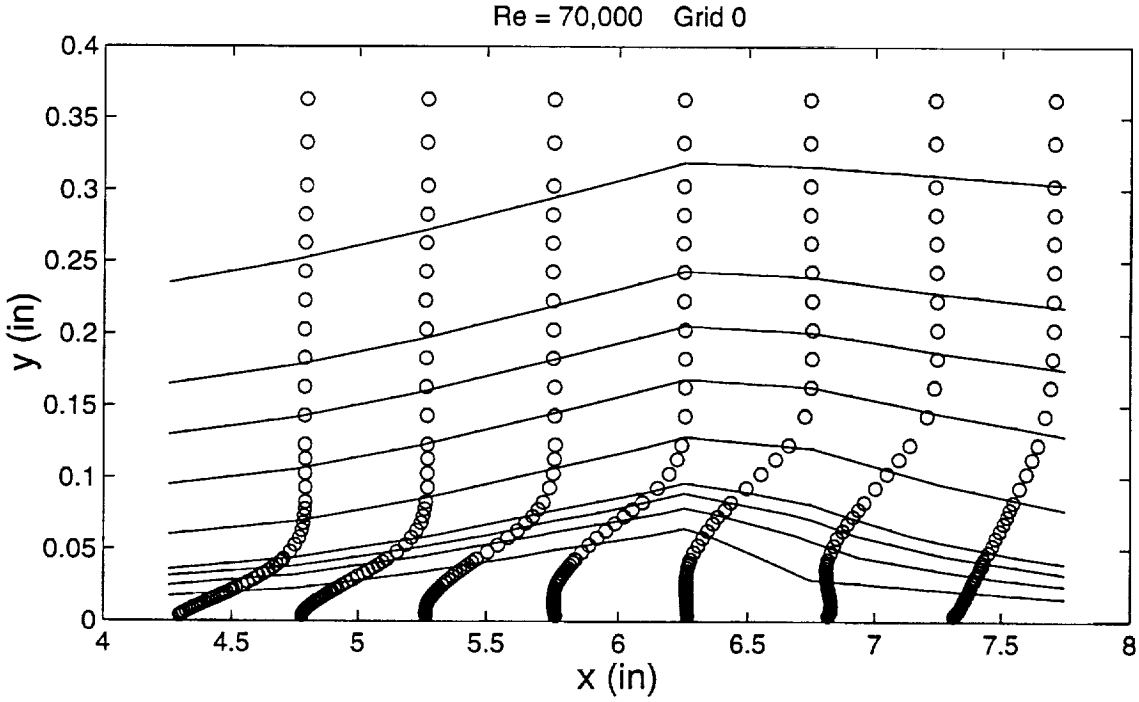

Figure 20a Distribution of U/U_{in} around separation bubble along with streamlines for Re = 70,000, Grid 0

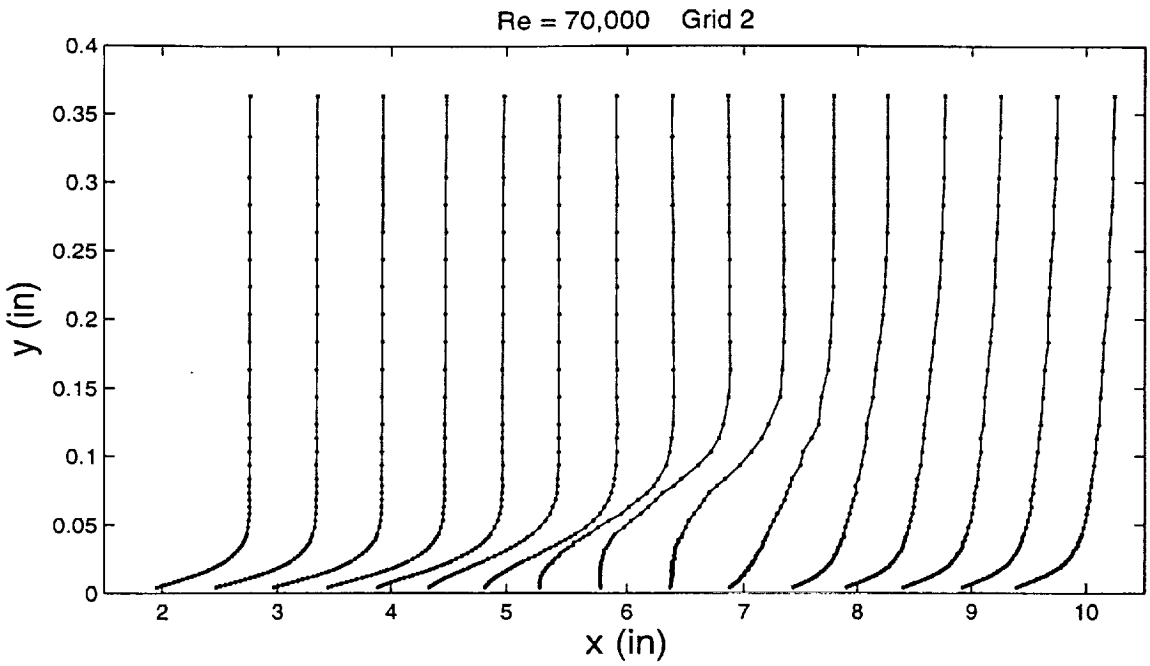

Figure 21 Distribution of U/U_{in} for Re = 70,000, Grid 2

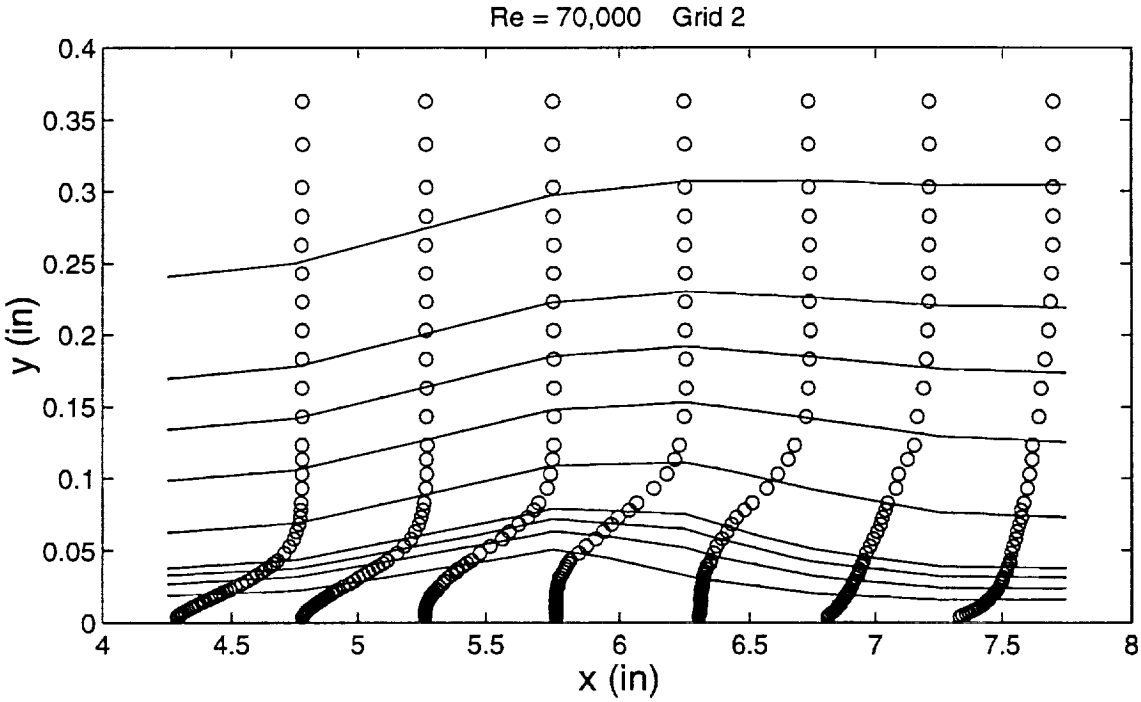

Figure 21a Distribution of U/U_{in} around separation bubble along with streamlines for Re = 70,000, Grid 2

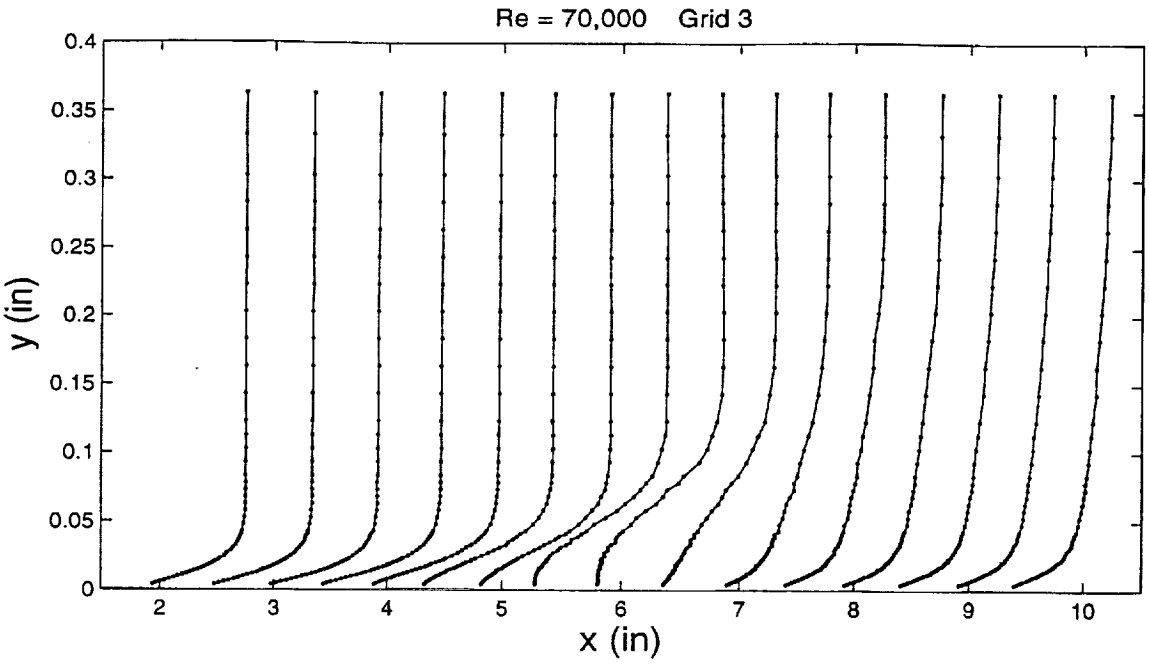

Figure 22 Distribution of U/U_{in} for Re = 70,000, Grid 3

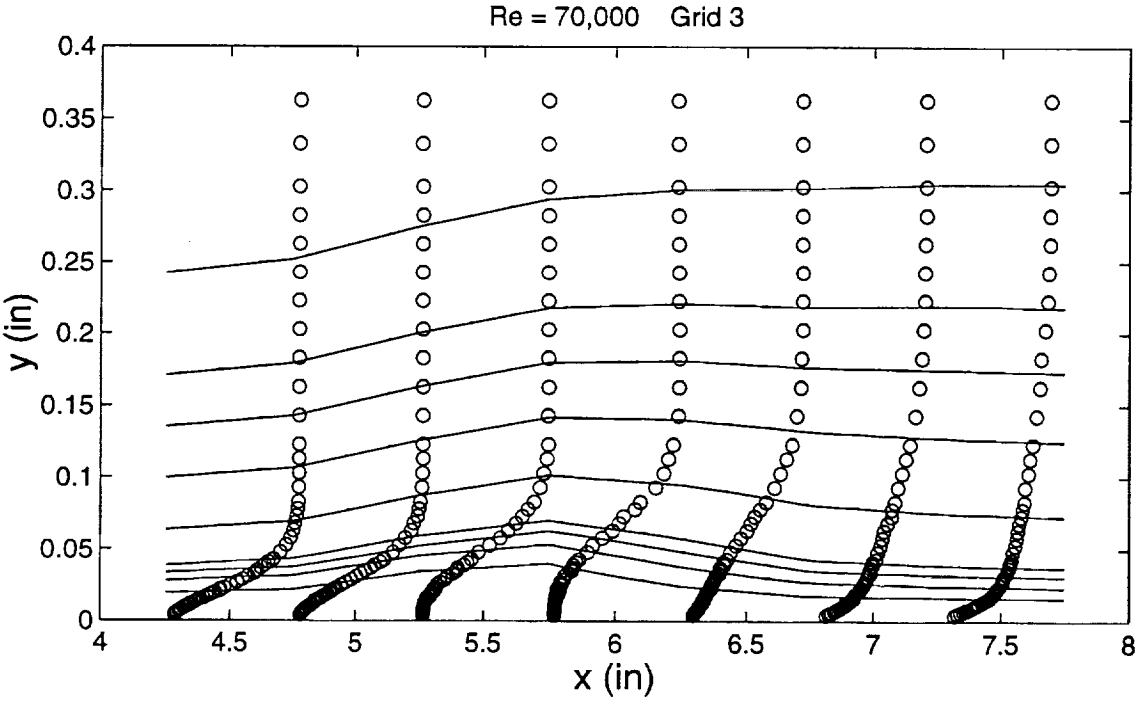

Figure 22a Distribution of U/U_{in} around separation bubble along with streamlines for Re = 70,000, Grid 3

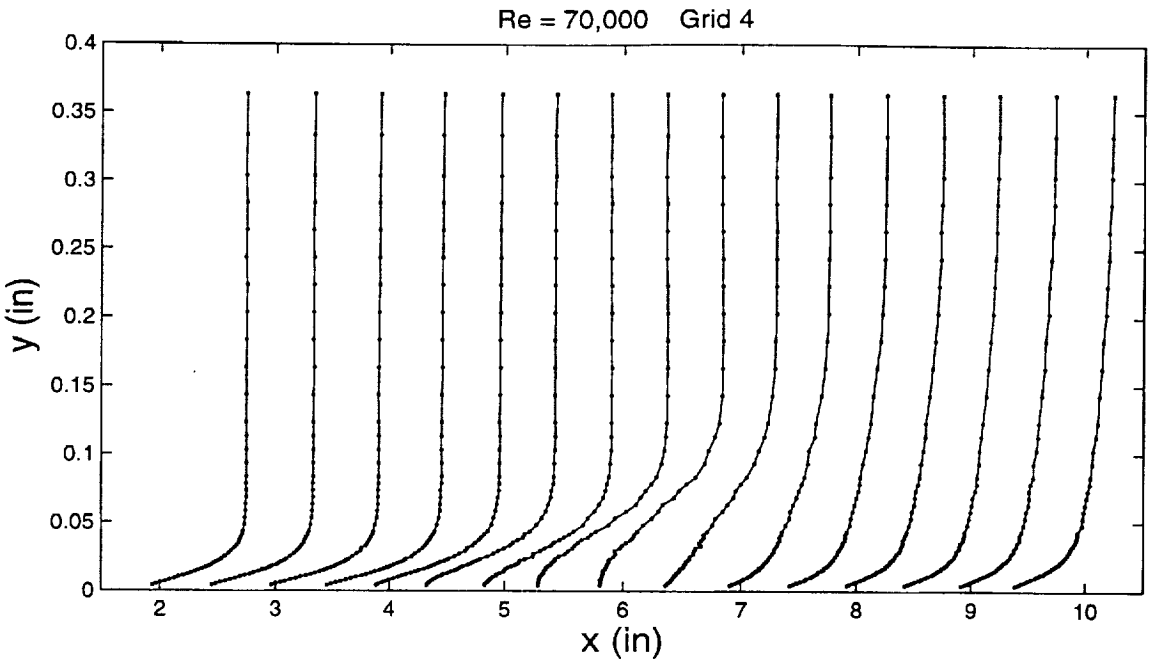

Figure 23 Distribution of U/U_{in} for Re = 70,000, Grid 4

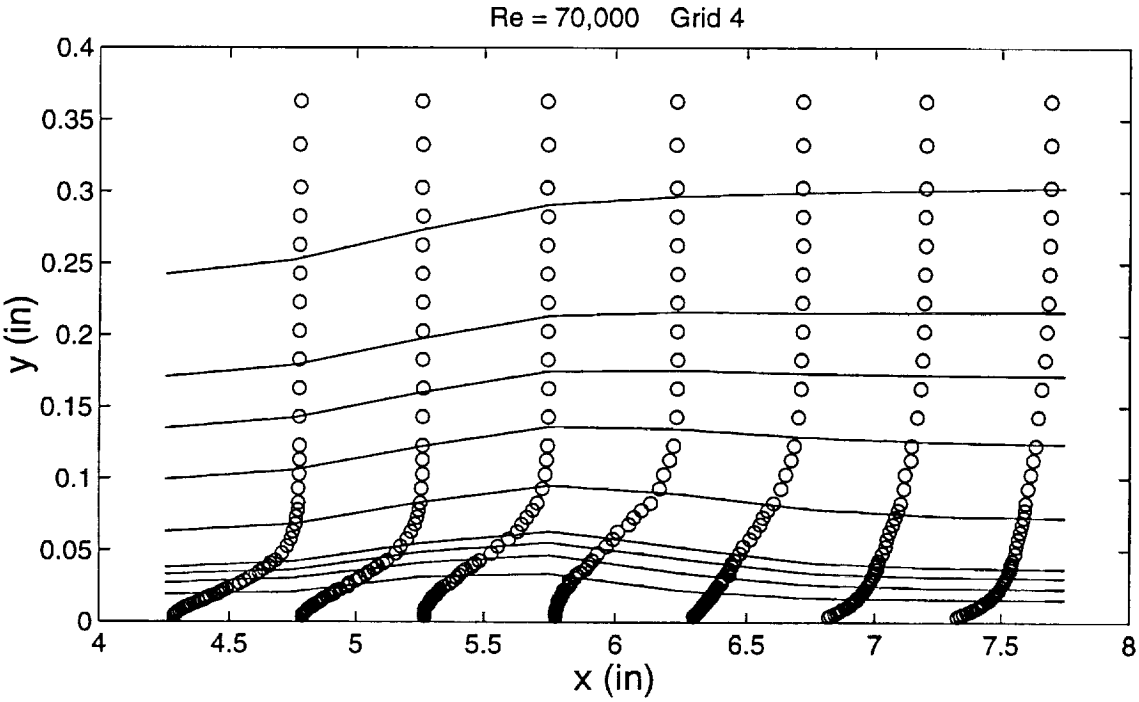

Figure 23a Distribution of U/U_{in} around separation bubble along with streamlines for Re = 70,000, Grid 4

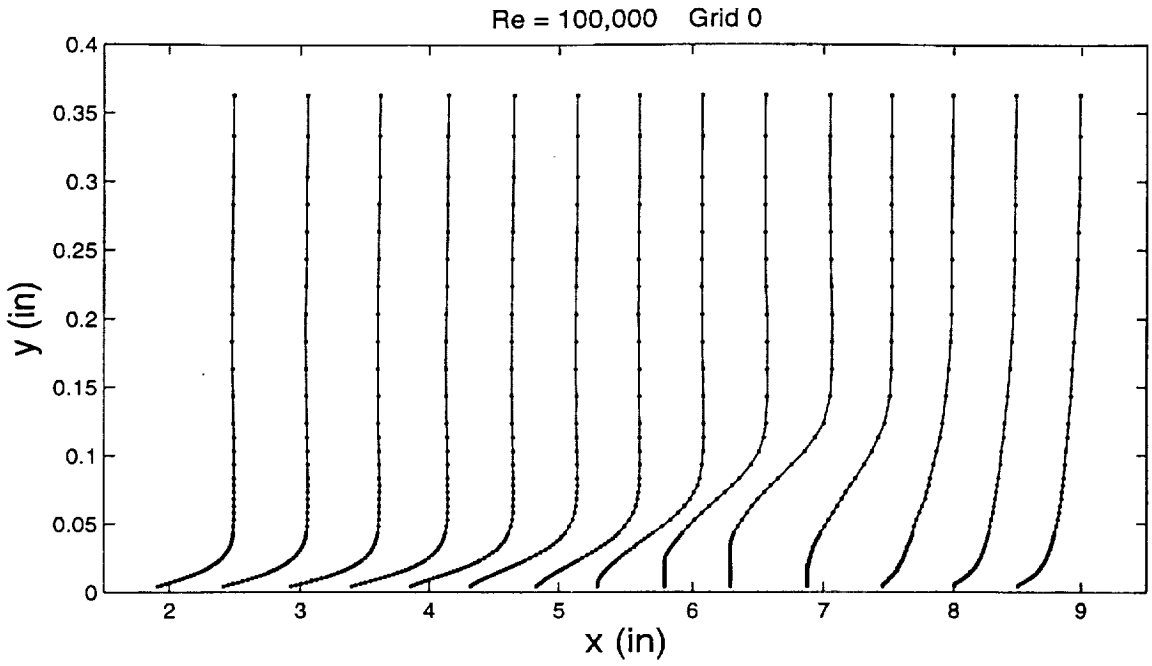

Figure 24 Distribution of U/U_{in} for Re = 100,000, Grid 0

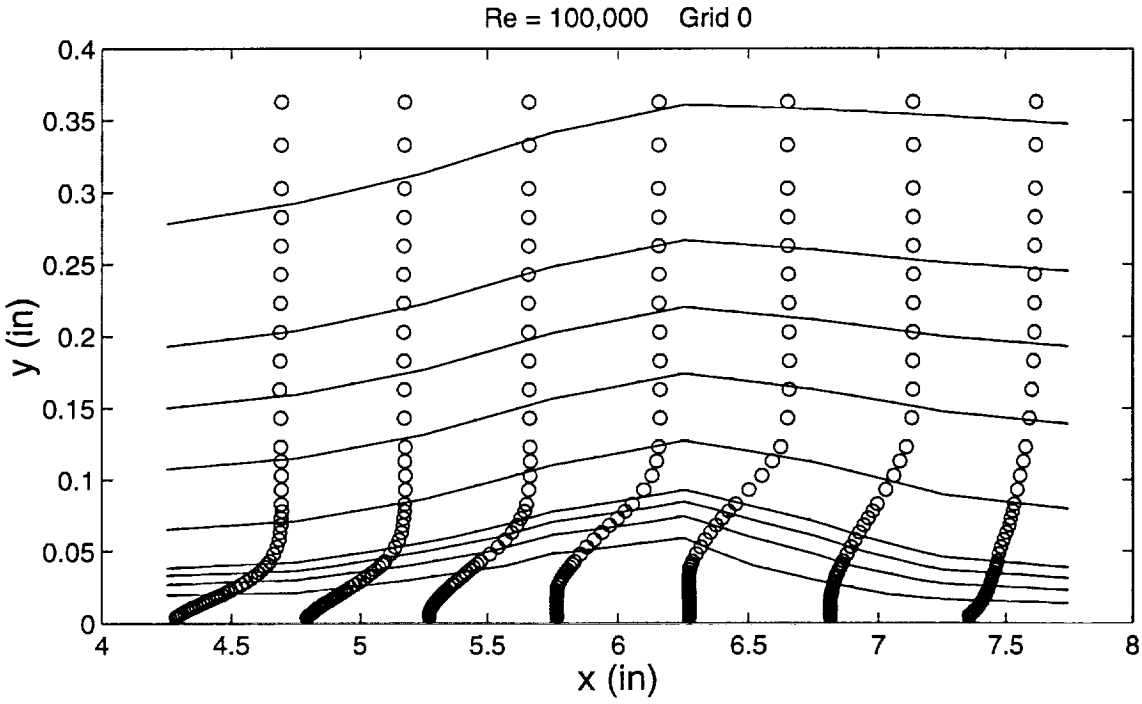

Figure 24a Distribution of U/U_{in} around separation bubble along with streamlines for Re = 100,000, Grid 0

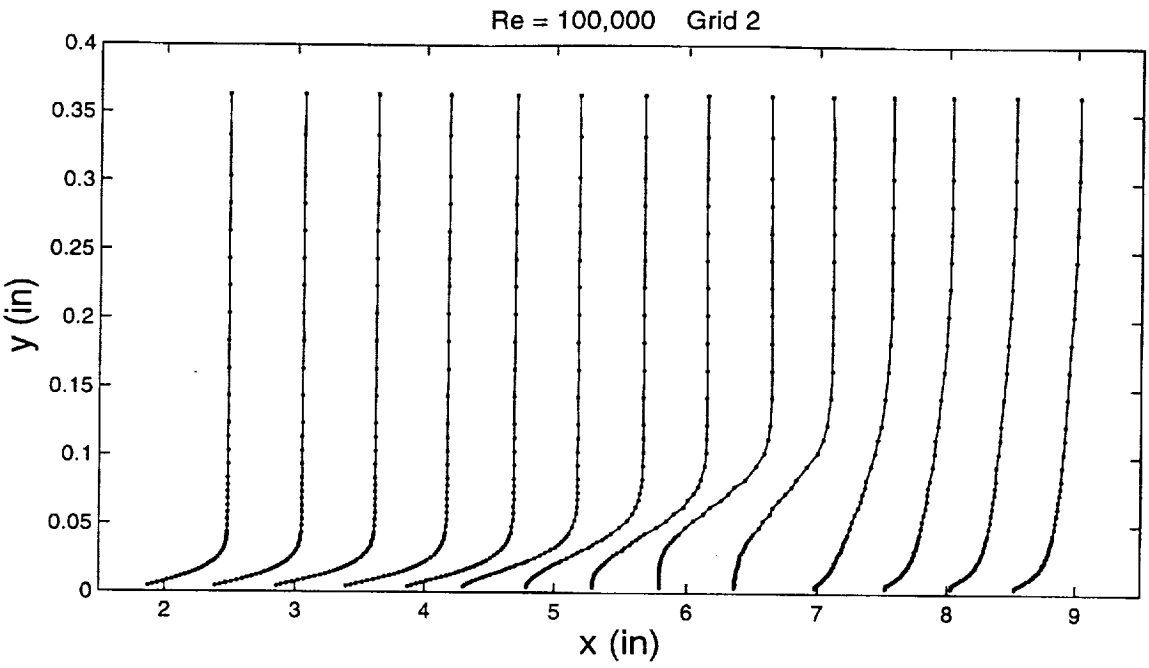

Figure 25 Distribution of U/U_{in} for Re = 100,000, Grid 2

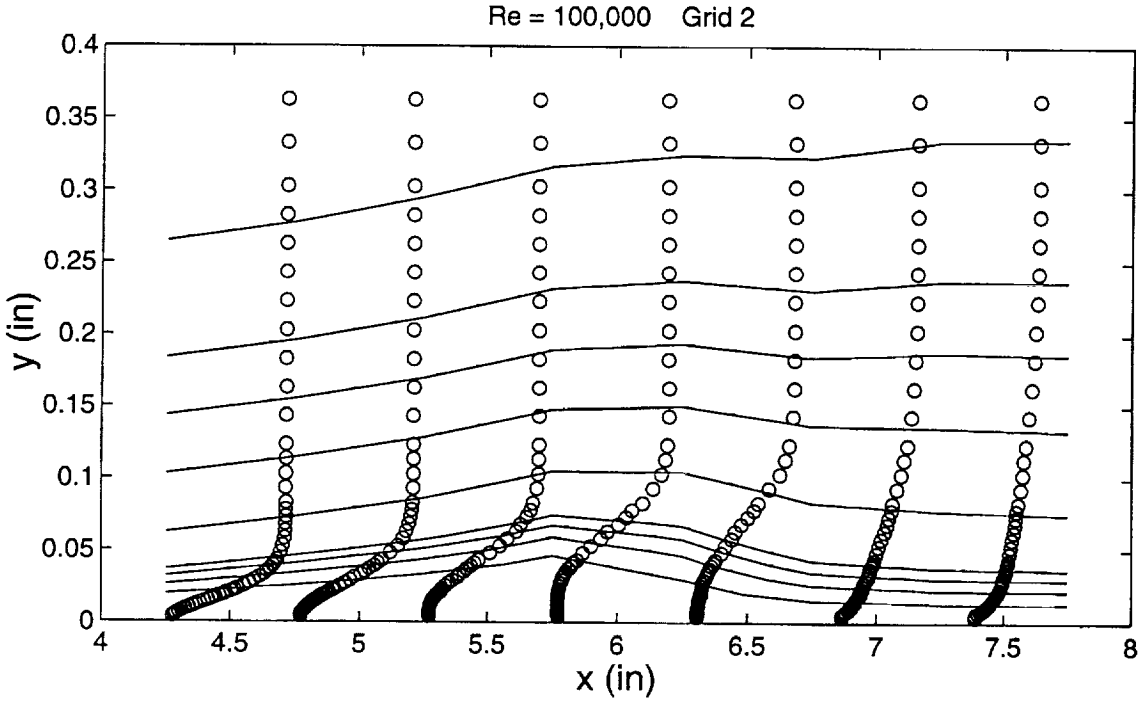

Figure 25a Distribution of U/U_{in} around separation bubble along with streamlines for Re = 100,000, Grid 2

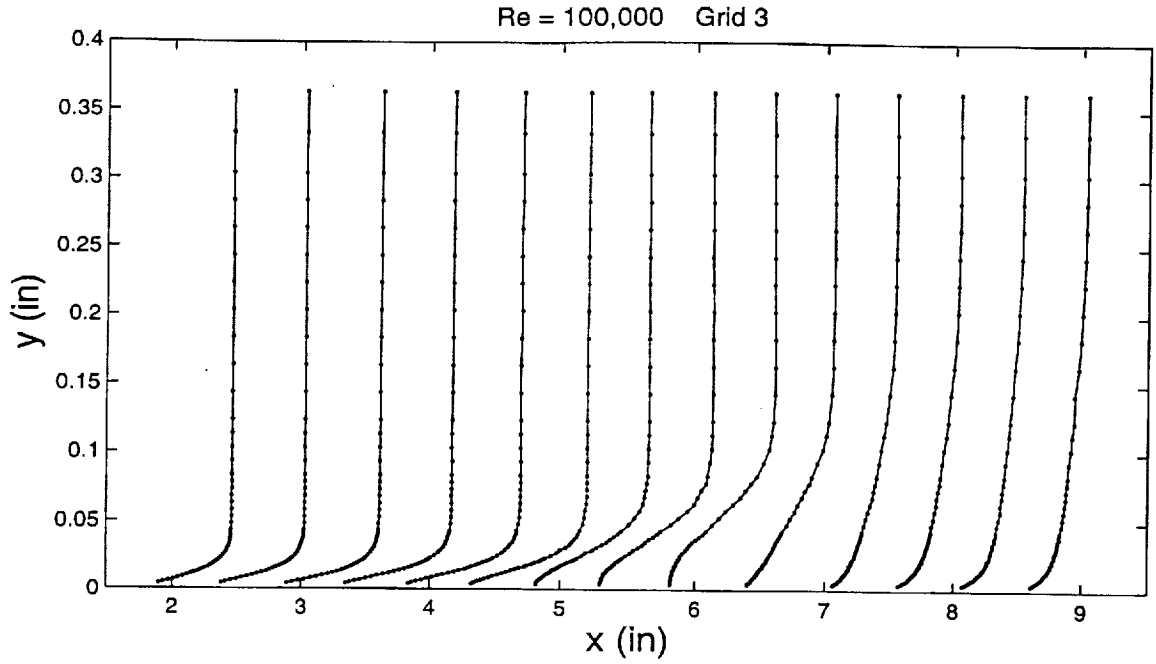

Figure 26 Distribution of U/U_{in} for Re = 100,000, Grid 3

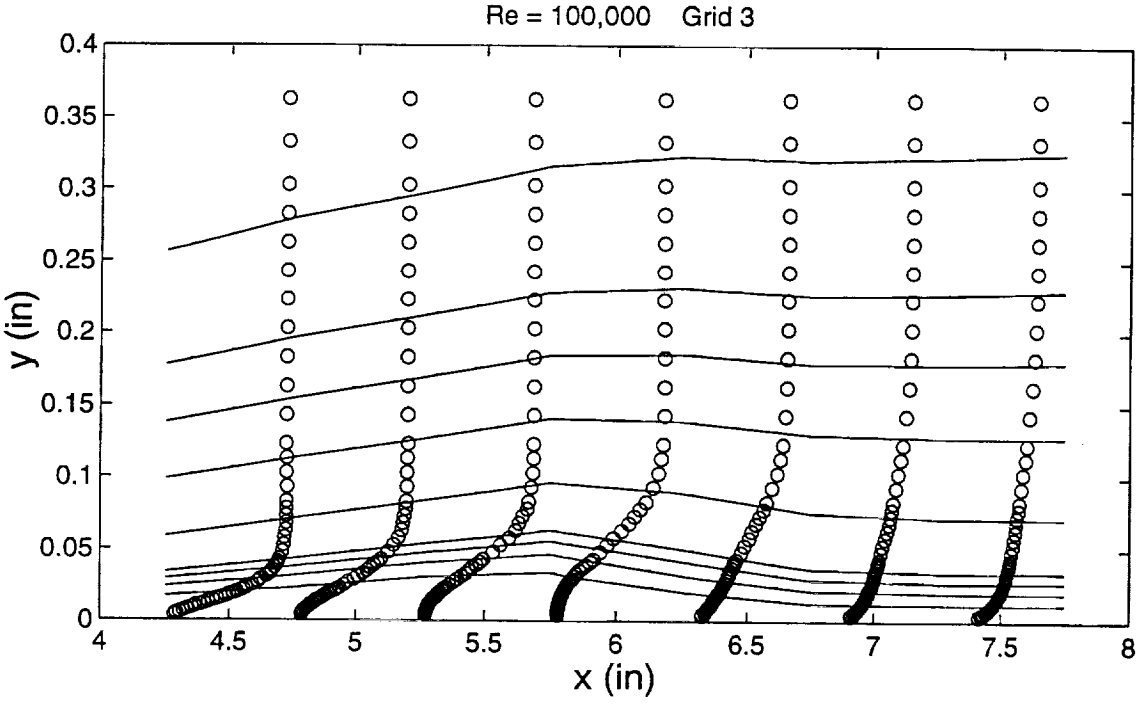

Figure 26a Distribution of U/U_{in} around separation bubble along with streamlines for Re = 100,000, Grid 3

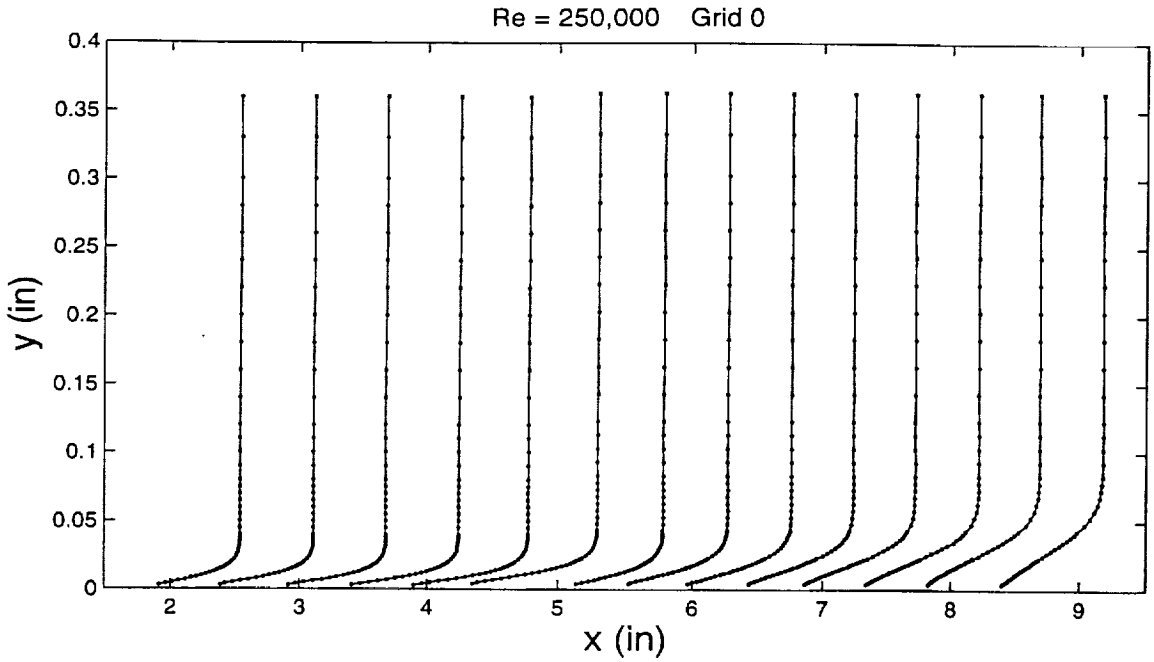

Figure 27 Distribution of U/U_{in} for Re = 250,000, Grid 0

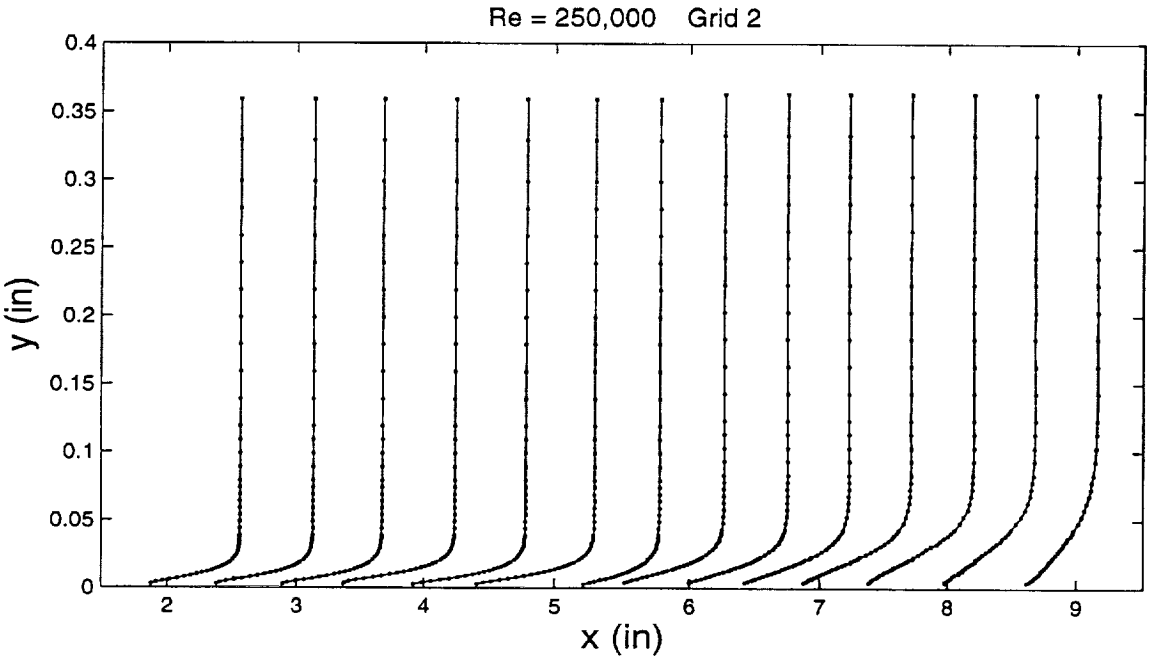

Figure 28 Distribution of U/U_{in} for Re = 250,000, Grid 2

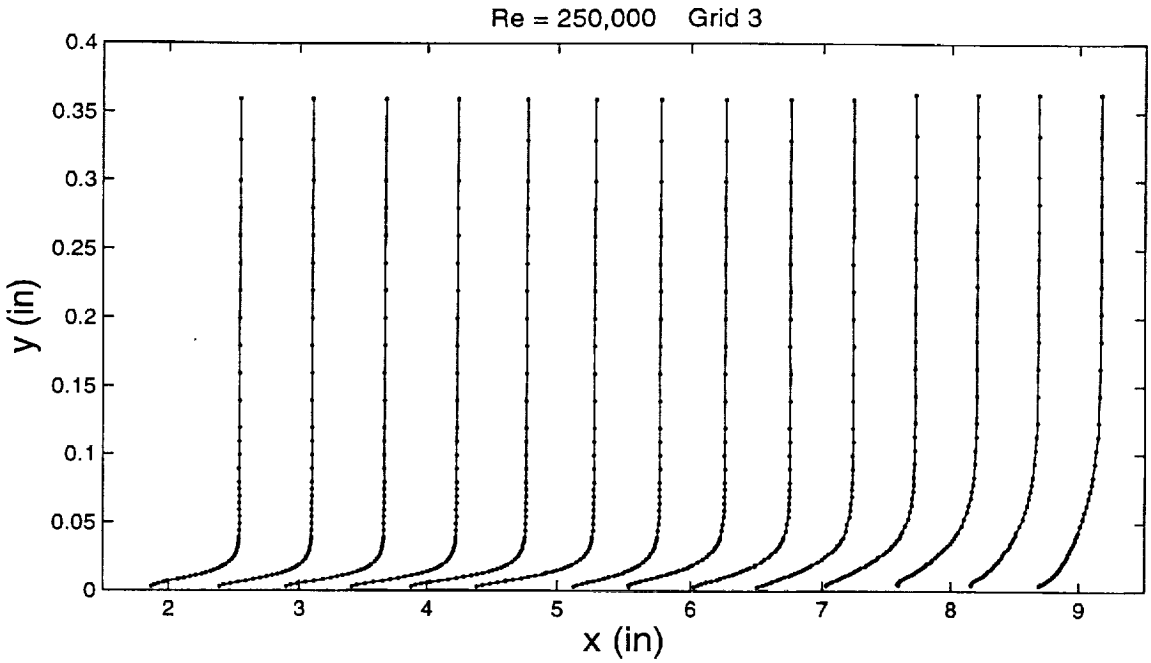

Figure 29 Distribution of U/U_{in} for Re = 250,000, Grid 3

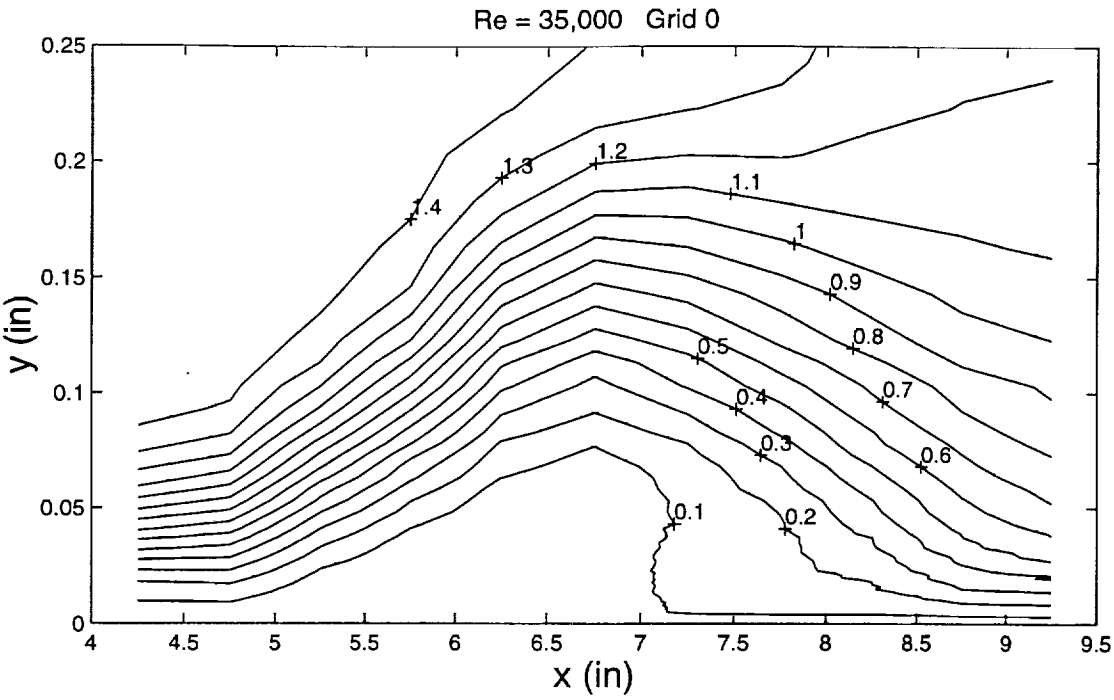

Figure 30 Contour plots of U/U_{in} for Re = 35,000, Grid 0

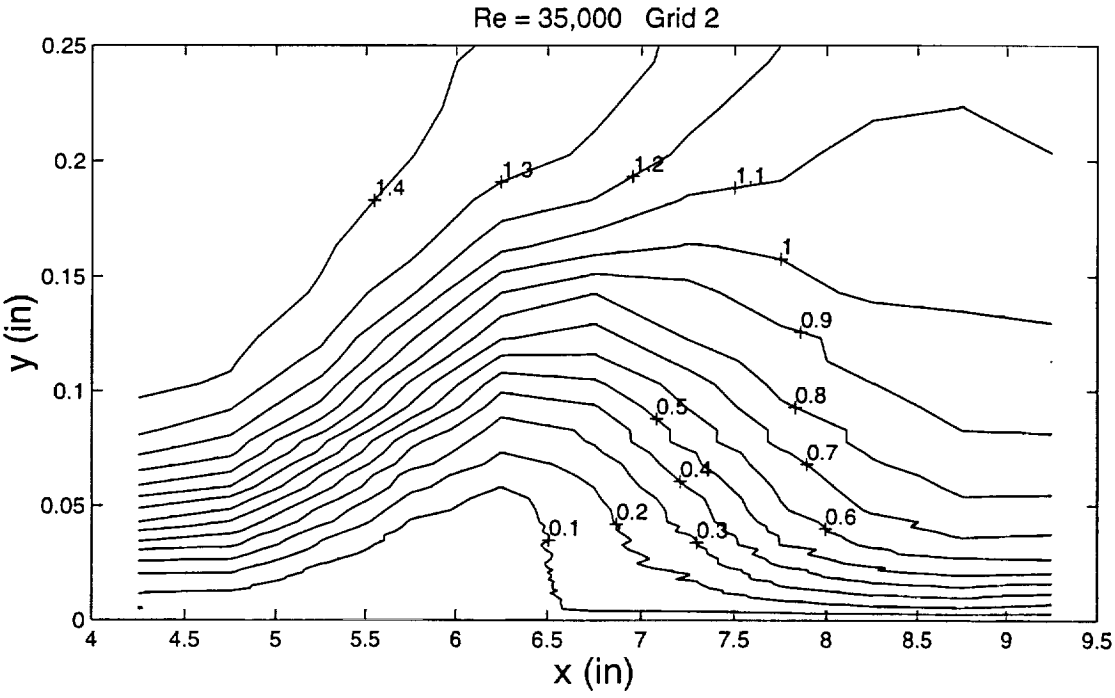

Figure 31 Contour plots of U/U_{in} for Re = 35,000, Grid 2

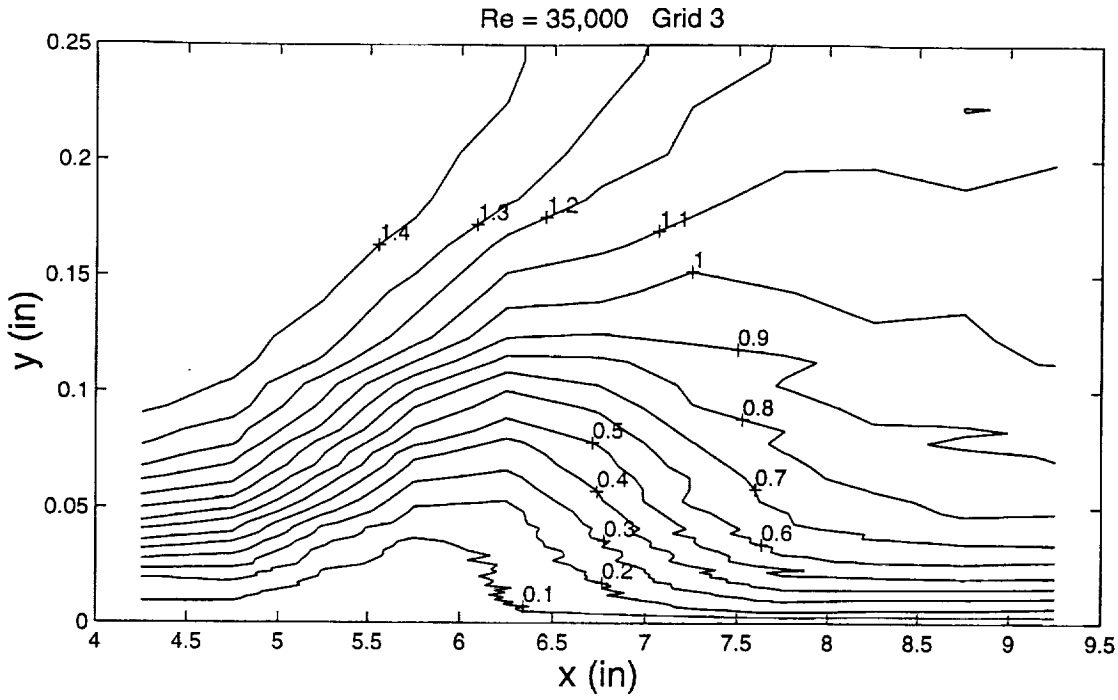

Figure 32 Contour plots of U/U_{in} for Re = 35,000, Grid 3

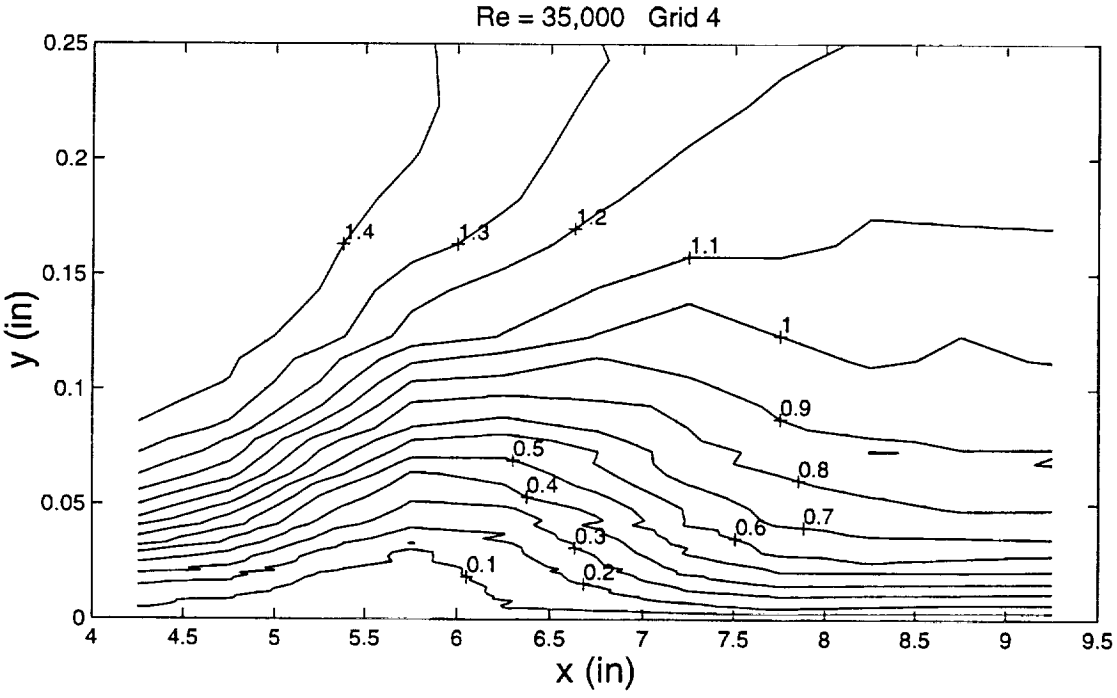

Figure 33 Contour plots of U/U_{in} for Re = 35,000, Grid 4

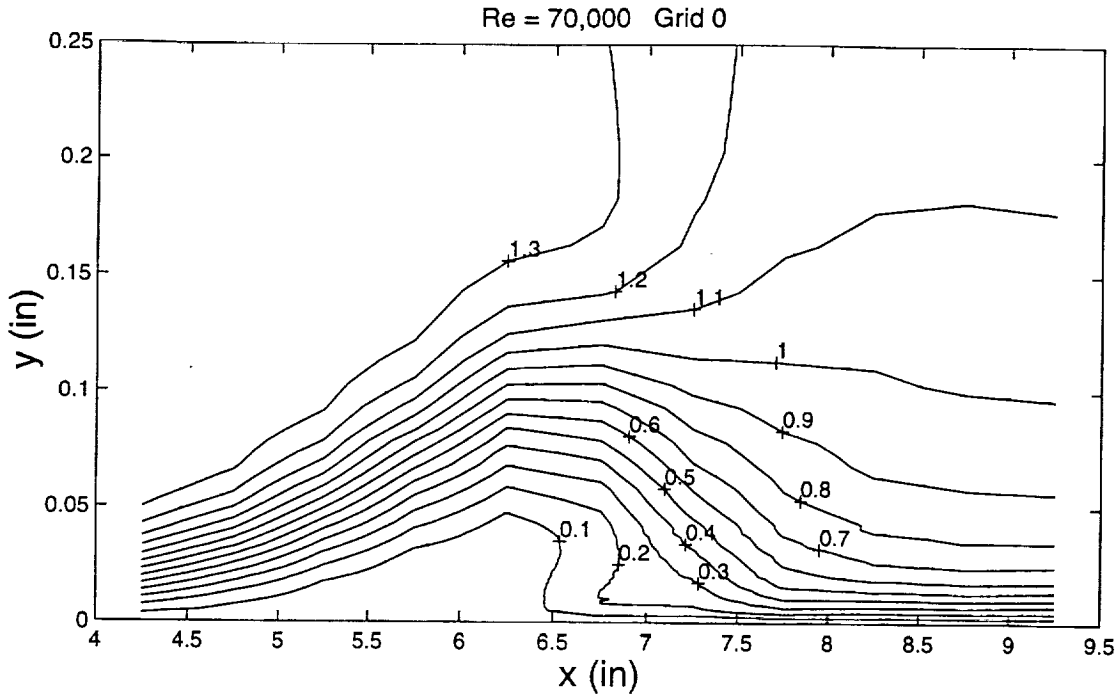

Figure 34 Contour plots of U/U_{in} for Re = 70,000, Grid 0

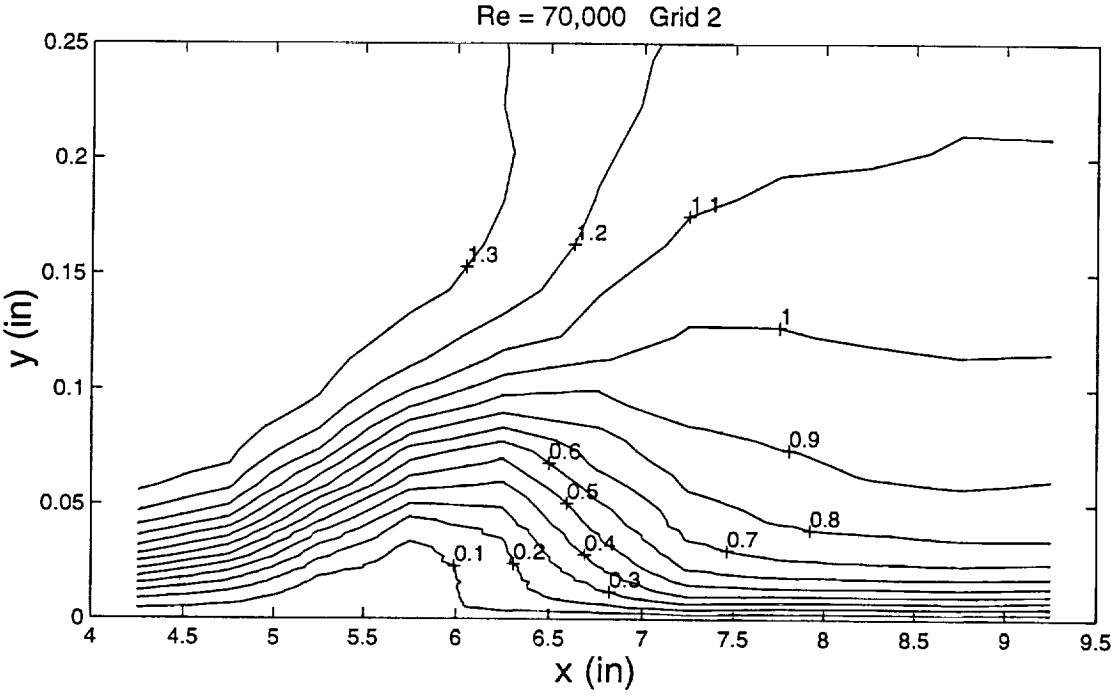

Figure 35 Contour plots of U/U_{in} for Re = 70,000, Grid 2

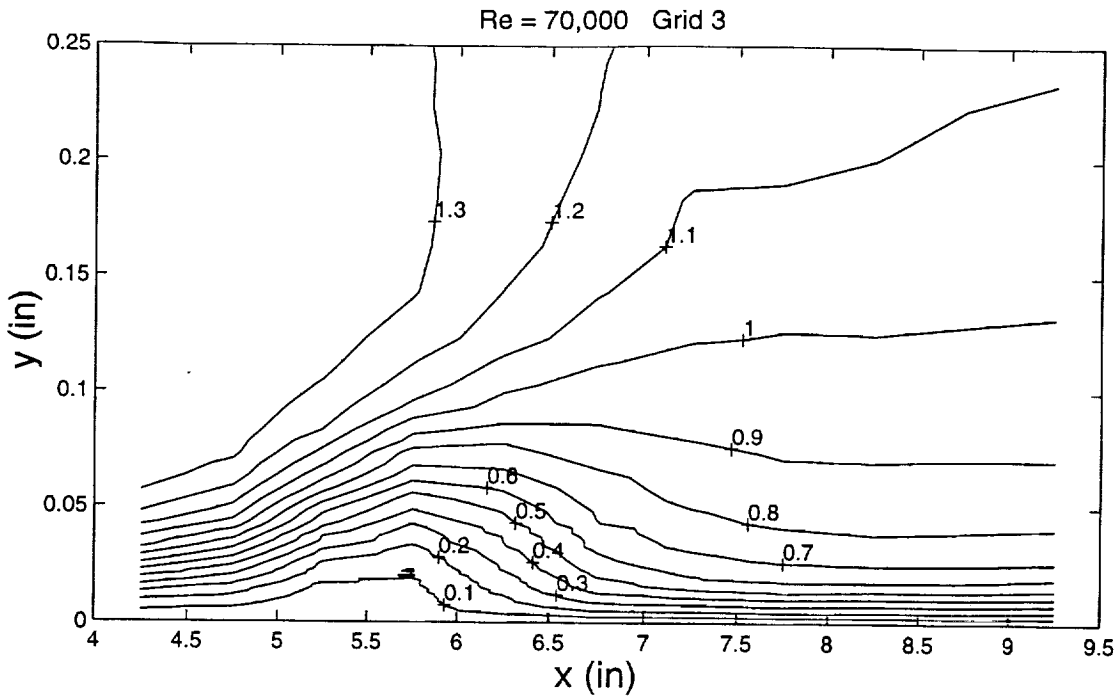

Figure 36 Contour plots of U/U_{in} for Re = 70,000, Grid 3

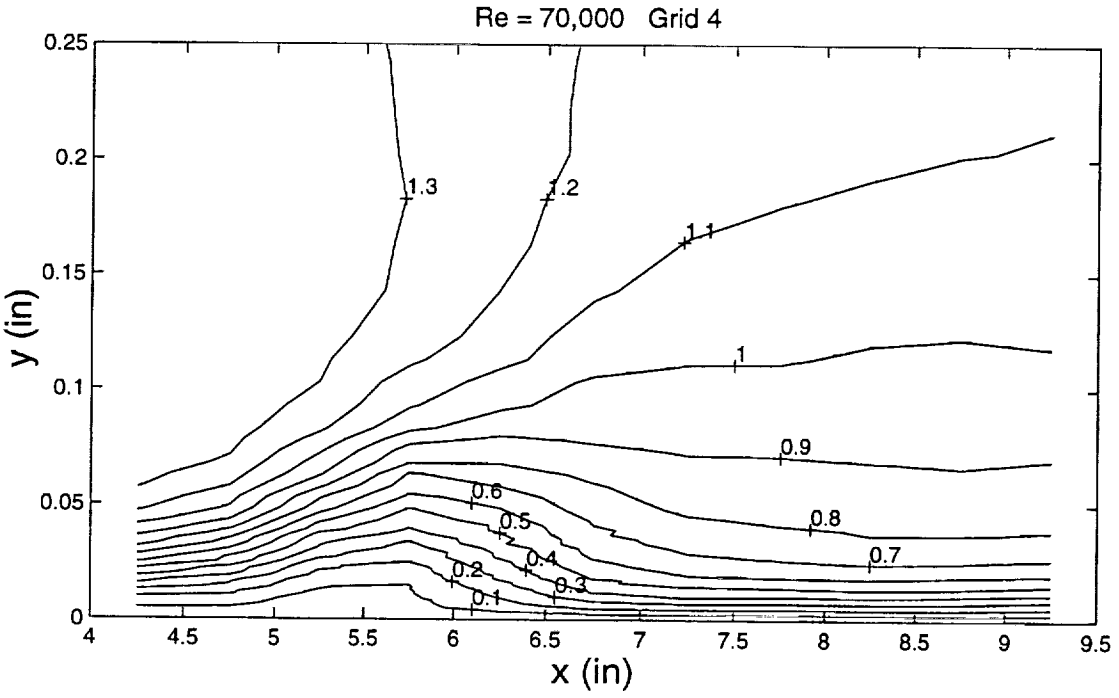

Figure 37 Contour plots of U/U_{in} for Re = 70,000, Grid 4

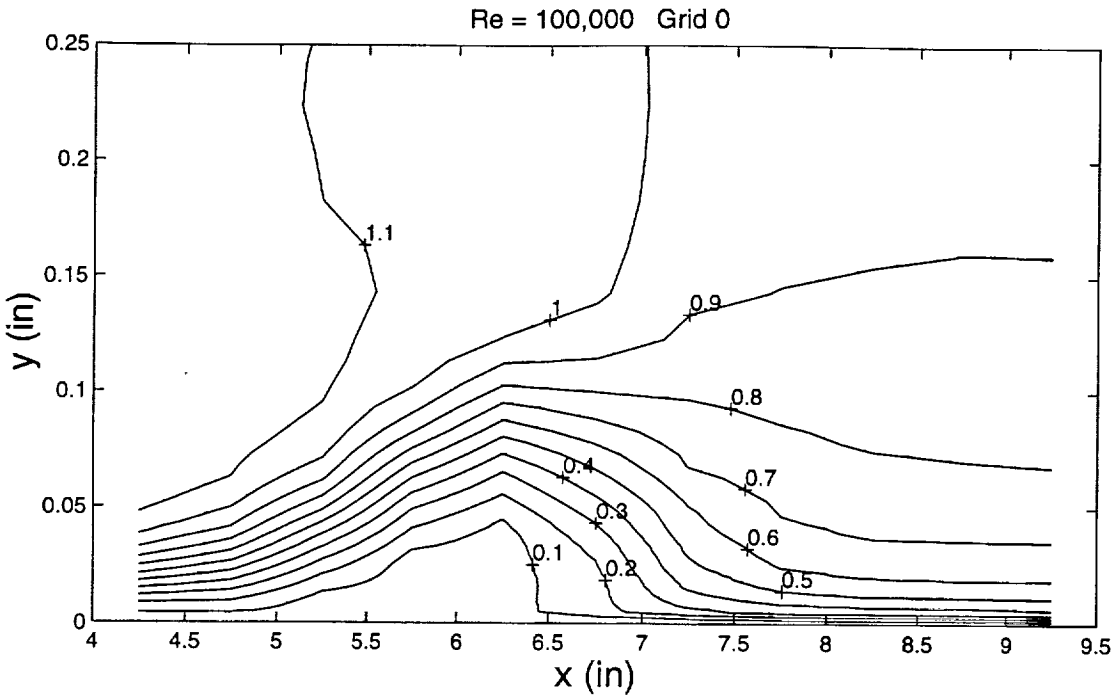

Figure 38 Contour plots of U/U_{in} for Re = 100,000, Grid 0

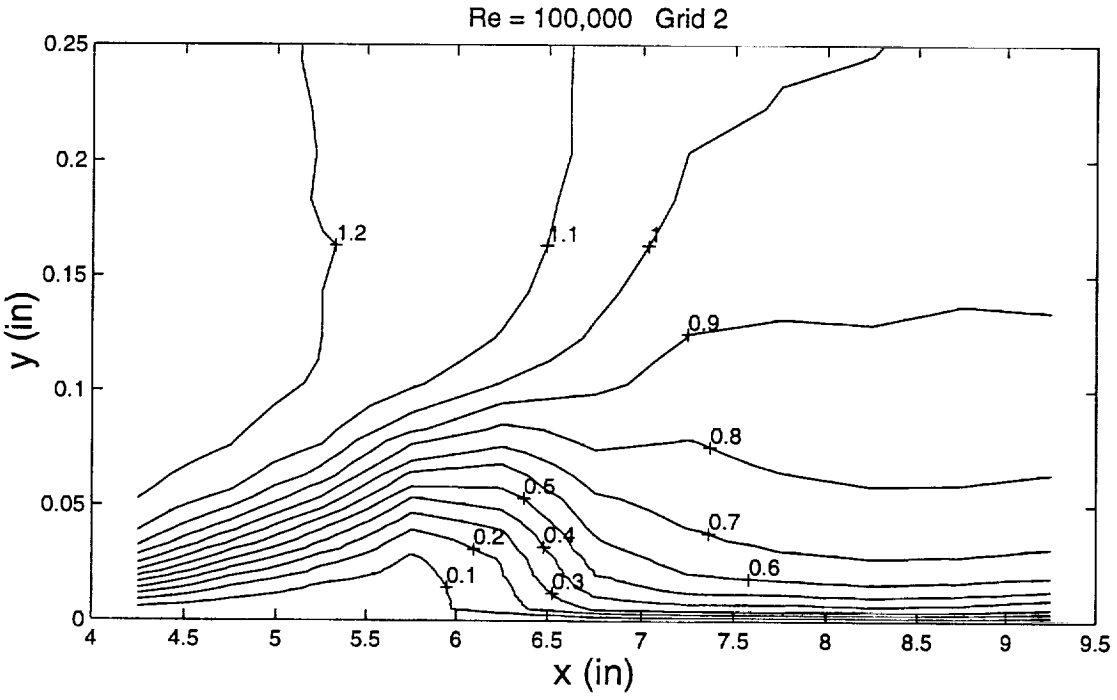

Figure 39 Contour plots of U/U_{in} for Re = 100,000, Grid 2

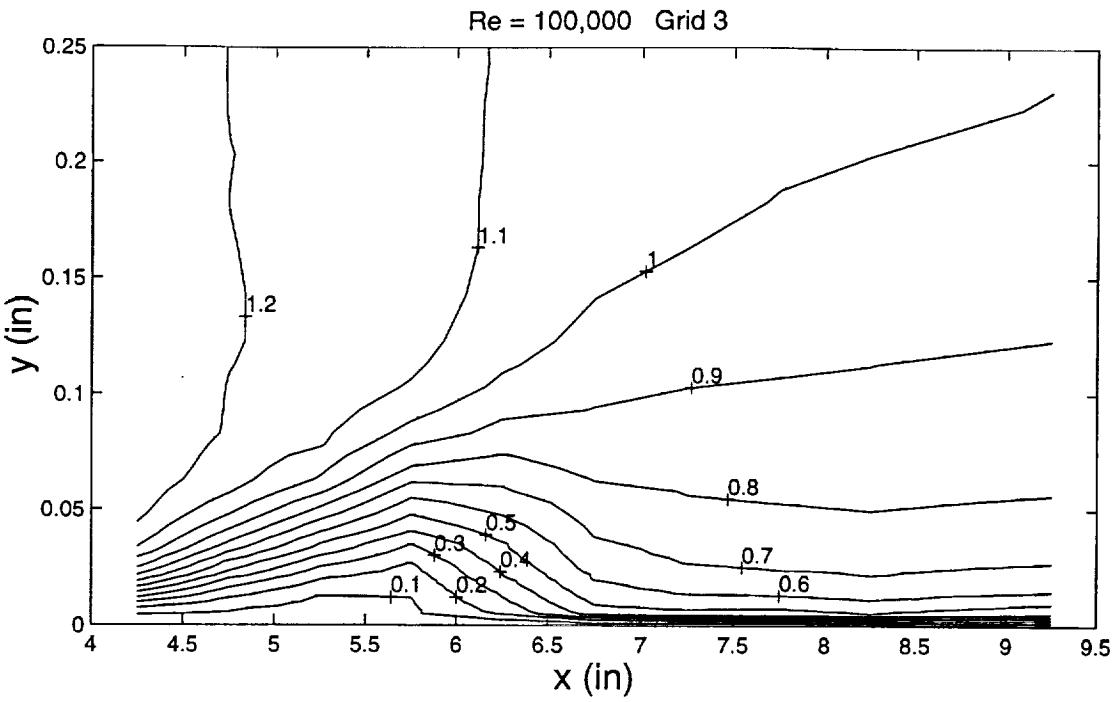

Figure 40 Contour plots of U/U_{in} for Re = 100,000, Grid 3

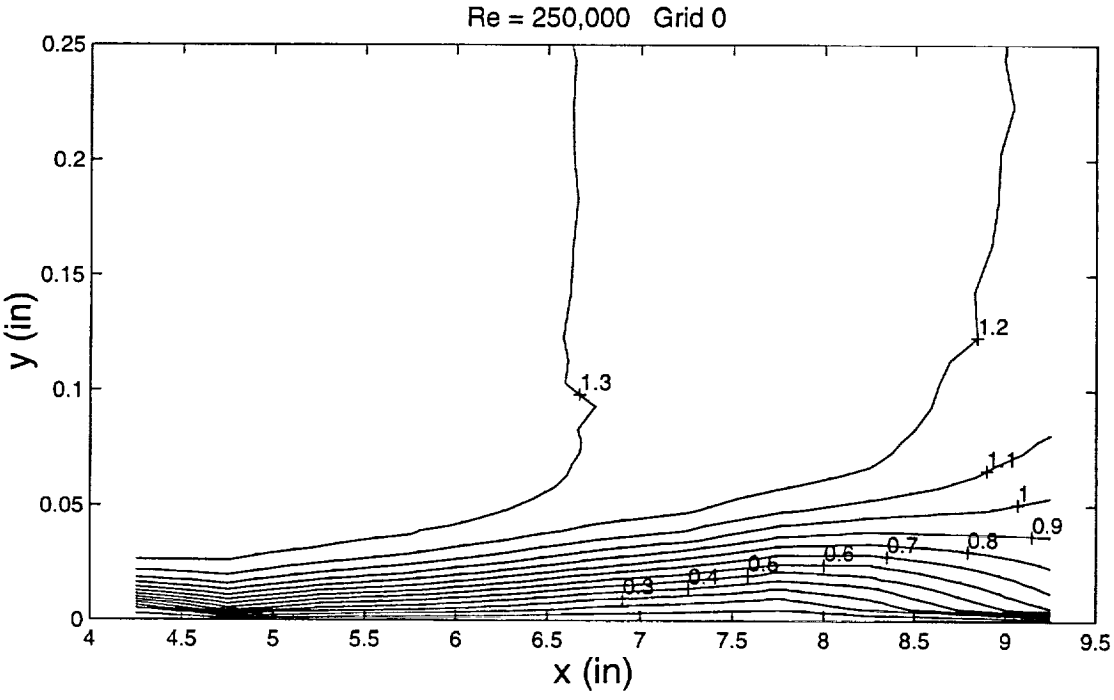

Figure 41 Contour plots of U/U_{in} for Re = 250,000, Grid 0

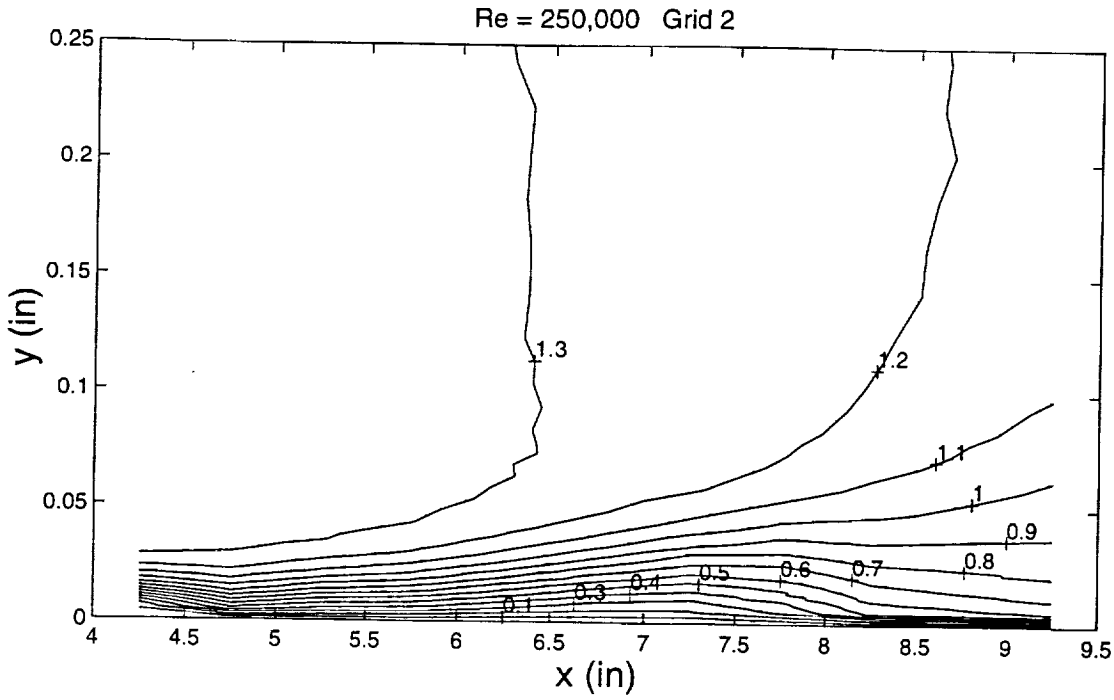

Figure 42 Contour plots of U/U_{in} for Re = 250,000, Grid 2

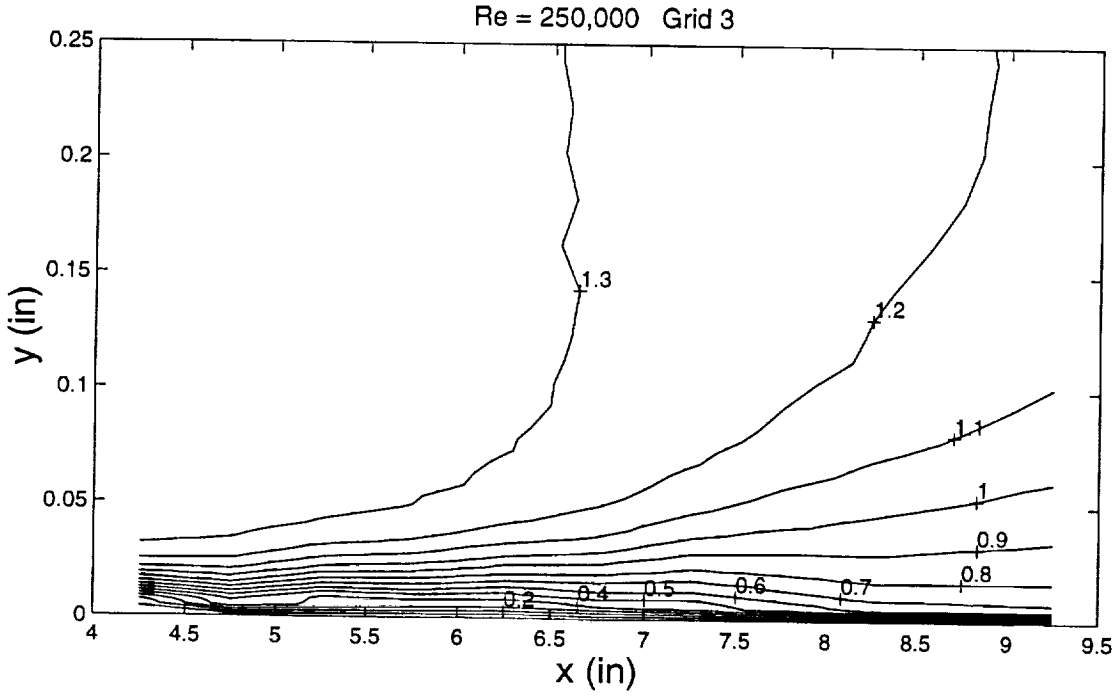

Figure 43 Contour plots of U/U_{in} for Re = 250,000, Grid 3

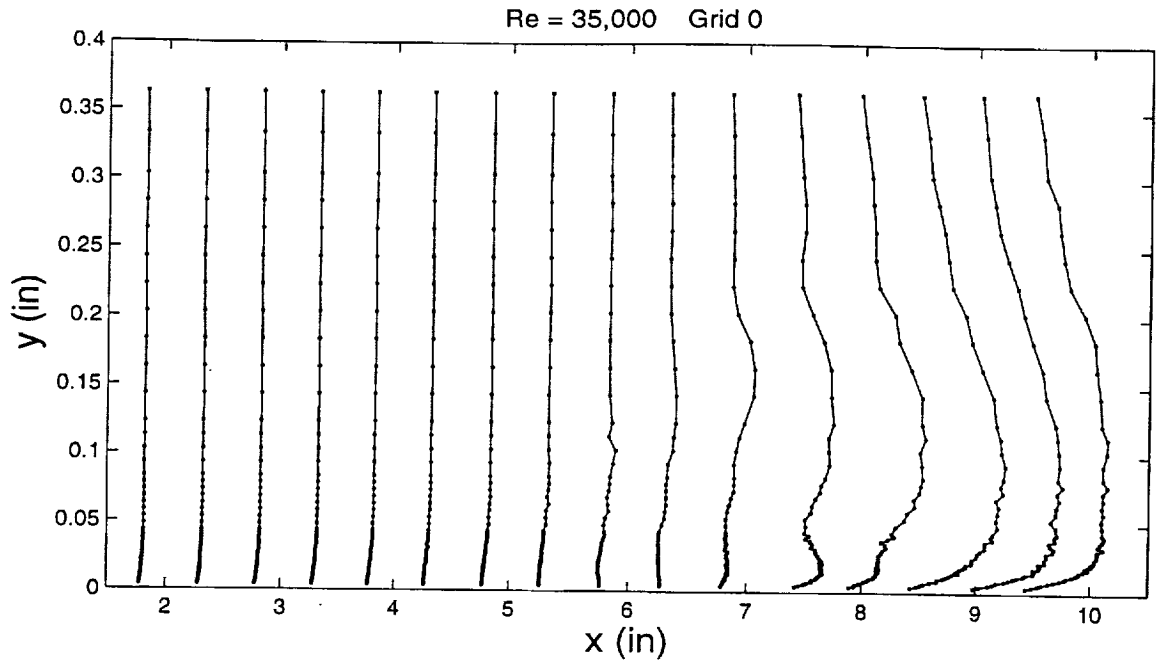

Figure 44 Distribution of u'/U_{in} for Re = 35,000, Grid 0

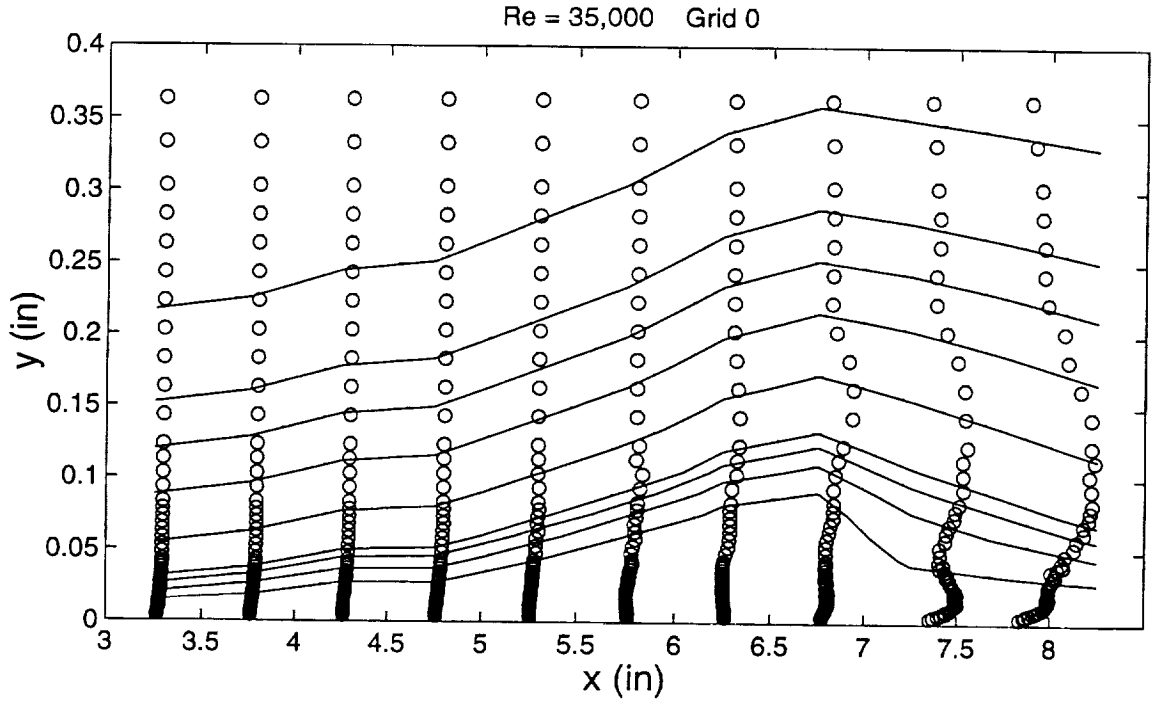

Figure 44a Distribution of u'/U_{in} around separation bubble along with streamlines for Re = 35,000, Grid 0

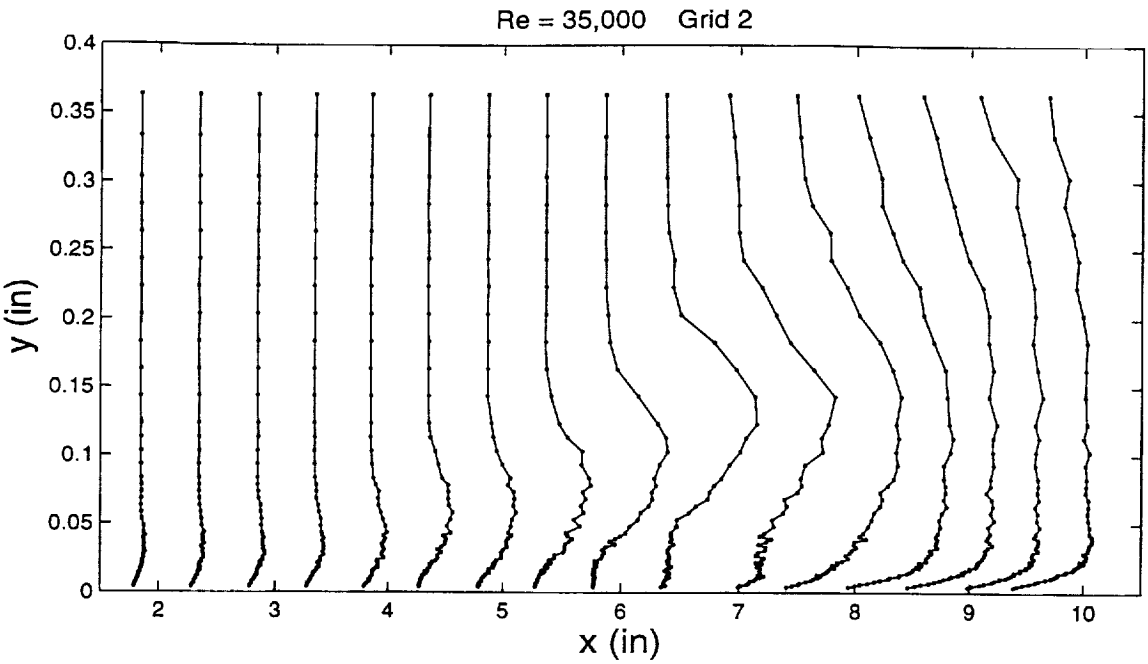

Figure 45 Distribution of u'/U_{in} for Re = 35,000, Grid 2

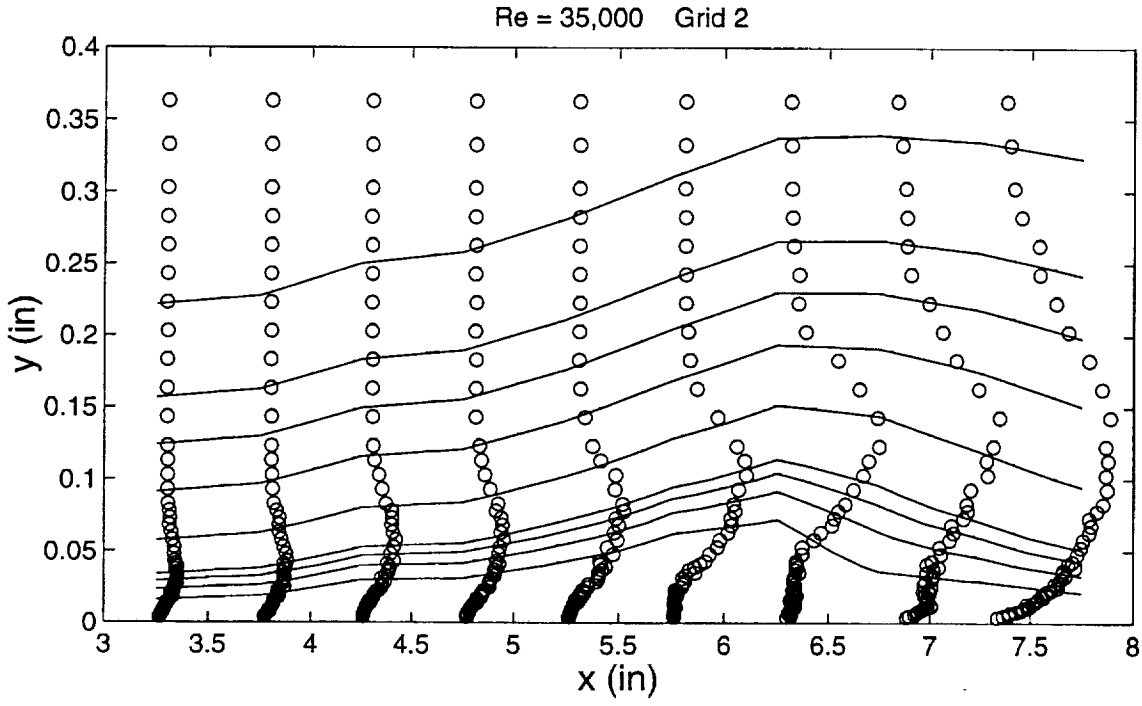

Figure 45a Distribution of u'/U_{in} around separation bubble along with streamlines for Re = 35,000, Grid 2

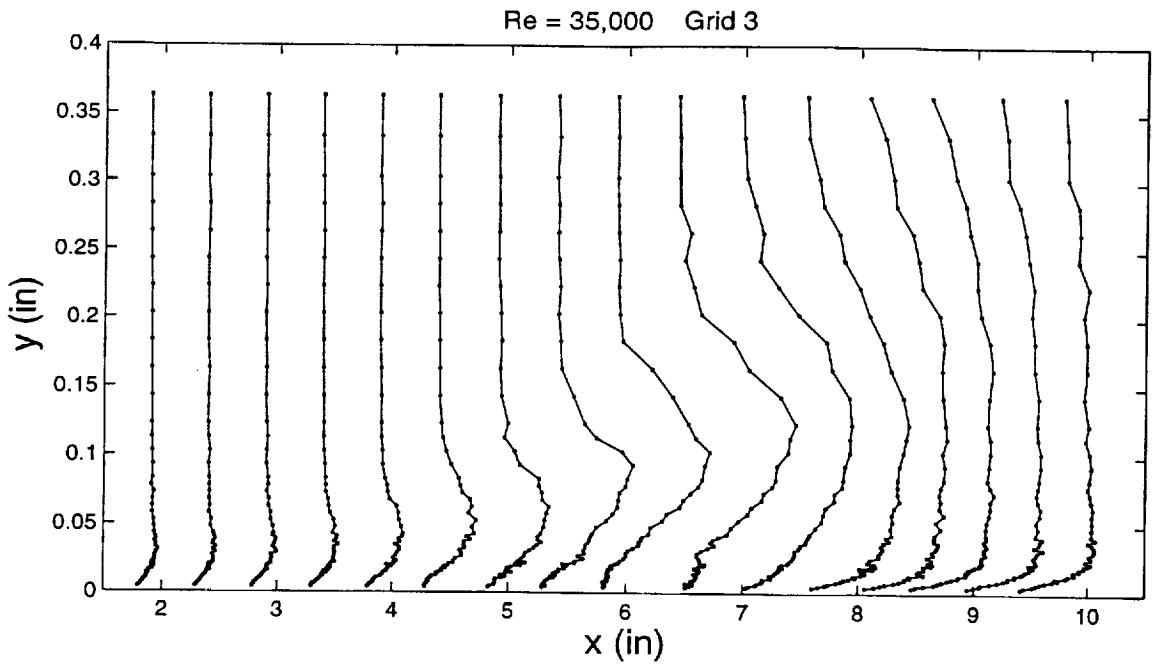

Figure 46 Distribution of u'/U_{in} for Re = 35,000, Grid 3

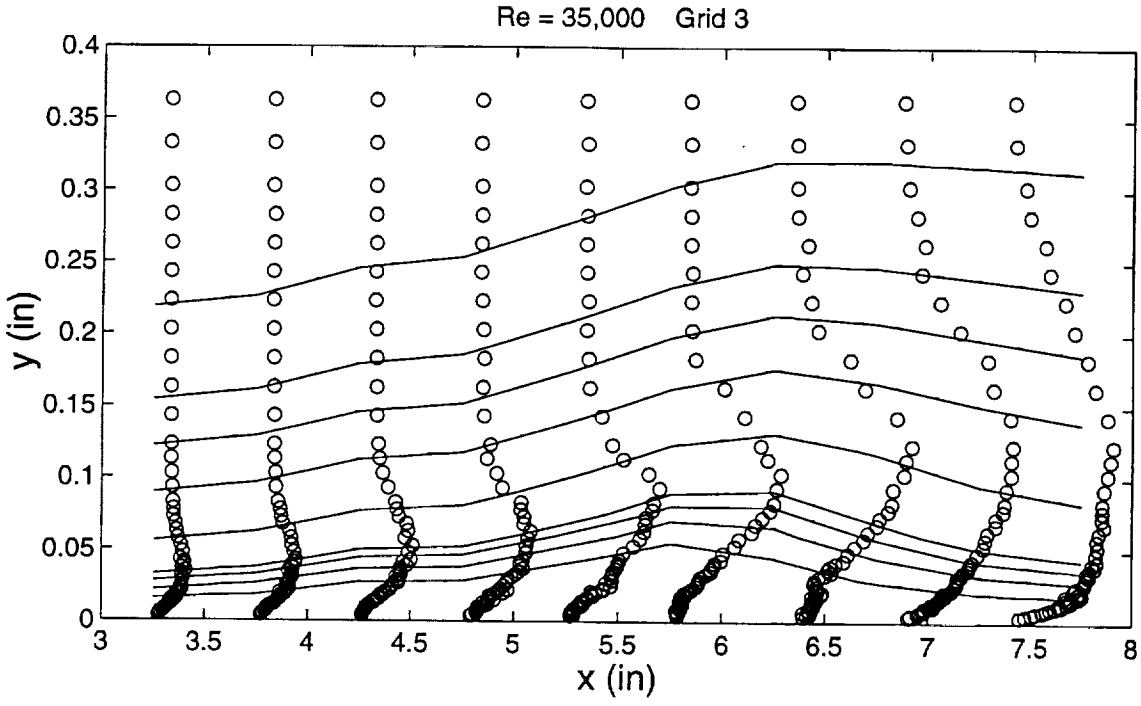

Figure 46a Distribution of u'/U_{in} around separation bubble along with streamlines for Re = 35,000, Grid 3

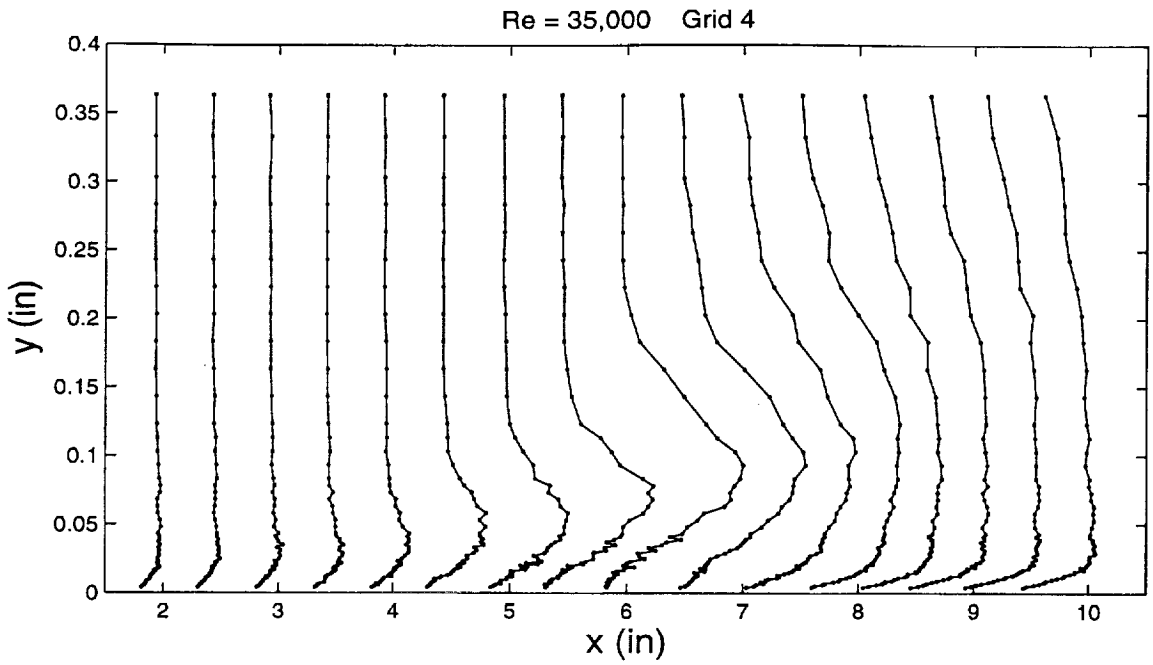

Figure 47 Distribution of u'/U_{in} for Re = 35,000, Grid 4

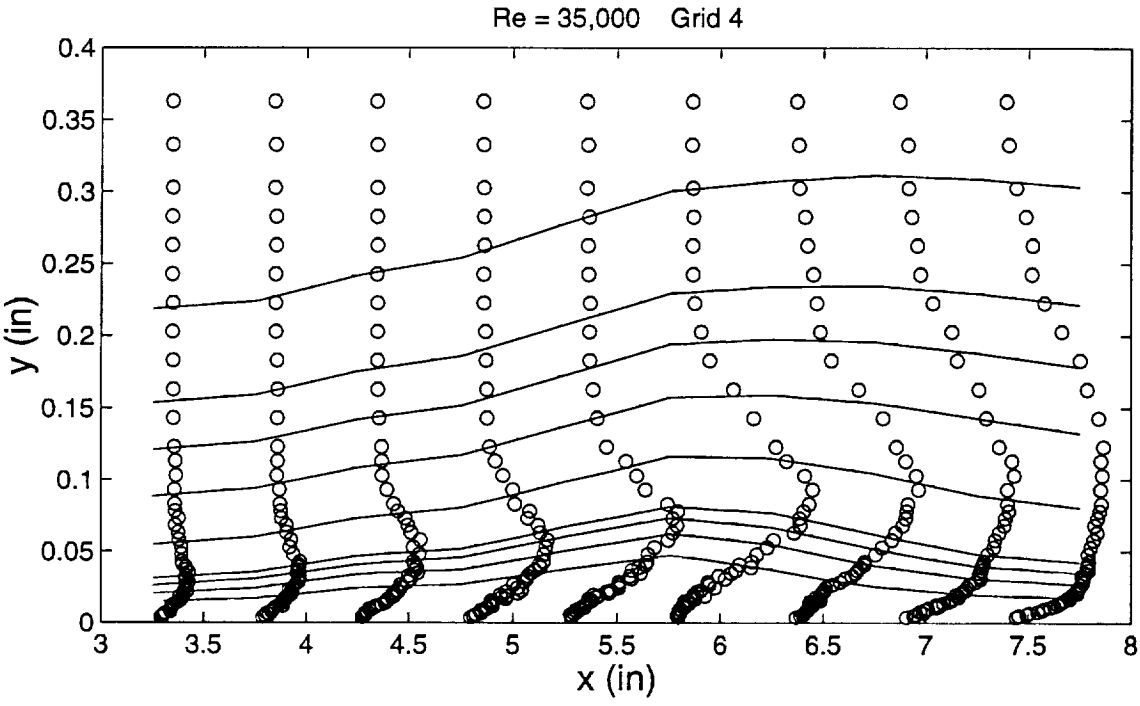

Figure 47a Distribution of u'/U_{in} around separation bubble along with streamlines for Re = 35,000, Grid 4

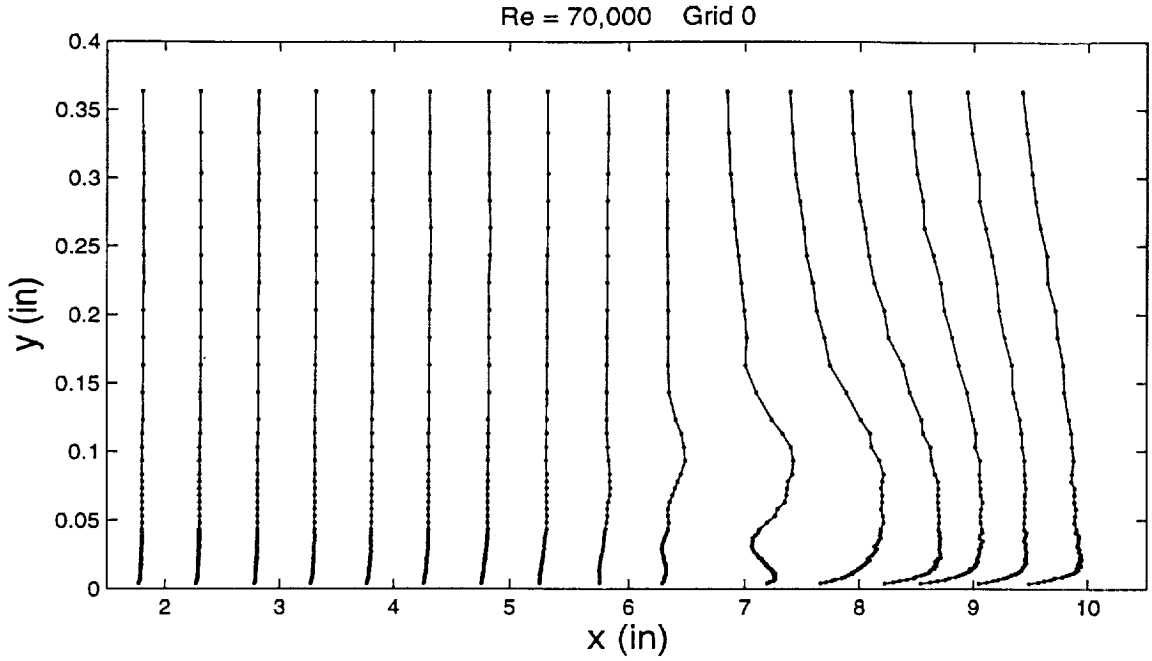

Figure 48 Distribution of u'/U_{in} for Re = 70,000, Grid 0

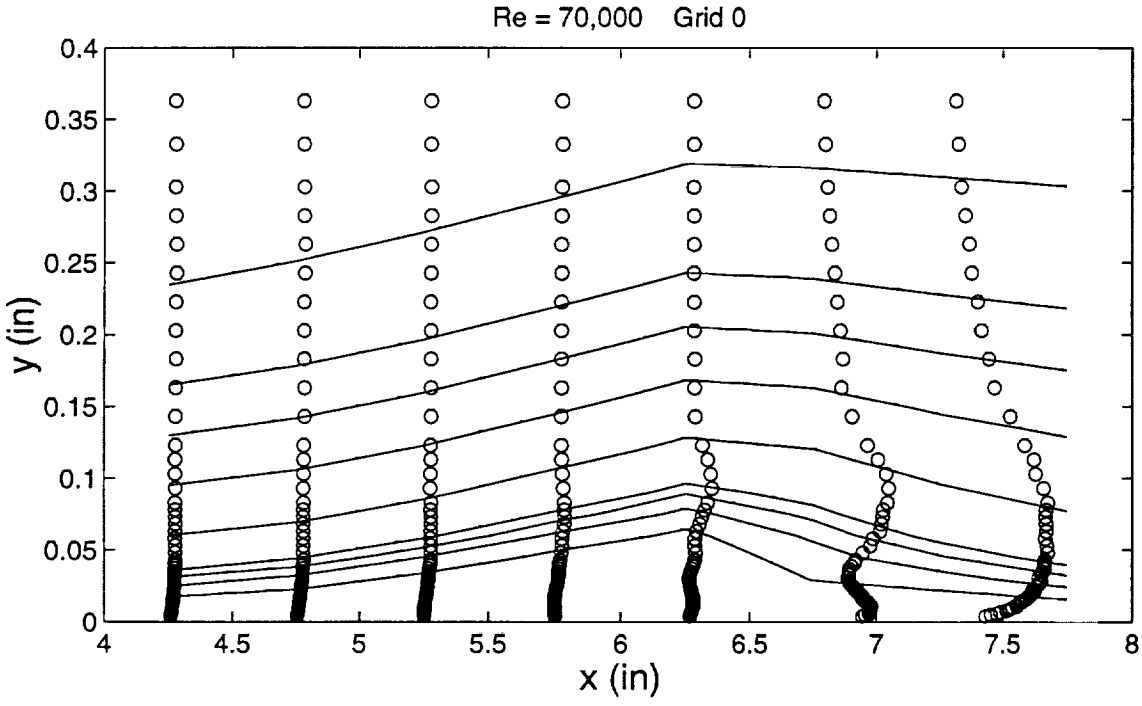

Figure 48a Distribution of u'/U_{in} around separation bubble along with streamlines for Re = 70,000, Grid 0

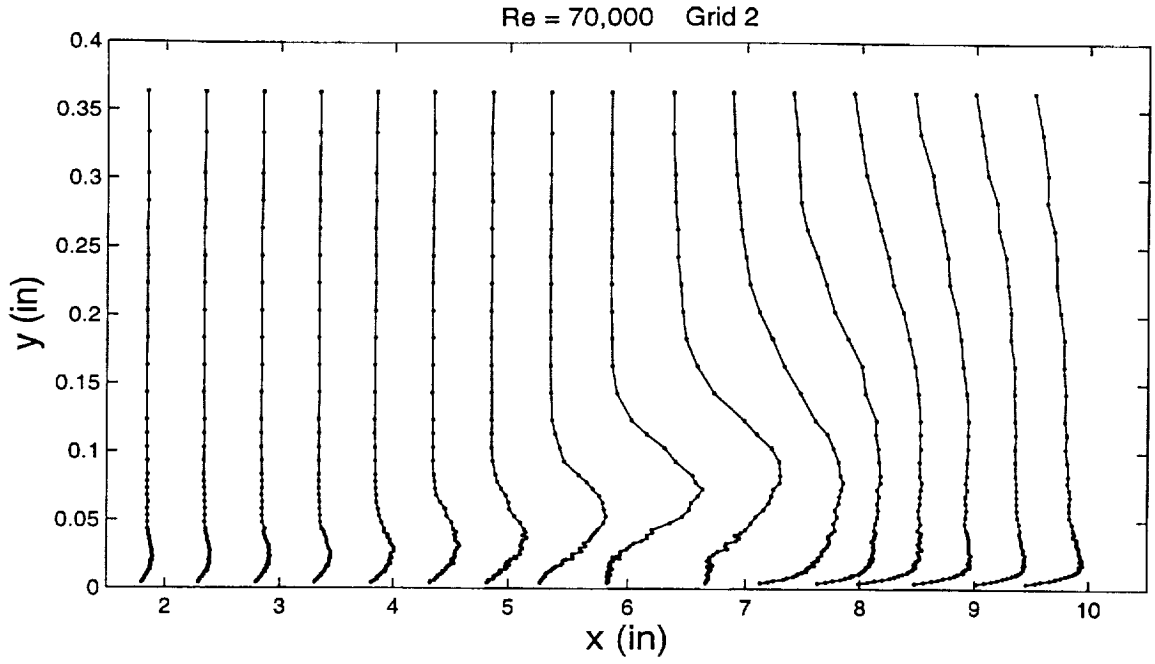

Figure 49 Distribution of u'/U_{in} for Re = 70,000, Grid 2

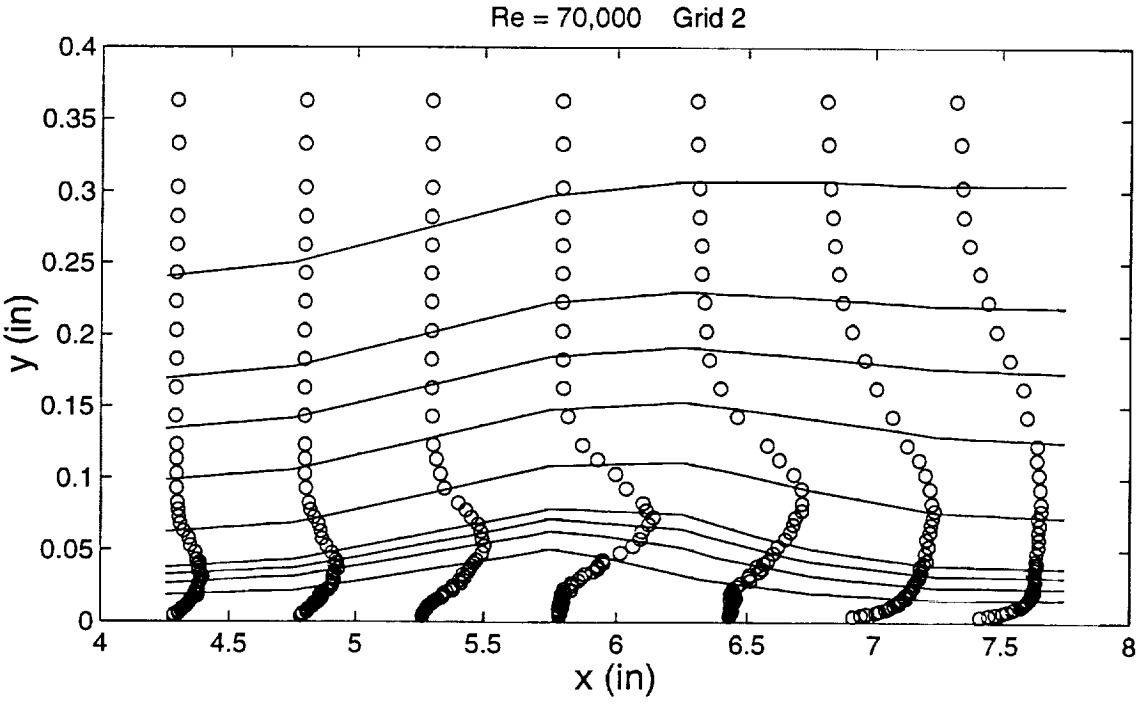

Figure 49a Distribution of u'/U_{in} around separation bubble along with streamlines for Re = 70,000, Grid 2

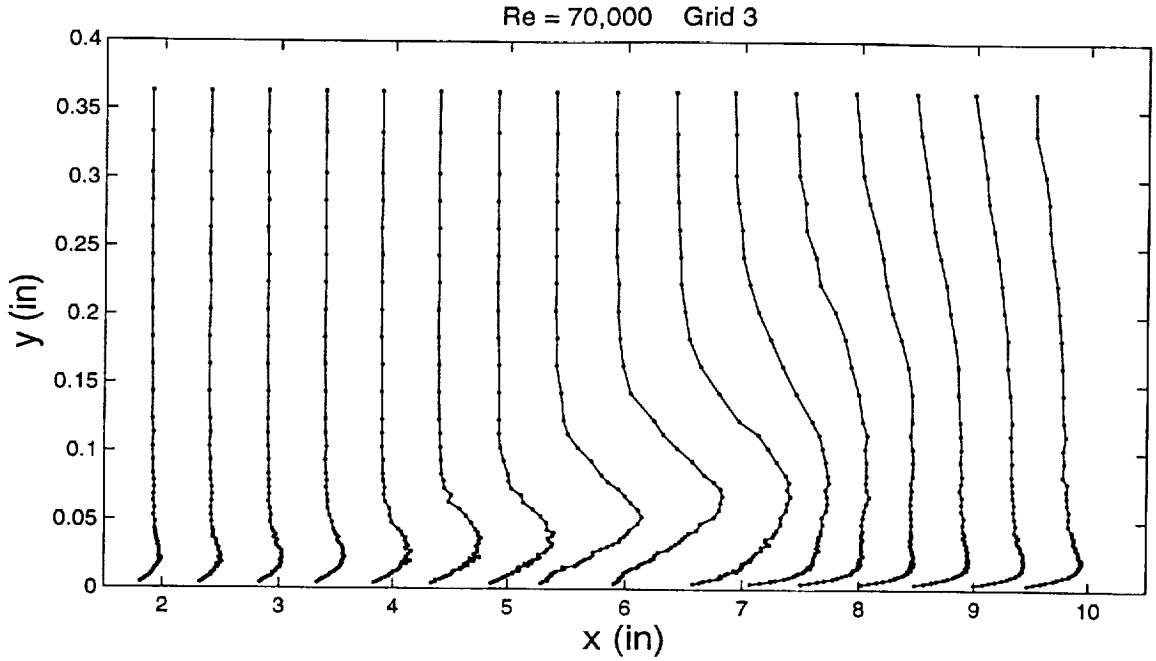

Figure 50 Distribution of u'/U_{in} for Re = 70,000, Grid 3

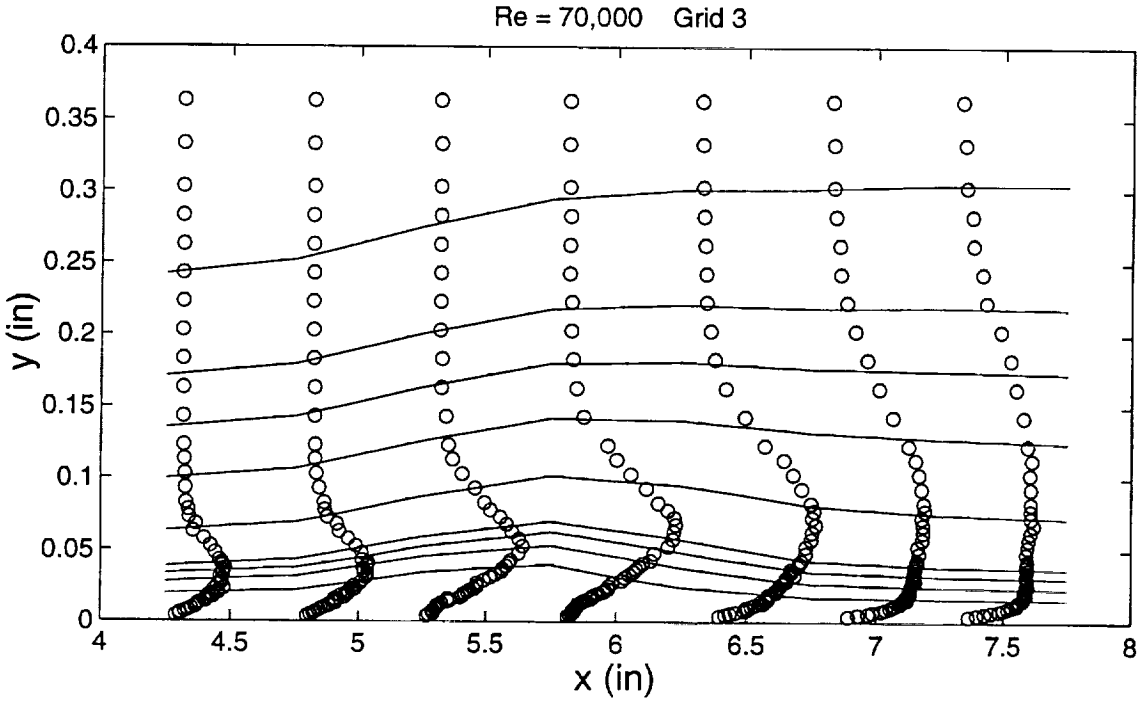

Figure 50a Distribution of u'/U_{in} around separation bubble along with streamlines for Re = 70,000, Grid 3

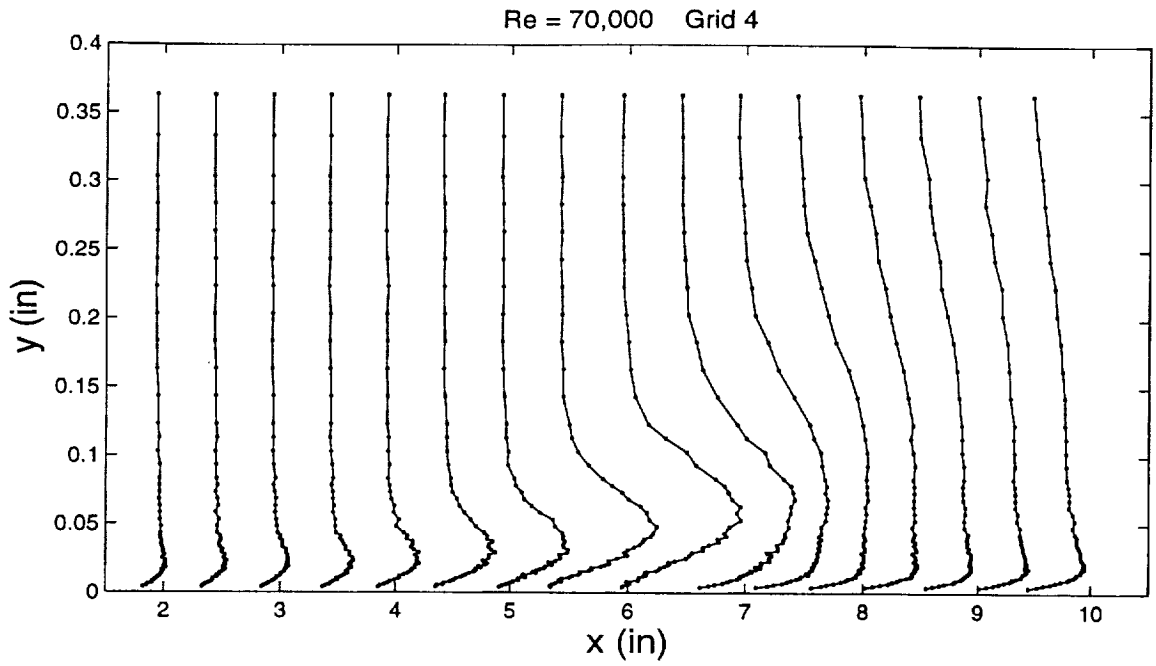

Figure 51 Distribution of u'/U_{in} for Re = 70,000, Grid 4

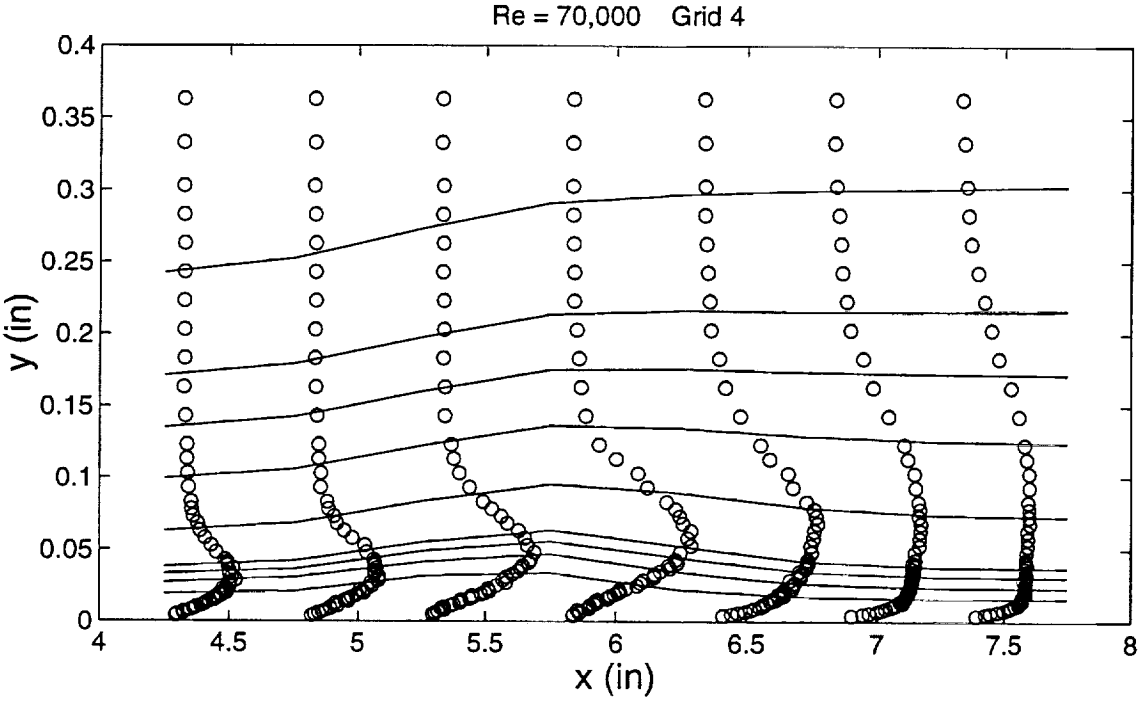

Figure 51a Distribution of u'/U_{in} around separation bubble along with streamlines for Re = 70,000, Grid 4

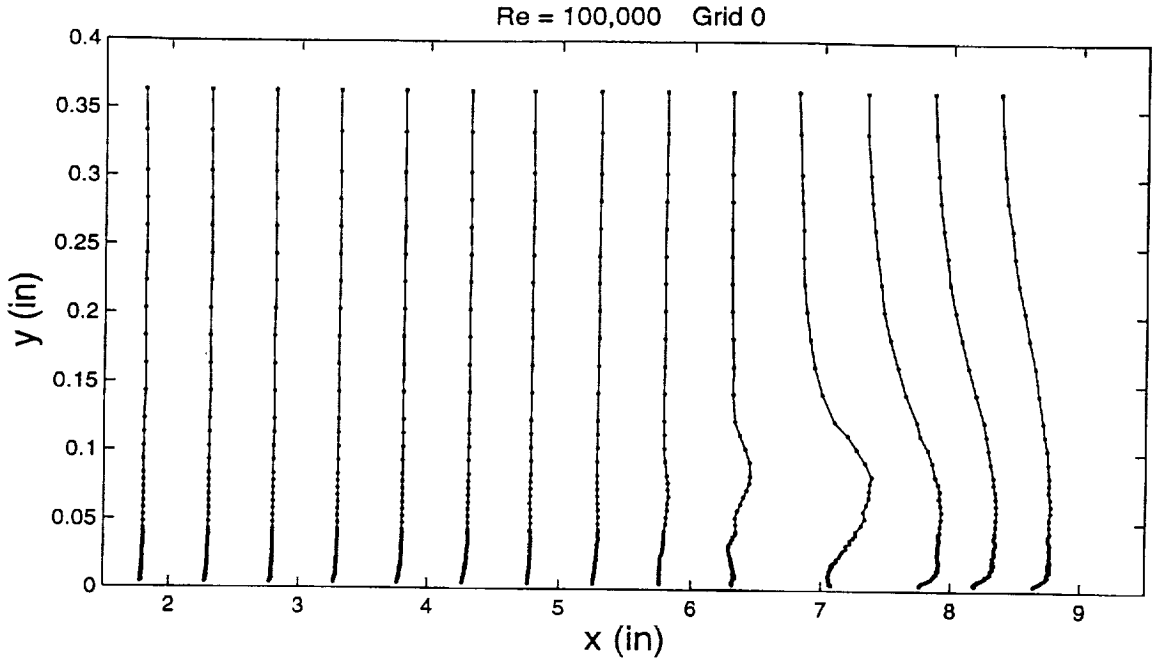

Figure 52 Distribution of u'/U_{in} for Re = 100,000, Grid 0

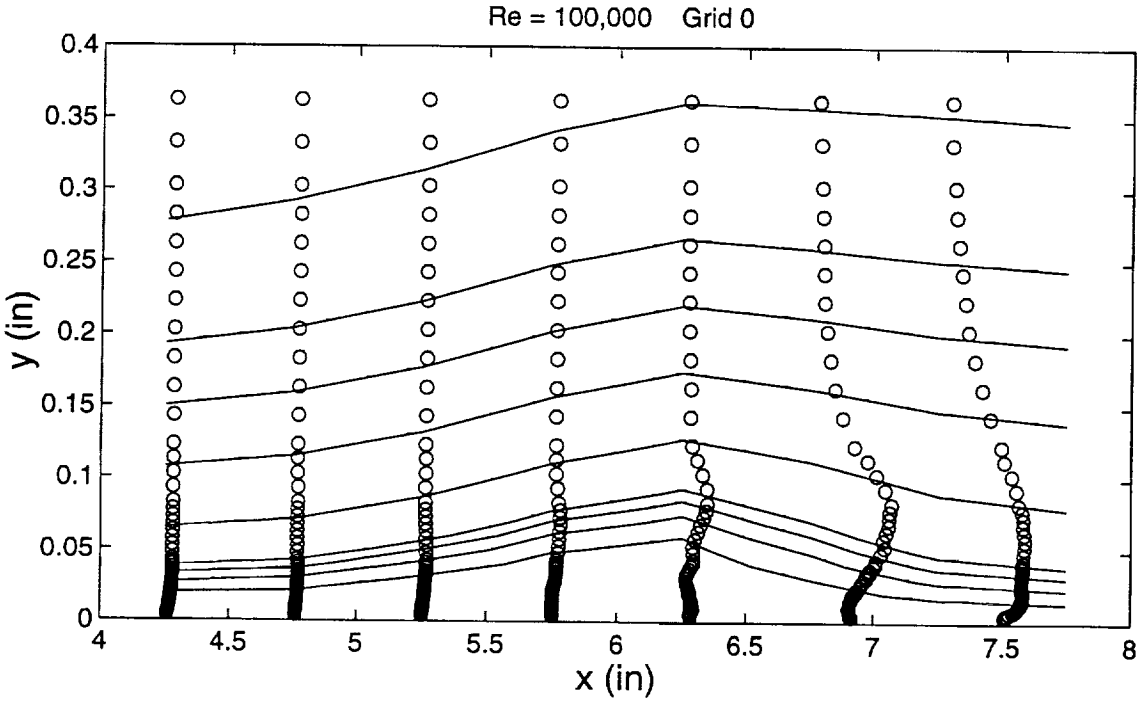

Figure 52a Distribution of u'/U_{in} around separation bubble along with streamlines for Re = 100,000, Grid 0

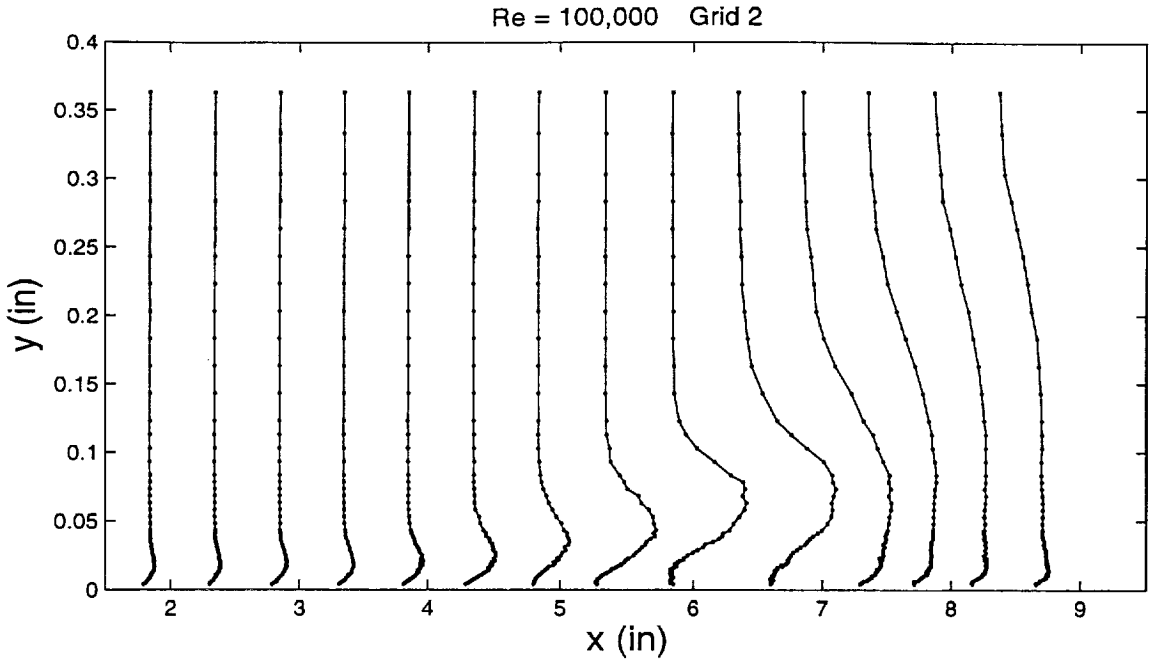

Figure 53 Distribution of u'/U_{in} for Re = 100,000, Grid 2

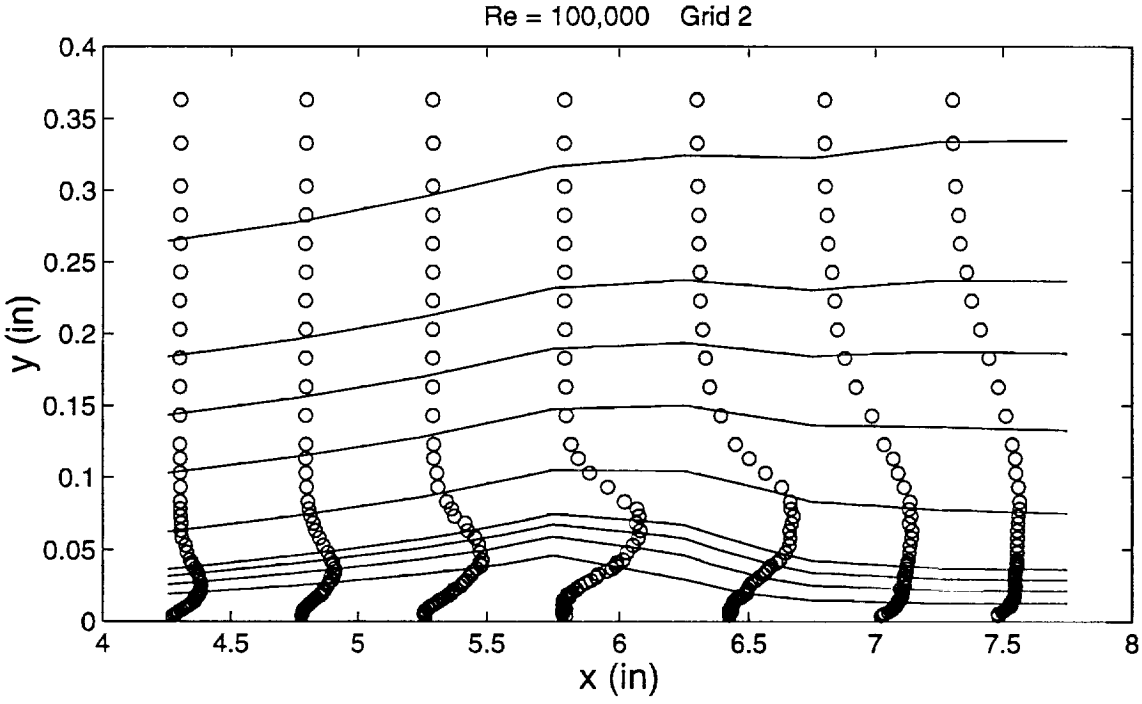

Figure 53a Distribution of u'/U_{in} around separation bubble along with streamlines for Re = 100,000, Grid 2

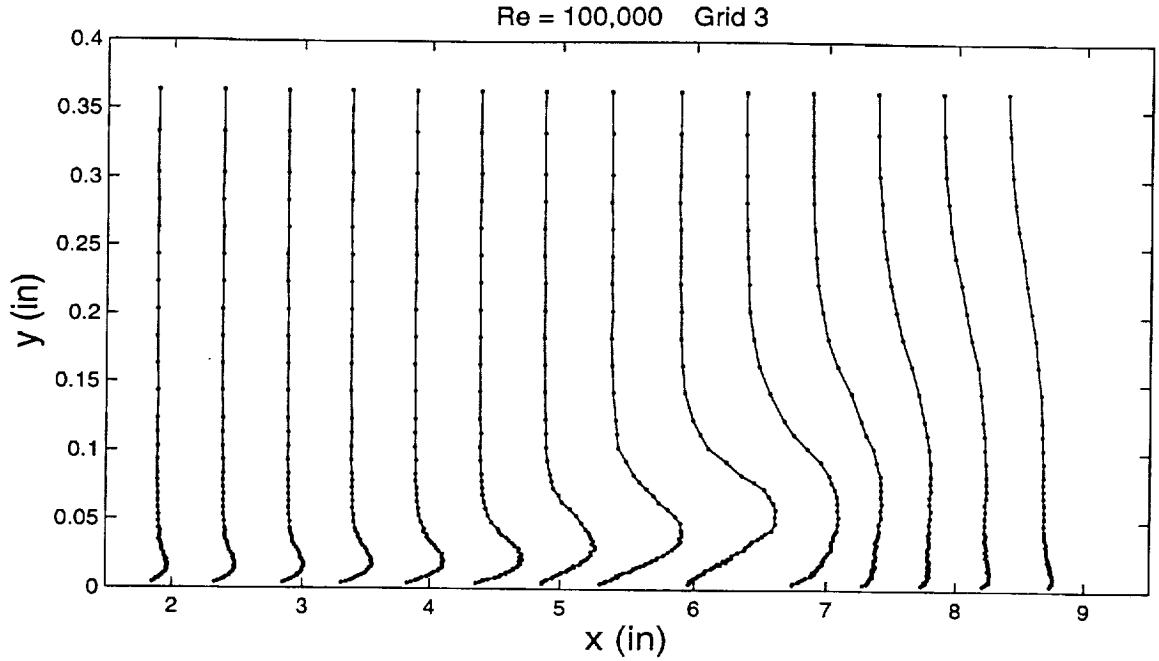

Figure 54 Distribution of u'/U_{in} for Re = 100,000, Grid 3

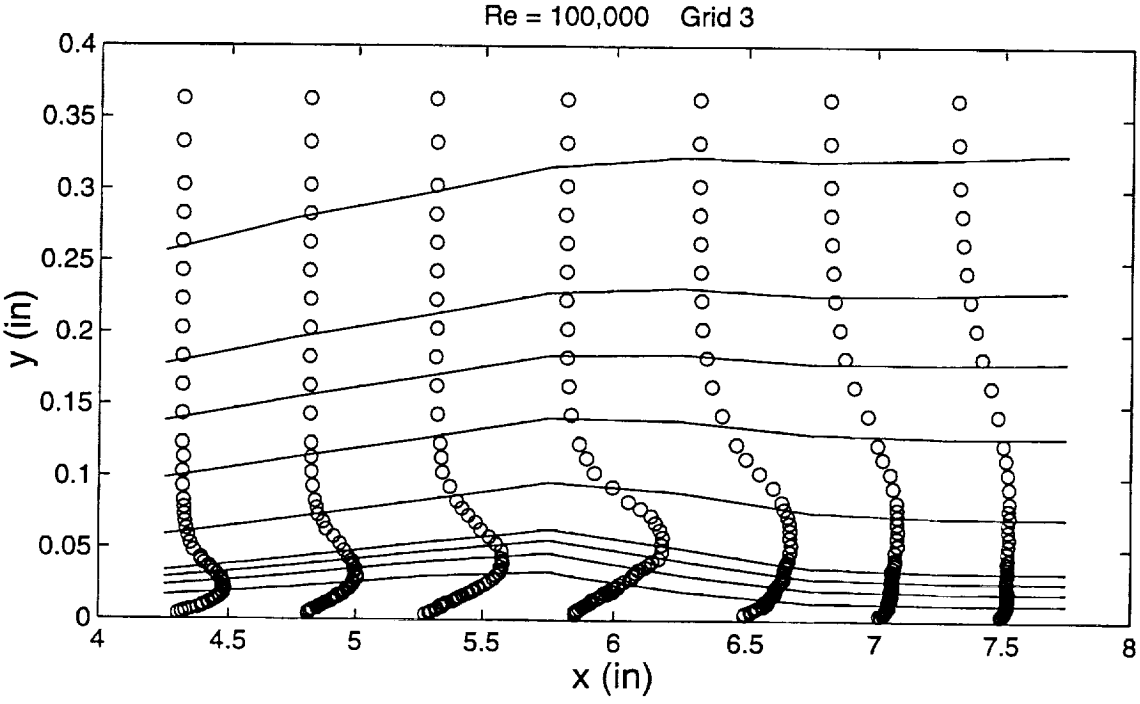

Figure 54a Distribution of u'/U_{in} around separation bubble along with streamlines for Re = 100,000, Grid 3

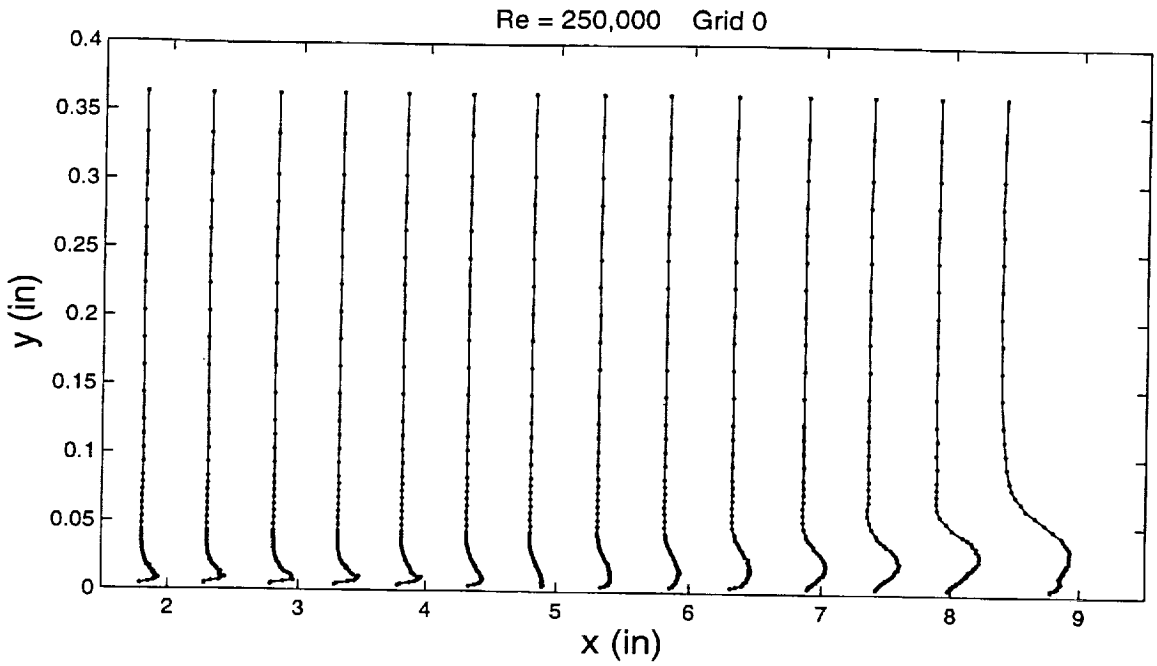

Figure 55 Distribution of u'/U_{in} for Re = 250,000, Grid 0

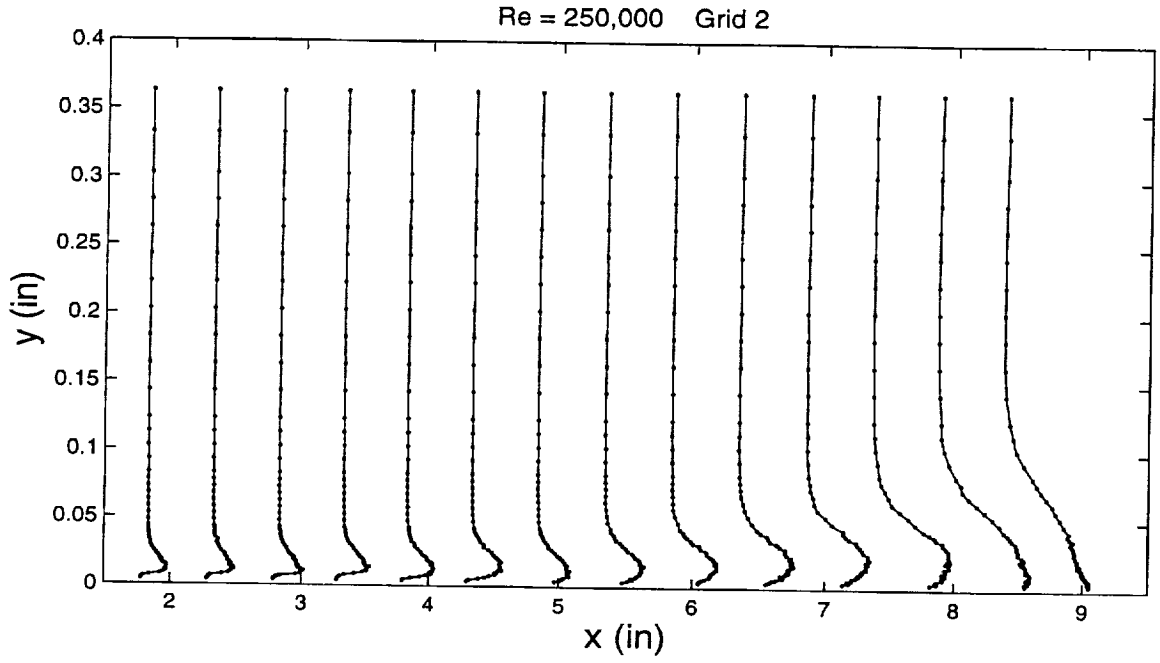

Figure 56 Distribution of u'/U_{in} for Re = 250,000, Grid 2

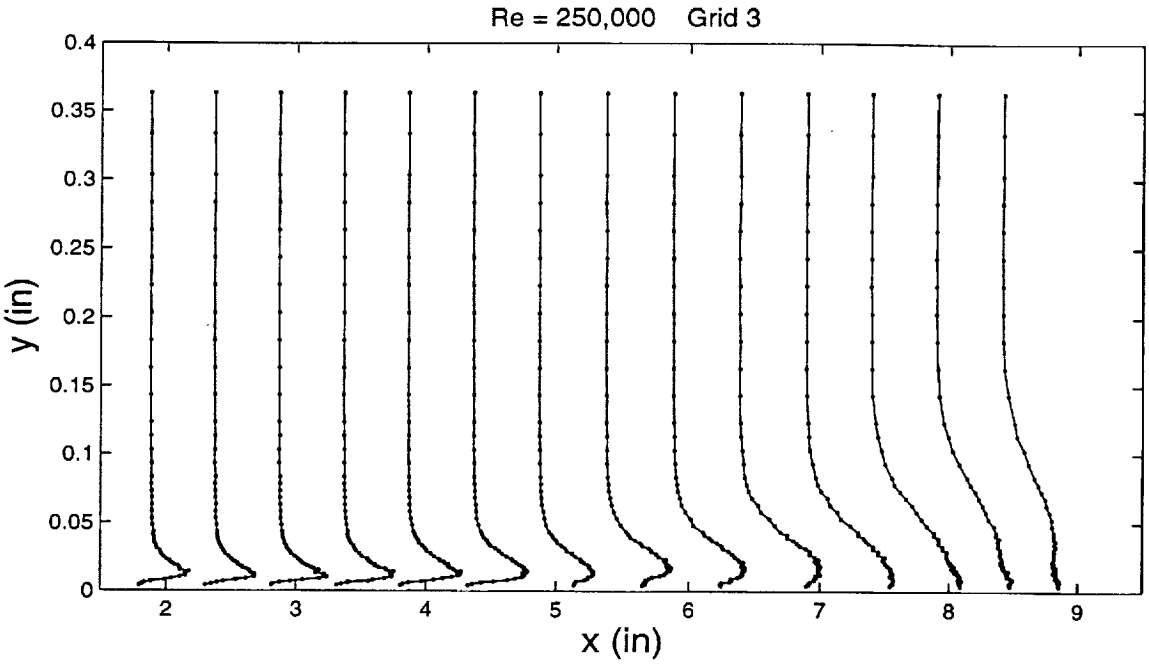

Figure 57 Distribution of u'/U_{in} for Re = 250,000, Grid 3

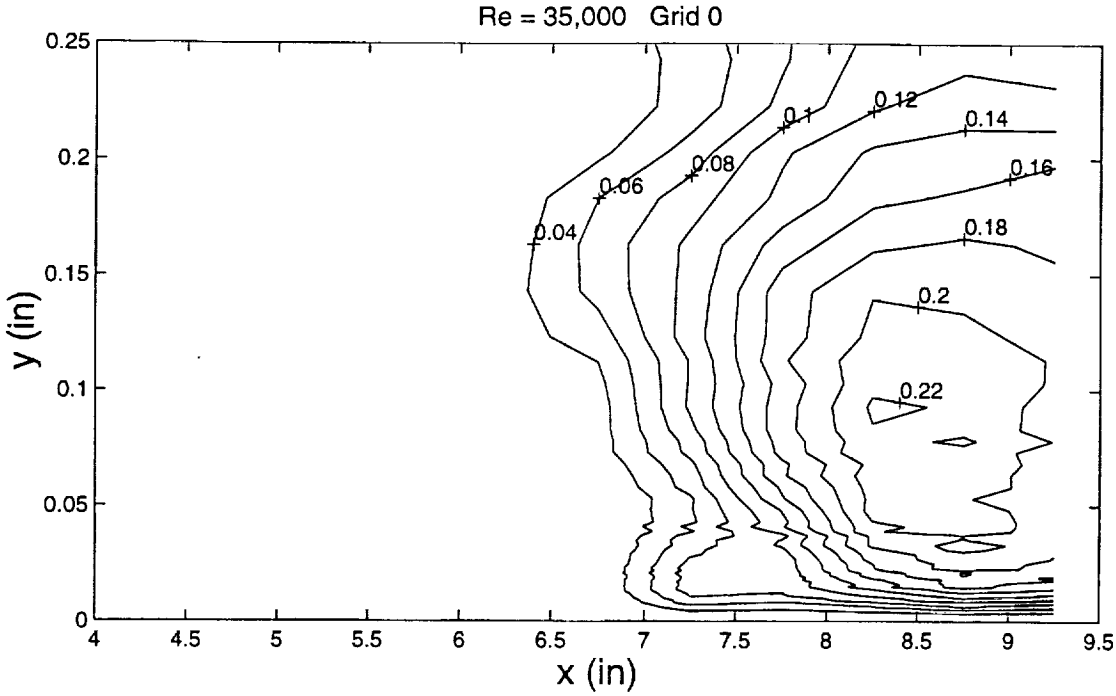

Figure 58 Contour plots of u'/U_{in} for Re = 35,000, Grid 0

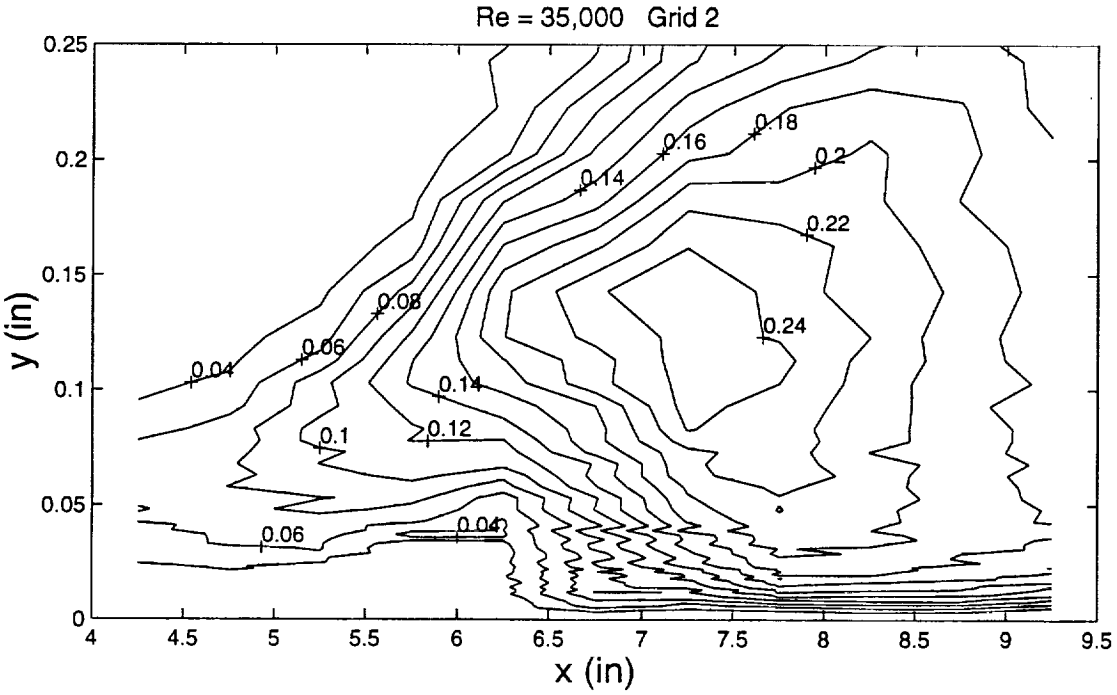

Figure 59 Contour plots of u'/U_{in} for Re = 35,000, Grid 2

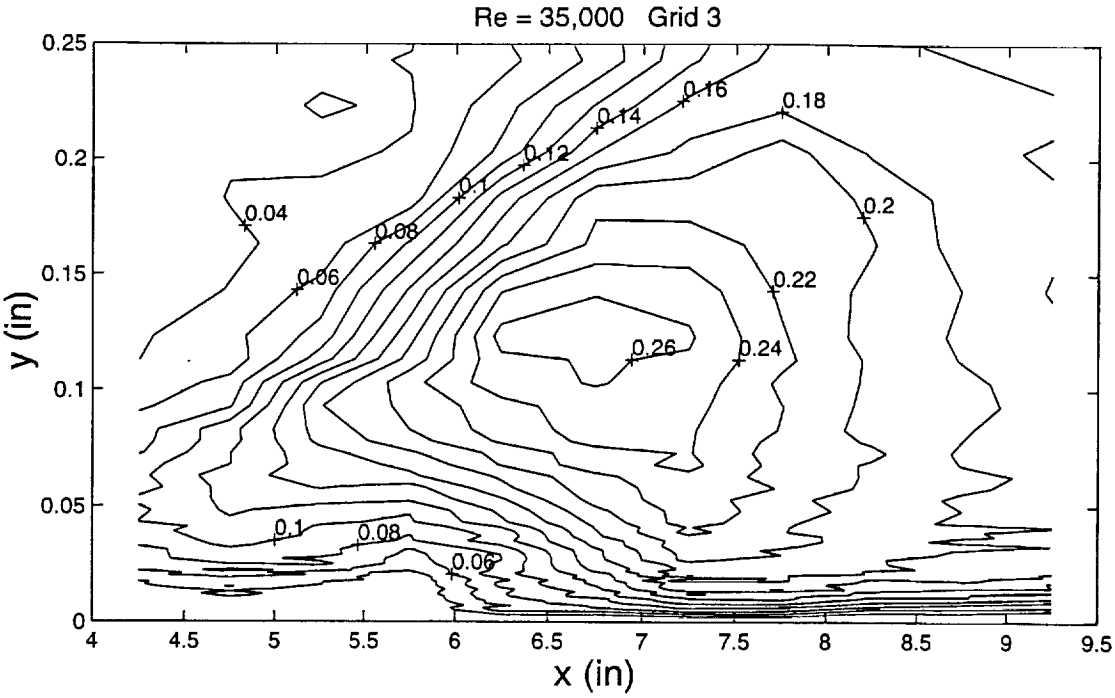

Figure 60 Contour plots of u'/U_{in} for Re = 35,000, Grid 3

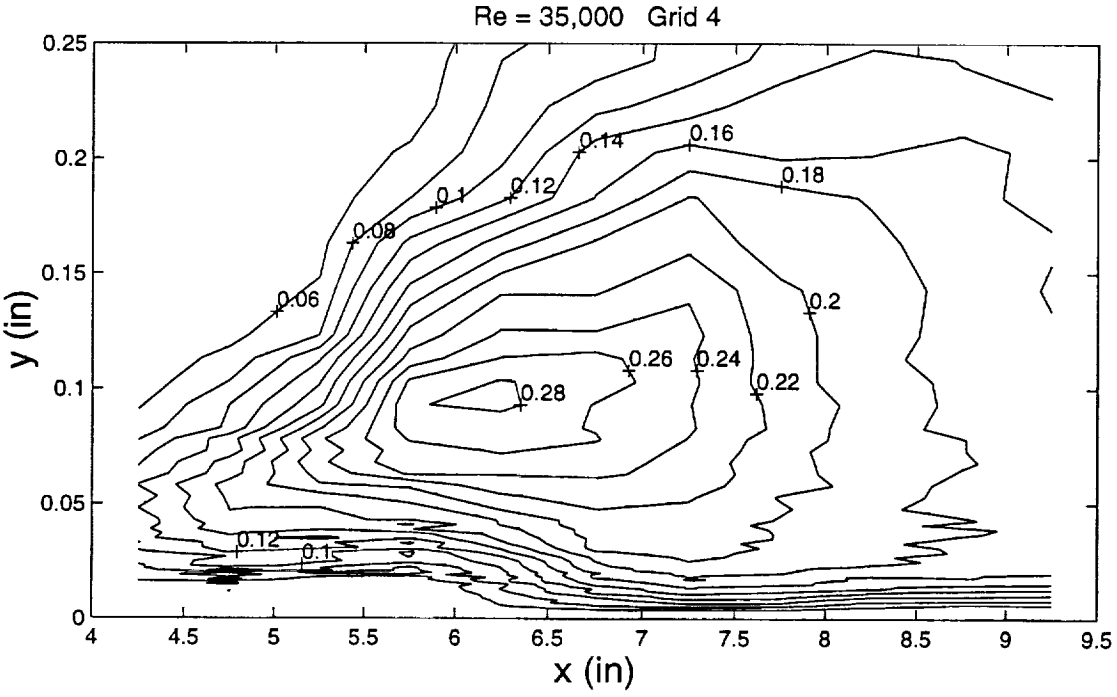

Figure 61 Contour plots of u'/U_{in} for Re = 35,000, Grid 4

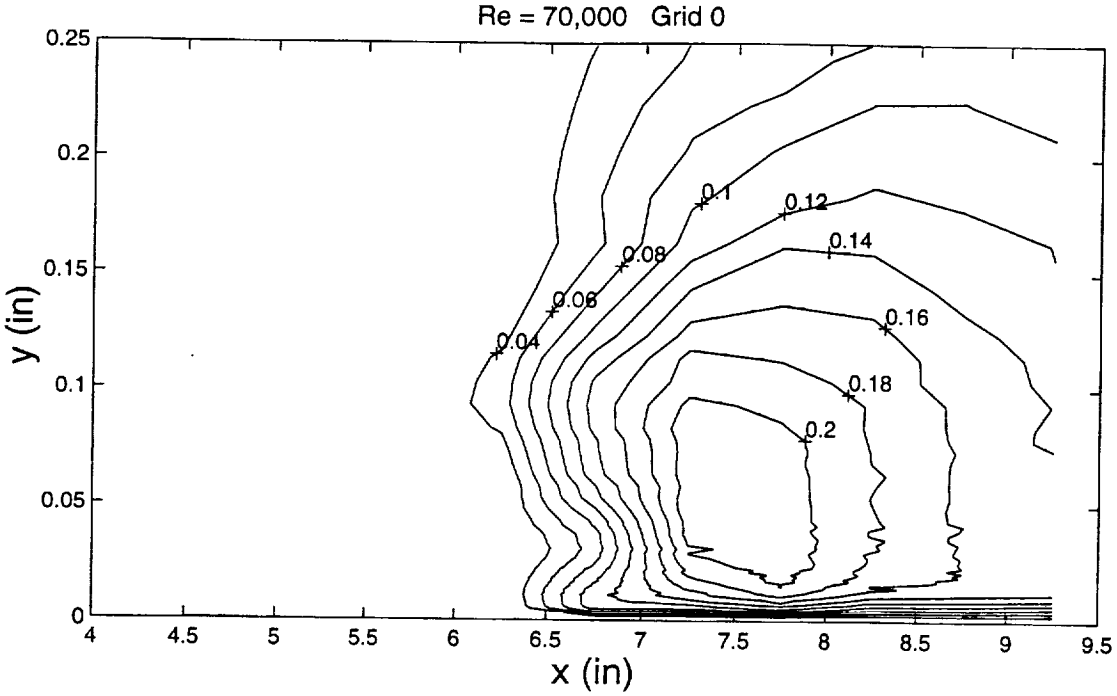

Figure 62 Contour plots of u'/U_{in} for Re = 70,000, Grid 0

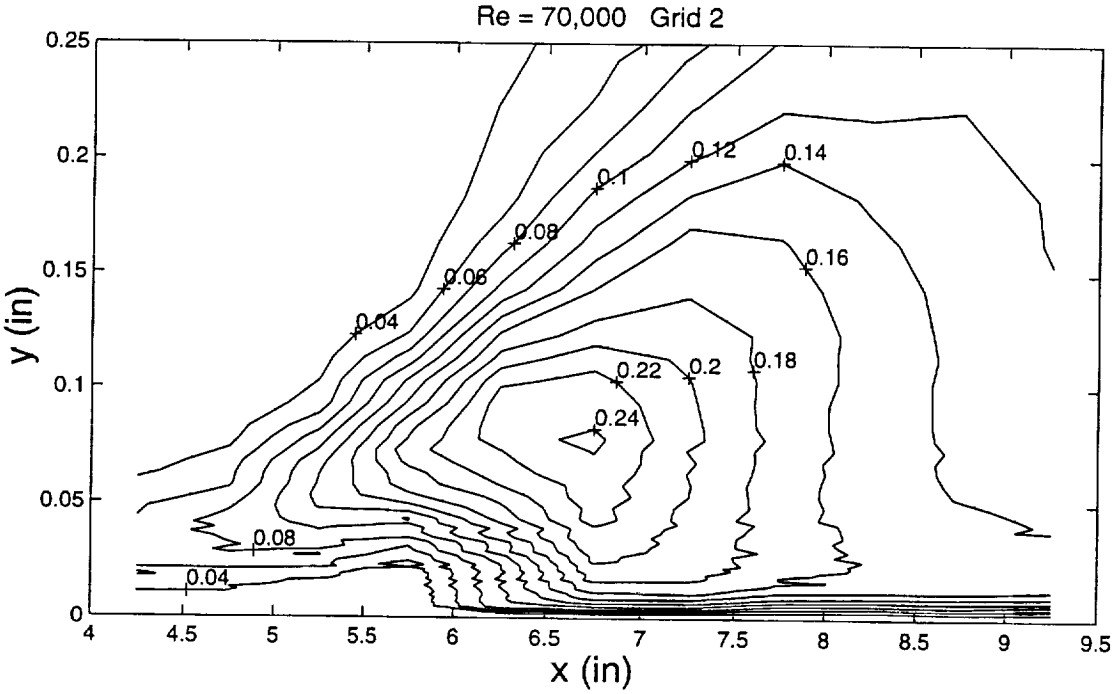

Figure 63 Contour plots of u'/U_{in} for Re = 70,000, Grid 2

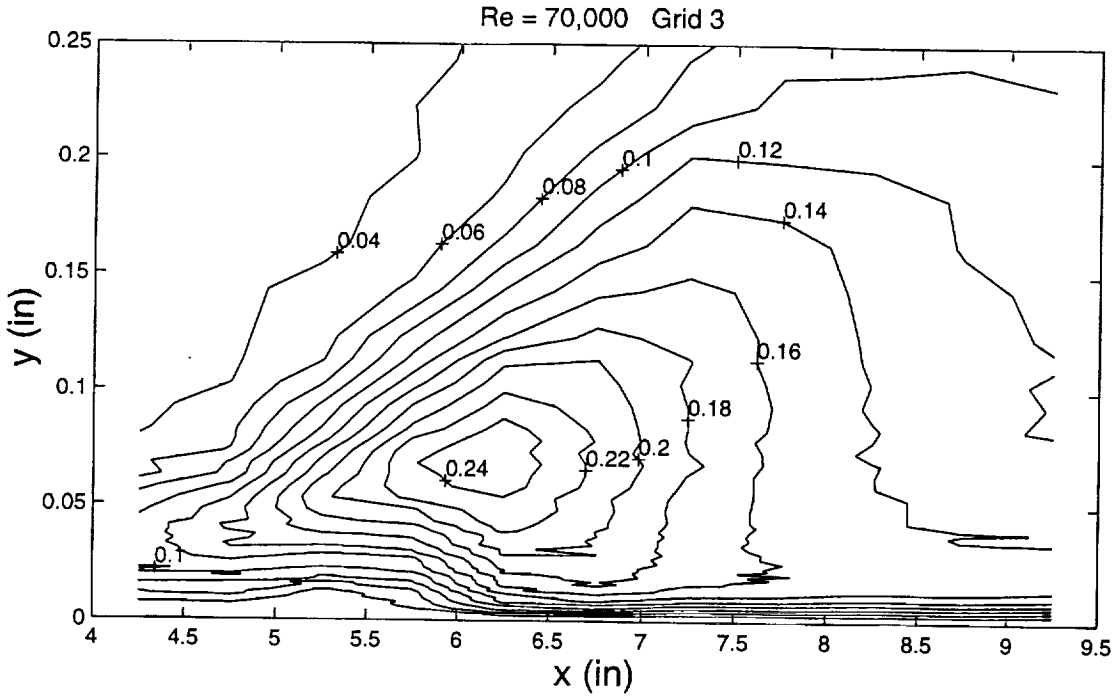

Figure 64 Contour plots of u'/U_{in} for Re = 70,000, Grid 3

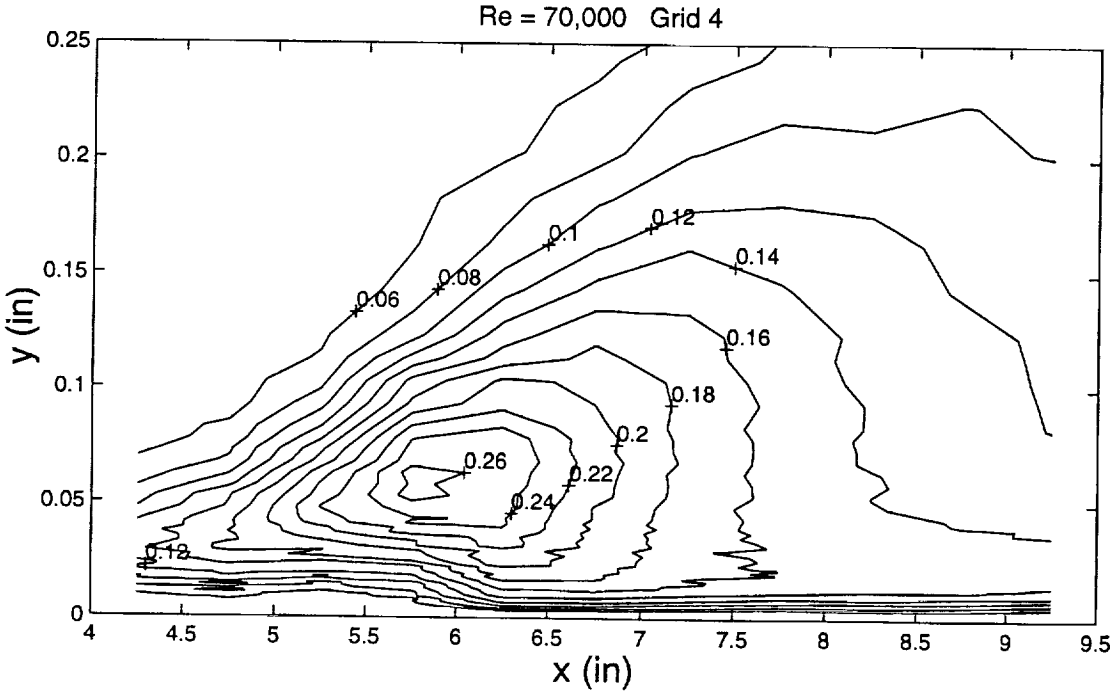

Figure 65 Contour plots of u'/U_{in} for Re = 70,000, Grid 4

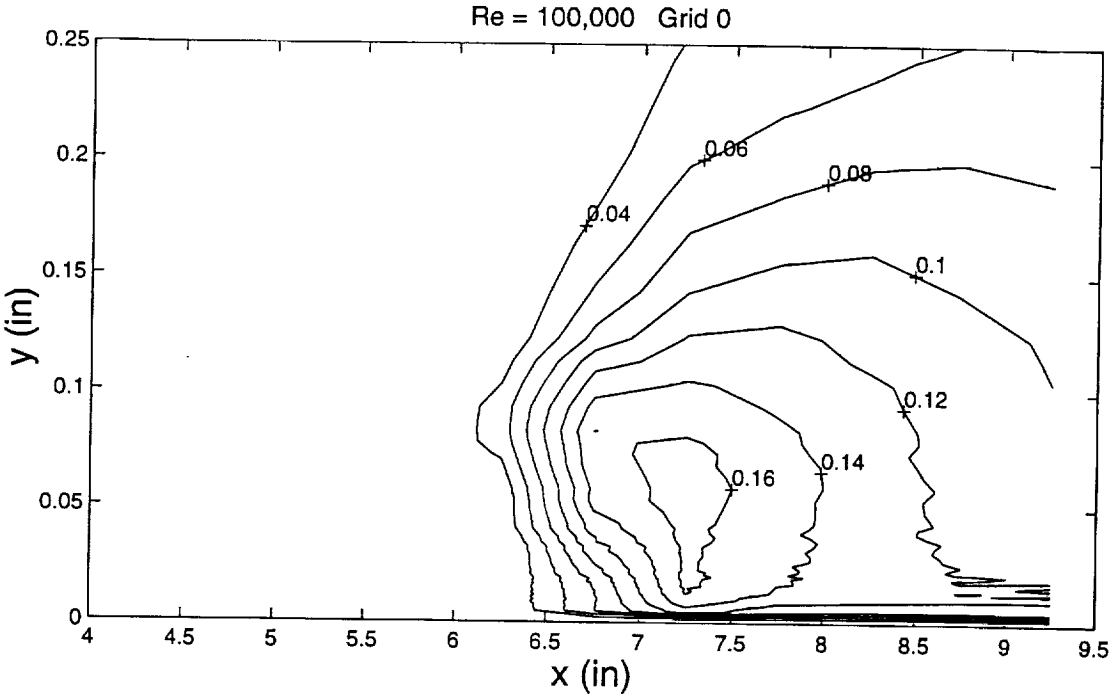

Figure 66 Contour plots of u'/U_{in} for Re = 100,000, Grid 0

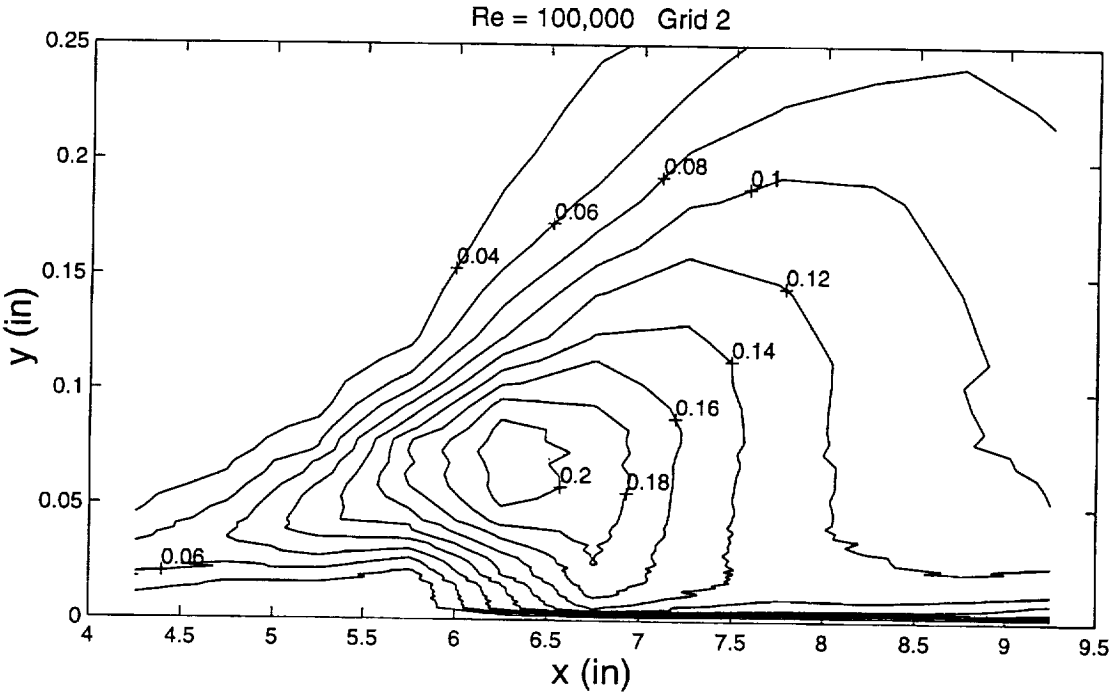

Figure 67 Contour plots of u'/U_{in} for Re = 100,000, Grid 2

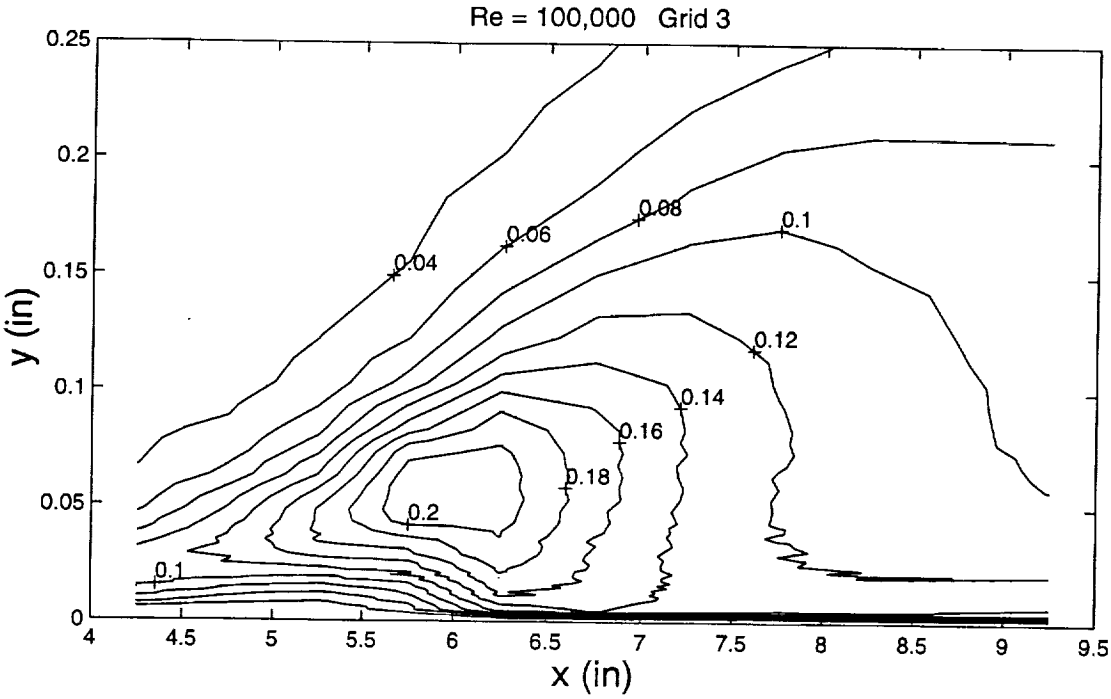

Figure 68 Contour plots of u'/U_{in} for Re = 100,000, Grid 3

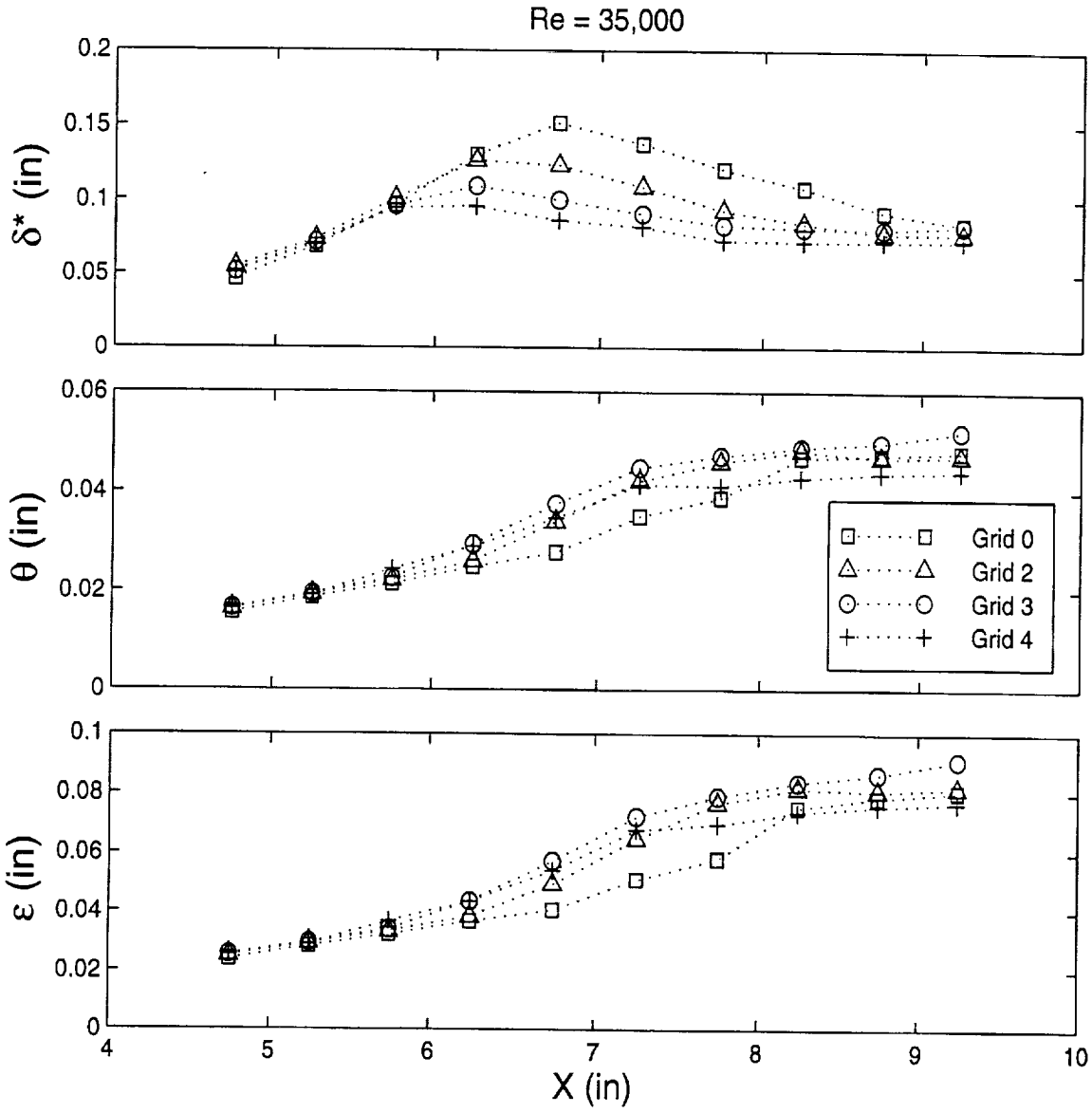

Figure 69 Variation of integral quantities, displacement thickness (δ^*), momentum thickness (θ) and energy thickness (ε), for Re = 35,000

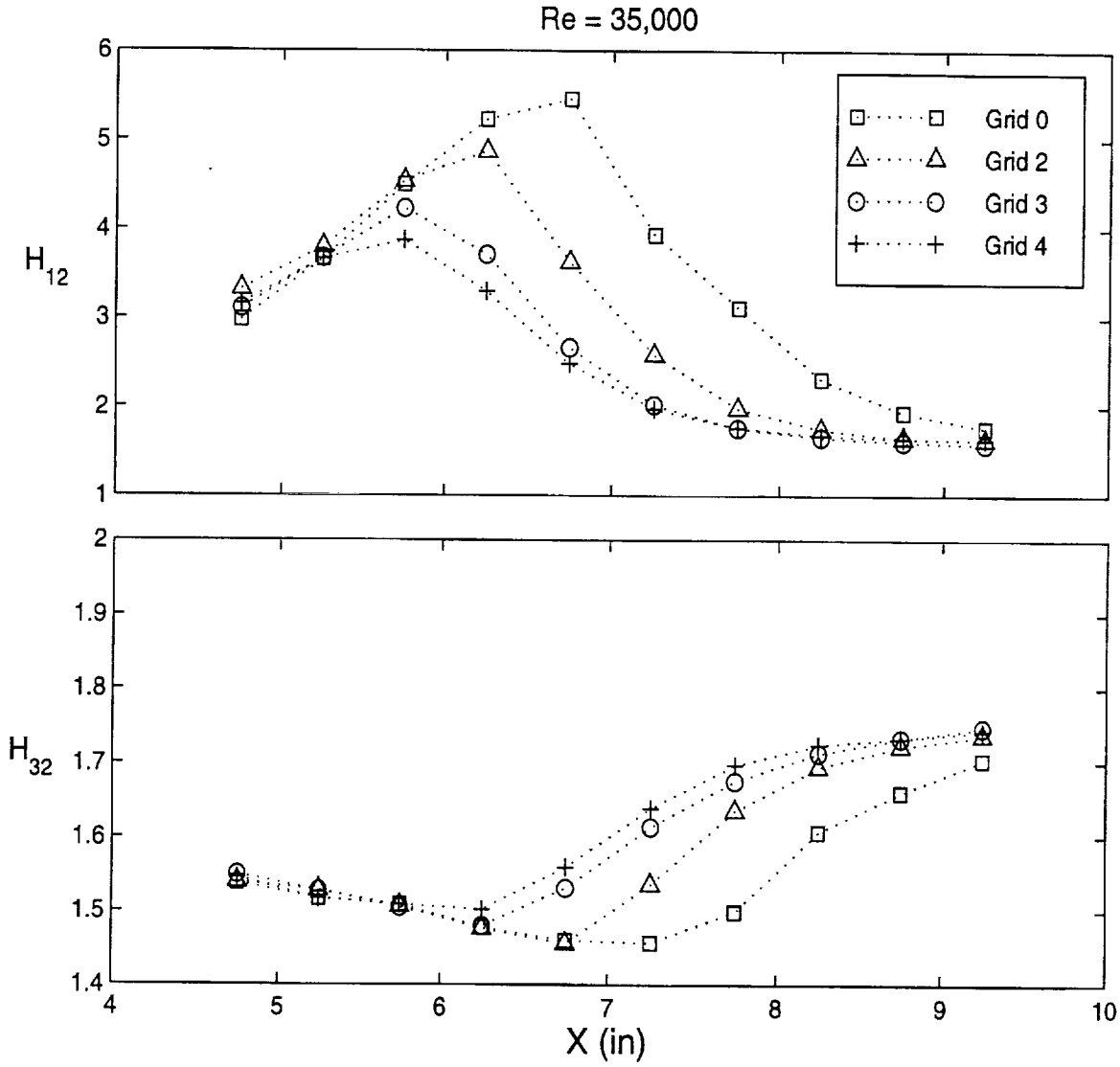

Figure 70 Variation of shape factors, H_{12} (= δ^*/θ) and H_{32} (= ε/θ), for Re = 35,000

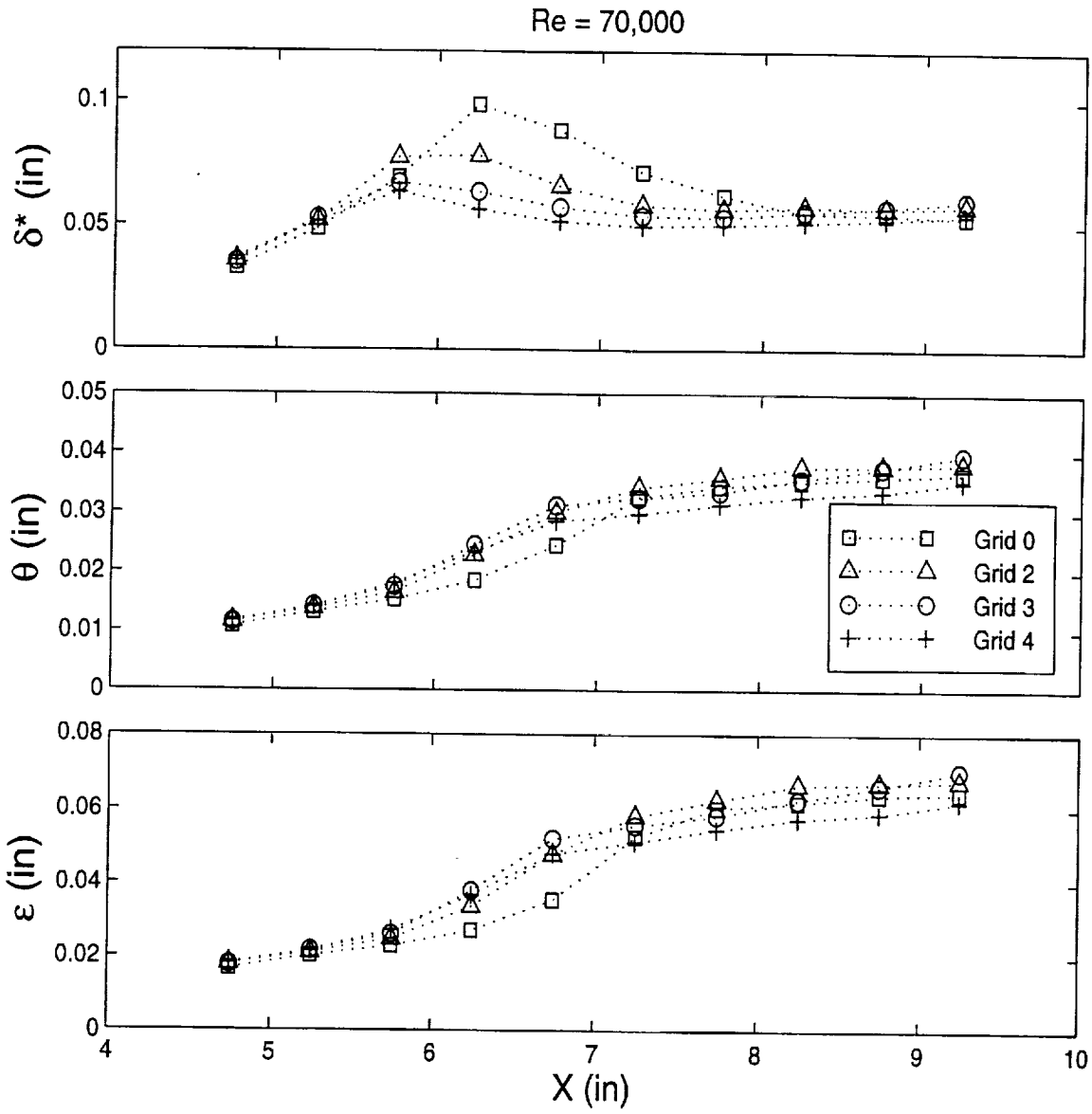

Figure 71 Variation of integral quantities, displacement thickness (δ^*), momentum thickness (θ) and energy thickness (ε), for Re = 70,000

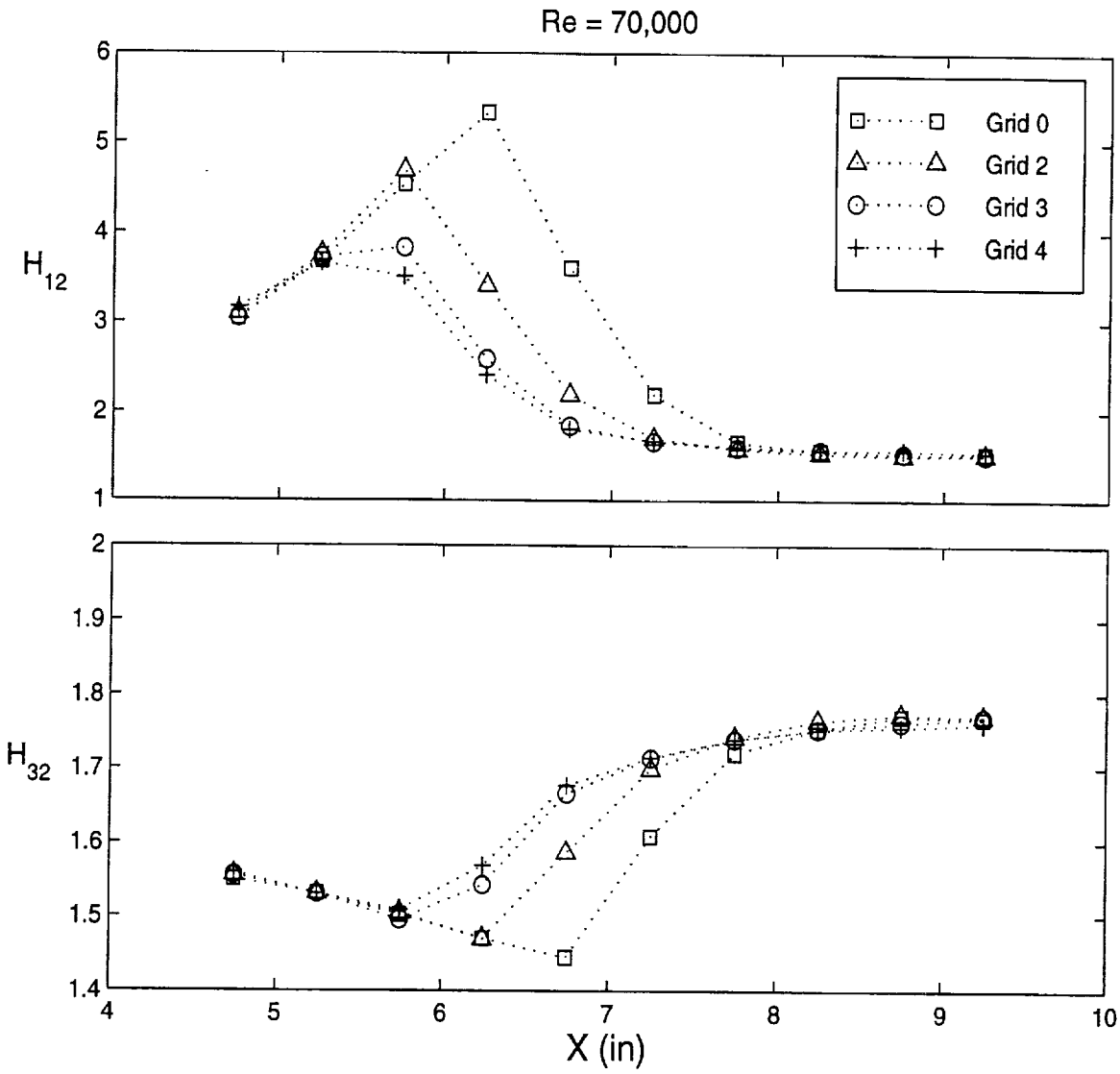

Figure 72 Variation of shape factors, H_{12} (= δ^*/θ) and H_{32} (= ε/θ), for Re = 70,000

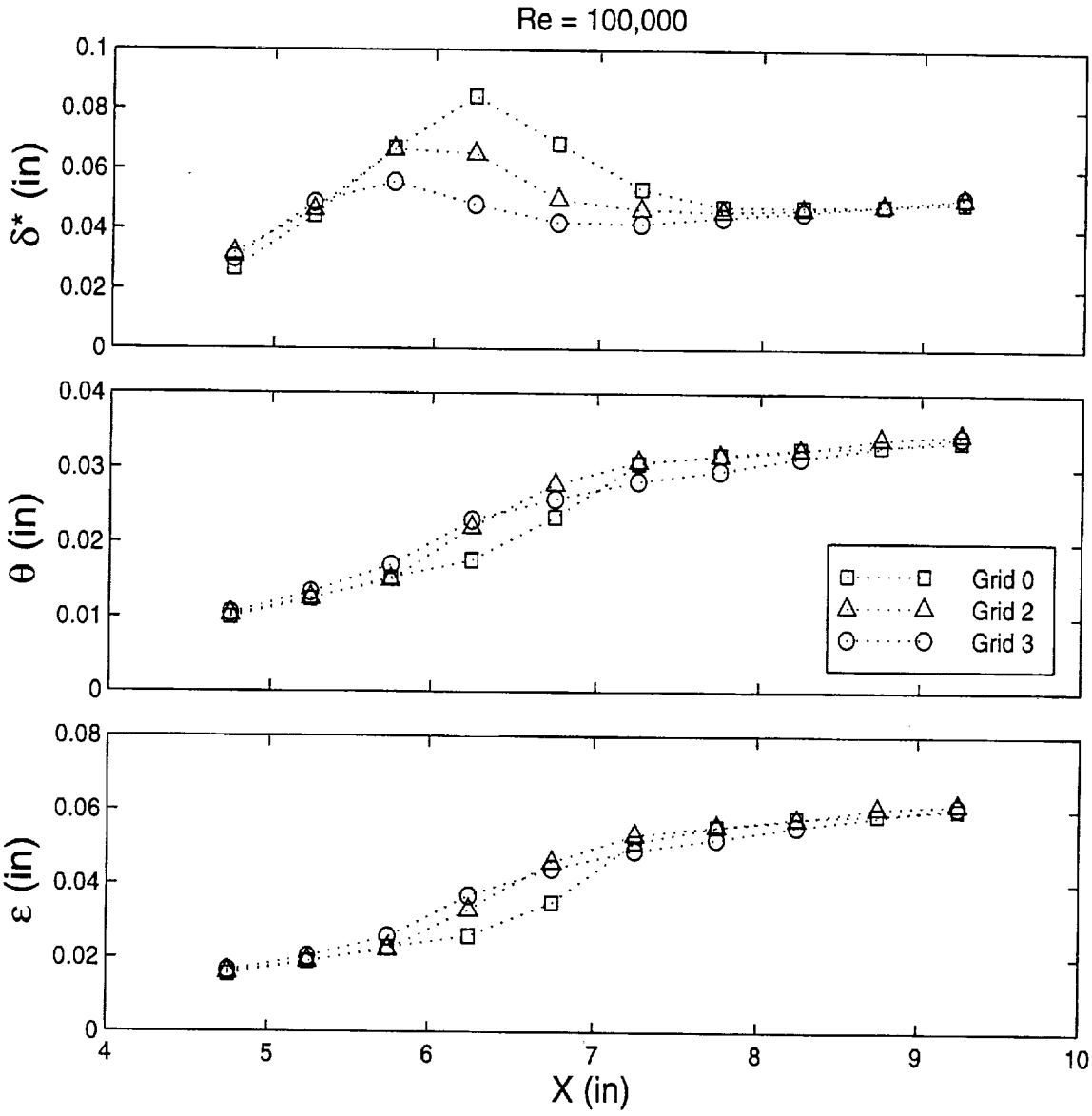

Figure 73 Variation of integral quantities, displacement thickness (δ^*), momentum thickness (θ) and energy thickness (ε), for Re = 100,000

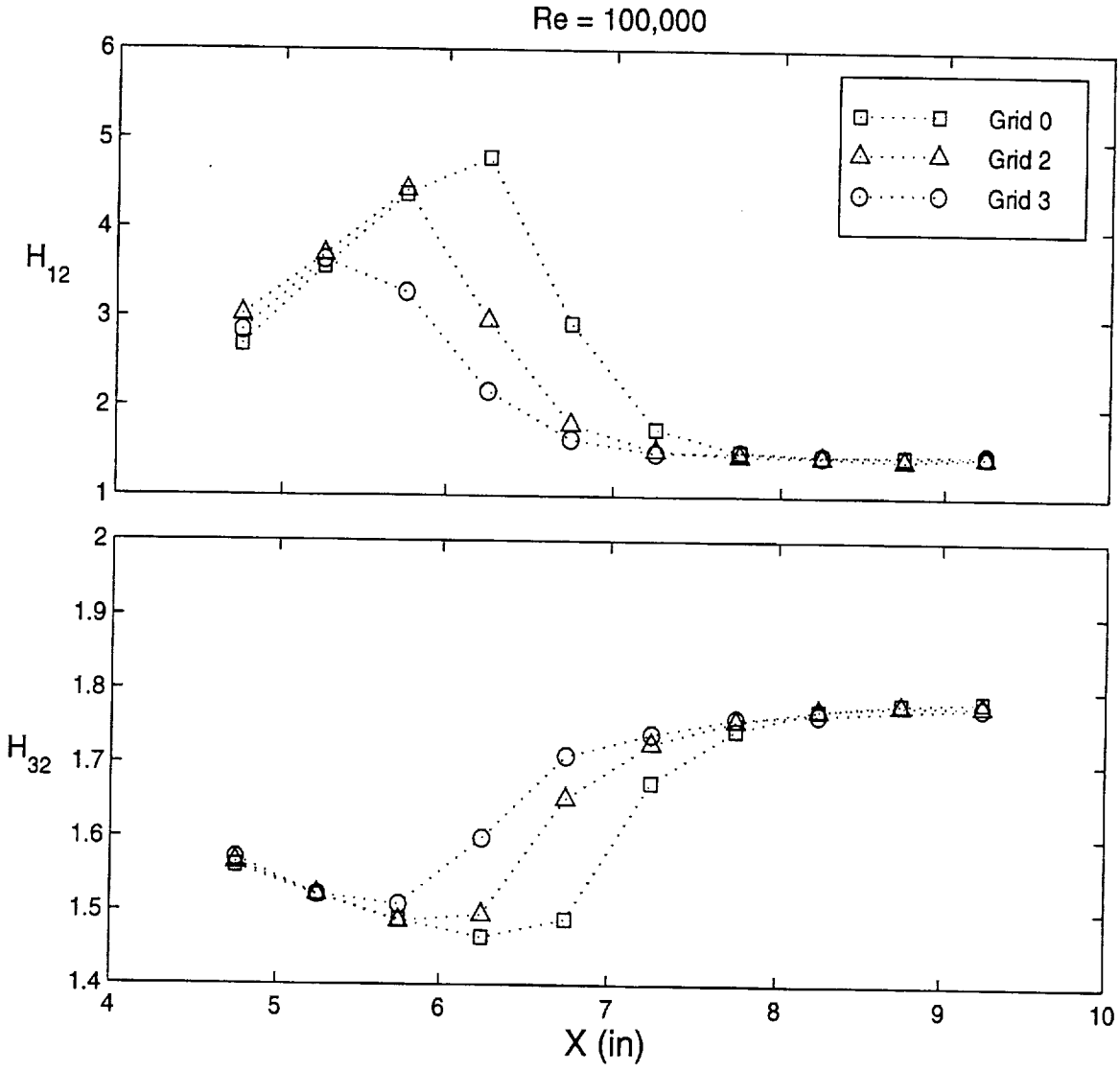

Figure 74 Variation of shape factors, H_{12} (= δ^*/θ) and H_{32} (= ε/θ), for Re = 100,000

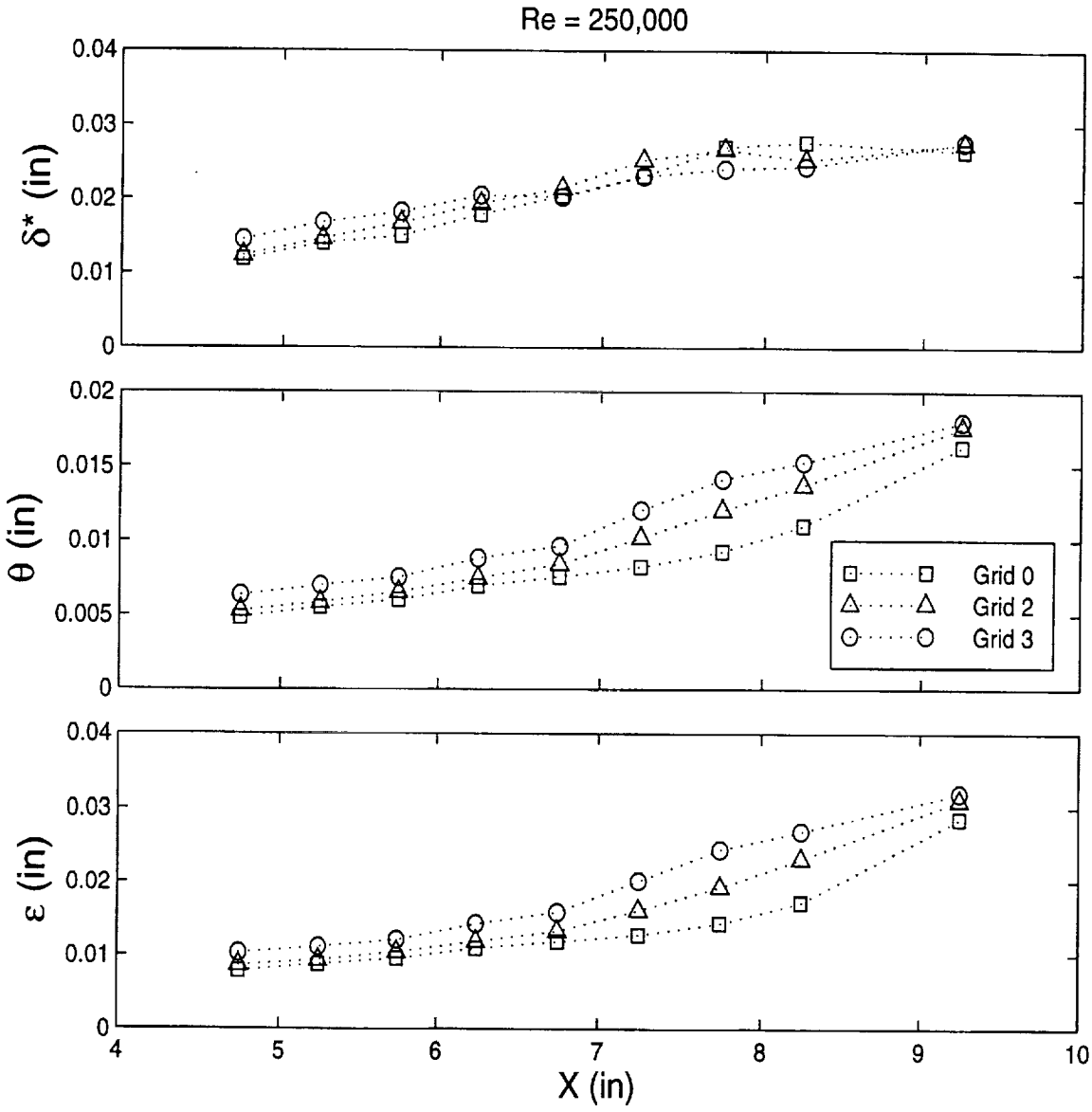

Figure 75 Variation of integral quantities, displacement thickness (δ^*), momentum thickness (θ) and energy thickness (ε), for Re = 250,000

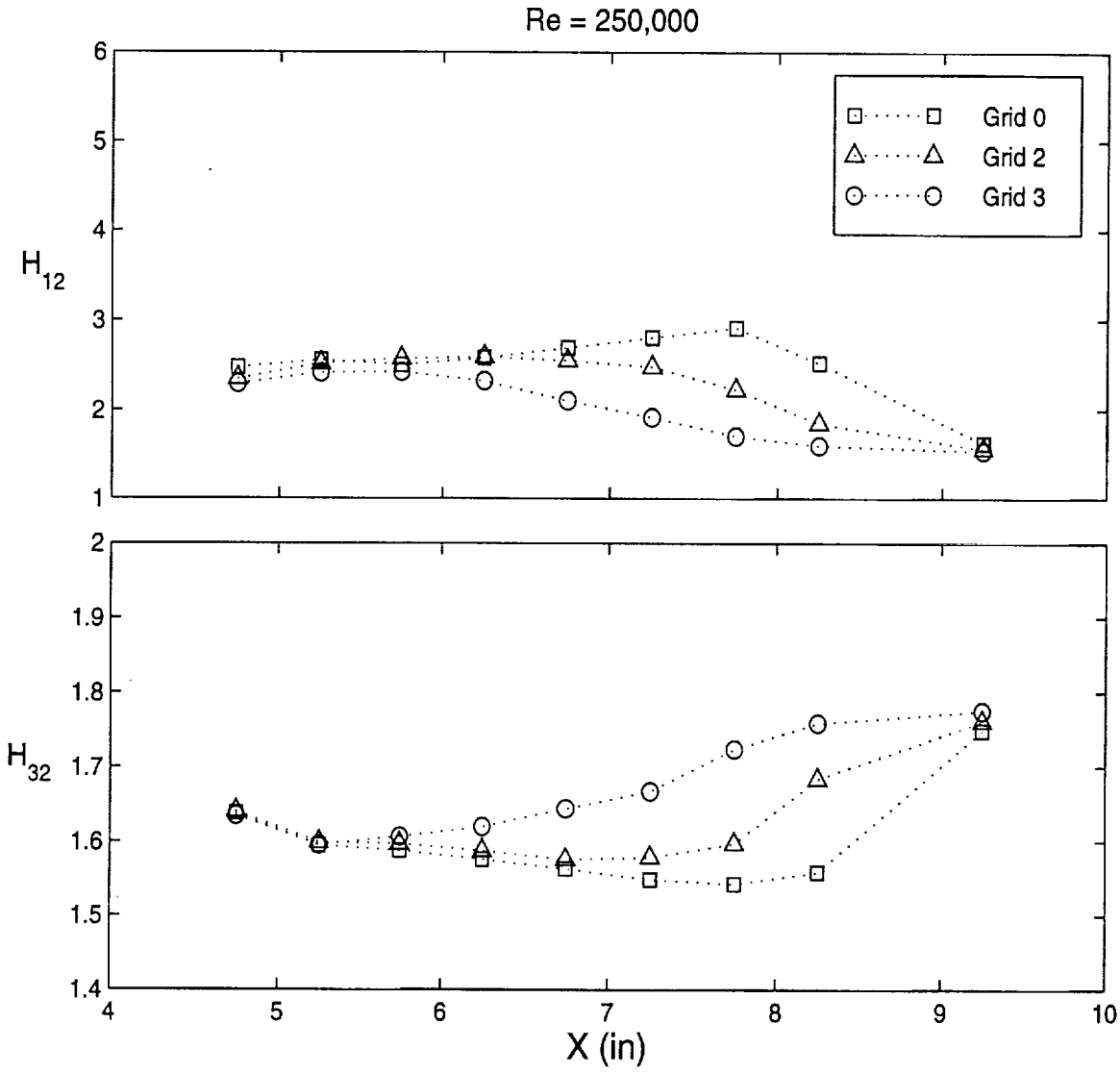

Figure 76 Variation of shape factors, H_{12} (= δ^*/θ) and H_{32} (= ε/θ), for Re = 250,000

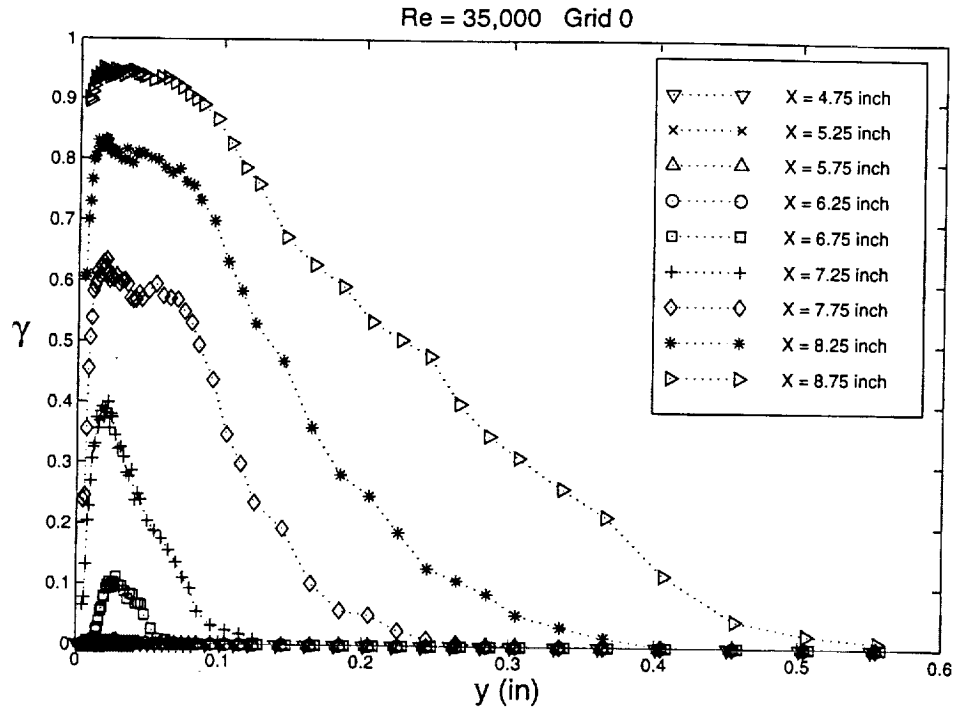

Figure 77 Variation of intermittency in normal direction, y, for Re = 35,000, Grid 0

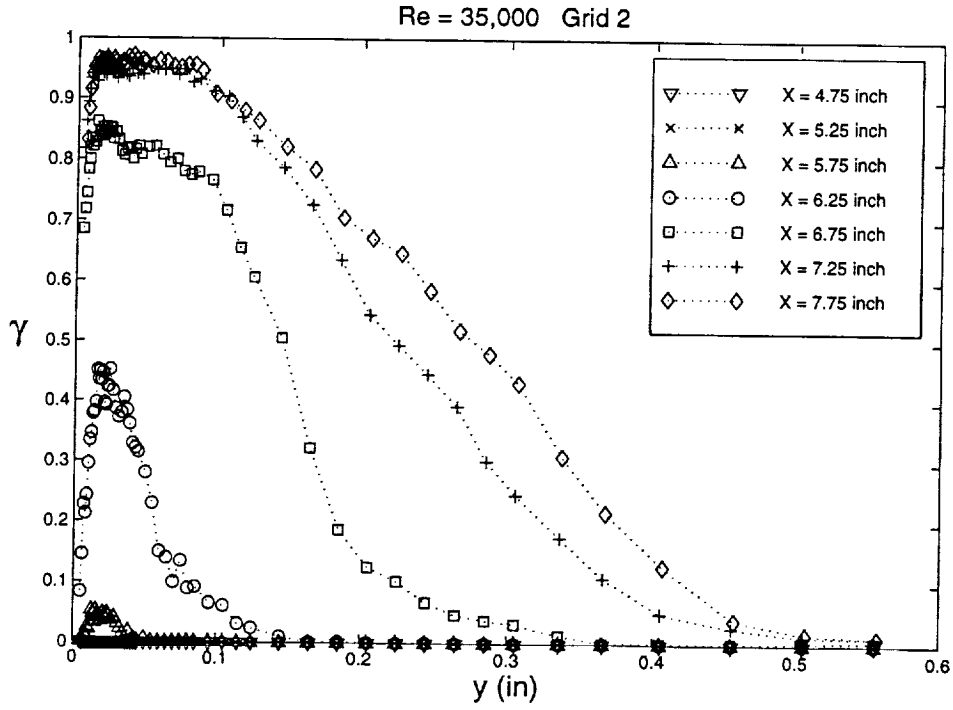

Figure 78 Variation of intermittency in normal direction, y, for Re = 35,000, Grid 2

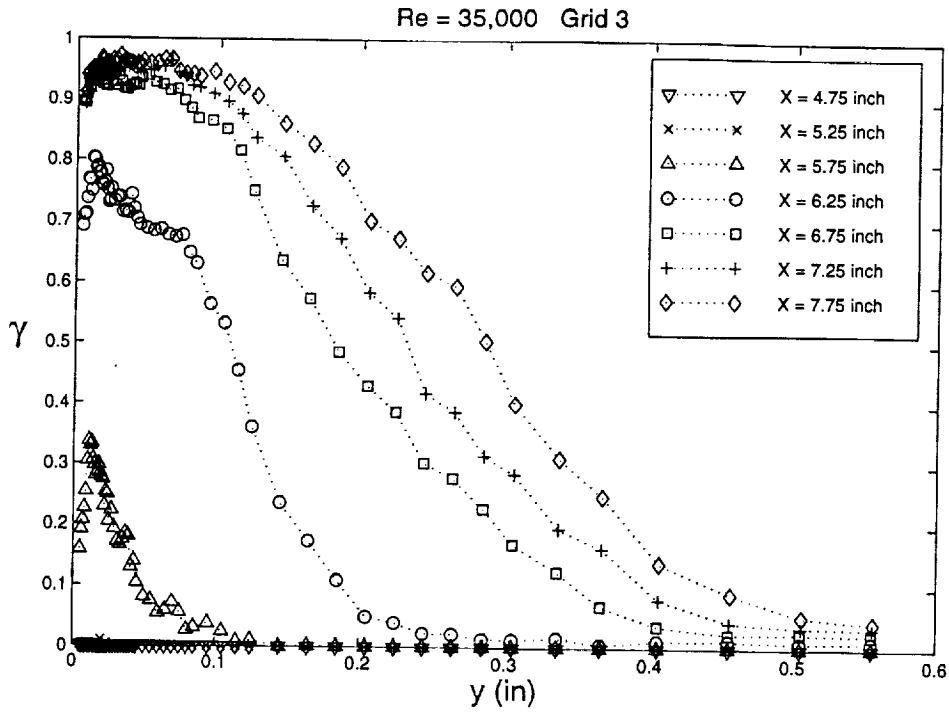

Figure 79 Variation of intermittency in normal direction, y, for Re = 35,000, Grid 3

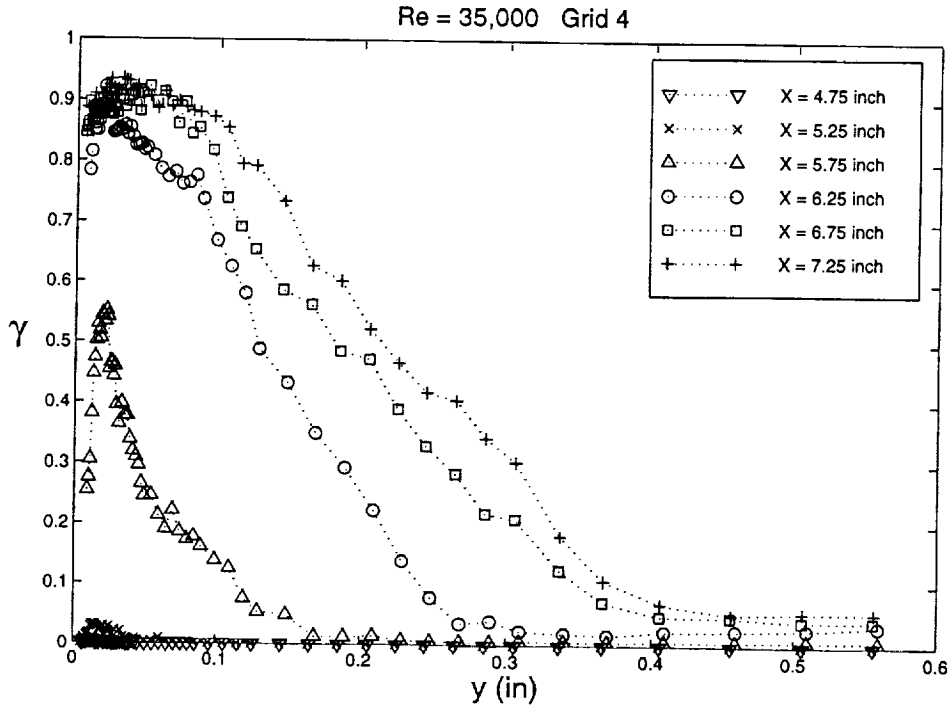

Figure 80 Variation of intermittency in normal direction, y, for Re = 35,000, Grid 4

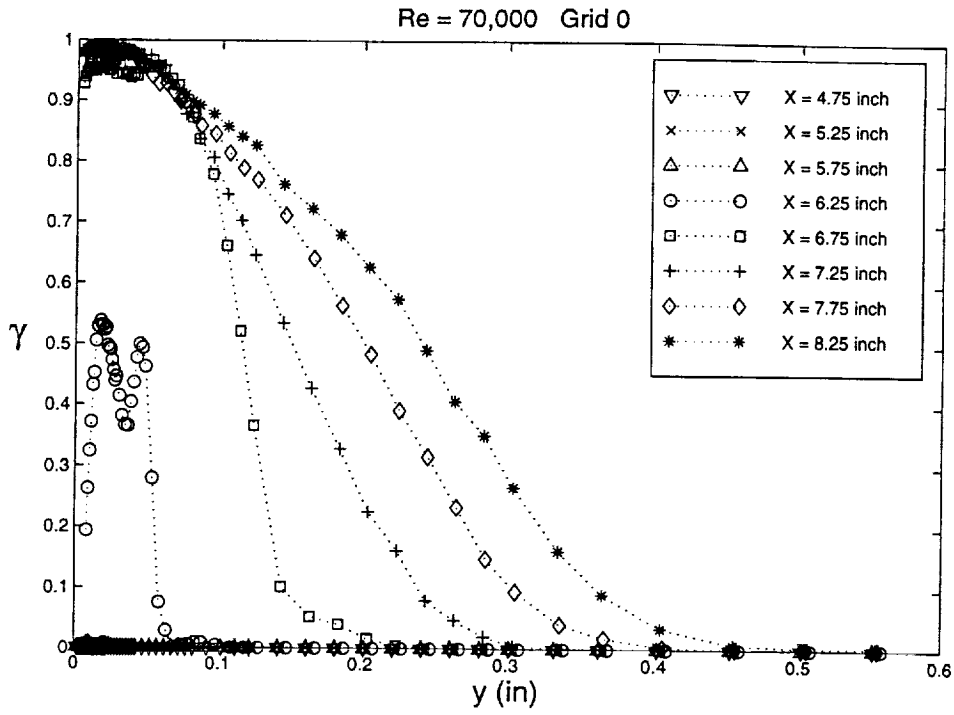

Figure 81 Variation of intermittency in normal direction, y, for Re = 70,000, Grid 0

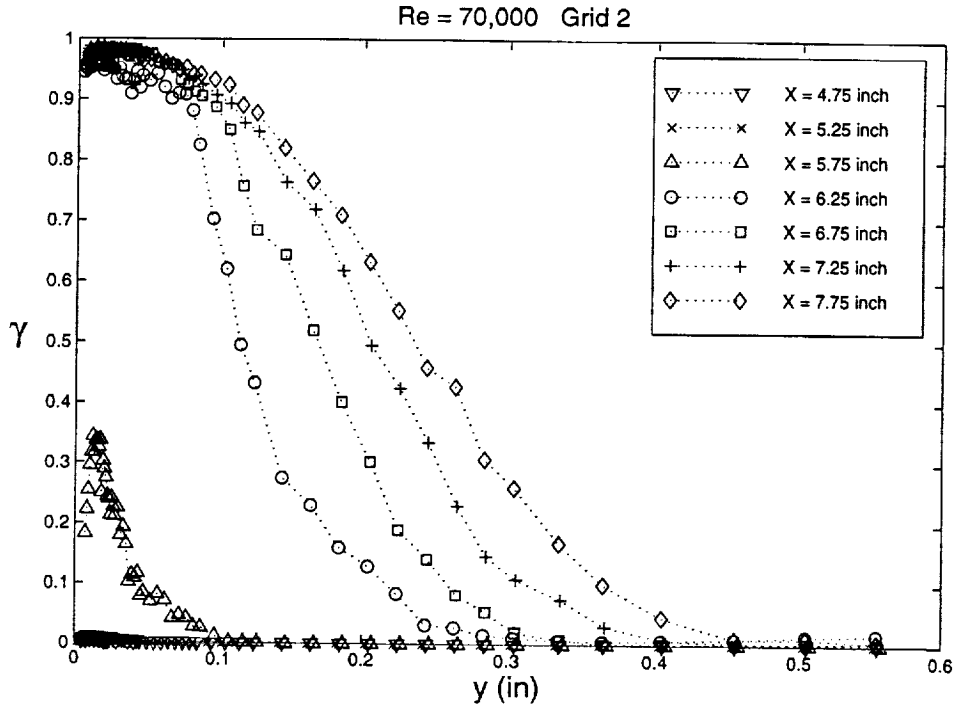

Figure 82 Variation of intermittency in normal direction, y, for Re = 70,000, Grid 2

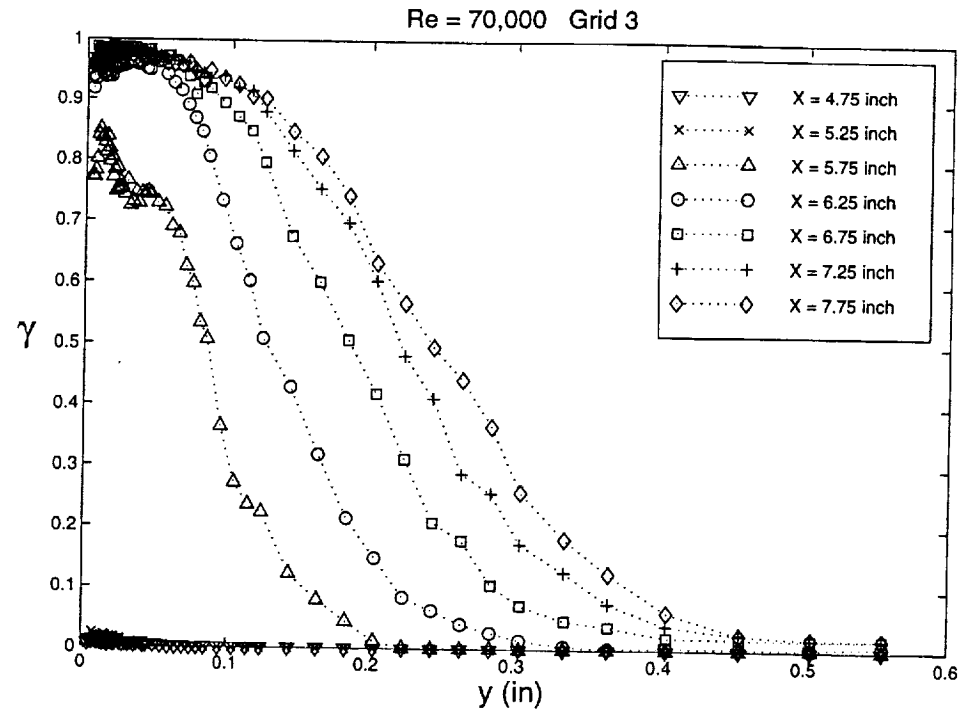

Figure 83 Variation of intermittency in normal direction, y, for Re = 70,000, Grid 3

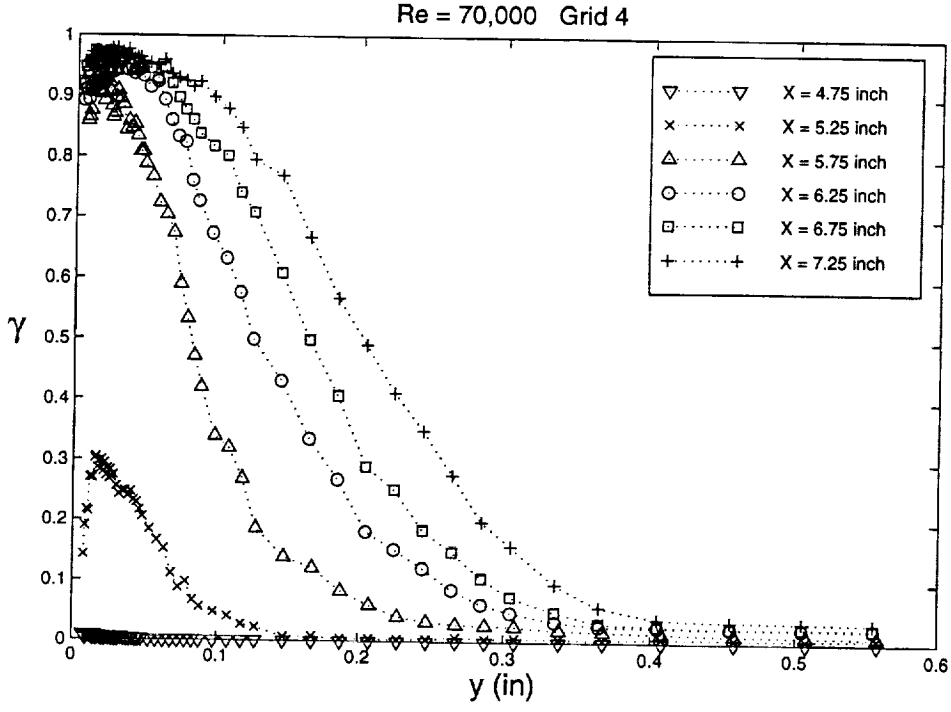

Figure 84 Variation of intermittency in normal direction, y, for Re = 70,000, Grid 4

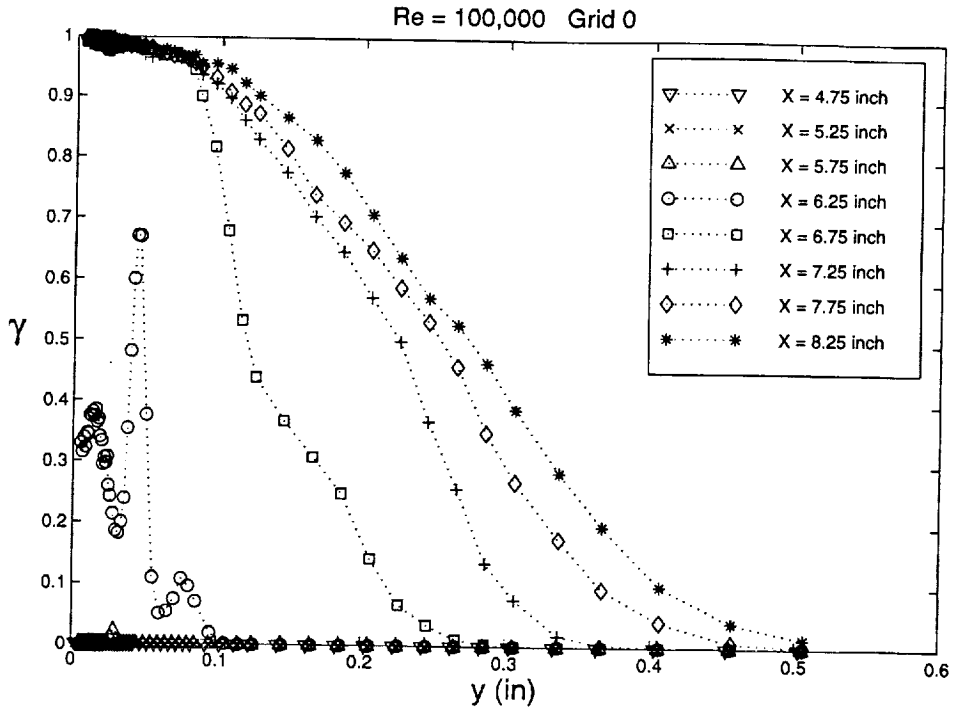

Figure 85 Variation of intermittency in normal direction, y, for Re = 100,000, Grid 0

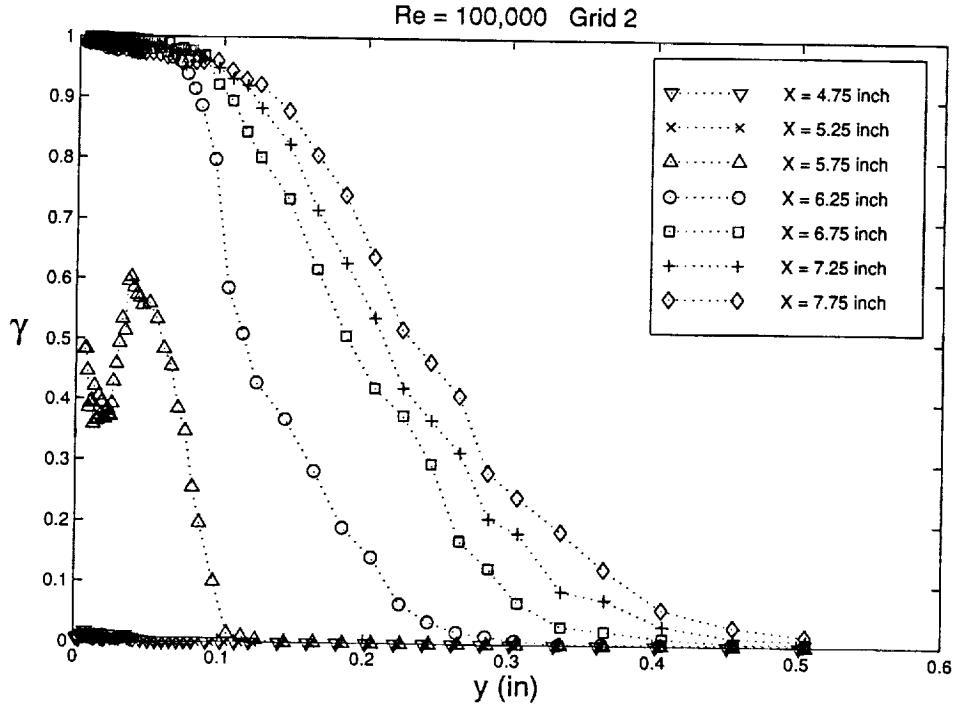

Figure 86 Variation of intermittency in normal direction, y, for Re = 100,000, Grid 2

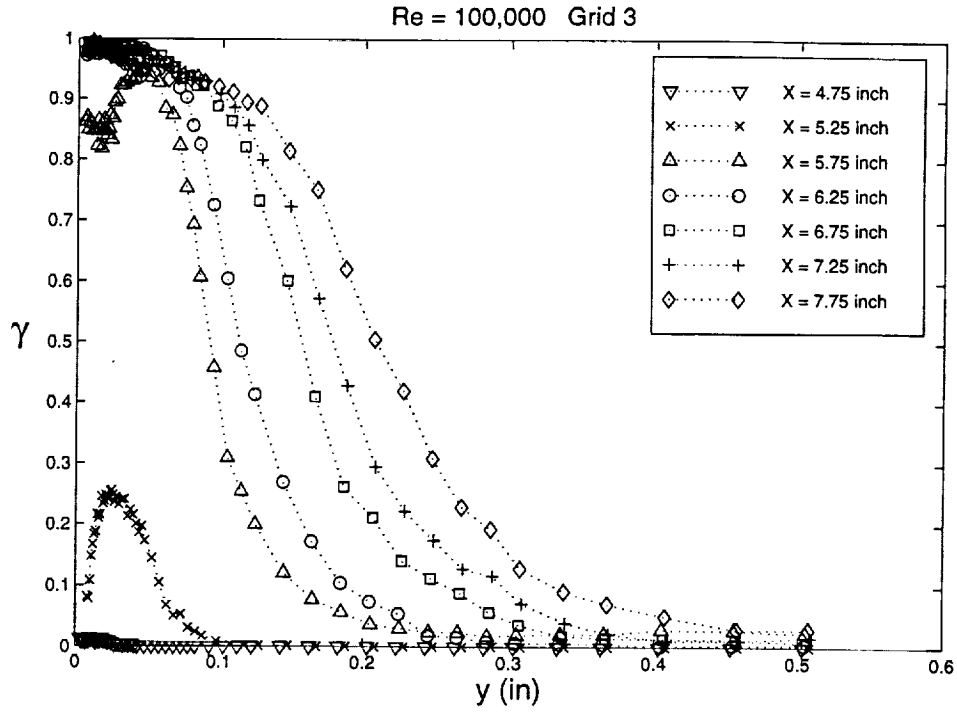

Figure 87 Variation of intermittency in normal direction, y, for Re = 100,000, Grid 3

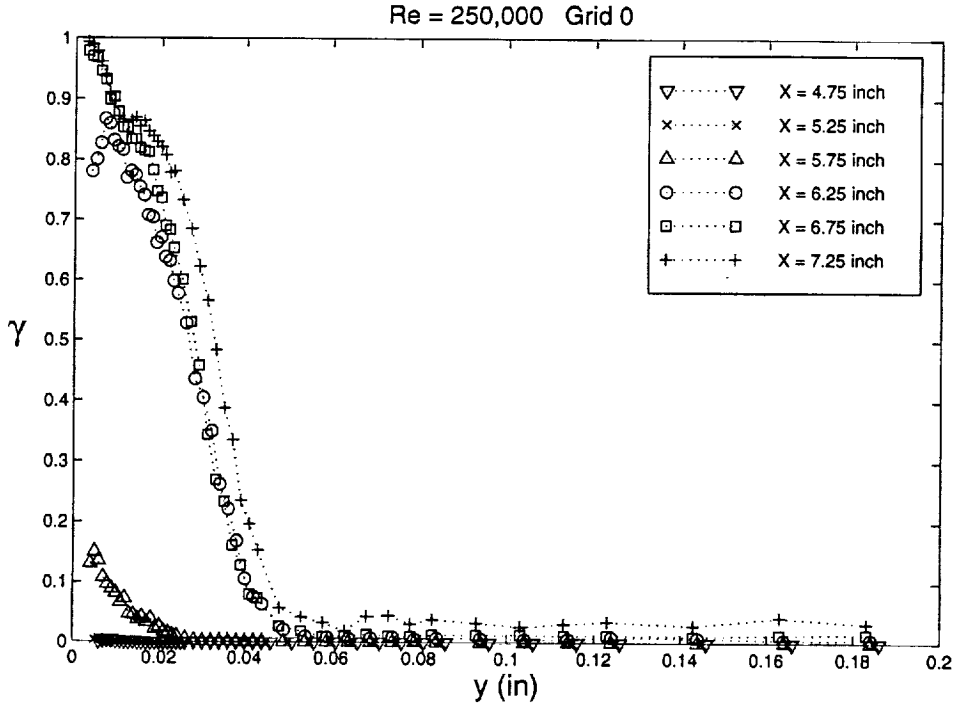

Figure 88 Variation of intermittency in normal direction, y, for Re = 250,000, Grid 0

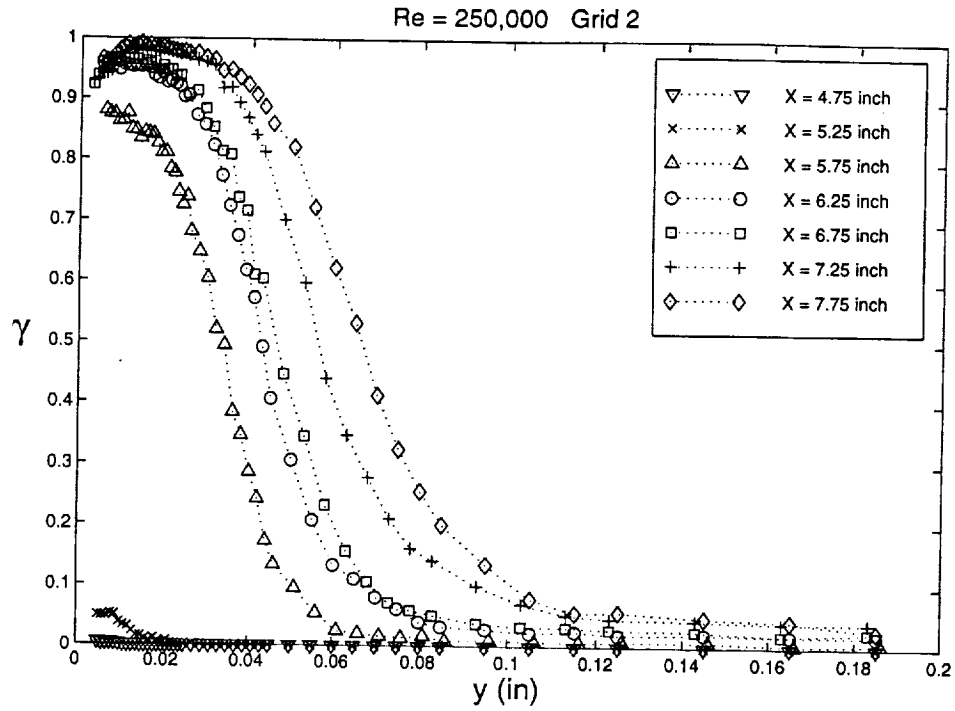

Figure 89 Variation of intermittency in normal direction, y, for Re = 250,000, Grid 2

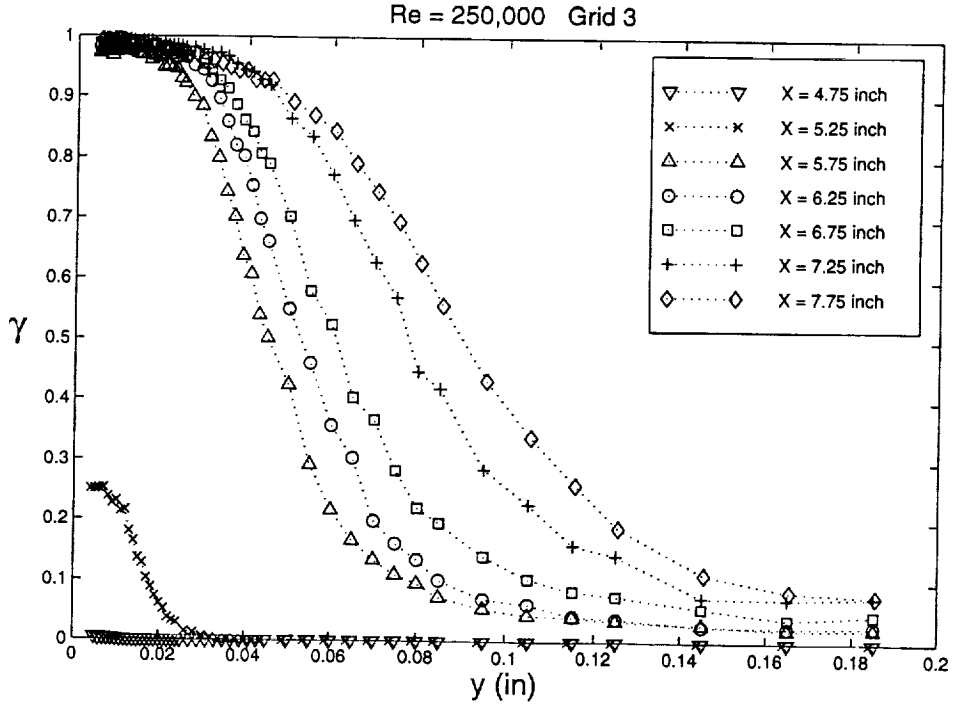

Figure 90 Variation of intermittency in normal direction, y, for Re = 250,000, Grid 3

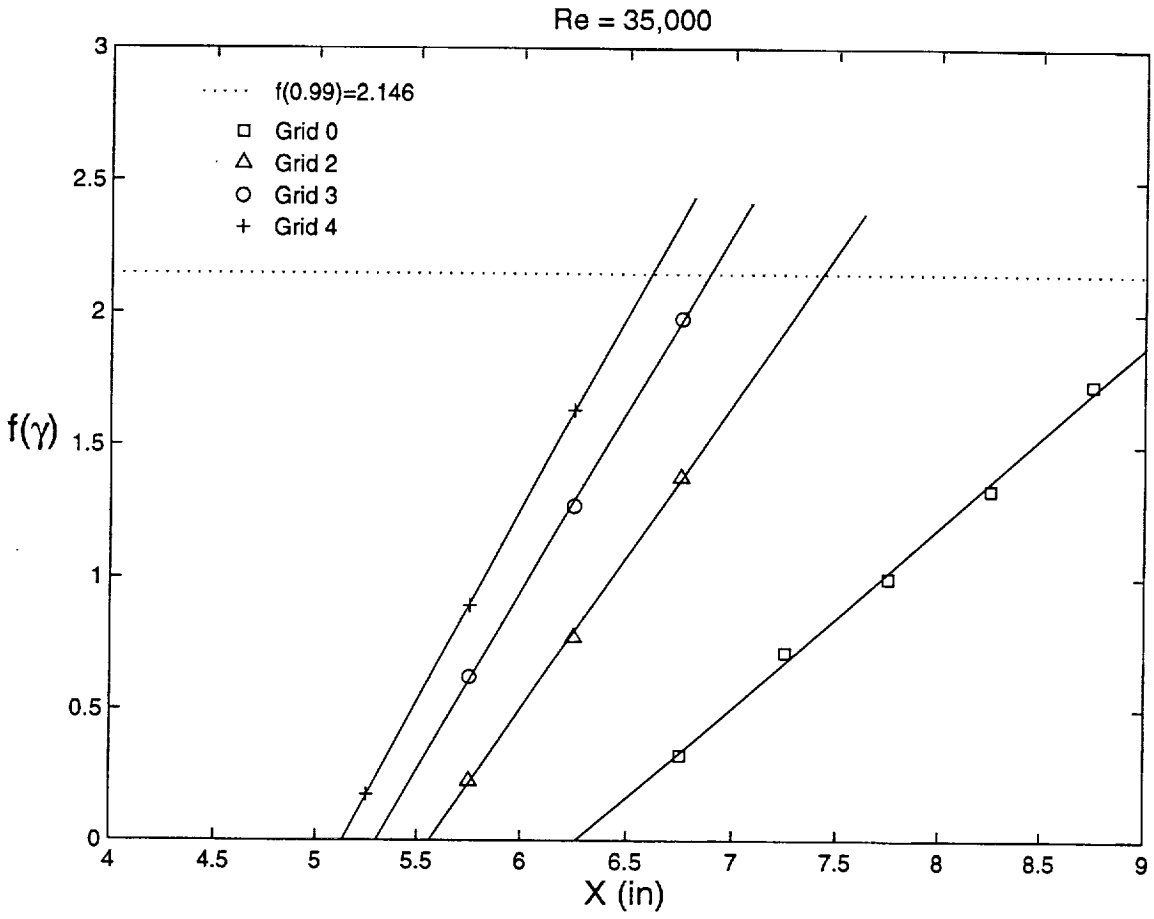

Figure 91 Variation of peak intermittency in the form of f(γ) [$=\sqrt{-\ln(1-\gamma)}$] with x

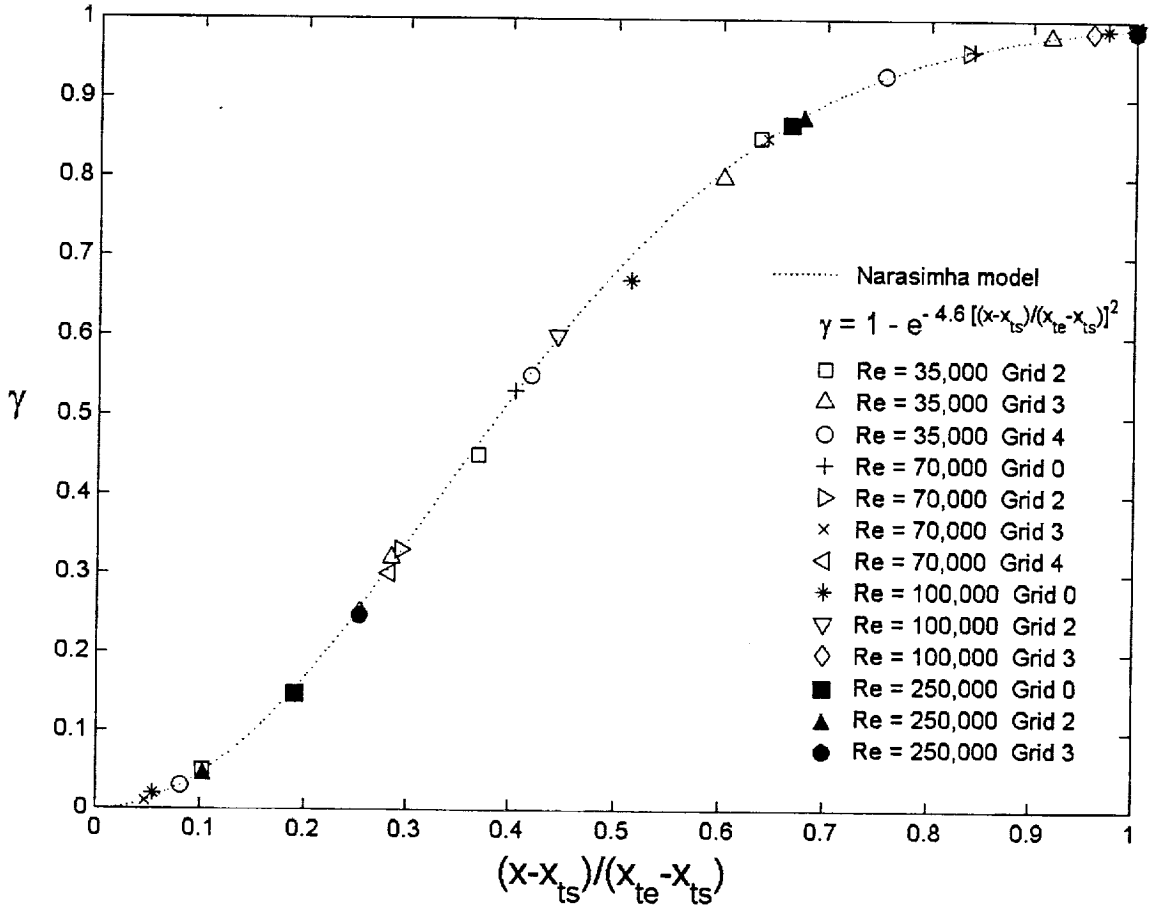

Figure 92 Streamwise variation of peak intermittency in transition region

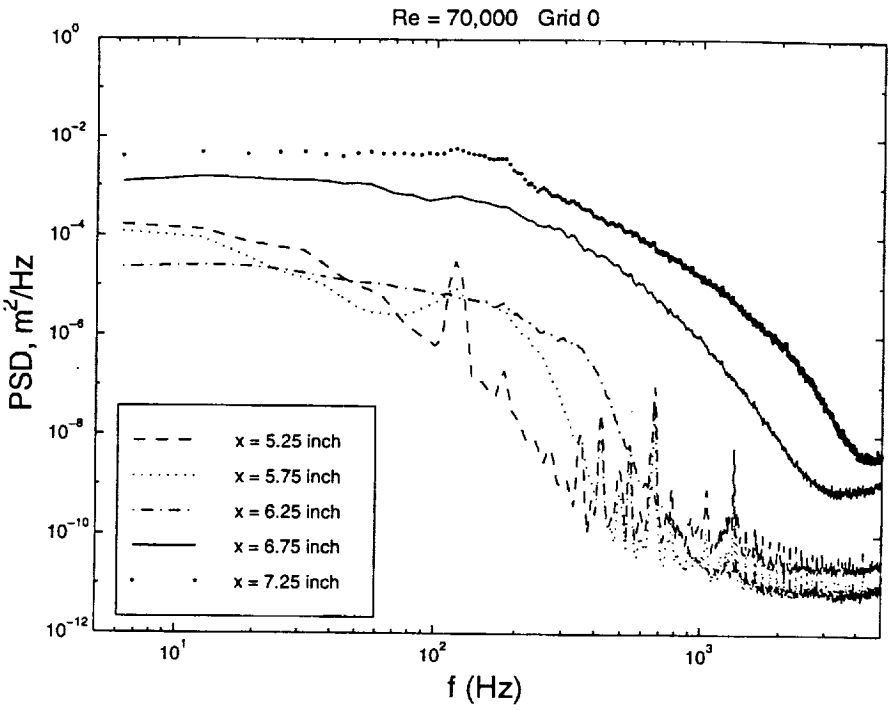

Figure 93 Power spectra measured at y = y(u'_{max}) for Re = 70,000, Grid 0

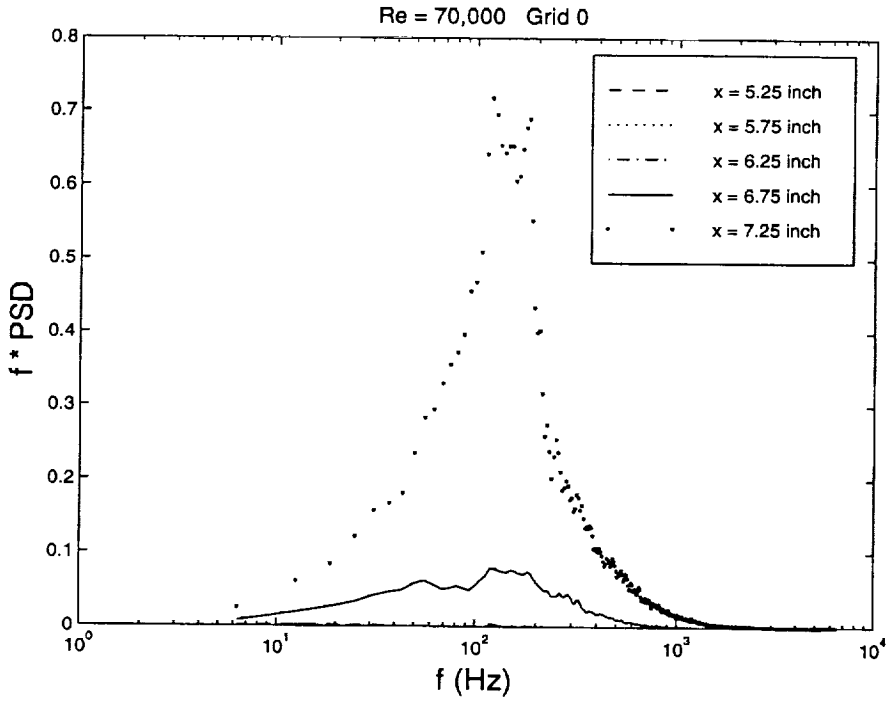

Figure 93a Power spectra at y = y(u'_{max}) in energy coordinates, for Re = 70,000, Grid 0

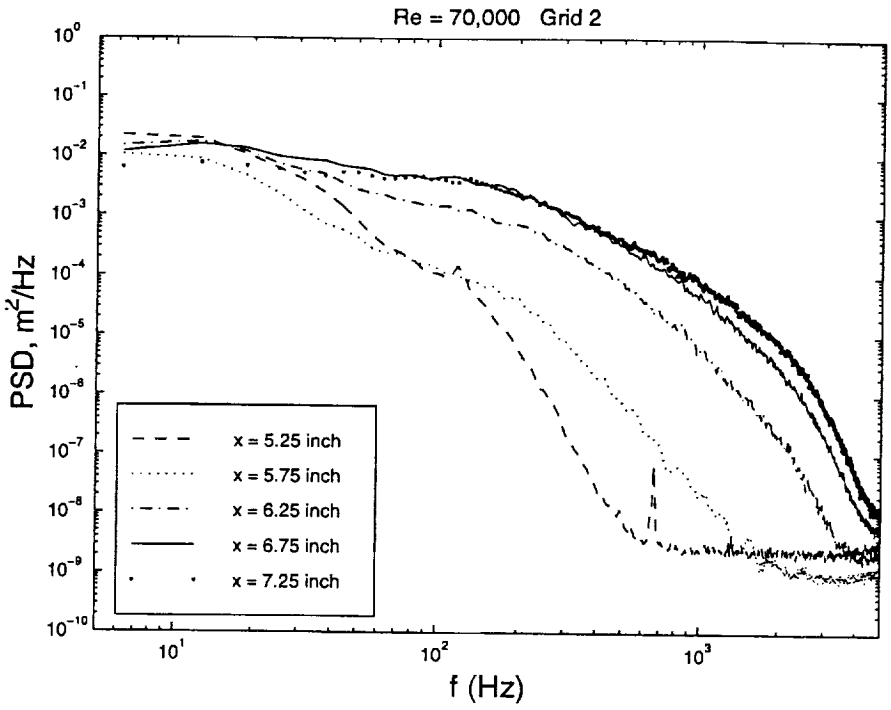

Figure 94 Power spectra measured at y = y(u'_{max}) for Re = 70,000, Grid 2

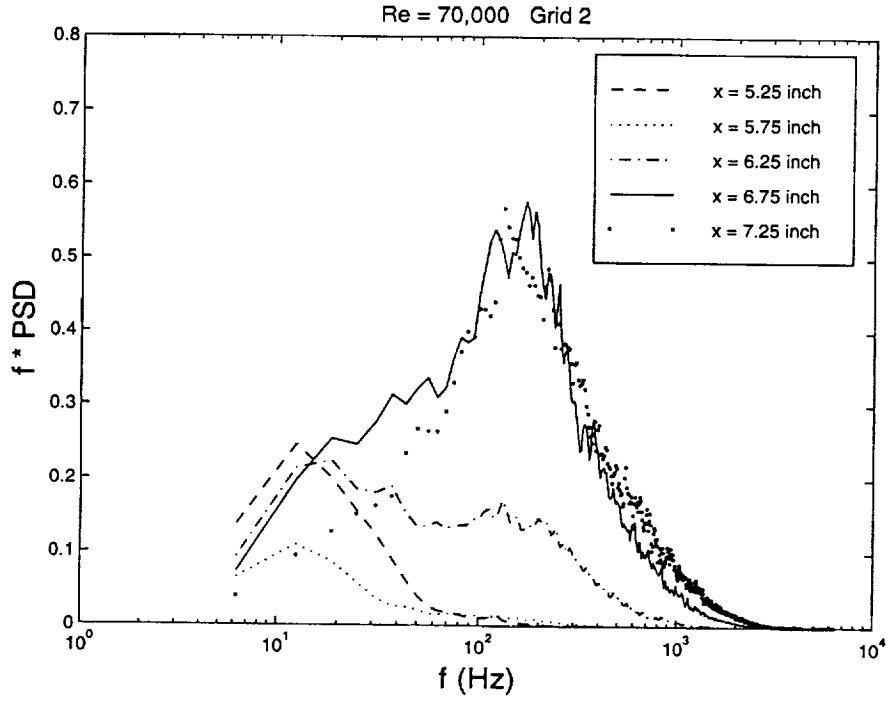

Figure 94a Power spectra at y = y(u'_{max}) in energy coordinates, for Re = 70,000, Grid 2

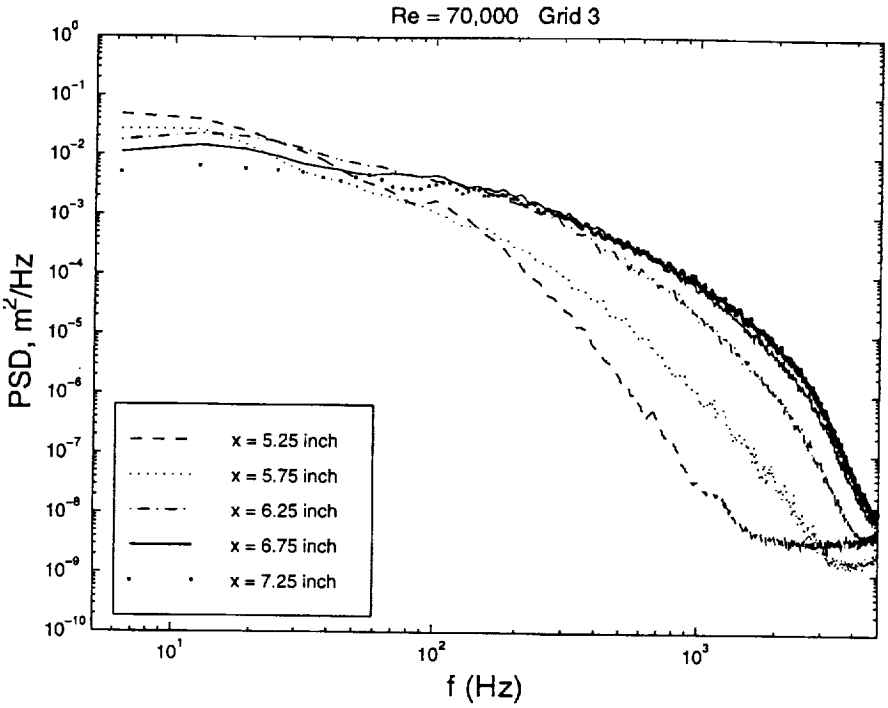

Figure 95 Power spectra measured at y = y(u'_{max}) for Re = 70,000, Grid 3

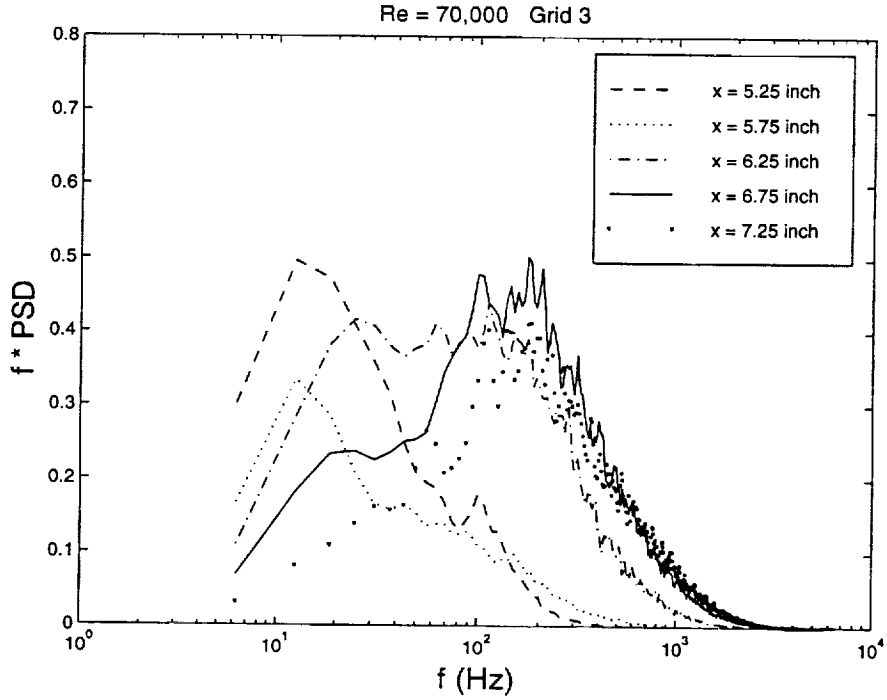

Figure 95a Power spectra at y = y(u'_{max}) in energy coordinates, for Re = 70,000, Grid 3

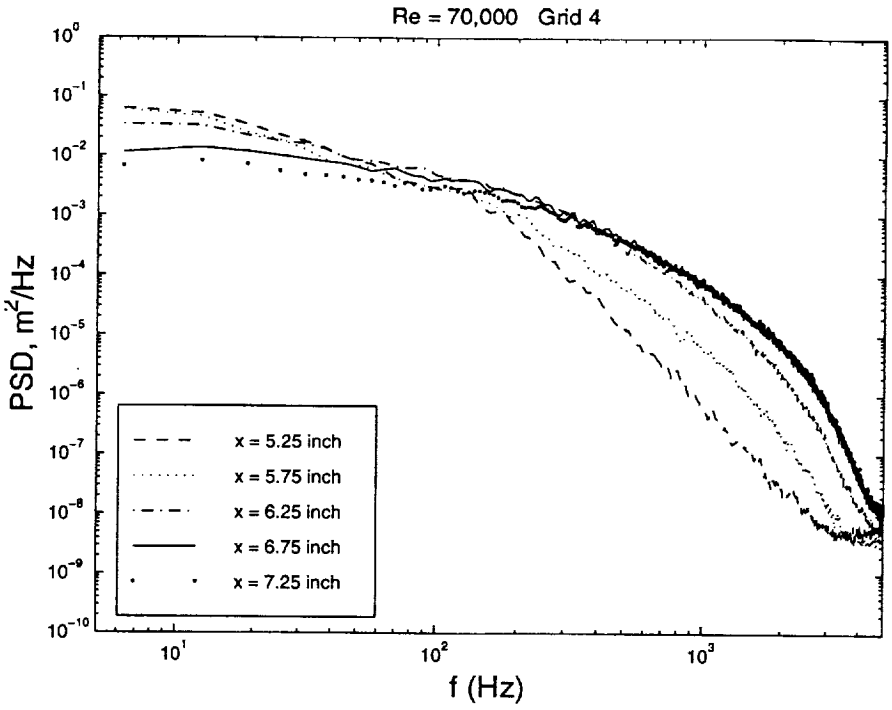

Figure 96 Power spectra measured at y = y(u'_{max}) for Re = 70,000, Grid 4

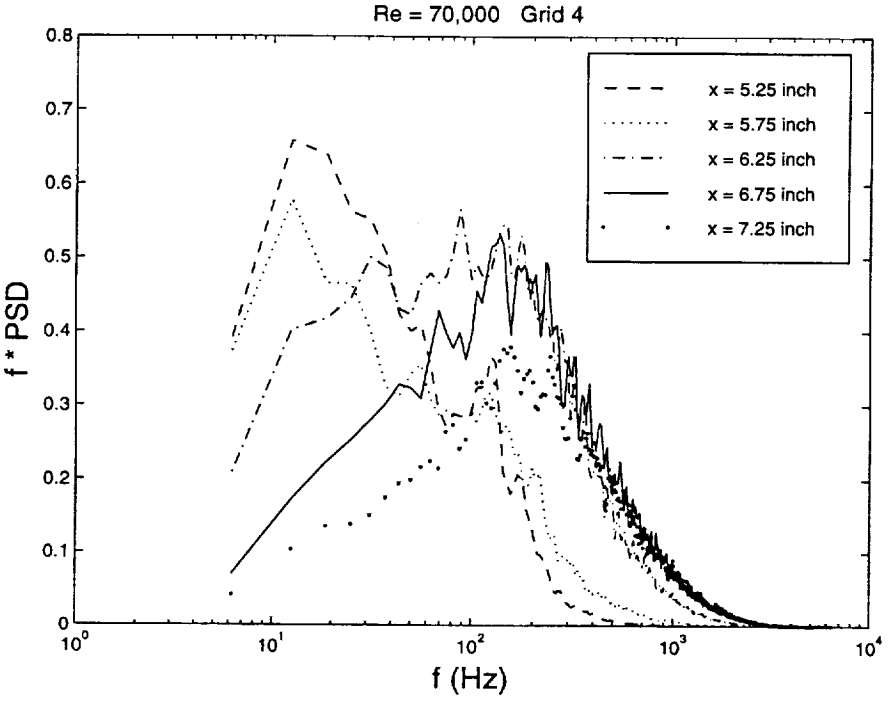

Figure 96a Power spectra at y = y(u'_{max}) in energy coordinates, for Re = 70,000, Grid 4

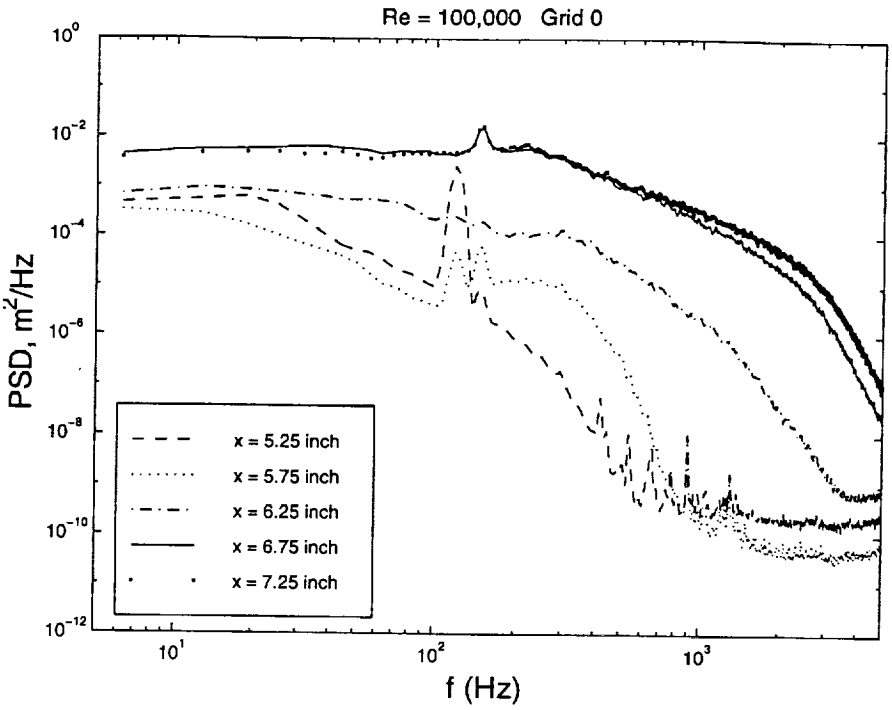

Figure 97 Power spectra measured at y = y(u'_{max}) for Re = 100,000, Grid 0

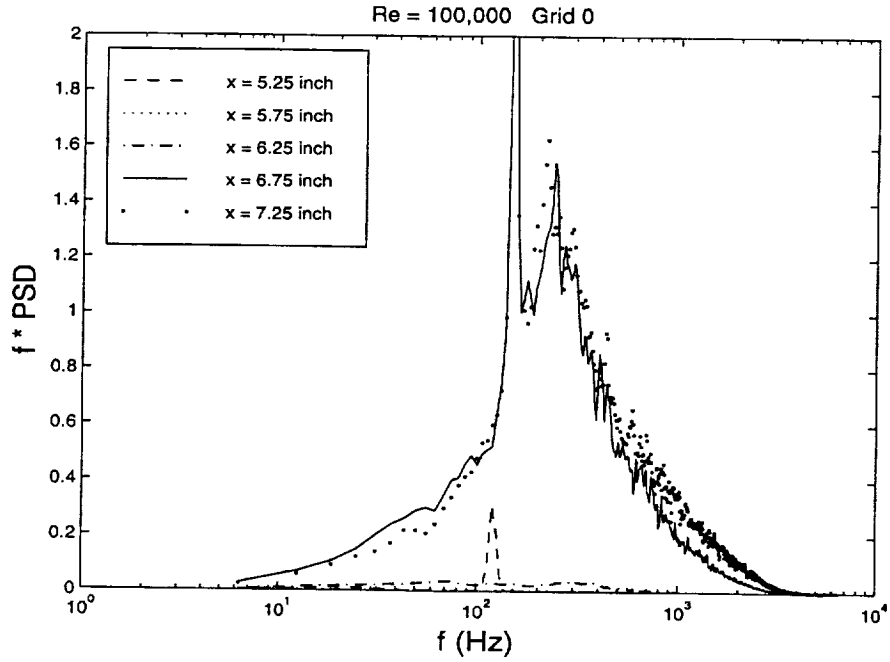

Figure 97a Power spectra at y = y(u'_{max}) in energy coordinates, for Re = 100,000, Grid 0

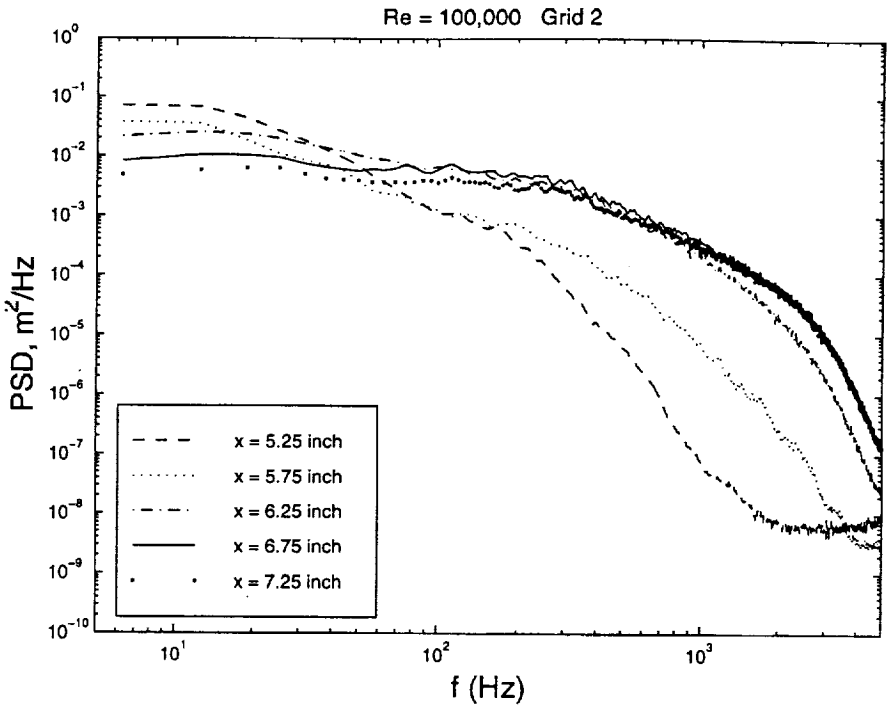

Figure 98 Power spectra measured at y = y(u'_{max}) for Re = 100,000, Grid 2

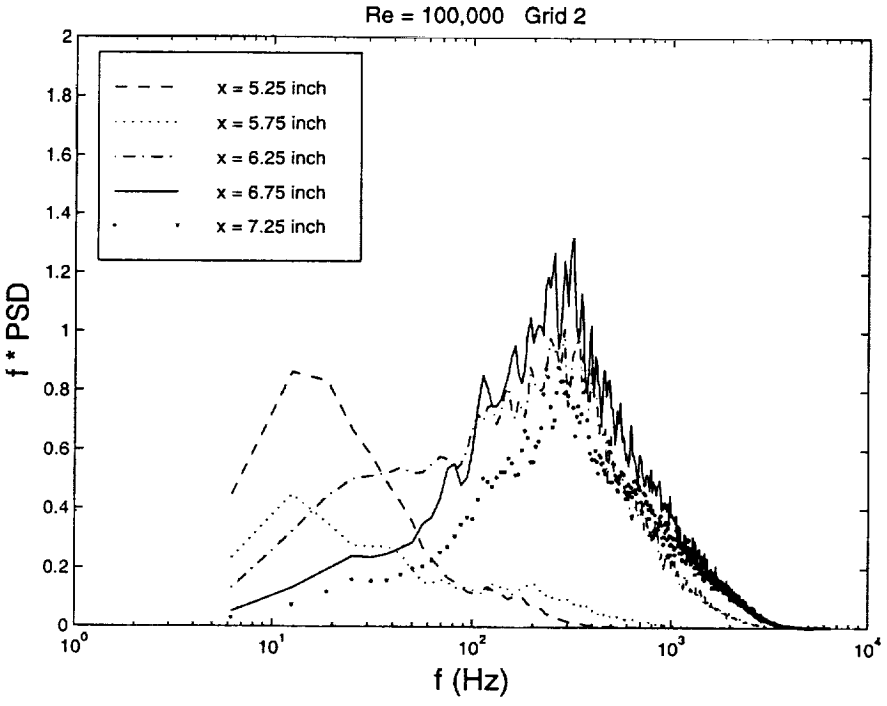

Figure 98a Power spectra at y = y(u'_{max}) in energy coordinates, for Re = 100,000, Grid 2

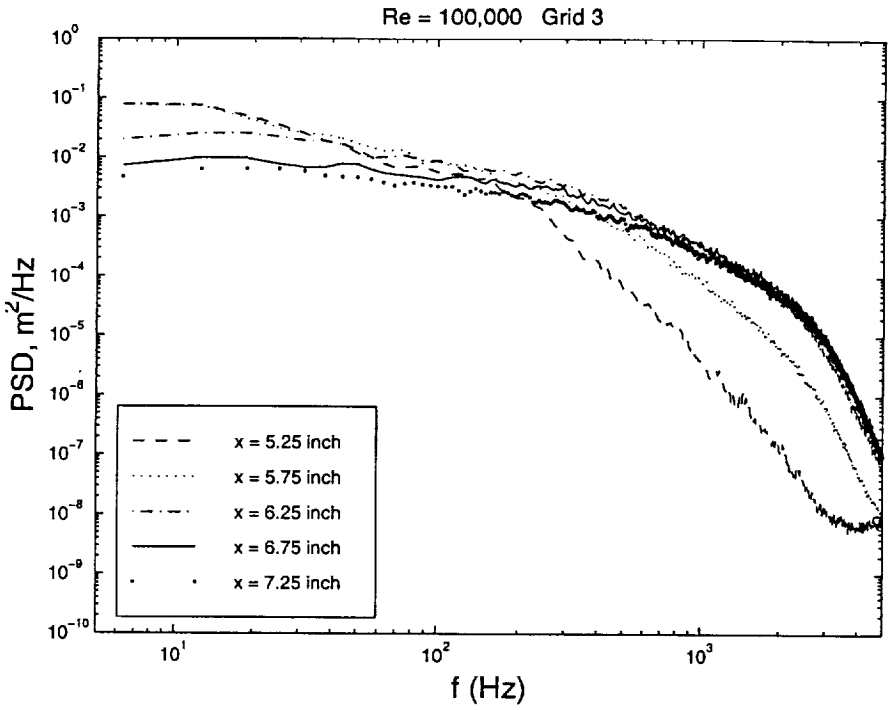

Figure 99 Power spectra measured at y = y(u'_{max}) for Re = 100,000, Grid 3

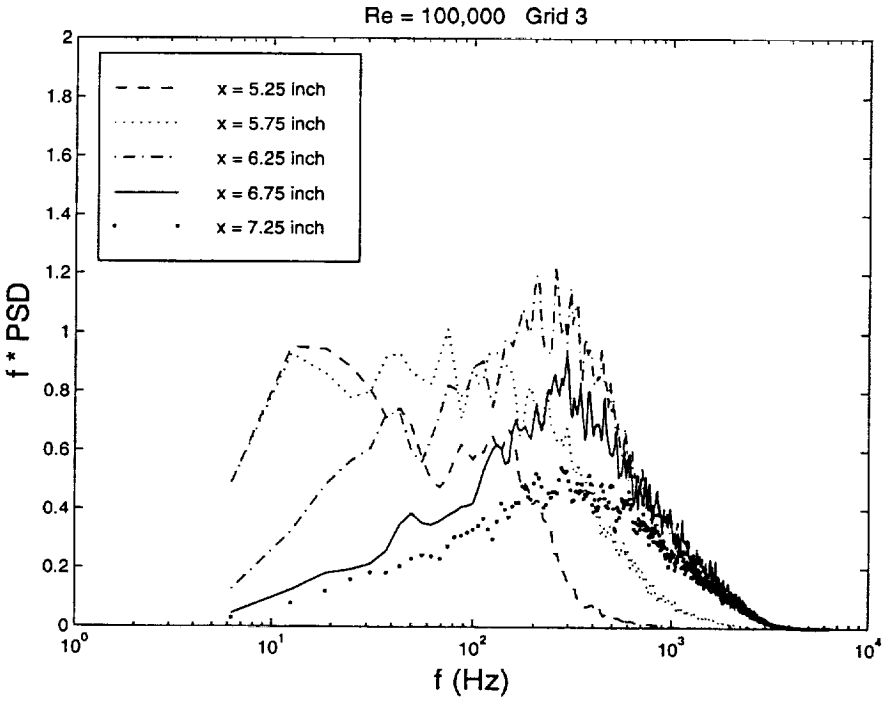

Figure 99a Power spectra at y = y(u'_{max}) in energy coordinates, for Re = 100,000, Grid 3

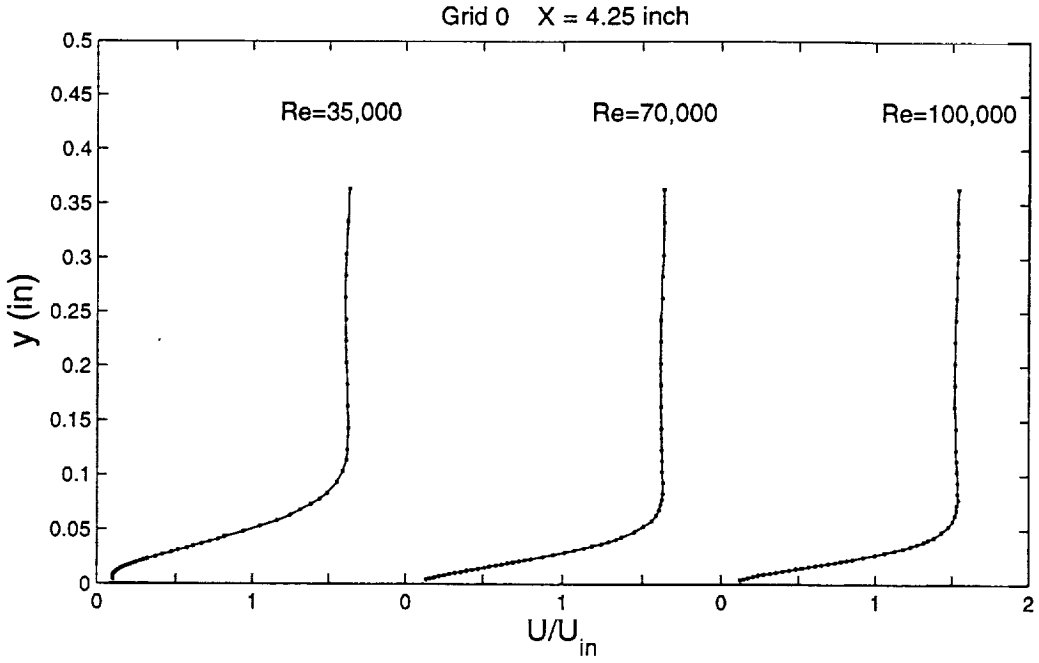

Figure 100 Variation of mean velocity profiles with Re at x = 4.25 inches, Grid 0

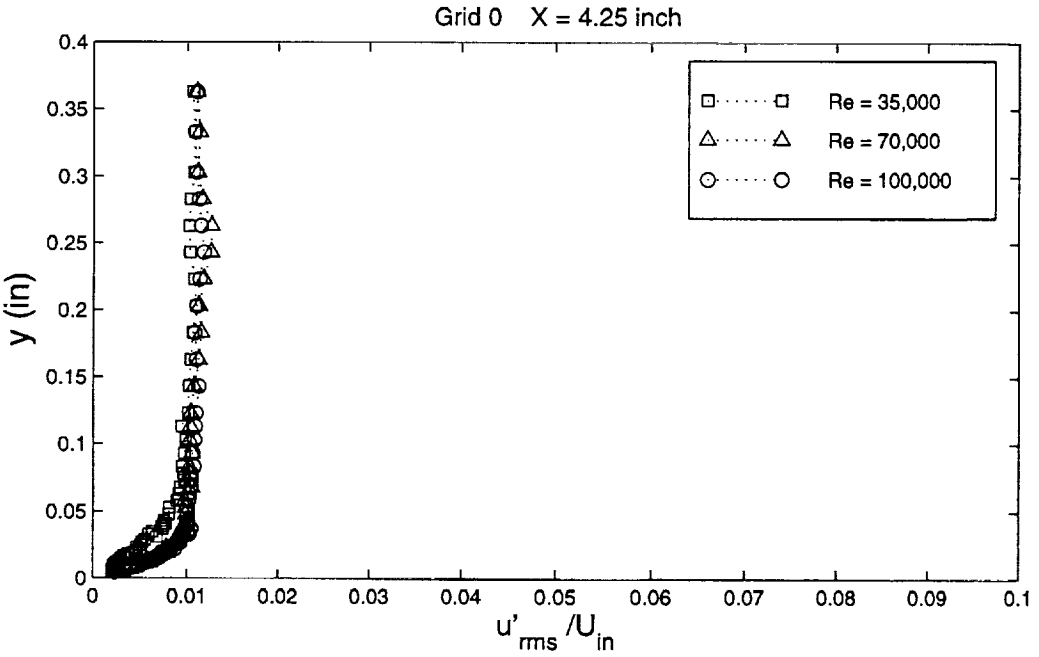

Figure 101 Variation of fluctuating velocity profiles with Re at x = 4.25 inches, Grid 0

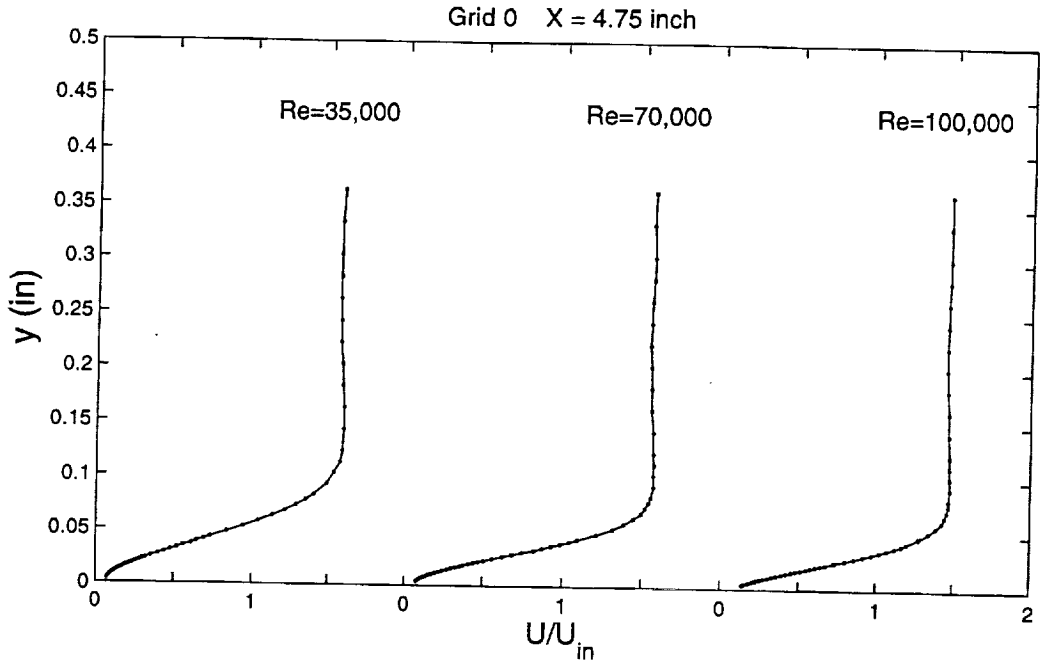

Figure 102 Variation of mean velocity profiles with Re at x = 4.75 inches, Grid 0

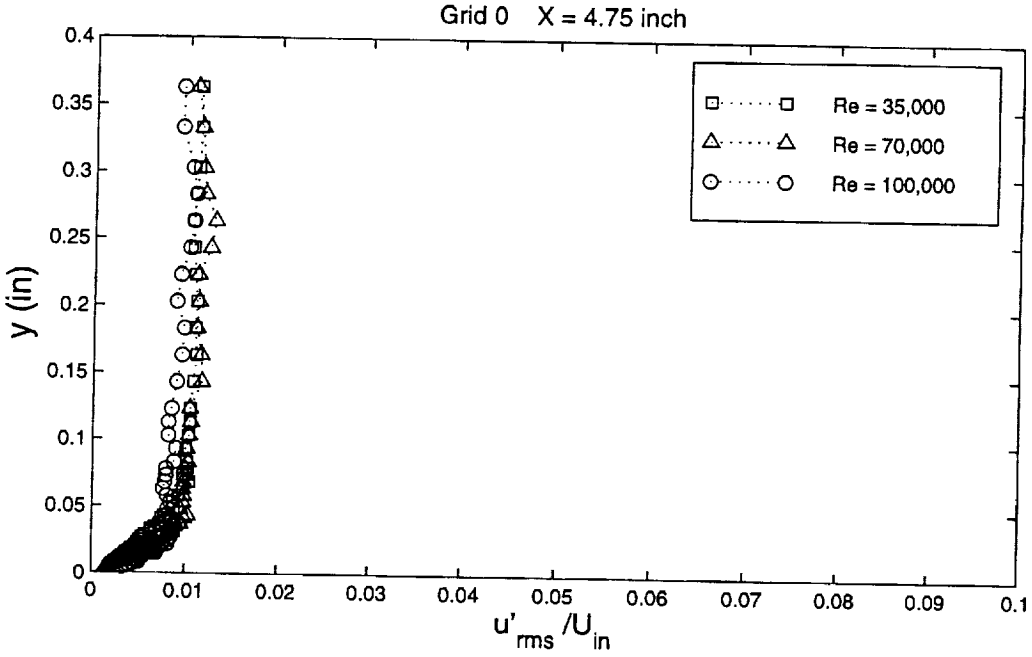

Figure 103 Variation of fluctuating velocity profiles with Re at x = 4.75 inches, Grid 0

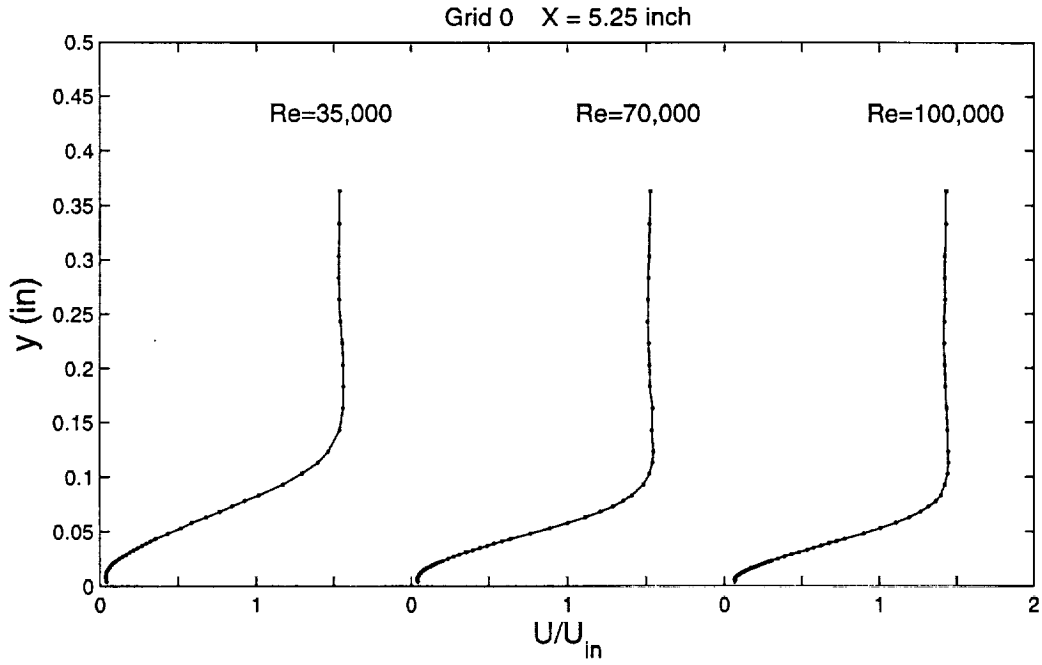

Figure 104 Variation of mean velocity profiles with Re at x = 5.25 inches, Grid 0

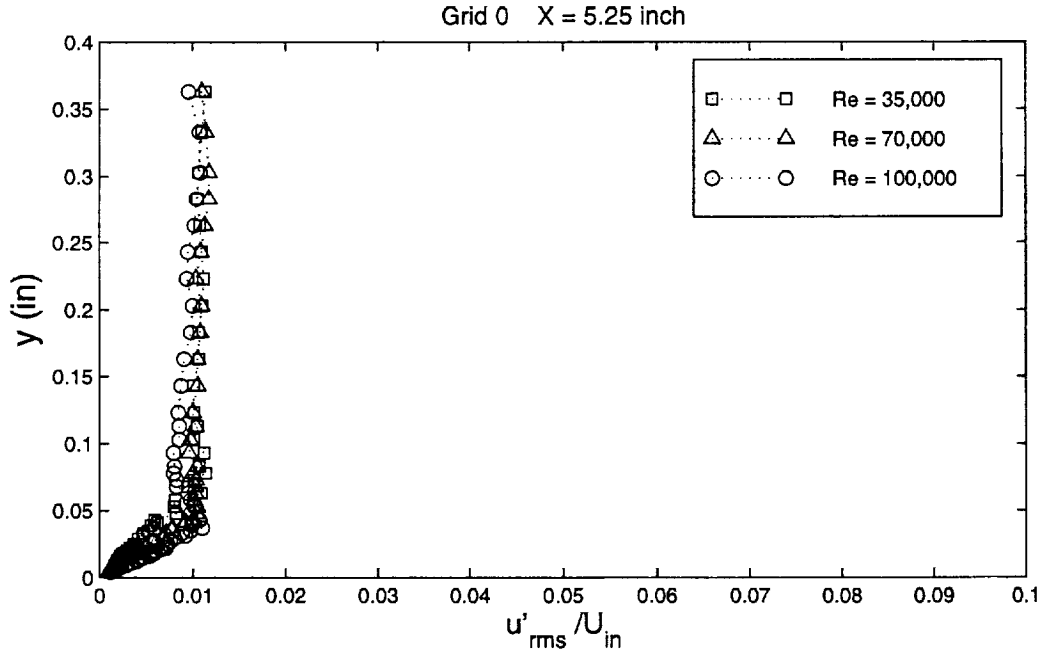

Figure 105 Variation of fluctuating velocity profiles with Re at x = 5.25 inches, Grid 0

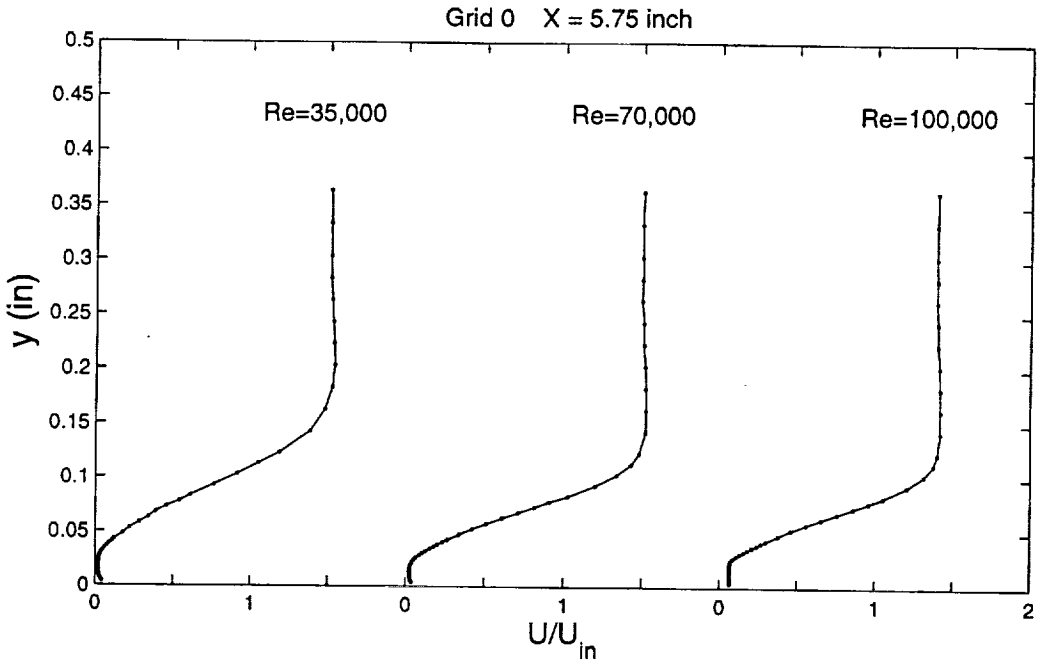

Figure 106 Variation of mean velocity profiles with Re at x = 5.75 inches, Grid 0

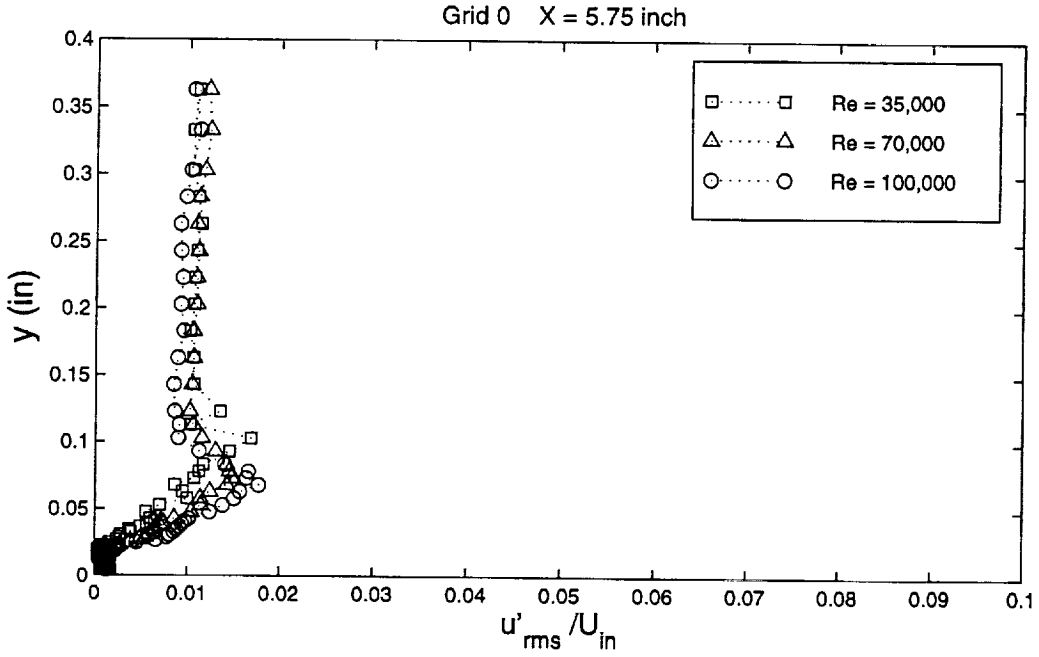

Figure 107 Variation of fluctuating velocity profiles with Re at x = 5.75 inches, Grid 0

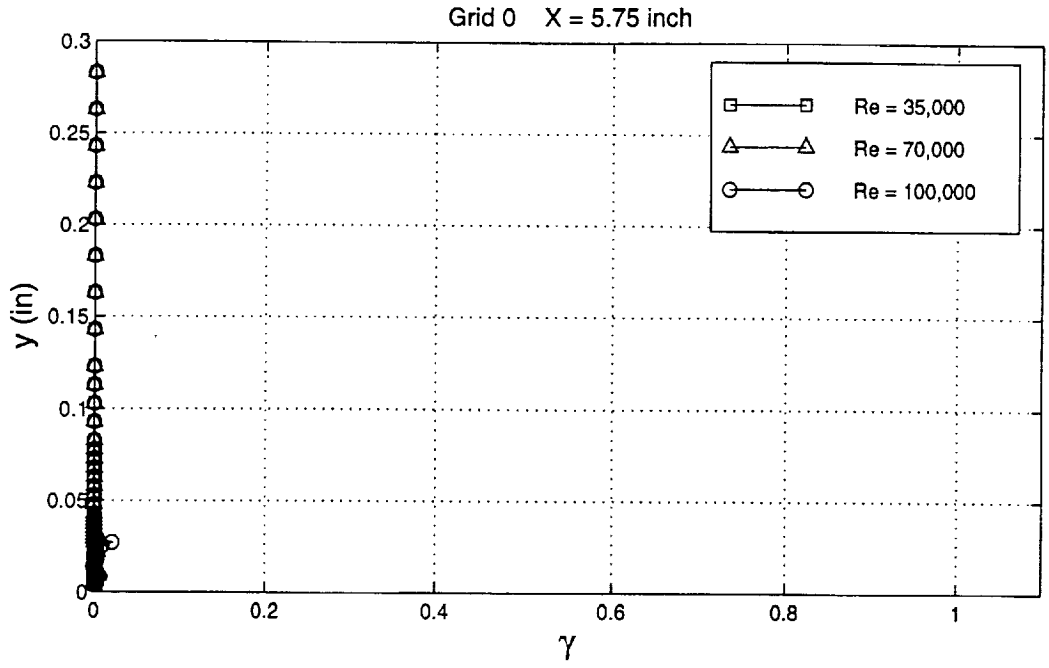

Figure 108 Variation of intermittency profiles with Re at x = 5.75 inches, Grid 0

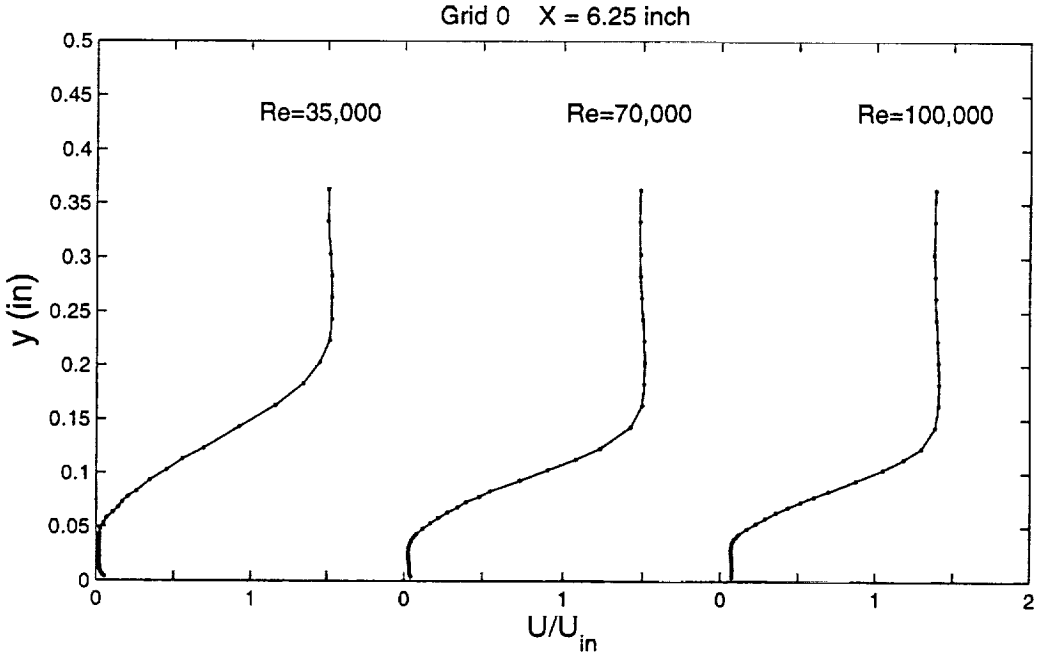

Figure 109 Variation of mean velocity profiles with Re at x = 6.25 inches, Grid 0

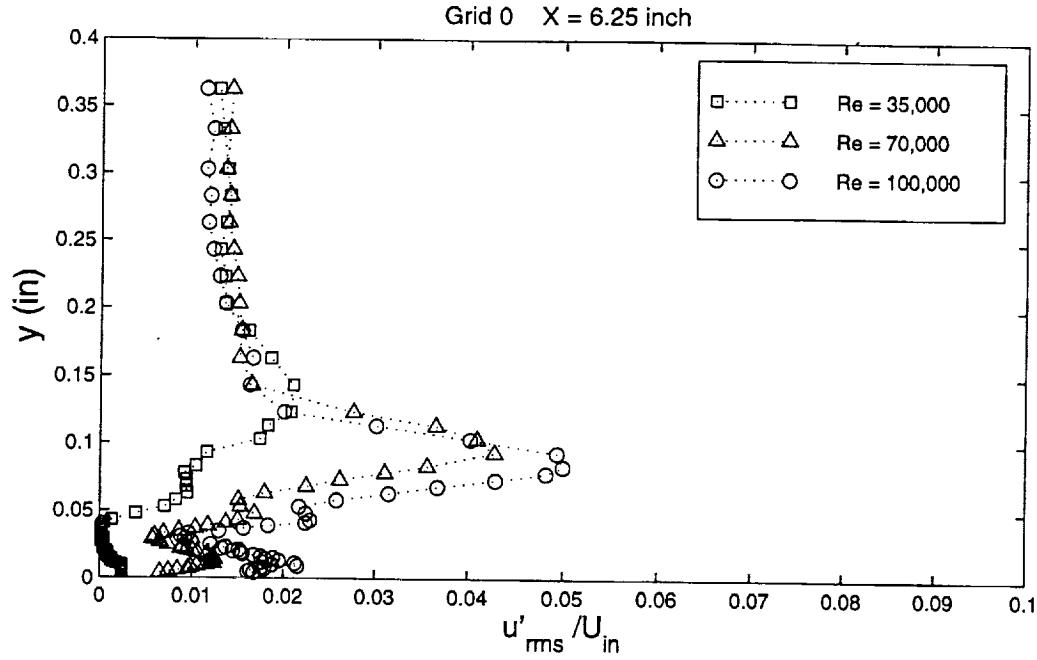

Figure 110 Variation of fluctuating velocity profiles with Re at x = 6.25 inches, Grid 0

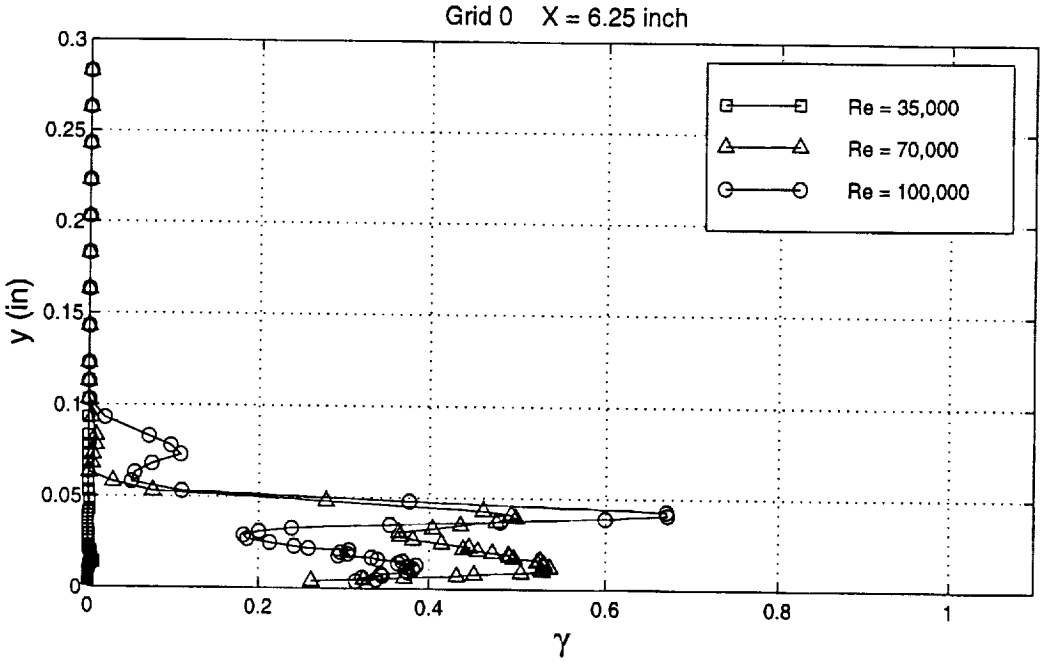

Figure 111 Variation of intermittency profiles with Re at x = 6.25 inches, Grid 0

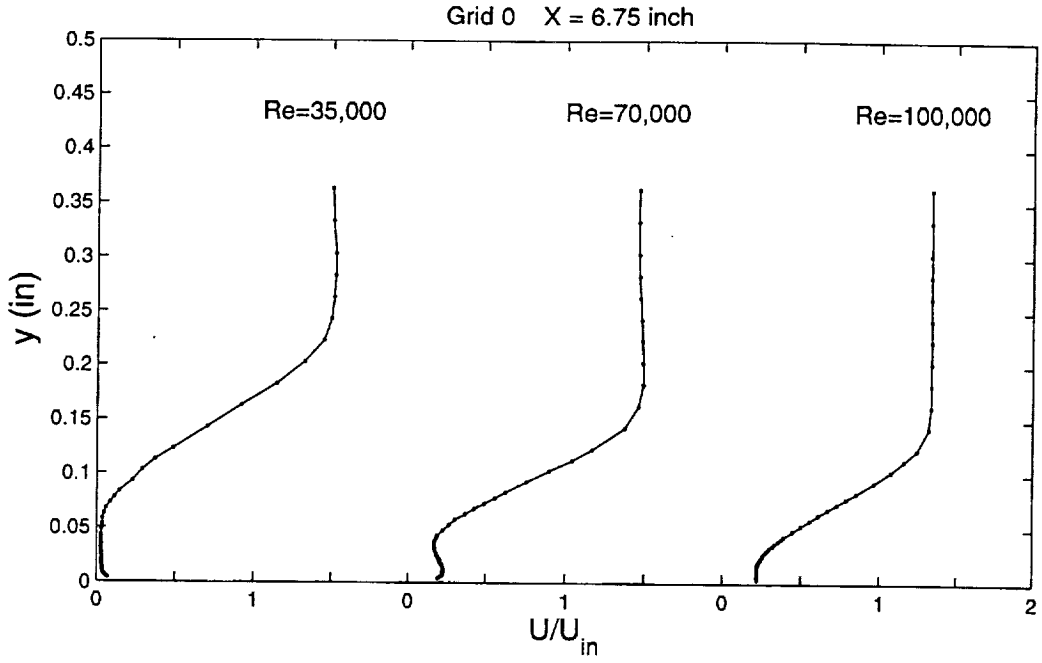

Figure 112 Variation of mean velocity profiles with Re at x = 6.75 inches, Grid 0

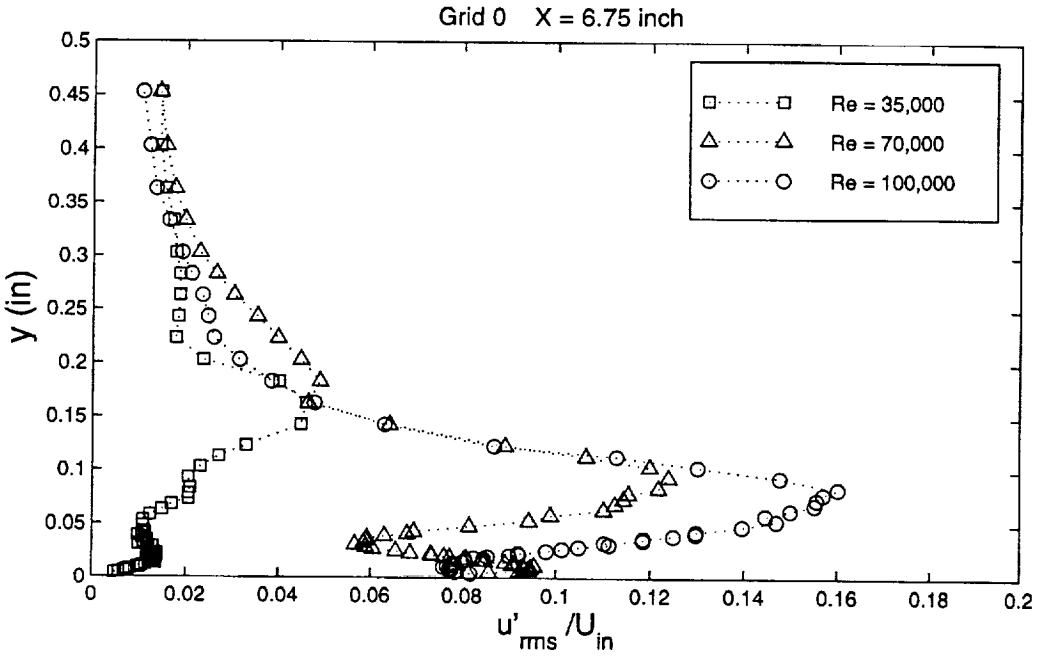

Figure 113 Variation of fluctuating velocity profiles with Re at x = 6.75 inches, Grid 0

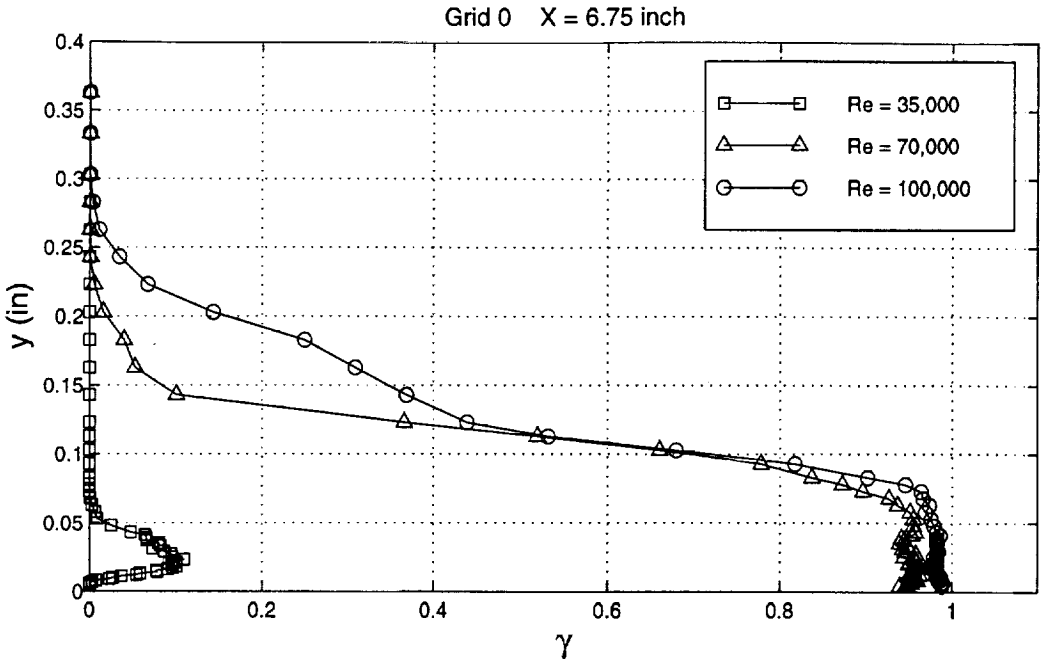

Figure 114 Variation of intermittency profiles with Re at x = 6.75 inches, Grid 0

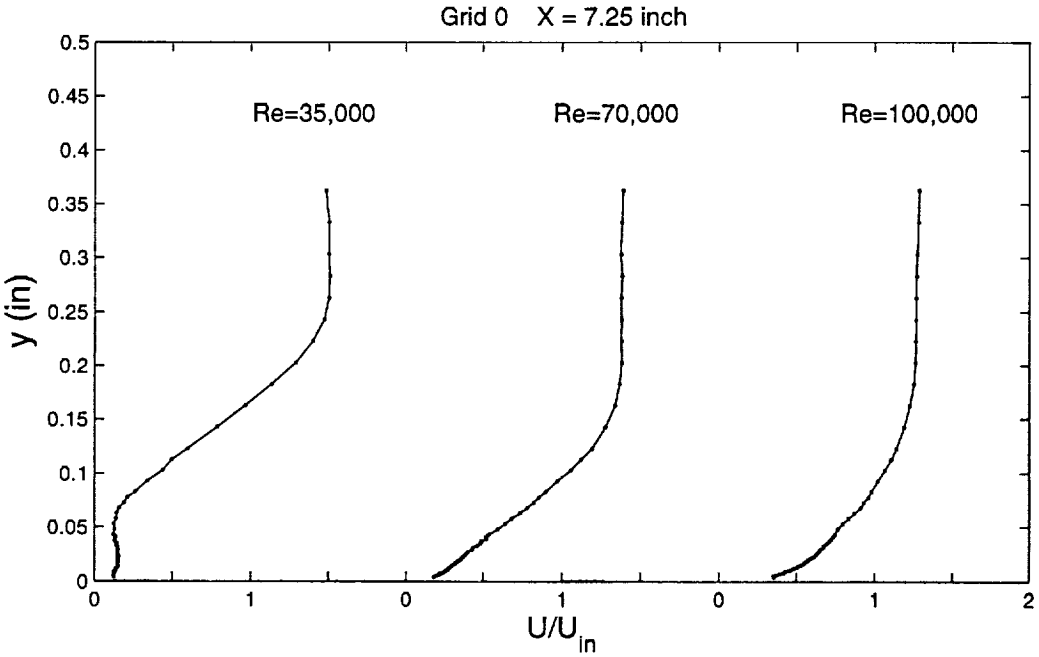

Figure 115 Variation of mean velocity profiles with Re at x = 7.25 inches, Grid 0

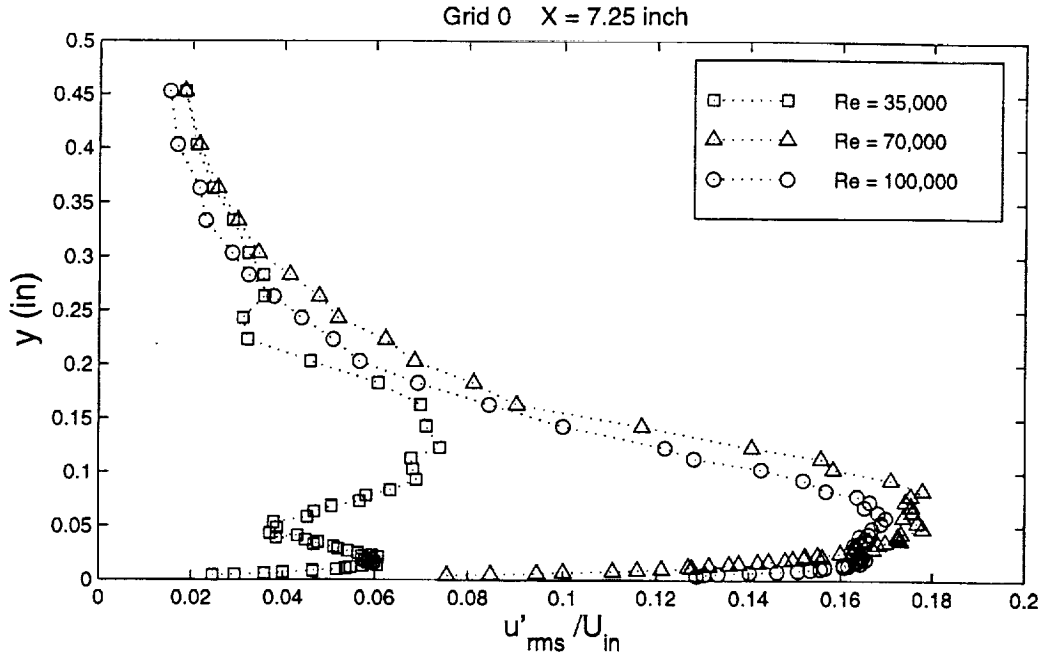

Figure 116 Variation of fluctuating velocity profiles with Re at x = 7.25 inches, Grid 0

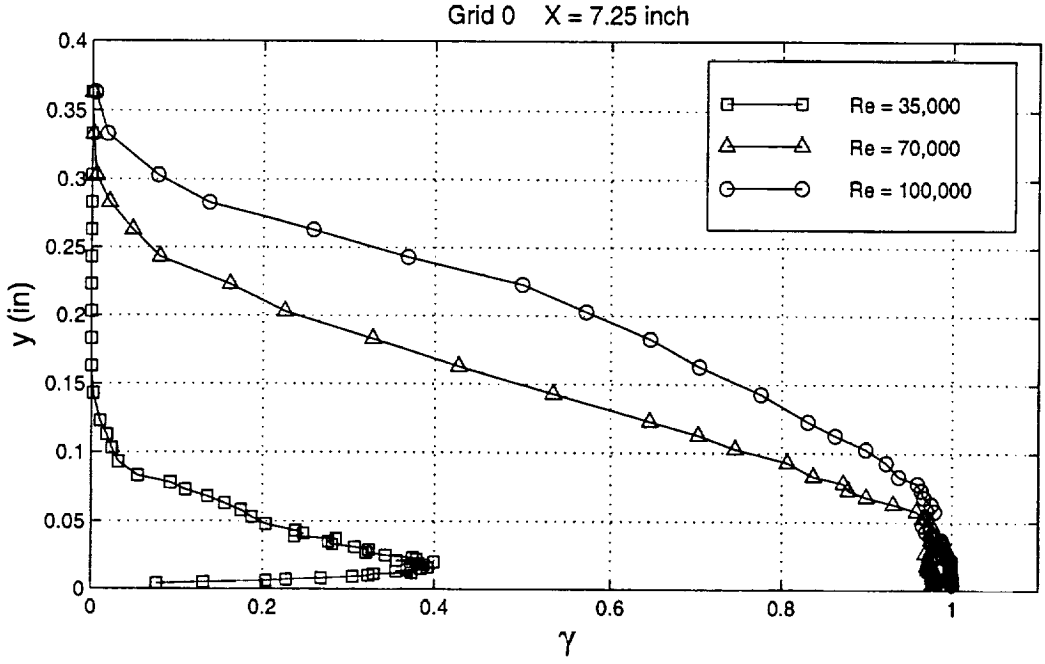

Figure 117 Variation of intermittency profiles with Re at x = 7.25 inches, Grid 0

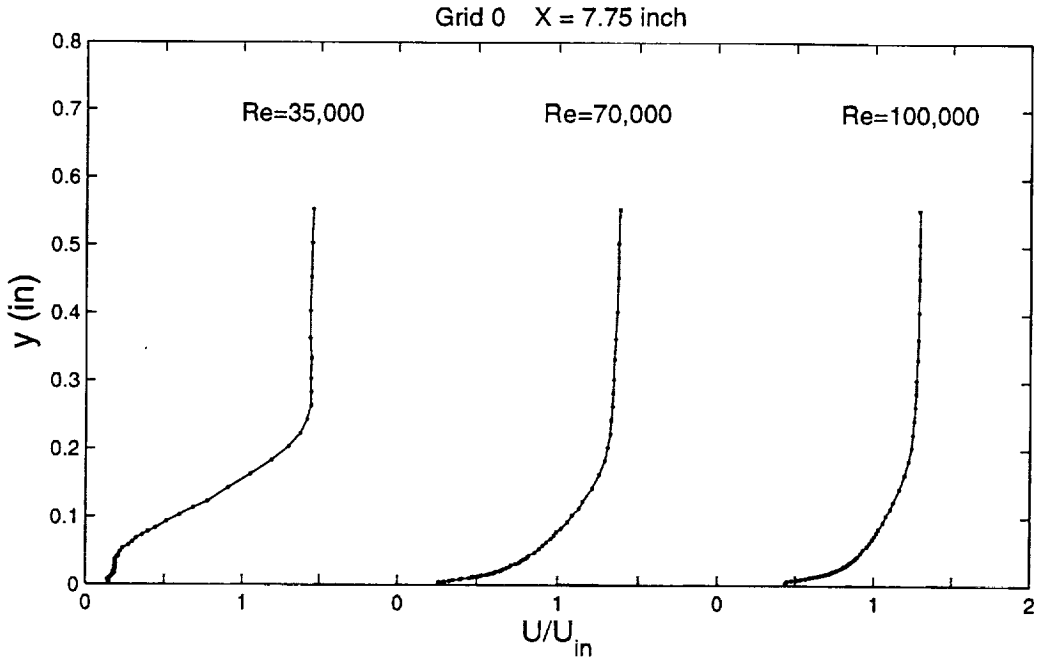

Figure 118 Variation of mean velocity profiles with Re at x = 7.75 inches, Grid 0

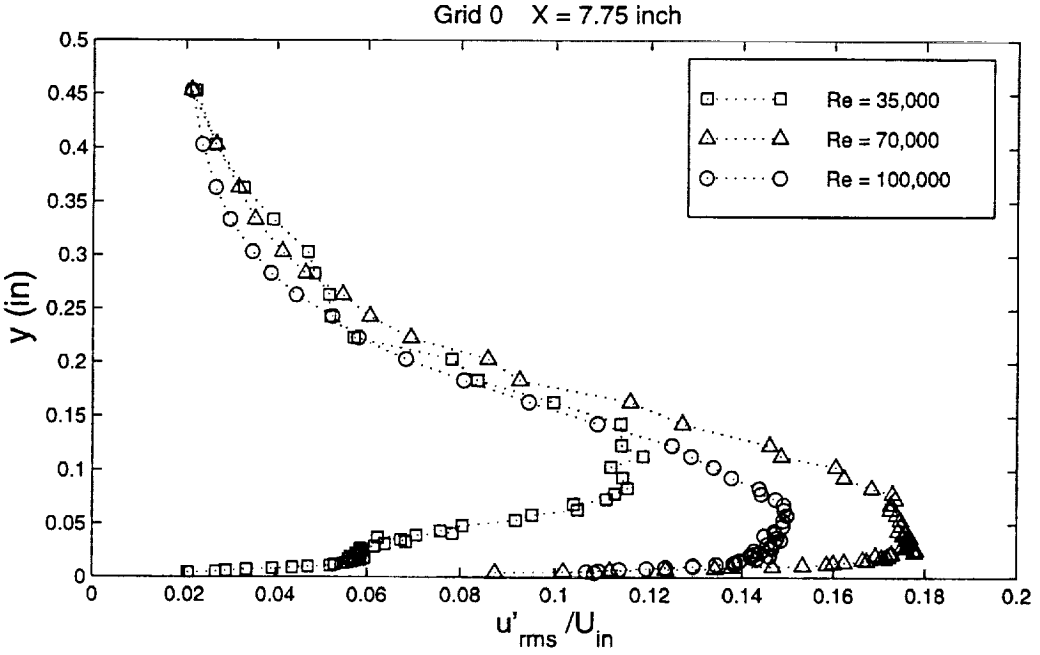

Figure 119 Variation of fluctuating velocity profiles with Re at x = 7.75 inches, Grid 0

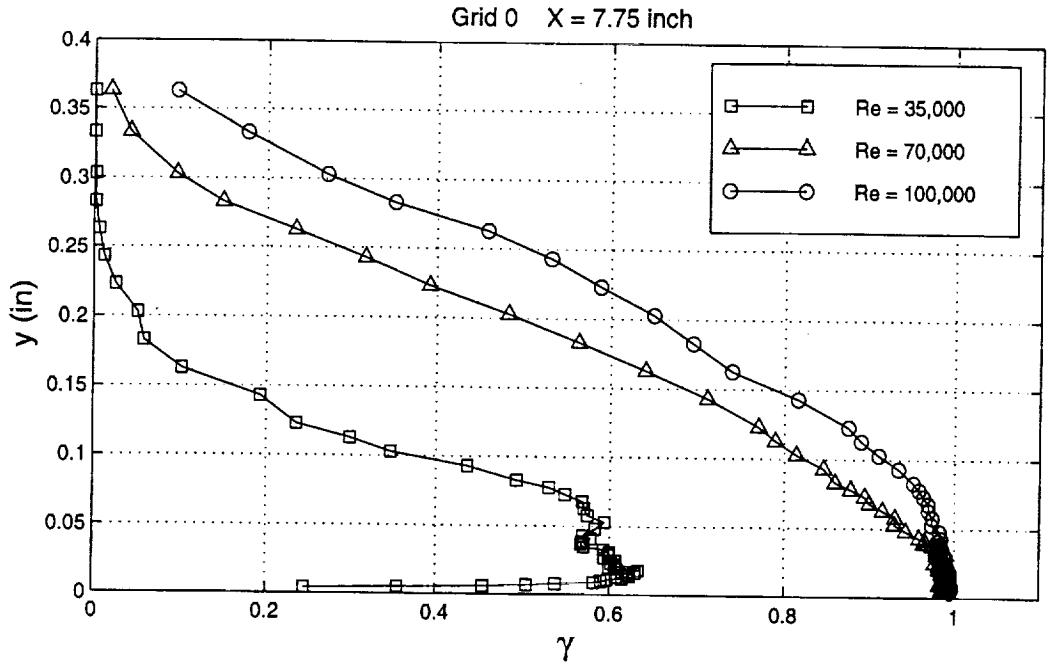

Figure 120 Variation of intermittency profiles with Re at x = 7.75 inches, Grid 0

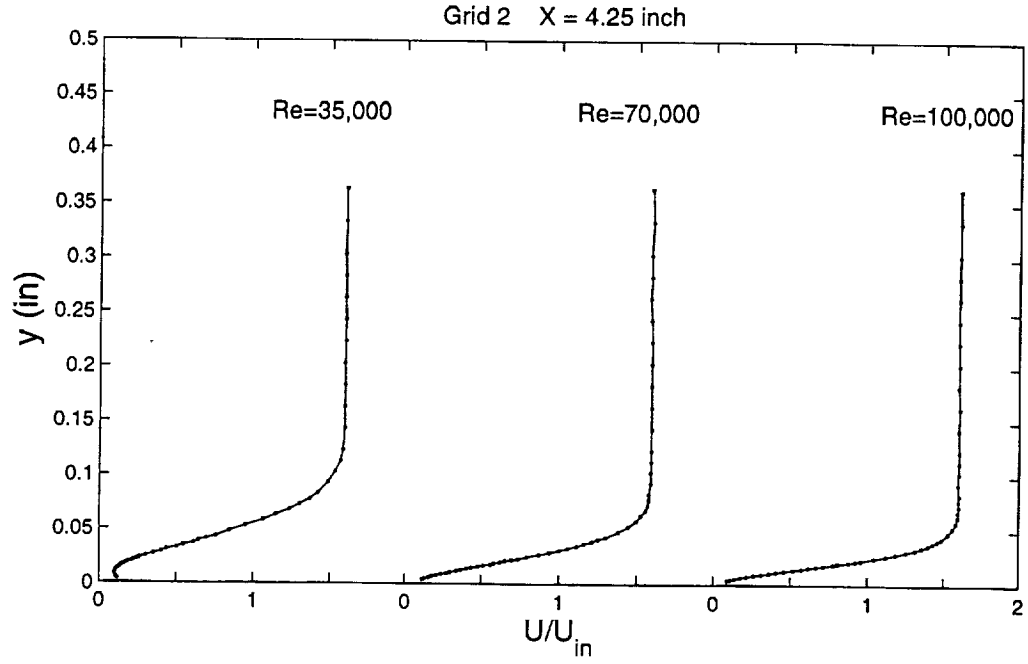

Figure 121 Variation of mean velocity profiles with Re at x = 4.25 inches, Grid 2

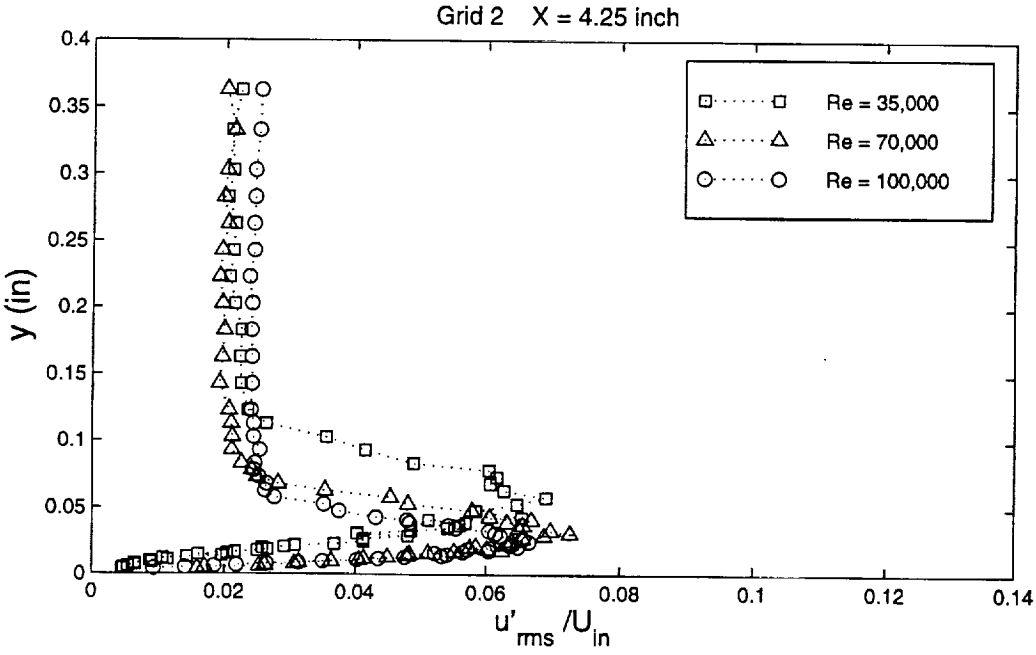

Figure 122 Variation of fluctuating velocity profiles with Re at x = 4.25 inches, Grid 2

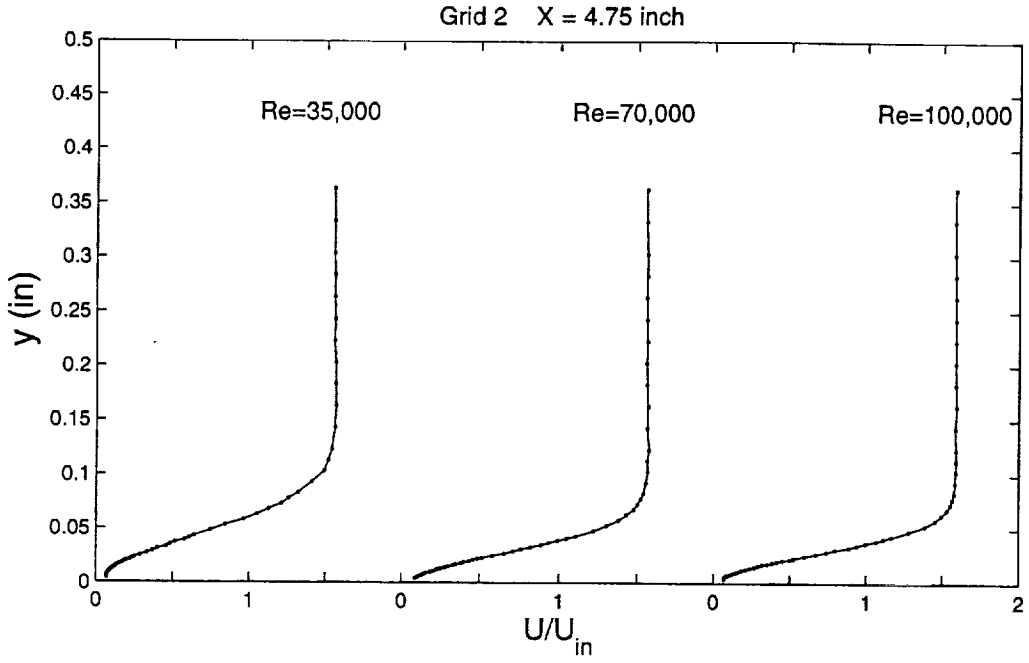

Figure 123 Variation of mean velocity profiles with Re at x = 4.75 inches, Grid 2

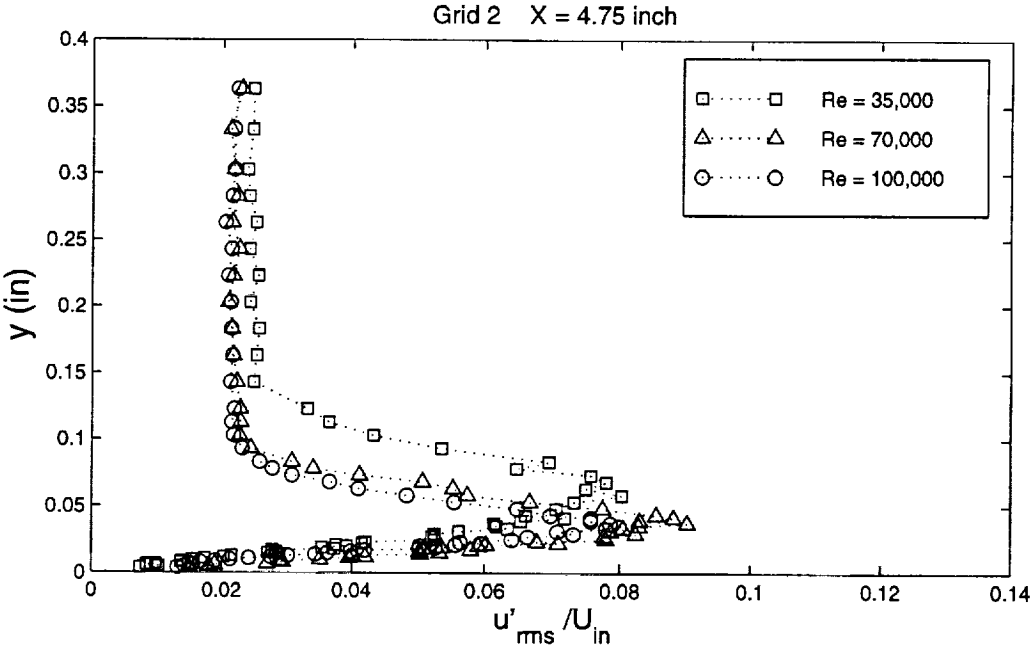

Figure 124 Variation of fluctuating velocity profiles with Re at x = 4.75 inches, Grid 2

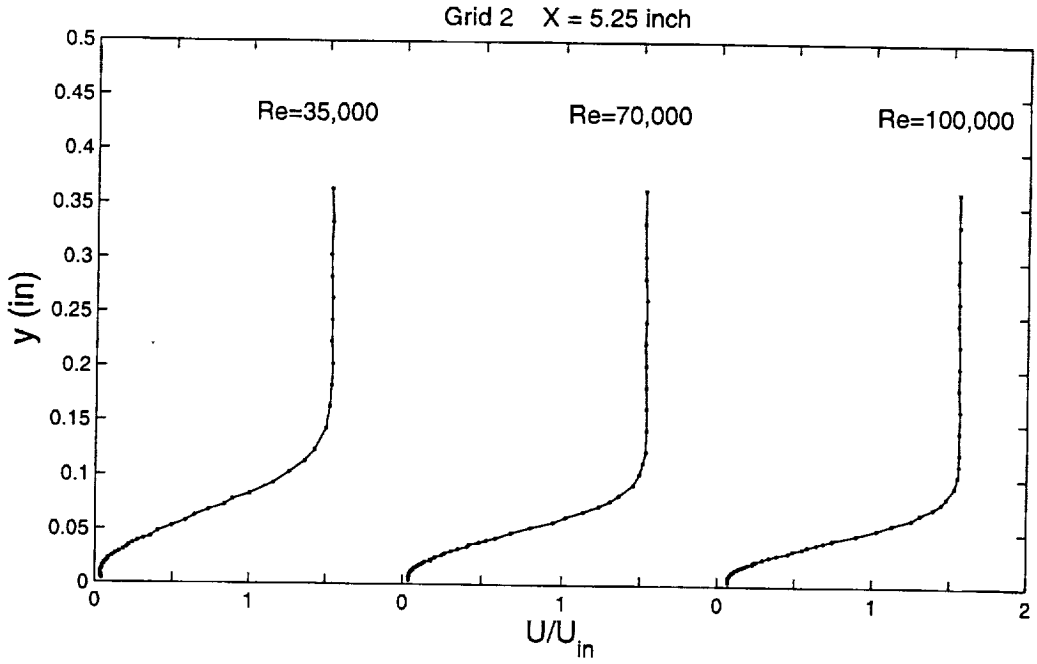

Figure 125 Variation of mean velocity profiles with Re at x = 5.25 inches, Grid 2

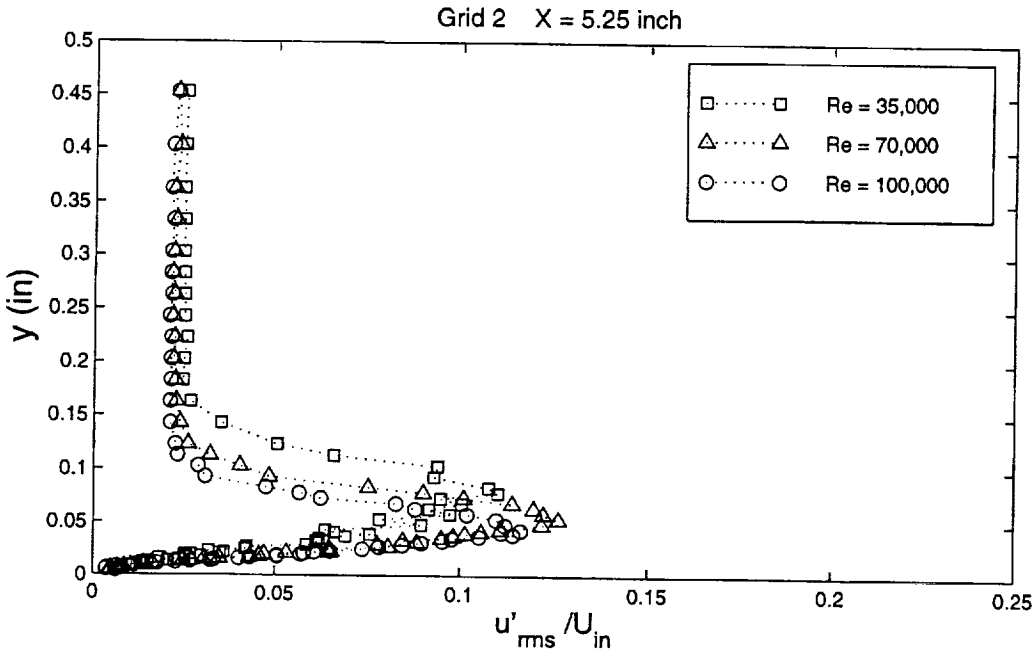

Figure 126 Variation of fluctuating velocity profiles with Re at x = 5.25 inches, Grid 2

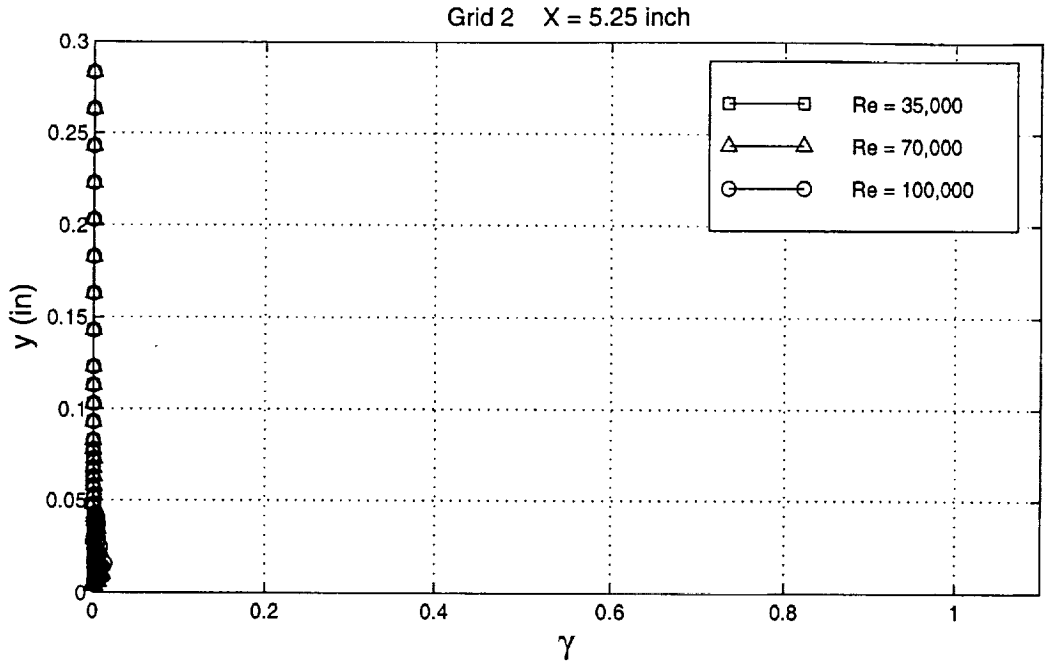

Figure 127 Variation of intermittency profiles with Re at x = 5.25 inches, Grid 2

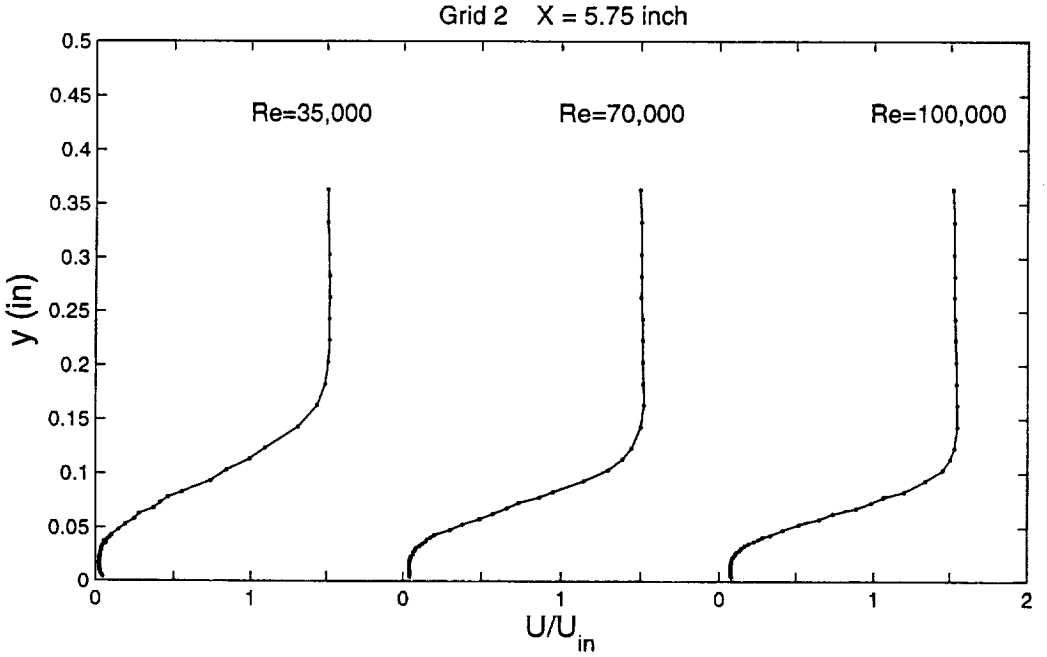

Figure 128 Variation of mean velocity profiles with Re at x = 5.75 inches, Grid 2

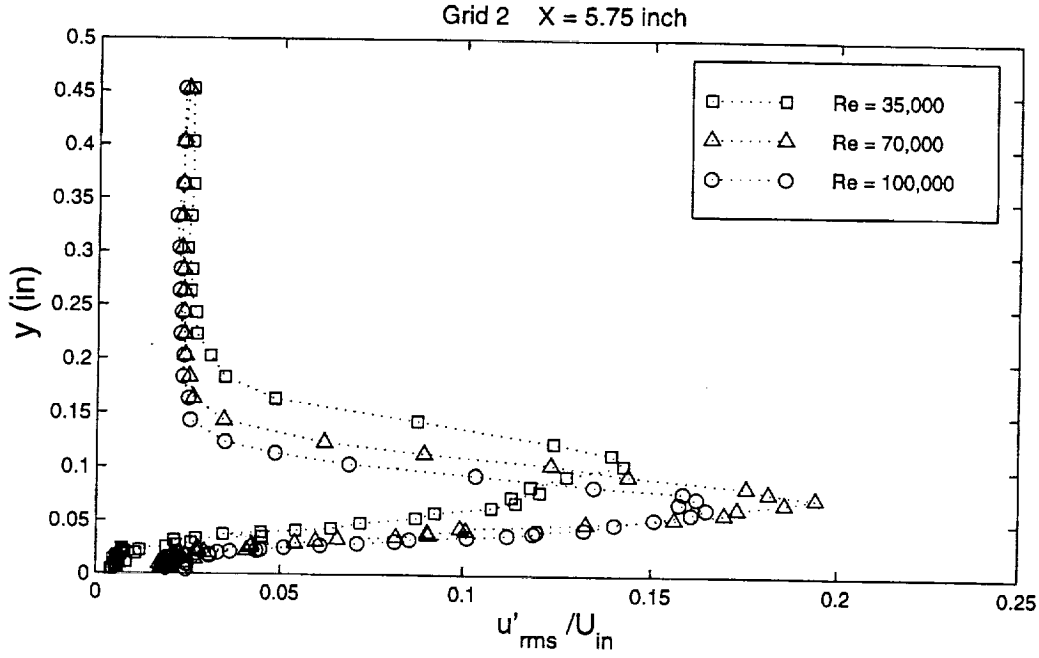

Figure 129 Variation of fluctuating velocity profiles with Re at x = 5.75 inches, Grid 2

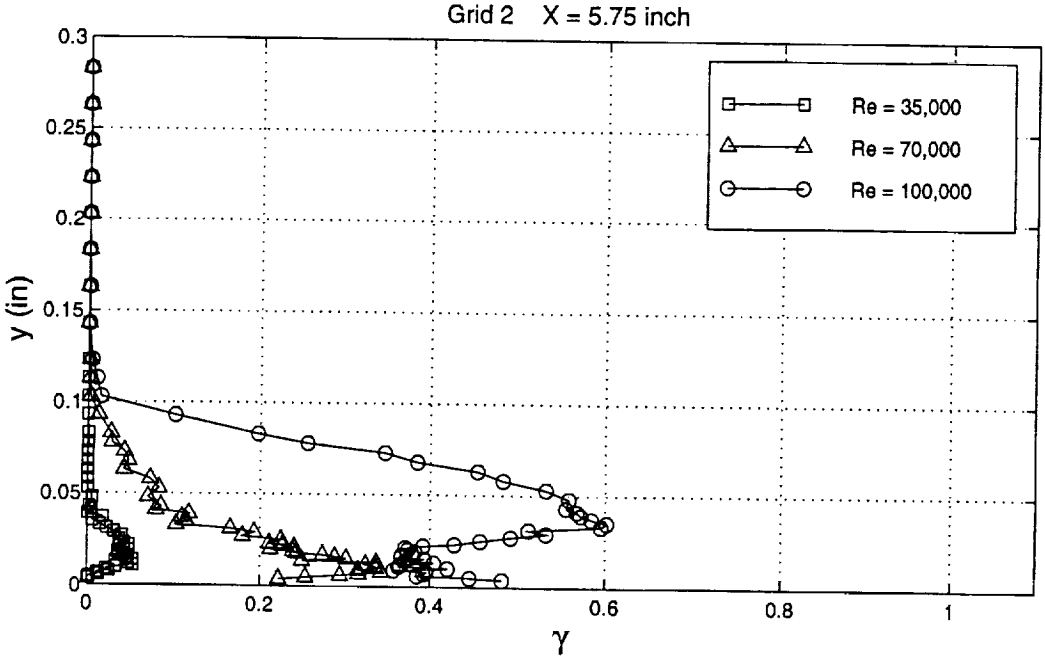

Figure 130 Variation of intermittency profiles with Re at x = 5.75 inches, Grid 2

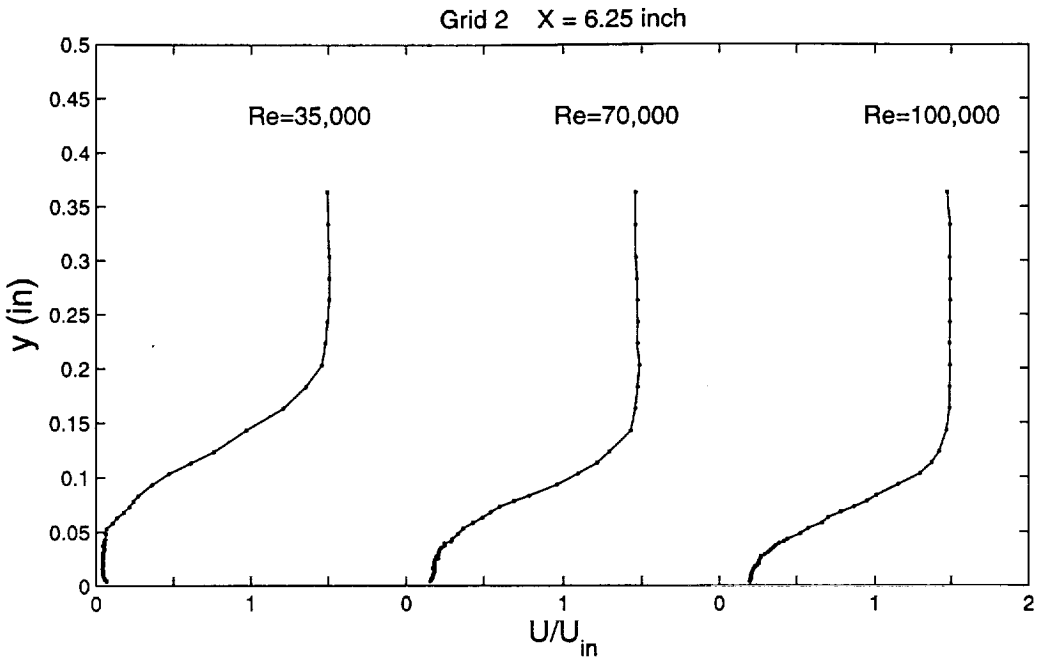

Figure 131 Variation of mean velocity profiles with Re at x = 6.25 inches, Grid 2

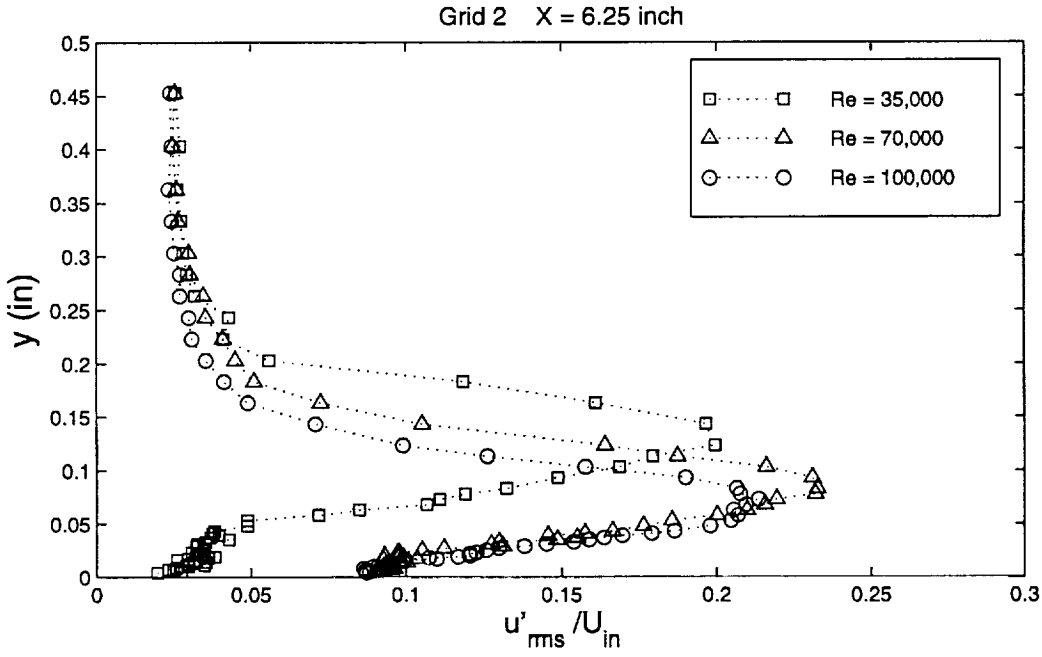

Figure 132 Variation of fluctuating velocity profiles with Re at x = 6.25 inches, Grid 2

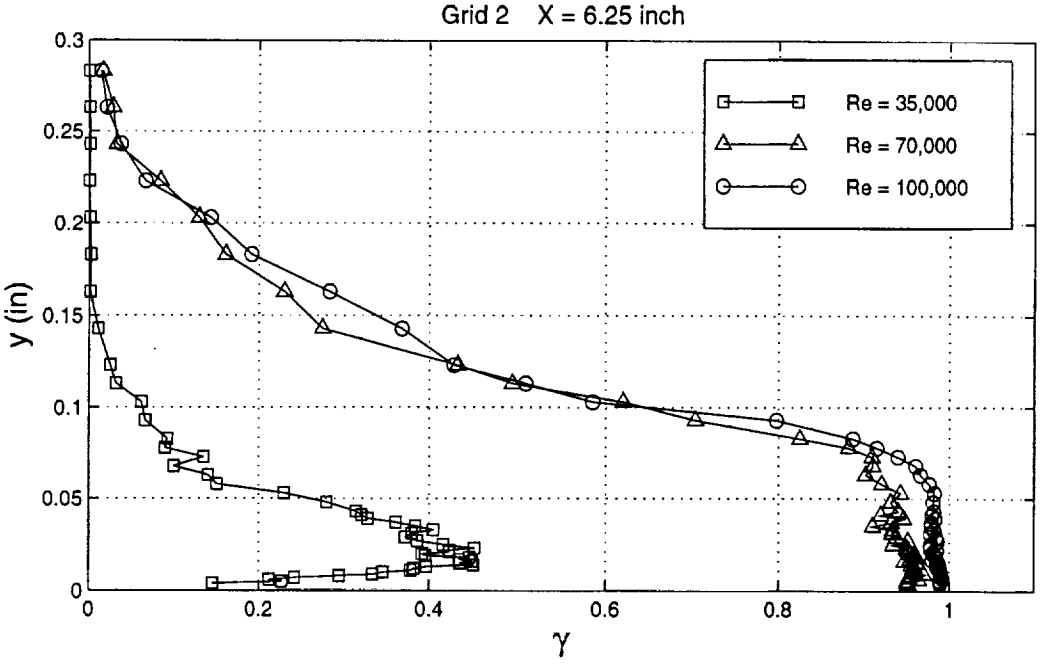

Figure 133 Variation of intermittency profiles with Re at x = 6.25 inches, Grid 2

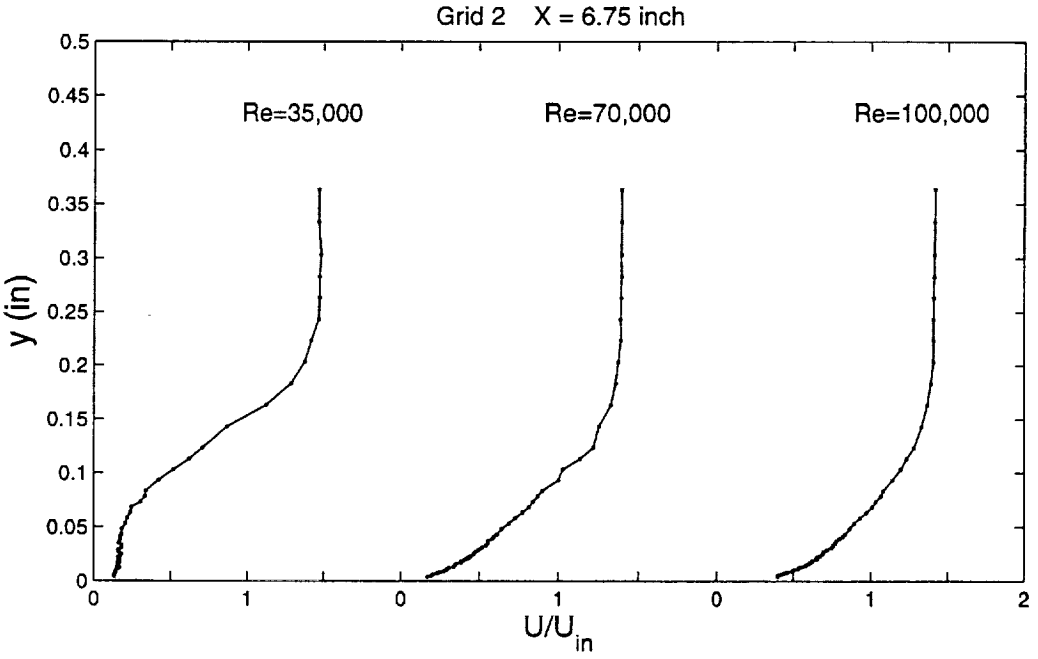

Figure 134 Variation of mean velocity profiles with Re at x = 6.75 inches, Grid 2

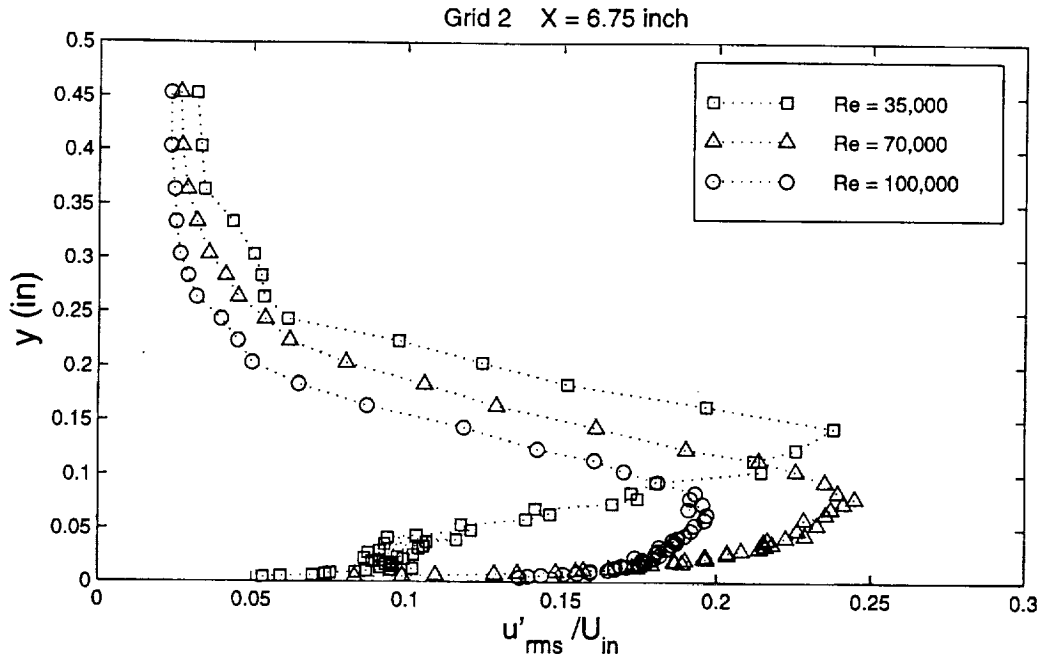

Figure 135 Variation of fluctuating velocity profiles with Re at x = 6.75 inches, Grid 2

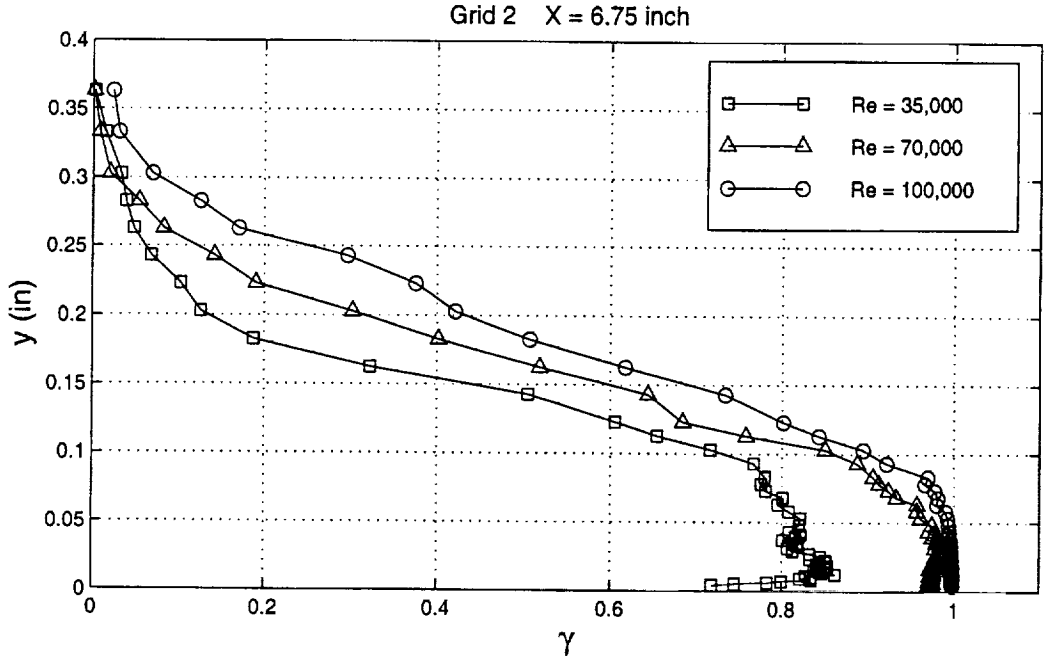

Figure 136 Variation of intermittency profiles with Re at x = 6.75 inches, Grid 2

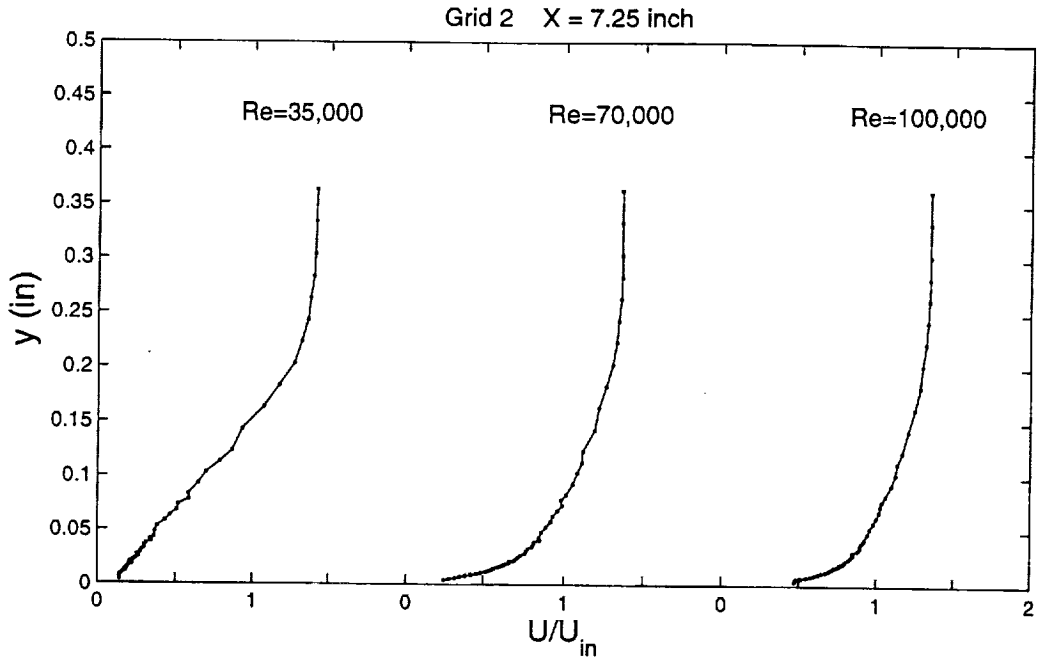

Figure 137 Variation of mean velocity profiles with Re at x = 7.25 inches, Grid 2

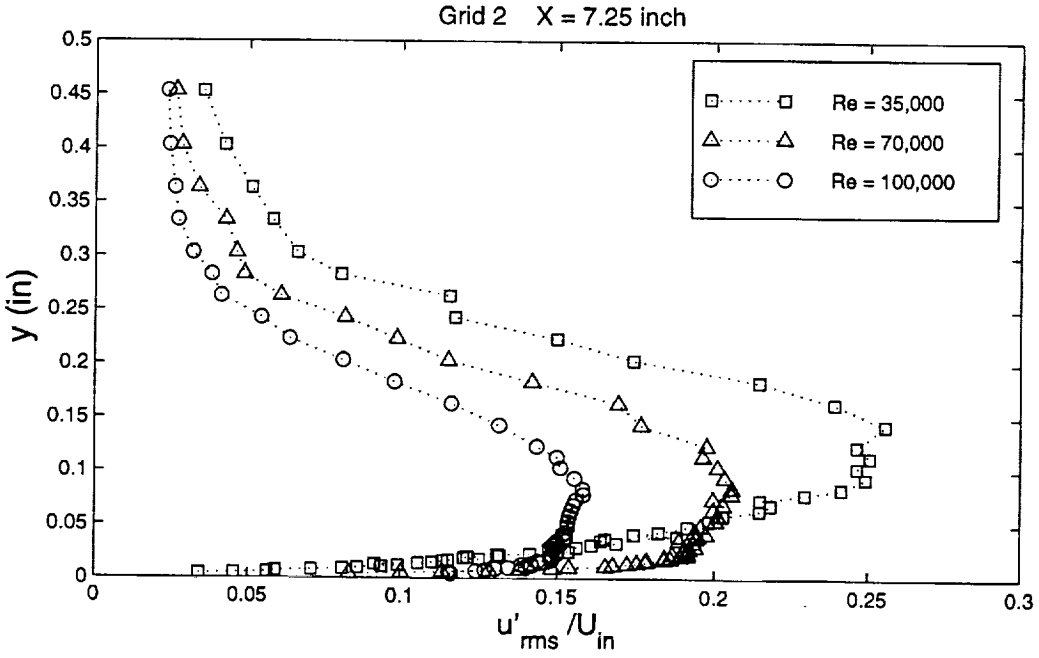

Figure 138 Variation of fluctuating velocity profiles with Re at x = 7.25 inches, Grid 2

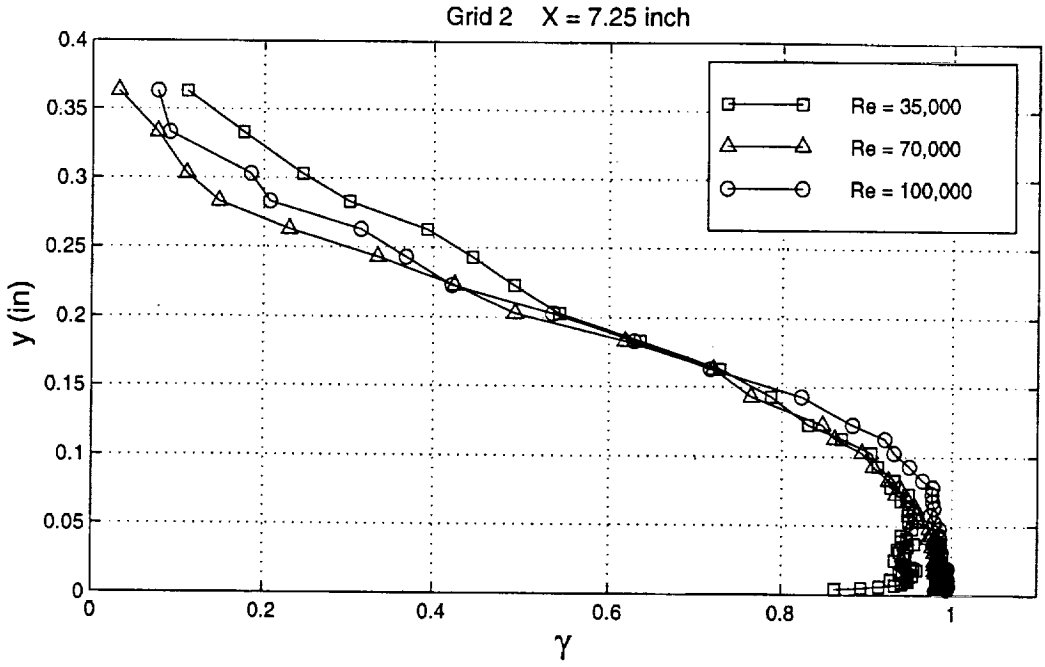

Figure 139 Variation of intermittency profiles with Re at x = 7.25 inches, Grid 2

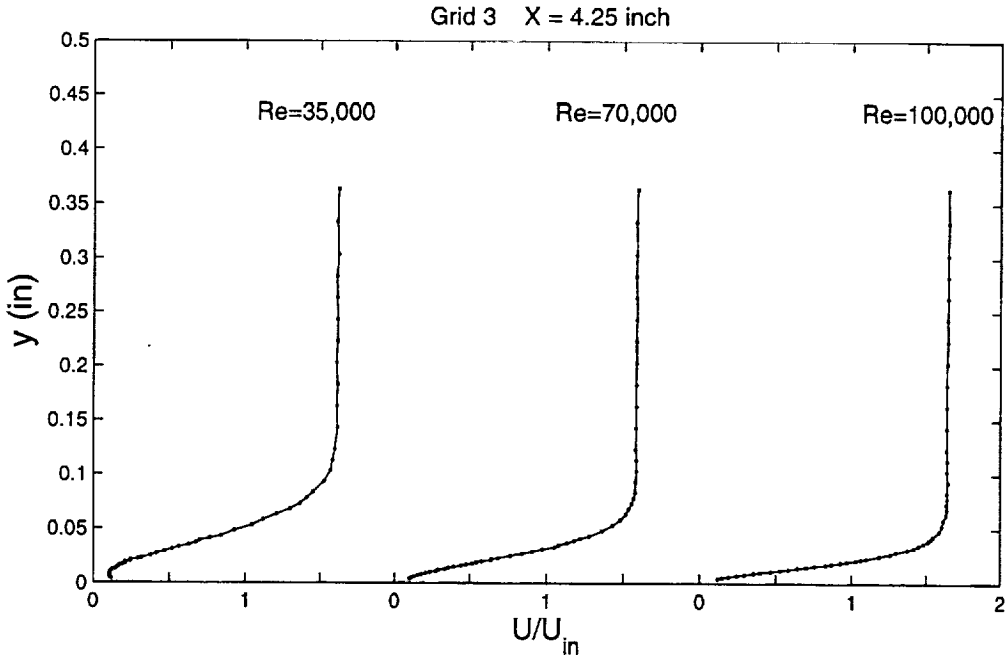

Figure 140 Variation of mean velocity profiles with Re at x = 4.25 inches, Grid 3

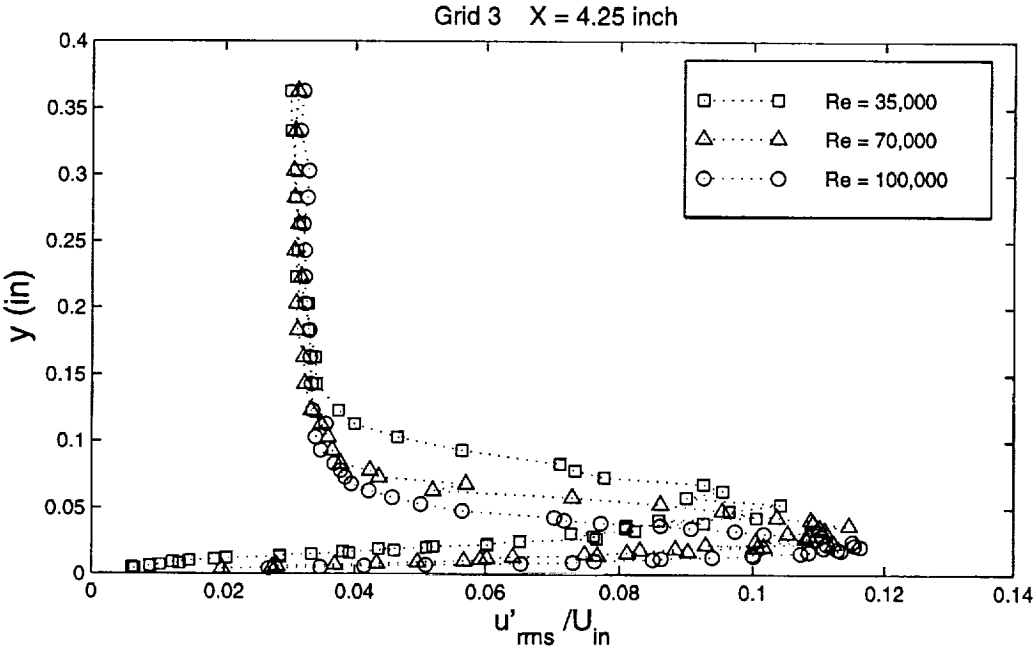

Figure 141 Variation of fluctuating velocity profiles with Re at x = 4.25 inches, Grid 3

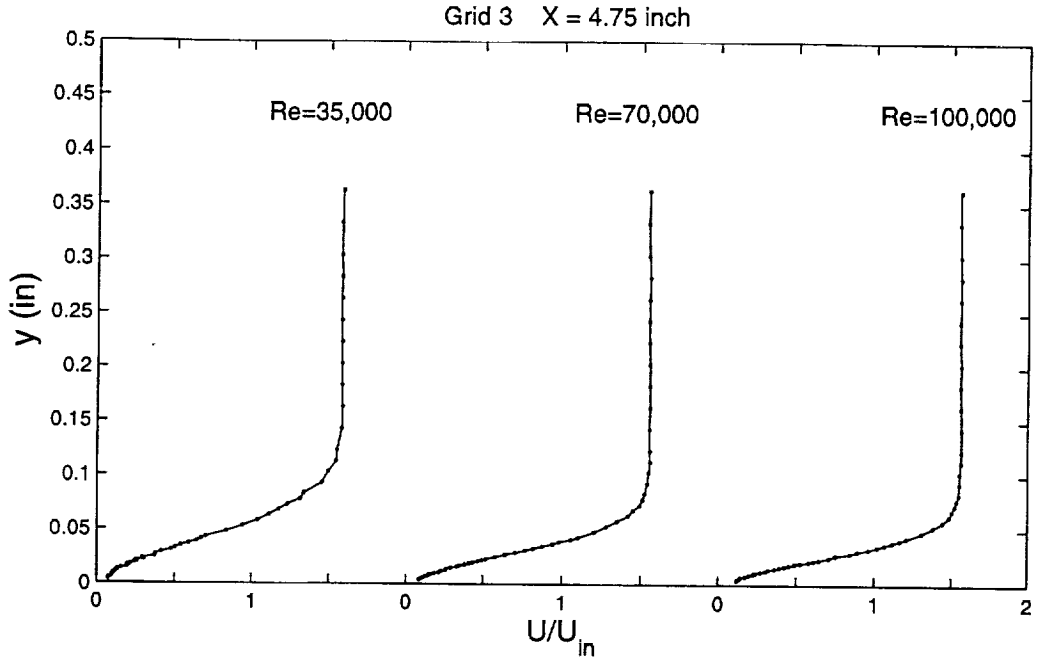

Figure 142 Variation of mean velocity profiles with Re at x = 4.75 inches, Grid 3

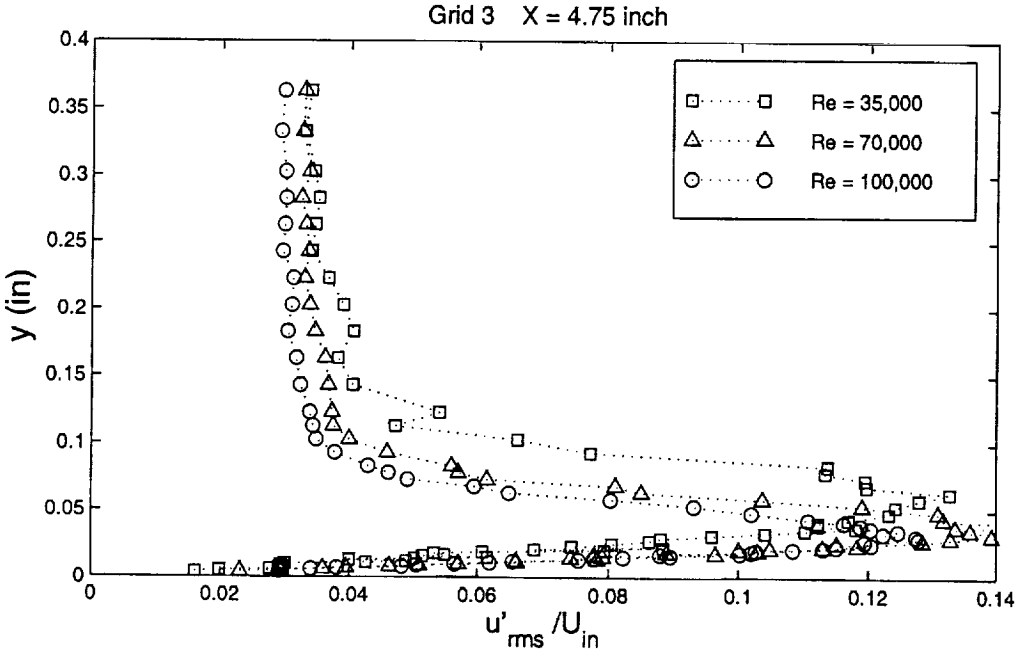

Figure 143 Variation of fluctuating velocity profiles with Re at x = 4.75 inches, Grid 3

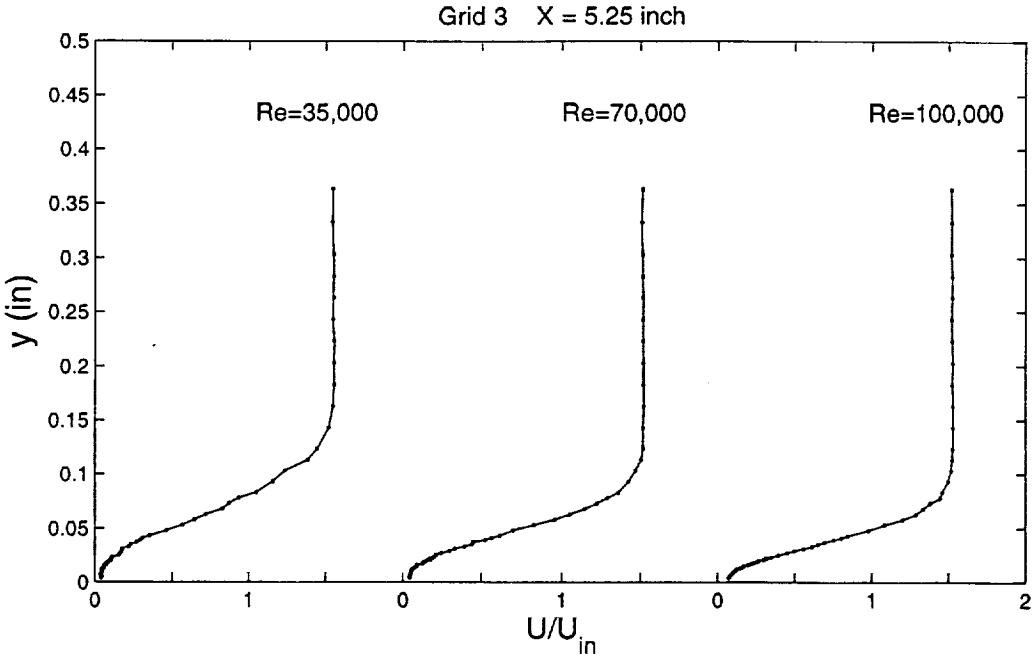

Figure 144 Variation of mean velocity profiles with Re at x = 5.25 inches, Grid 3

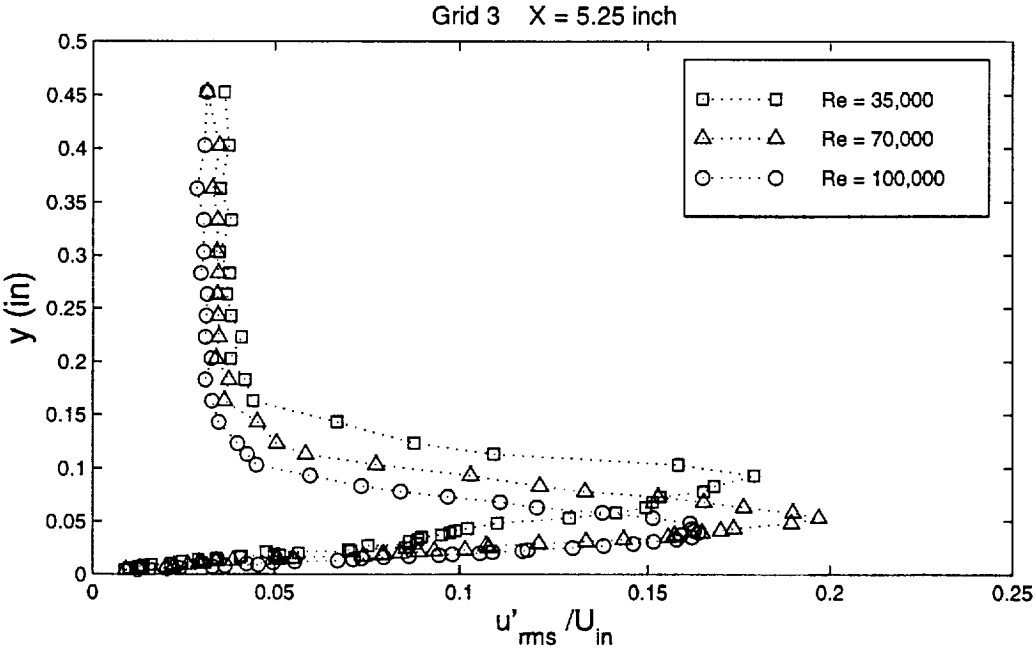

Figure 145 Variation of fluctuating velocity profiles with Re at x = 5.25 inches, Grid 3

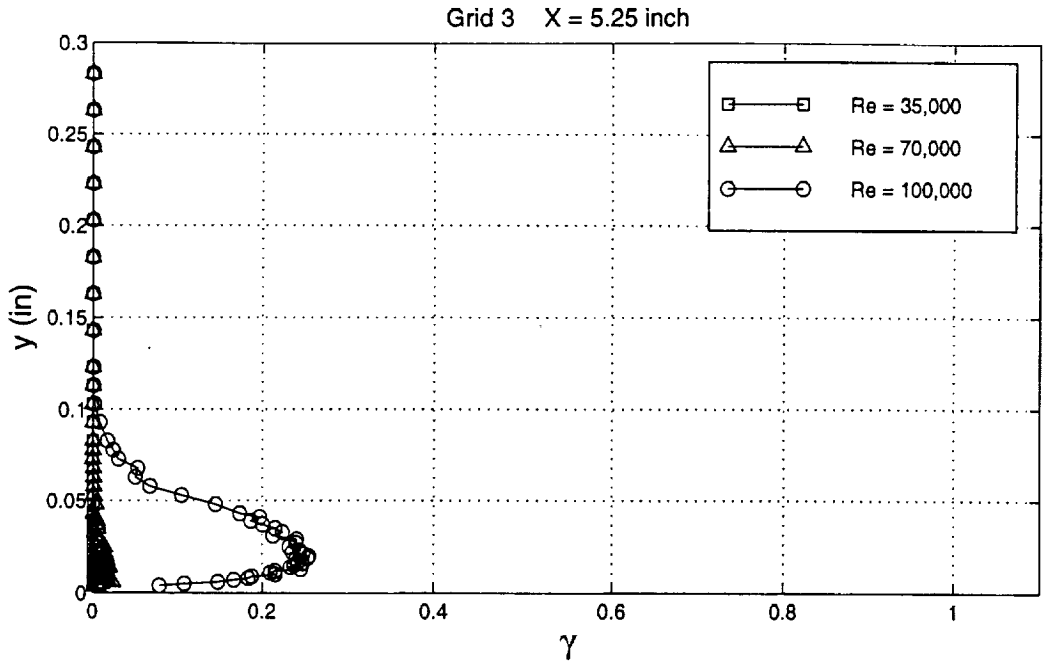

Figure 146 Variation of intermittency profiles with Re at x = 5.25 inches, Grid 3

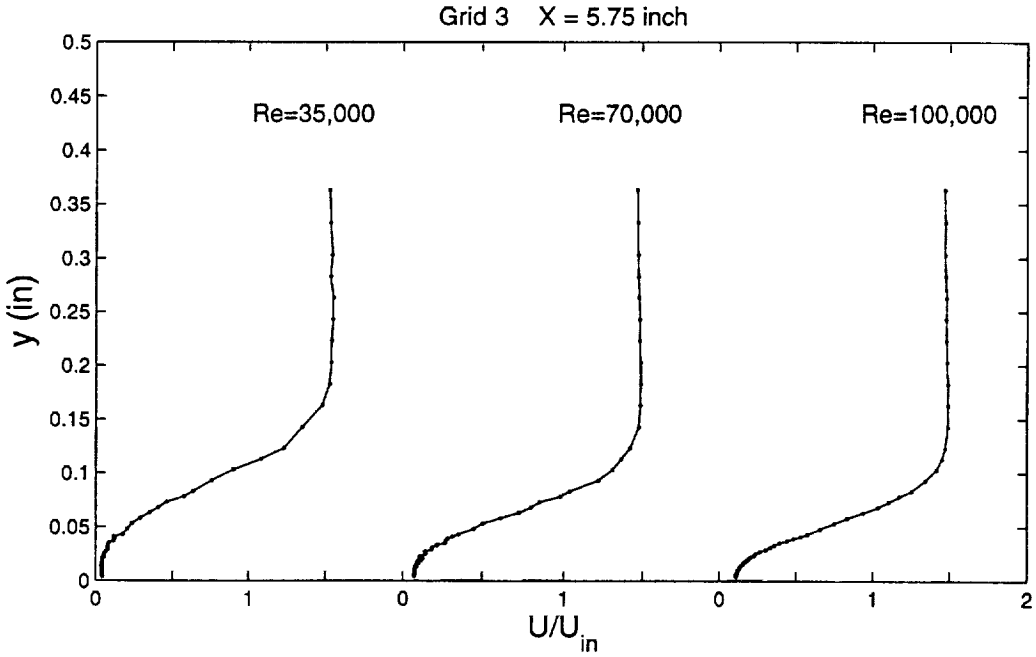

Figure 147 Variation of mean velocity profiles with Re at x = 5.75 inches, Grid 3

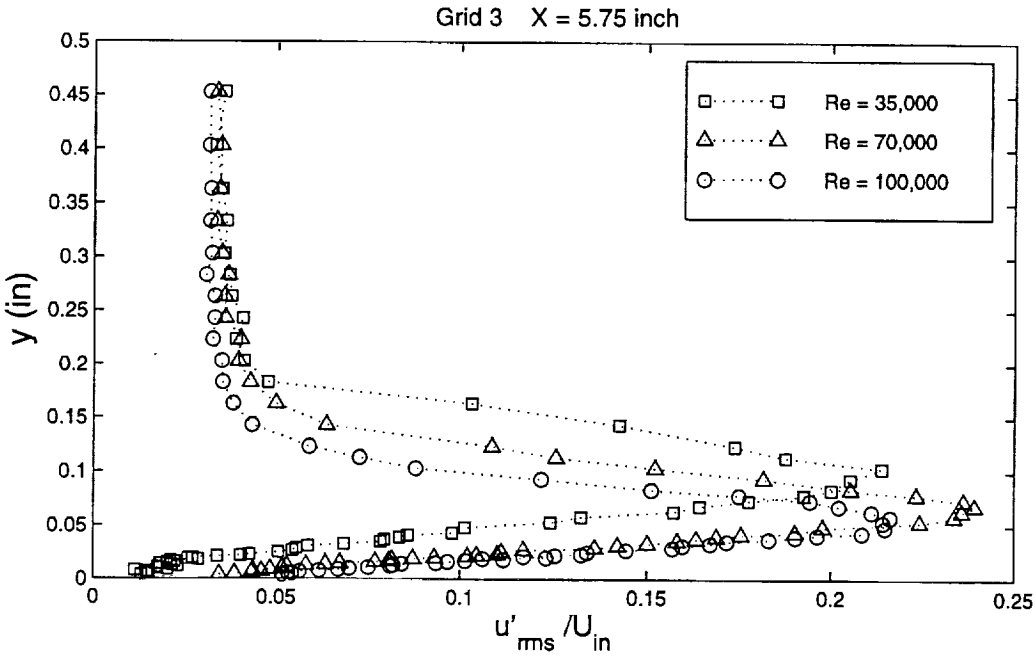

Figure 148 Variation of fluctuating velocity profiles with Re at x = 5.75 inches, Grid 3

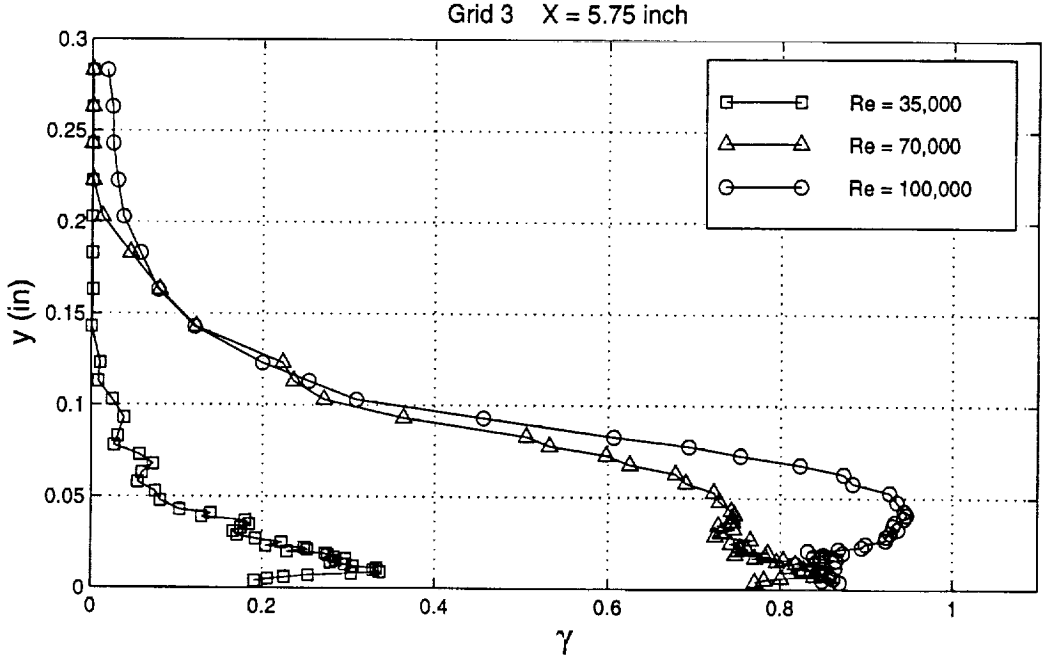

Figure 149 Variation of intermittency profiles with Re at x = 5.75 inches, Grid 3

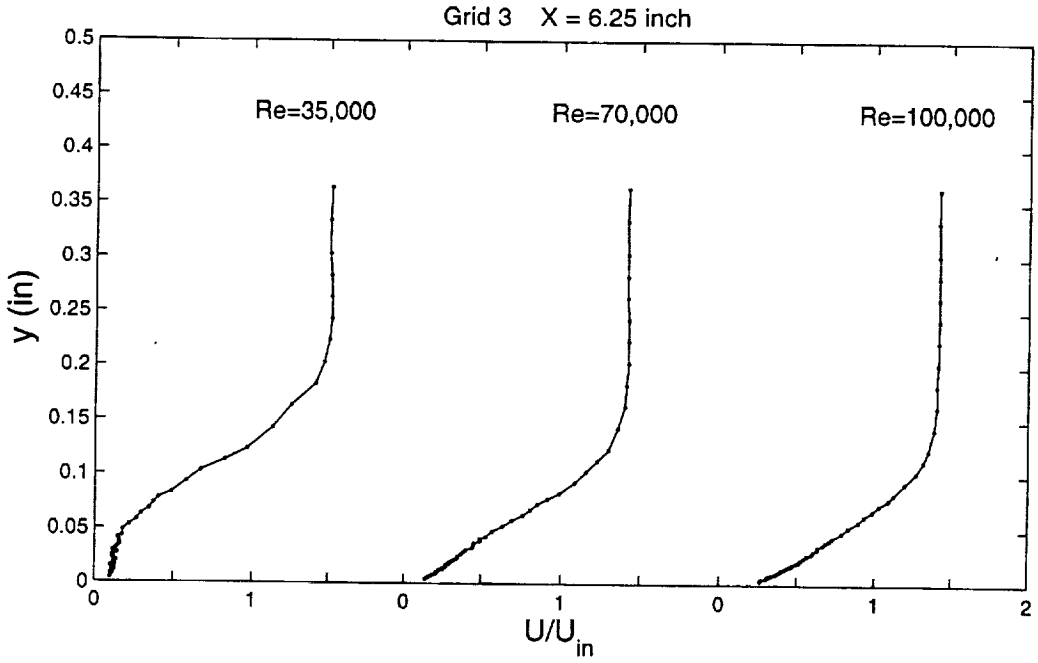

Figure 150 Variation of mean velocity profiles with Re at x = 6.25 inches, Grid 3

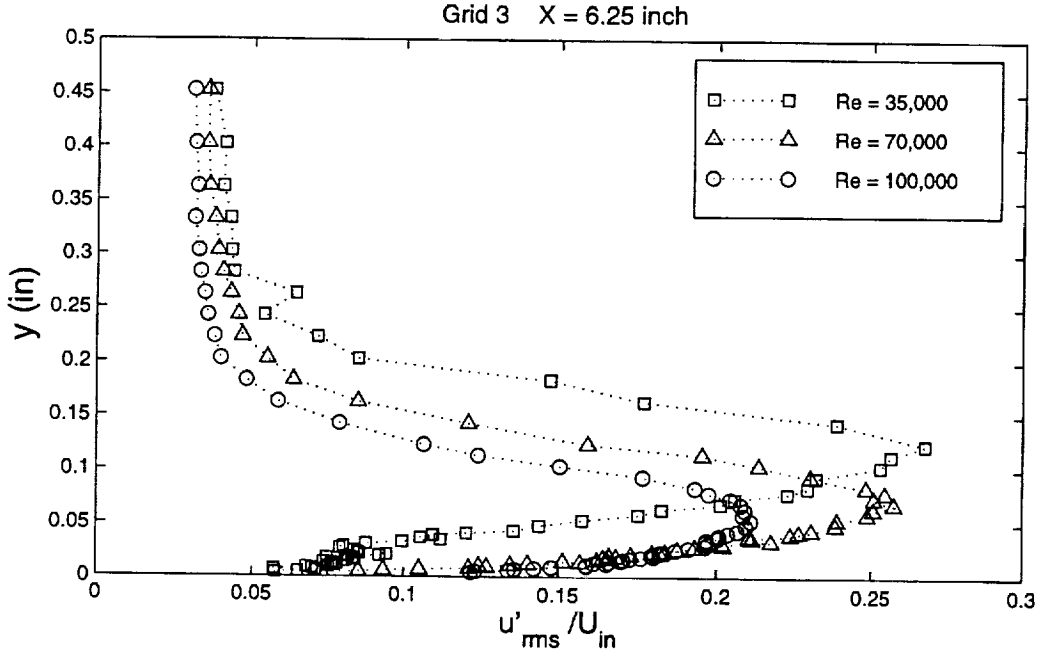

Figure 151 Variation of fluctuating velocity profiles with Re at x = 6.25 inches, Grid 3

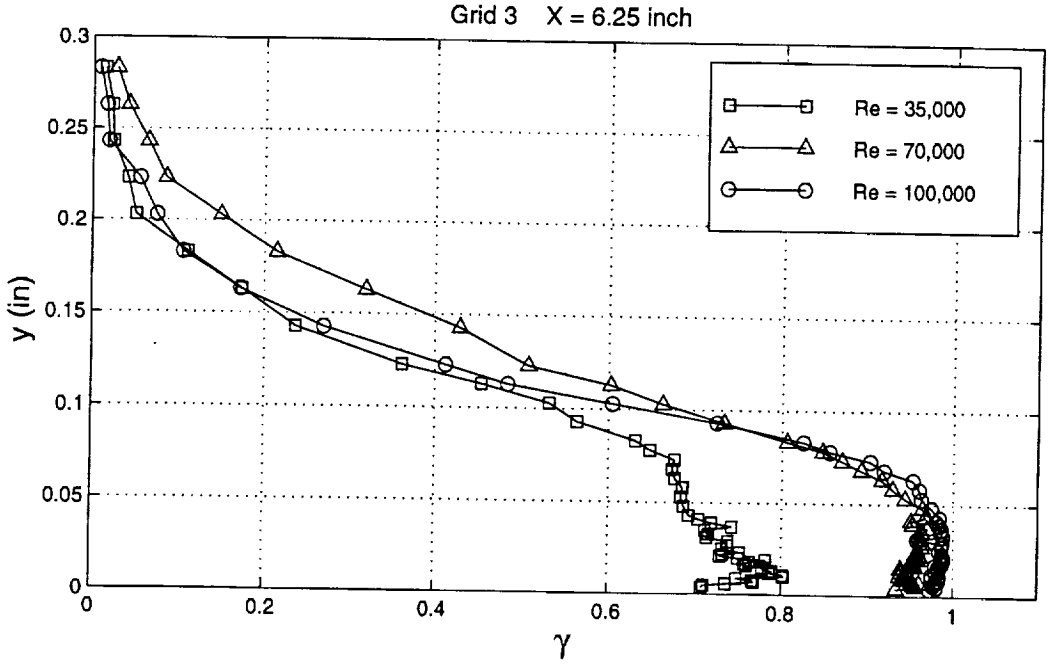

Figure 152 Variation of intermittency profiles with Re at x = 6.25 inches, Grid 3

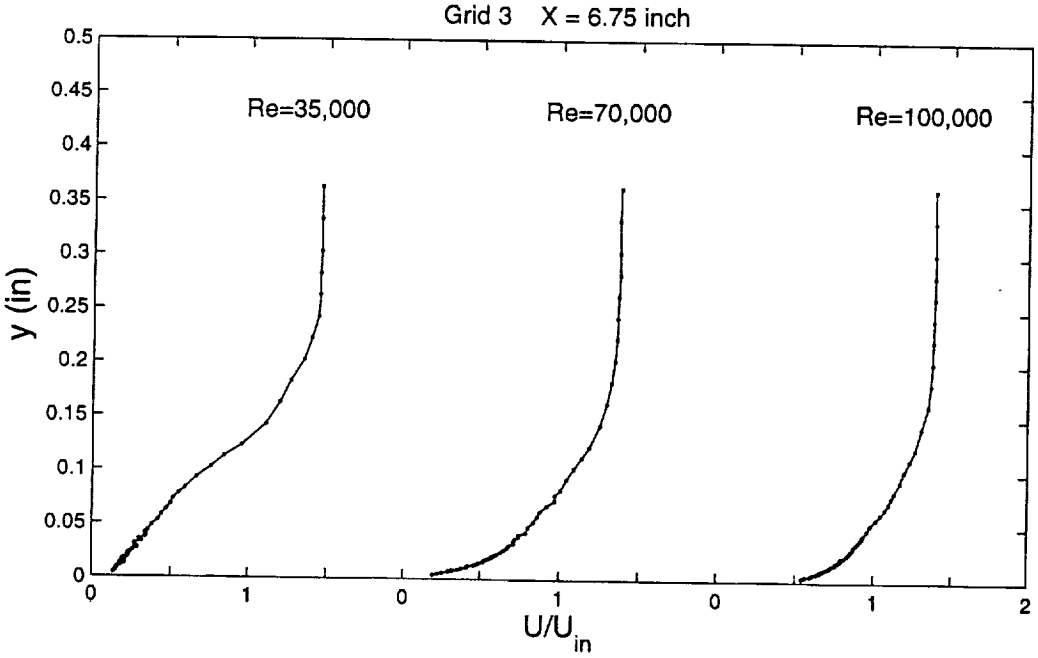

Figure 153 Variation of mean velocity profiles with Re at x = 6.75 inches, Grid 3

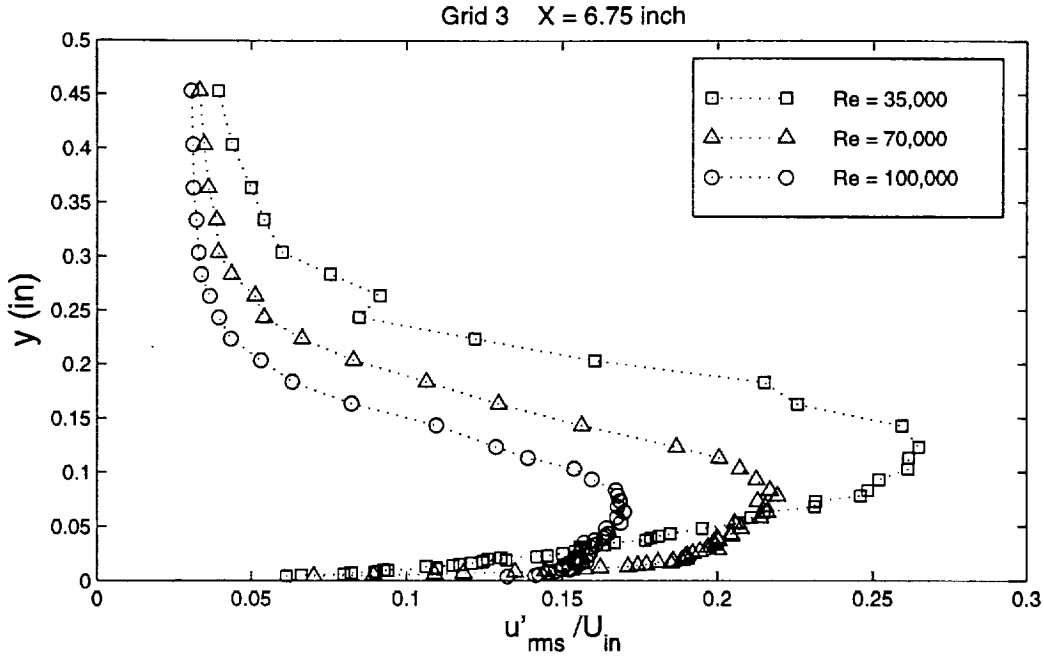

Figure 154 Variation of fluctuating velocity profiles with Re at x = 6.75 inches, Grid 3

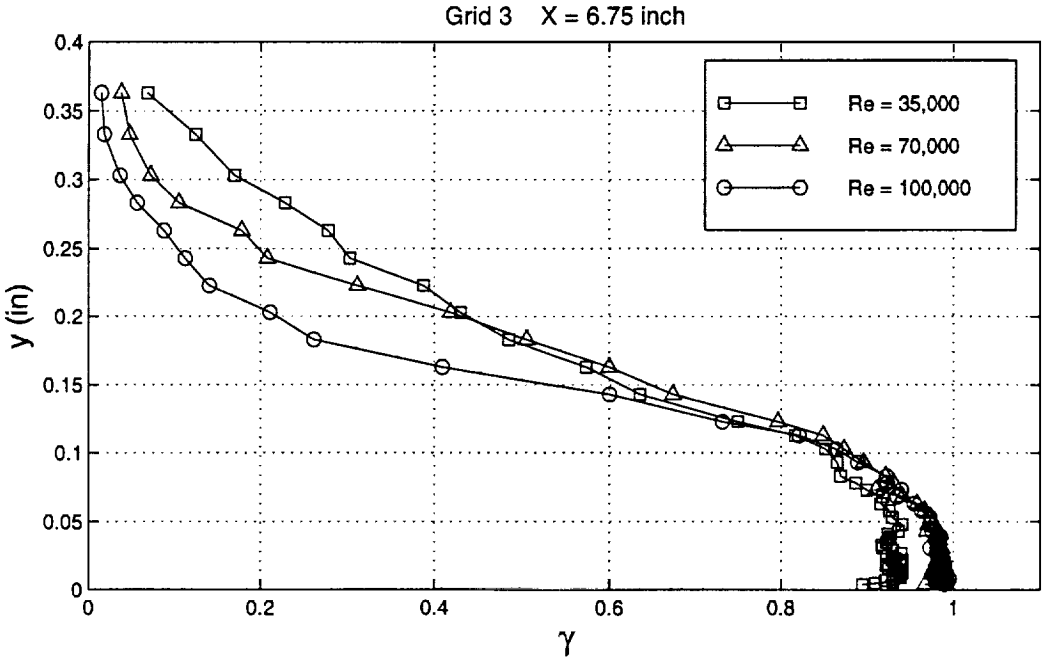

Figure 155 Variation of intermittency profiles with Re at x = 6.75 inches, Grid 3

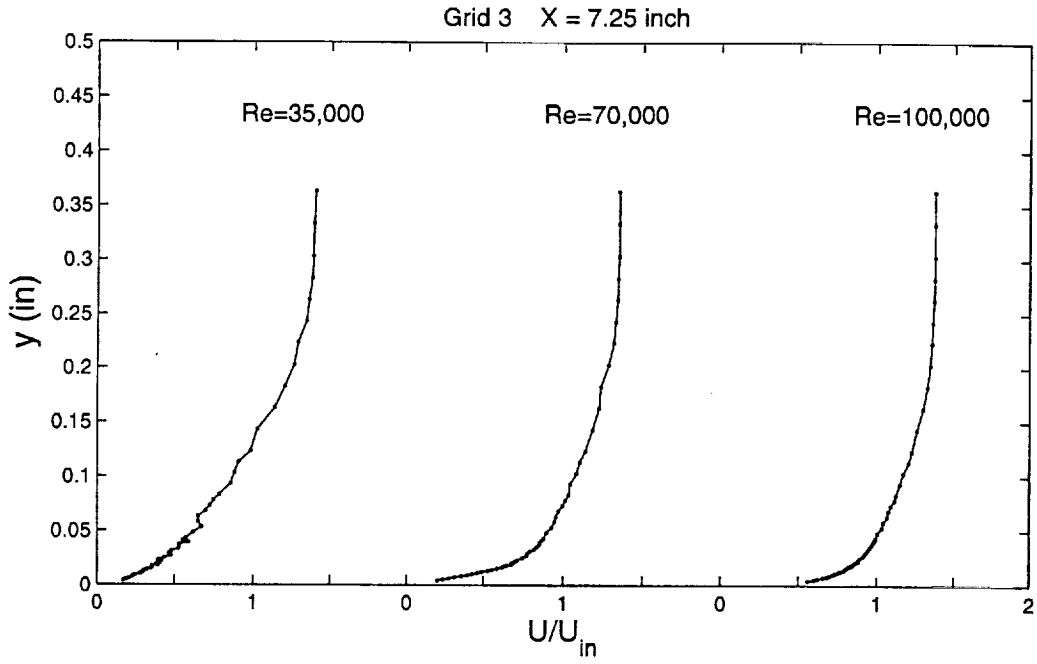

Figure 156 Variation of mean velocity profiles with Re at x = 7.25 inches, Grid 3

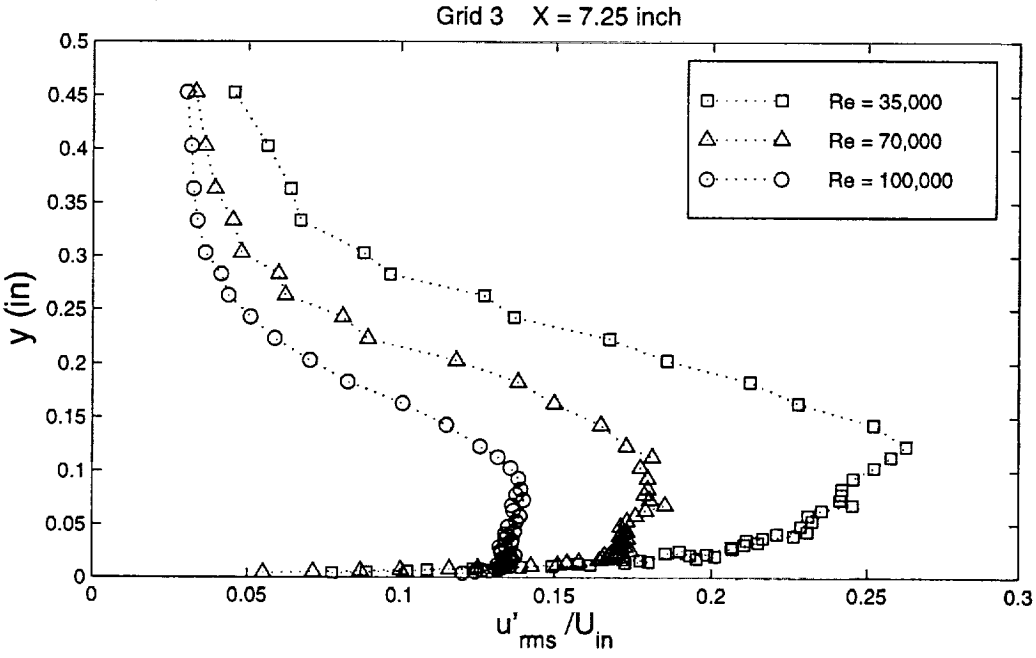

Figure 157 Variation of fluctuating velocity profiles with Re at x = 7.25 inches, Grid 3

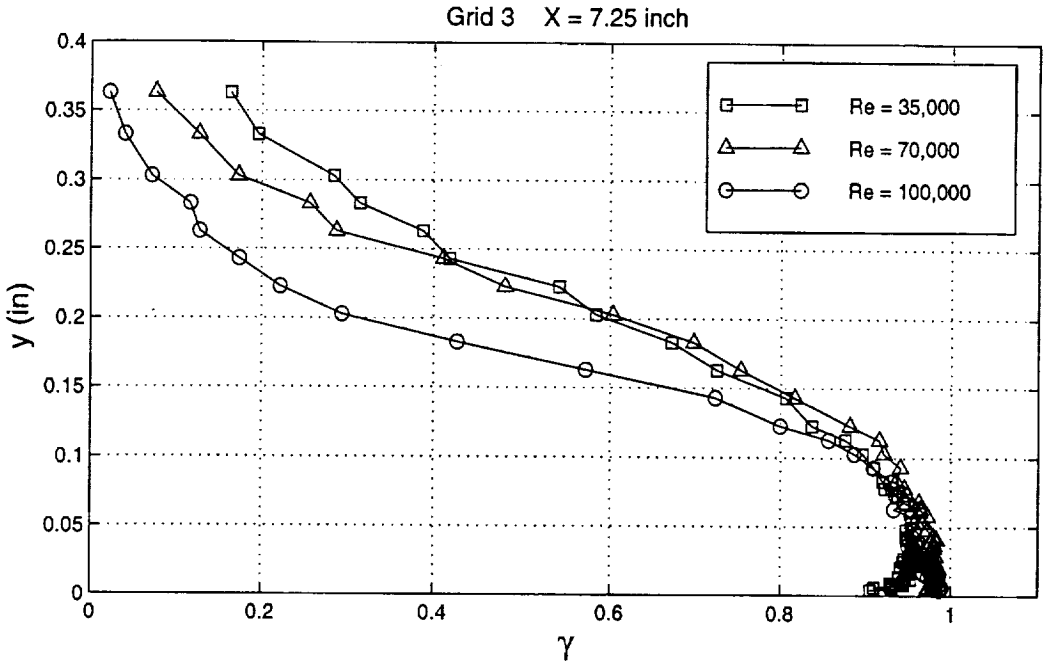

Figure 158 Variation of intermittency profiles with Re at x = 7.25 inches, Grid 3

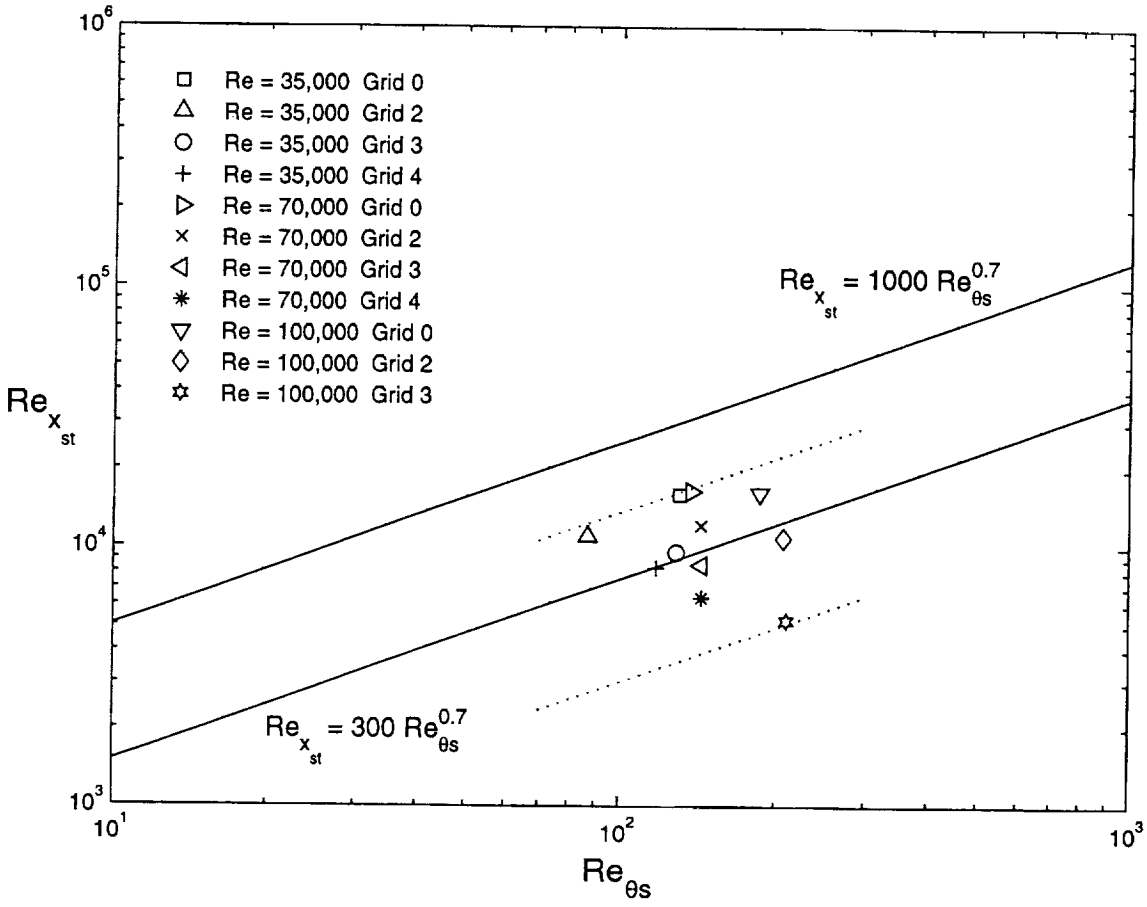

Figure 159 Variation of Reynolds number based on length between separation and start of transition ($Re_{x_{st}}$) with separation momentum Reynolds number ($Re_{\theta s}$)

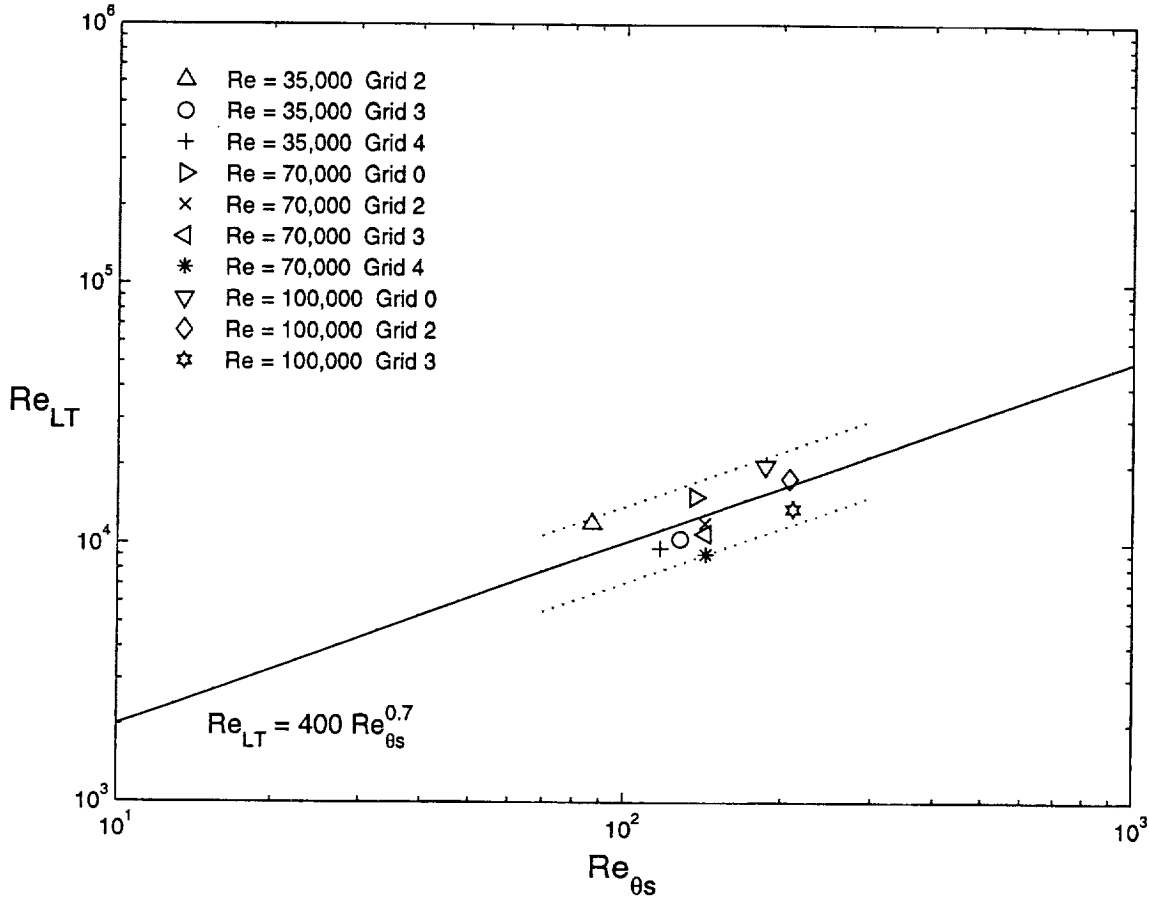

Figure 160 Variation of Reynolds number based on transition length (Re_{LT}) with separation momentum Reynolds number ($Re_{\theta s}$)

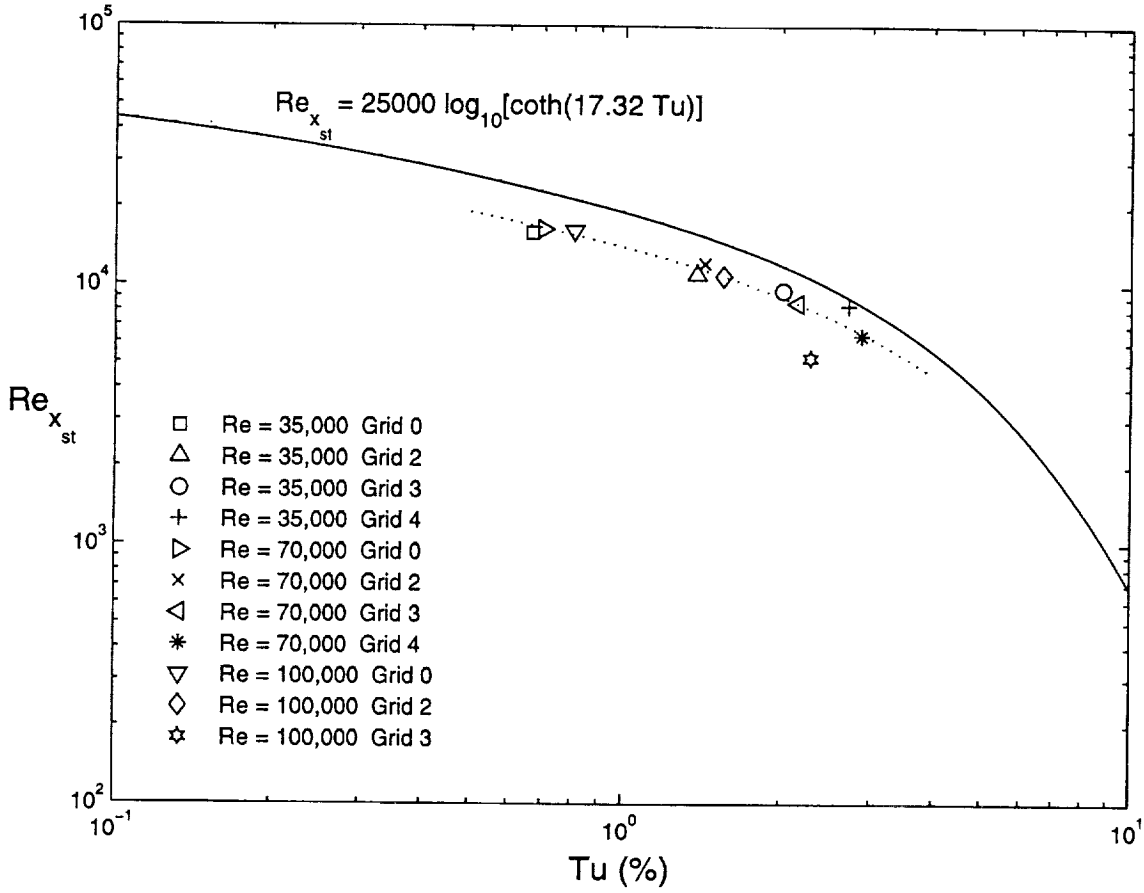

Figure 161 Variation of Reynolds number based on distance between separation and start of transition ($Re_{x_{st}}$) with local freestream turbulence level (Tu) and comparison to the modified Roberts' correlation

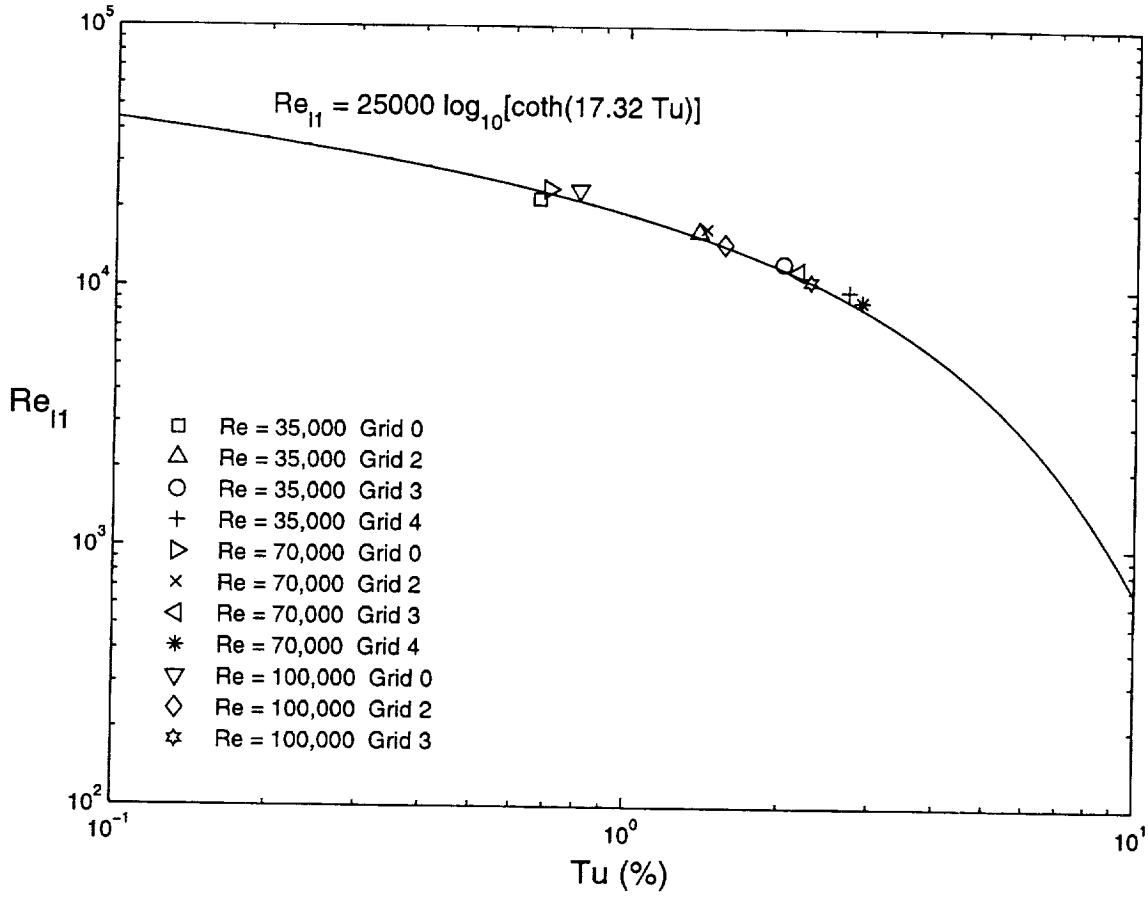

Figure 162 Variation of Reynolds number based on distance between separation and max. bubble height location (Re_{l1}) with local freestream turbulence level (Tu) and comparison to the modified Roberts' correlation